The Anatomy of Quantum Many-Body Scars: Origins and Implementations

Kieran Bull

School of Physics and Astronomy

University of Leeds

Submitted in accordance with the requirement for the degree of

Doctor of Philosophy

November 2022

The candidate confirms that the work submitted is his/her own, except where work which has formed part of jointly-authored publications has been included. The contribution of the candidate and the other authors to this work has been explicitly indicated below. The candidate confirms that appropriate credit has been given within the thesis where reference has been made to the work of others.

Chapter 4 contains work from the following publication (Ref. (16)):

Quantum scars as embeddings of weakly broken Lie algebra representations – K. Bull, J.-Y Desaules, Z. Papic, Physical Review B 101, 165139 (2020)

In this paper: I constructed an analytical derivation of previously known perturbations to the PXP model (23) which enhance scarring, by identifying a relevant error term emerging from a commutator. Discussions with collaborators about this approach led to the concept of 'broken Lie algebras'. I then proceeded to derive higher order corrections previously not known. To calculate the errors I wrote code which symbolically computes nested commutators. Using this code, I also identified perturbations which stabilise revivals from arbitrary charge density wave initial states by considering distinct representations of a broken su(2) Lie algebra. Finally, I computed all numerical results, including optimising perturbations obtained analytically with respect to fidelity revivals, verifying the deformed models stabilise scarred dynamics. The contributions of the other authors include independent analytical verification of the error terms my symbolic code produced.

Chapter 5 contains work from the following publication (Ref. (27)):

Hypergrid subgraphs and the origin of scarred quantum walks in many-body Hilbert space – J.-Y Desaules, K. Bull, A. Daniel, Z. Papic, Physical Review B 105, 245137 (2022)

In this paper: I made the initial conjecture that a broken su(2) Lie algebra responsible for QMBS may be understood from a graph theoretic approach by identifying relevant embedded hypercube structures. I identified the relevant embedded structure in the PXP model, performed numerics which identified reviving initial states and scarred eigenstates in several of the other models discussed within this paper, proposed several methods to interpolate between two graphs relevant for scarring and implemented these methods numerically to probe for scarred models. The contribution of the other authors was to propose physical Hamiltonians which lie along this interpolation, construct additional algorithms to perform the interpolation between relevant graphs, to identify relevant embedded substructures in additional scarred models and to independently verify the presence of reviving initial states and scarred eigenstates in several of the models considered.

Chapter 6 contains work from the following publication (Ref. (17)):

Systematic construction of scarred many-body dynamics in 1D lattice models – K. Bull, I. Martin, Z. Papic, Physical Review Letters 123, 030601 (2019)

In this paper: I performed all numerics, implementing many kinetically constrained PCP models, verifying they host scarred eigenstates, identifying reviving initial states and constructing phase diagrams of scarred models numerically. Furthermore, I analytically calculated equations for the lines of scarred models observed in these phase diagrams by identifying a simple criteria which predicts the presence of scarring. Finally, I made contributions to the general construction which embeds periodic unitary dynamics into a many-bodied interacting system, specifically I suggested taking the logarithm of the unitary

was a necessary step. Contributions of other authors include the initial proposal to use projector dressings to construct scarred models and interpretation of the resulting dynamics observed in clock models considered in this paper.

Chapter 7 is predominately based on currently unpublished results (to appear on arXiv), which was completed by myself, Zlatko Papic and Sonika Johri.

In this currently unpublished work: I performed all numerical work, both classically and on quantum hardware. This included MPS numerics which justify the use of a shallow depth unitary to simulate the PXP model, coding of the variational quantum algorithm used for time evolution, classical optimisations necessary to obtain values for quantum circuit ansatz parameters, classical benchmarking of the variational quantum algorithm, automating the optimisation of a given unitary circuit to prepare it for use on quantum hardware, submitting jobs to the quantum computer and interpreting the resulting data. The contribution of other authors were general arguments as to why quantum computers should yield useful results for QMBS systems, providing access to IONQ's quantum hardware and various techniques to reduce the hardware error when implementing a quantum circuit.

Abstract

Quantum many-body scars (QMBS) are a mechanism for many-body interacting systems to resist thermalisation. QMBS systems host a subset of atypical, non thermal eigenstates which are responsible for coherent oscillatory dynamics when these systems are prepared in special initial states. There exist two categories of QMBS. Firstly, there are 'exact scars', which arise due to spectrum generating algebras (SGA), resulting in perfect oscillations for all times. On the other hand, there exist 'approximate scars' (16, 116, 130), which have been observed in experiment (7) and are responsible for decaying oscillatory dynamics. The purpose of this thesis is to explain the origin of approximate scars, make predictions of new models expected to host them, and to realise approximate scarred dynamics experimentally. We show approximate scars arise due to algebraic structures analogous to SGA. These structures are known as 'broken' Lie algebras. Understanding approximate scars at the level of a Lie algebra allows us to systematically derive higher order corrections which interpolate between approximate scarring and exact scarring. In addition, for models with a single revival frequency, indicative of some su(2) algebraic structure, we introduce a complementary approach of studying embedded hypercubic structures contained within the adjacency graph of the scarred Hamiltonian. Inspired by the notions of approximate algebraic relations and embedded graph structures, we introduce a general method of constructing scarred models via kinetic constraints. Finally, by utilising the suppressed entropy growth typical of QMBS models, we implement scarred dynamics on a quantum computer.

Abbreviations

QMBS   Quantum many-body scars
ETH   Eigenstate thermalisation hypothesis
SGA   Spectrum generating algebra
RSGA   Restricted spectrum generating algebra
MBL   Many-body localisation
MPS   Matrix product state
MPO   Matrix product operator
SVD   Singular value decomposition
TDVP   Time dependent variational principle
TEBD   Time evolving block decimation
DMRG   Density matrix renormalisation group
RMT   Random matrix theory
PXP   Kinetically constrained spin 1/2 model hosting QMBS -
            defined by Hamiltonian in Eq. (2.41)
FSA   Forward-scattering approximation
S   Bipartite entanglement entropy, defined in Eq. (2.21)
ρ Density matrix
$|Z_2\rangle$ Néel state $|1010...\rangle$
I Spatial inversion symmetry operator (Parity)
$f(t)$ Fidelity (also called 'Loschmidt echo'), defined in Eq. (2.43)
$\langle r \rangle$ Mean level statistics

Contents

CONTENTS

List of Figures

LIST OF FIGURES

Chapter 1

Introduction

Many-body quantum systems with a large number of degrees of freedom are notoriously difficult to simulate classically. Describing a quantum state requires an exponentially growing number of bits in system size, due to the rapid growth of the Hilbert space. However, despite this seeming complexity, interacting systems are typically found to approach equilibrium states whose properties depend only on a single quantity - the energy density of the initial state. This is reminiscent of thermalisation of classical systems, which is well understood from statistical mechanics. Much effort has been directed towards understanding thermalisation of quantum systems, where it is now generally believed quantum systems thermalise in accordance with a conjecture known as the eigenstate thermalisation hypothesis (ETH) (25, 29, 31, 40, 123).

However, thermalisation presents problems if one wants to do useful work with quantum systems, for example, designing a quantum computer with many local degrees of freedom coupled by interactions. Interactions which result in an ETH system result in a scrambling of local information, causing the system to 'forget' its initial state, limiting the the computing potential of such devices. Therefore there has been a surge of interest in mechanisms which avoid thermalisation and violate ETH (1, 15, 80, 102, 119). The most well known mechanism is integrability (128), where a many-body quantum system hosts an extensive number of symmetries. Many-body localisation (MBL) (5, 49, 117), an analogue of Anderson localisation in many-body disordered systems, offers another way of avoiding thermalisation. MBL systems are similar to integrable systems, as they

1. INTRODUCTION

also possess an extensive number of conserved local integrals of motion (LIOM) (21, 61, 87, 105). MBL and integrability result in a complete lack of thermalisation, due to the additional conserved quantities, such that these systems may be said to strongly violate the ETH.

Quantum many-body scars (QMBS) (79, 116) are another mechanism for avoiding thermalisation, differing from the previous two methods in that QMBS systems only weakly violate the ETH. This is in the sense that a system hosting QMBS will avoid thermalisation when initialised in a few, special initial states, but will generically thermalise from all other initial states. Moreover, QMBS systems generally feature robust oscillatory dynamics when initialised in these special initial states. Absence of thermalisation and oscillatory dynamics in QMBS systems has been found to occur due to the presence of *scarred eigenstates* - a subset of eigenstates with atypical thermal properties. While the existence of these scarred eigenstates explains the atypical thermal behaviour of QMBS systems, it is still largely an open problem why these eigenstates are present in the model in the first place.

In this thesis we introduce theories which aim to understand the origin of QMBS. Our approach consists of studying algebraic structures which gives rise to scarred eigenstates. We further introduce a complementary graph-theoretic approach, yielding predictions of new models hosting QMBS. By considering how to engineer these algebraic structures using kinetic constraints, we also introduce a general construction of QMBS models. Finally, we simulate oscillatory scarred dynamics on real quantum hardware, demonstrating the practicality of simulating systems which resist thermalisation.

In Chapter 2, we review concepts pertaining to thermalisation, glossed over in this introduction. Specifically, we review the eigenstate thermalisation hypothesis (ETH) and its relevance for non-integrable many-body interacting quantum systems. We then proceed to discuss ways in which the ETH may be violated, where we are particularly interested in examples of weak ETH violation. Finally, we review experimental results from a 51-Rydberg atom simulator (7), which appears to weakly violate the ETH. By mapping the simulator to a kinetically constrained spin chain, called the 'PXP' model (130), we verify numerically the absence of thermalisation in this system.

In Chapter 3 we give an overview of quantum many-body scars (QMBS). We study the spectral properties of the PXP model (131), revealing a subset of atypical non-thermal eigenstates which is the defining property of quantum many-body scarring. We then proceed to review other mechanisms for which non-thermal eigenstates may arise, such as 'projector embeddings' (119) and Krylov restricted thermalisation (80). These mechanisms motivate an idealised limit of QMBS, so called 'exact' scarred models, which contrast with the QMBS observed in experiments now referred to as 'approximate' scars. By reviewing the underlying algebraic structure necessary for exact scarring, we provide the necessary background to understand the remainder of the thesis, which aims to explain the origin of 'approximate' scarred models.

In Chapter 4 we introduce the concept of a 'broken' Lie algebra representation as a mechanism for engineering approximate scarred models. We introduce a systematic way of deriving successively higher order correction terms to this Lie algebra, resulting in an interpolation between approximate and exact scarred models. We demonstrate this approach with the PXP model, successfully stabilising revivals from arbitrary charge density wave product states.

In Chapter 5 we introduce a graph-theoretic interpretation of scarred models with a single revival frequency, indicative of some su(2) algebraic structure. This framework compliments the broken Lie algebra approach discussed in Chapter 4, as it seeks to understand scars from embedded hypercubic structures in the adjacency graph of the scarred Hamiltonian, and hypercubic adjacency graphs are isomorphic to models with su(2) symmetry. We interpolate between a free paramagnet (full hypercube) and the PXP model using several methods, revealing new approximate scarred models for which we identify embedded hypercubic structures relevant for scarred dynamics.

Chapter 6 builds upon ideas in the previous two chapters, introducing a general construction of approximate scarred models via the use of kinetic constraints. We give an explicit example of this construction with 'scarred clock models'.

Finally in Chapter 7 we introduce a variational approach to simulating scarred dynamics on quantum computers, implementing the dynamics of the PXP model on IONQ's trapped ion platform.

1. INTRODUCTION

Chapter 2

Quantum ergodicity and its breakdown

In this chapter we review the concept of thermalisation, in the context of many-body quantum systems. Although dynamics in quantum systems is generated by the application of a unitary propagator and is therefore fully reversible, one can still define notions of thermalisation and equilibration if one considers local quantities. We begin by reviewing concepts related to thermalisation in a classical context, defining properties such as ergodicity, chaos and integrability. We then discuss analogous definitions of these concepts in a quantum setting, introducing the eigenstate thermalisation hypothesis (ETH) and its consequences for non-integrable systems (25, 29, 31, 40, 123).

Next we proceed to review ways in which the ETH may be violated. This can be in a strong sense, such as with integrability (128) or many-body localisation (49), or in a weak sense, such as with single particle quantum scarring (46, 73).

Finally, we review results from a recent experimental quench of a 51 Rydberg atom simulator (7), a many-body interacting system which appears to exhibit weak ergodicity breaking, similar to single particle quantum scarring. We will derive an effective model of this experimental Hamiltonian, the so called 'PXP' model (130), which is a kinetically constrained spin chain. We conclude by presenting numerical result which verify the presence of weak ergodicity breaking in the PXP model.

2.1 Thermalisation in classical systems

Before discussing thermalisation of quantum systems, we first review what thermalisation means in the context of classical systems, including related concepts such as ergodicity and chaos. Extending definitions of well known properties of classical systems, such as chaos, to quantum systems, is more difficult than one would naively expect. Nevertheless, a firm intuition of what these concepts means classically will prove useful in the quantum setting.

Consider a classical system with n degrees of freedom. Formally, this system is deterministic, and the state of the system may be described by $2n$ parameters, n position coordinates $\vec{x}$ and n momenta coordinates $\vec{p}$. The state of the system therefore resides in a $2n$ dimensional space $\vec{r} = \{\vec{x}, \vec{p}\}$, known as phase space. Upon initialising the system in a possible configuration, it will evolve according to Hamilton's equations of motion (66), which generate a trajectory in the $2n$ dimensional phase space.

Now consider the case where the number of degrees of freedom n is assumed to be extremely large. Such a scenario is typical of everyday, macroscopic objects we encounter. While in theory the state of this system at any time is described by $2n$ variables, in practice, it is well known fact that one only needs to utilise a few macroscopic variables to describe the average properties of this system at any given time. Furthermore, macroscopic objects which we encounter in our day to day lives appear rather static, that is, they are in equilibrium, such that their macroscopic properties are not changing, even though their phase space coordinates may be evolving continuously. In the Newtonian language of a trajectory in phase space, equilibrium values of local observables may be computed by evolving the initial configuration in phase space under Hamilton's equations and taking long time averages over this trajectory:

$$\langle O \rangle_{\text{eq}} = \lim_{t \to \infty} \frac{1}{t} \int_0^t O(\vec{x}(t)), \vec{p}(t)) dt \tag{2.1}$$

For a very high dimensional system, obtaining the precise trajectory in phase space to calculate the above integral becomes practically impossible.

Statistical mechanics is a different framework which yields successful predic-

tions of equilibrium values (95). Rather than being concerned with trajectories in phase space, one instead pursues a description of the system in terms of probability distributions, by assigning a certain probability for the system to be in a specific *microstate* (which corresponds to a single configuration in phase space $\vec{r} = \{\vec{x}, \vec{p}\}$). A common approach is to take the *microcanonical ensemble*, where one assigns an equal probability to every microstate with equal energy. In statistical mechanics, equilibrium values of observables are then calculated as ensemble averages over all microstates, weighted by the probability to be in a given microstate. For Hamiltonian systems energy is conserved. Therefore, to calculate equilibrium values, one needs only average over all microstates in phase space of the same energy. For the microcanonical ensemble this becomes:

$$\langle O \rangle_{\mathrm{eq}} = \frac{\int_E O(\vec{r}) d^{2n}\vec{r}}{\int_E d^{2n}\vec{r}} \tag{2.2}$$

But why should the equilibrium value obtained as an average over all states in phase space, Eq. (2.2) be equivalent to the value obtained as an average over a particular trajectory in phase space, Eq. (2.1)? What justifies the microcanonical ensemble?

An *ergodic* hypothesis provides the link between these two approaches. An ergodic system is one which evolves in time to explore all possible states. For Hamiltonian systems which conserve energy, this means that for any arbitrary initial configuration with some particular energy E, over time the system will explore the full phase space constrained along this energy surface. This energy surface will also be covered uniformly by the trajectory as a consequence of Liouville's theorem (95). A cartoon describing an ergodic trajectory is shown in Fig. 2.1(a). For this scenario, it becomes obvious that the long time average over an ergodic trajectory is equivalent to an average over all of phase space constrained along the energy surface.

A natural question which then arises is how can one know if an ergodic hypothesis is justified, such that one can compute equilibrium values using the microcanonical ensemble? Indeed, ergodicity has been proven explicitly for only a relatively few classical systems, such as 'Sinai billiards', a system comprising a set of hard spheres bounded by some volume (86, 121). A somewhat easier

(a) Ergodic   (b) Integrable
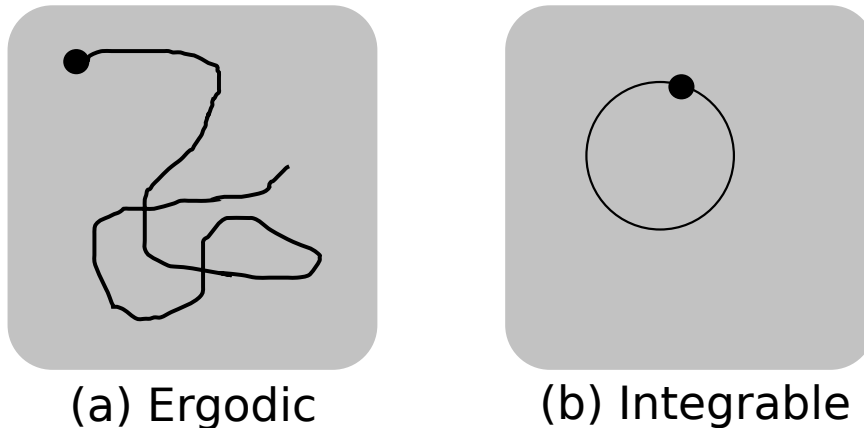
Figure 2.1: Different types of trajectories possible in a classical phase space consisting of position and momenta coordinates. (a) Corresponds to an ergodic trajectory, which explores the whole phase space given enough time, covering the space uniformly. As a consequence of this uniform exploration, equilibrium values of functions on phase space, which may be obtained by averaging over the trajectory, Eq. (2.1), may be equivalently calculated by averaging over the entire phase space, Eq. (2.2). (b) Corresponds to a quasi-periodic trajectory, typical of an integrable system, which possess an extensive number of conserved quantities, constraining possible trajectories.

question to answer is when can it be known for certain that a system is not ergodic? *Integrable* systems (3) are defined as systems possessing an extensive number of conserved quantities, known as integrals of motion, which are identified by commuting Poisson brackets with the total energy function (the *Hamiltonian* function). Integrable systems do not exhibit ergodic trajectories. The conservation of these integrals of motion constrains the permitted phase space to regions where these quantities are constant, resulting in trajectories that are generally quasi-periodic (3) (Fig. 2.1(b)) so that an ergodic hypothesis is no longer justified. By defining non-integrable systems as systems which only conserve energy and have only a small number or no additional integrals of motion, it is still not obvious if all non-integrable systems are generally ergodic. Even if the majority of trajectories may be ergodic, there may still exist some which are periodic. This is the case for a system of billiards in a Bunimovich stadium (18, 19), as shown in Fig. 2.2. This scenario would be described as 'weak ergodicity breaking' in a classical context - it is a termed 'weak' as only a few trajectories are

non-ergodic, in contrast to integrable systems, which would constitute 'strong ergodicity breaking', as all initial configurations result in non-ergodic trajectories. Nevertheless, it is found that weak ergodicity breaking, as is the case with billiards, is a rare phenomena, and generally, as the number of degrees of freedom $n \to \infty$, the fraction of quasi periodic orbits becomes vanishingly small (33), resulting in non-integrable classical systems generally being ergodic.
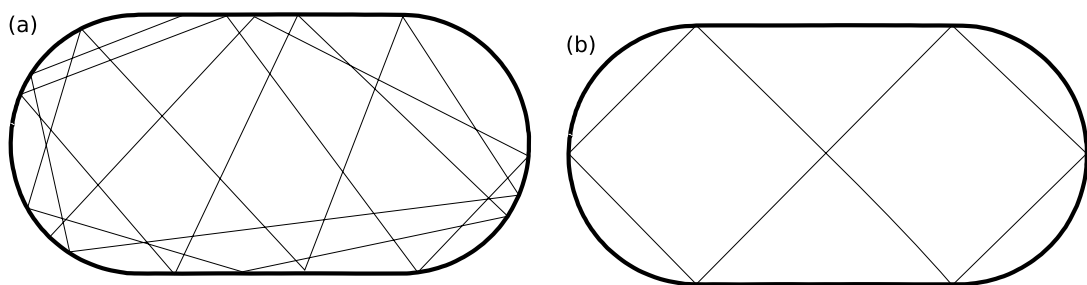
Figure 2.2: Weak ergodicity breaking for a classical billiard system bounded by a Bunimovich stadium, which is a stadium defined by a rectangular boundary capped by two semicircles. Generic trajectories of a billiard ball would be ergodic, exploring the entire stadium uniformly, as shown in panel (a). However, certain initial conditions result in unstable, periodic orbits, which are not ergodic. An example of one such orbit is shown in panel (b).

Therefore we have seen that typically, classical non-integrable systems are ergodic, such that after very long times, enough for the system to explore all of phase space, macroscopic observables will equilibrate to values dependent only on the initial configurations energy, referred to as thermal equilibrium. Equilibrium values of observables may be calculated using microcanonical ensemble averages. This process of reaching thermal equilibrium is referred to as *thermalisation*. However, it must be noted that thermalisation typically occurs on timescales much faster than it would take to explore the full phase space. This apparent faster thermalisation must therefore depend on some additional criteria other than ergodicity. Indeed, this faster onset of thermalisation in many classical systems is a consequence of many of the microstates along the constrained energy surface in phase space being nearly identical. There will be exponentially more microstates which look like the thermal equilibrium as opposed to some atypical configuration. Therefore even if the system is initialised in some atypical configuration, given

the ergodic trajectory, the system will quickly find itself in microstates resembling the thermal equilibrium long before it has explored the full phase space.

Classical non-integrable systems with a large number of degrees of freedom typically possess another property as well as ergodicity; they are *chaotic*. Chaotic systems are those for which the separation between two trajectories in phase space, initialised at coordinates very close to each other, grows exponentially in time, as determined by their Lyapunov exponent (133). In other words, chaotic systems are extremely sensitive to initial conditions, such that a slight perturbation in the initial configuration results in wildly different dynamics at later times. Examples of chaotic systems include coupled pendulums, the gravitational three body problem and the previously mentioned billiards on the Bunimovich stadium (18, 19). Note chaos is a stronger property than ergodicity. Ergodicity describes how a single trajectory behaves, whereas chaos describes how distinct trajectories differ. Nevertheless, for a classical non-integrable system with large number of degrees of freedom, which are typically both chaotic and ergodic, even if two trajectories become very different as a consequence of chaos, they will both still explore phase space uniformly due to ergodicity, therefore equilibrium values may still be calculated using microcanonical ensemble averages.

2.2 Thermalisation in quantum systems

In the previous section we have introduced important concepts related to thermalisation in the context of a classical system with many degrees of freedom. This included integrability, ergodicity and chaos. Consider now many-body interacting quantum systems with many degrees of freedom. Would these systems also thermalise?

Thermal equilibrium refers to a system reaching an equilibrium state whose properties, dependant only on the initial states energy, may be obtained from appropriate ensemble averages, for example, the microcanonical ensemble, which was justified by an ergodic hypothesis. However, our definition of classical ergodicity relied on having a concrete notion of a trajectory in phase space. For quantum systems, due to the non commutativity of position and momenta variables, one can no longer describe the state of the system by a trajectory in phase

space. In addition, the classical definition of chaos relied on an exponential scaling of the distance between two trajectories in phase space. In quantum systems, the distance between two distinct trajectories in a Hilbert space, generated by evolution under some Hamiltonian H, is a conserved quantity, due to the unitarity of the propagator $U(t) = e^{-iHt}$. It is therefore not immediately obvious how to extend definitions of ergodicity and chaos to quantum systems.

A natural first step to probe if many-body quantum systems do thermalise is to consider the behaviour of local observables at late times, which would be expected to equilibrate for a thermalising system. Consider an arbitrary initial state, expressed in the eigenbasis of some Hamiltonian:

$$|\psi\rangle = \sum_n c_n |E_n\rangle \tag{2.3}$$

For some arbitrary operator Q, the time evolution of the expectation value of this operator may be expressed as:

$$\langle Q(t)\rangle = \sum_n |c_n|^2 Q_{nn} + \sum_{n\neq m} c_n c_m^* Q_{mn} e^{-i(E_n - E_m)t} \tag{2.4}$$

where $Q_{mn} = \langle E_m|Q|E_n\rangle$ are the matrix elements of the operator Q in the energy basis. In the limit $t >> 1$, this expectation value does equilibrate to some stationary value, as the second term containing off diagonal matrix elements will generically average to zero for eigenvalues and initial states which are not fine tuned. The equilibrium value is given by the diagonal matrix elements of Q in the energy basis, weighted by the initial states support on the eigenstates:

$$\langle Q\rangle_{\text{eq}} = \lim_{t\to\infty} \langle Q(t)\rangle = \sum_n |c_n|^2 Q_{nn} \tag{2.5}$$

An analogue of the ergodic hypothesis for quantum systems would therefore demand that this equilibrium value should be the same for any initial state with the same energy density. If the system is thermal, equilibrium values should be in some sense related to the microcanonical ensemble, as in the classical case. For a quantum system, microcanonical ensemble averages may be expressed as

averaging a quantity over some small energy window (31):

$$\langle Q \rangle_{\text{micro}}(E) = \frac{1}{D} \sum_{E' \in [E + \Delta E]} \langle E' | Q | E' \rangle \tag{2.6}$$

where D is the number of energy eigenstates E' in the window $E + \Delta E$.

Thermalisation is the process of approaching an equilibrium state. Therefore for quantum systems, the thermalisation timescale refers to how long until the off-diagonal contribution to the time evolved expectation value in Eq. (2.4) averages to zero. As many-body level spacings are exponentially small in the number of degrees of freedom, it could take an exponentially long time for these off diagonal contributions to average to zero. This is similar to how formally, thermalisation in classical system should occur on the timescale to explore the full phase space, yet in practice it occurs much faster, due to the large number of typical configurations. For thermalisation to occur faster than expected for quantum systems, one must assume that the off diagonal matrix elements Q_{mn} are sufficiently small (135).

In direct analogy with results from classical systems, one would expect an ergodic hypothesis to apply only to non-integrable quantum systems. In the remainder of this section, we will first define integrability of a quantum system, before discussing properties of non-integrable Hamiltonians obtained from random matrix theory (75). This includes the remarkable fact that, for non-integrable systems, diagonal elements of observables $Q_{nn} = \langle E_n | Q | E_n \rangle$, which contribute to long time equilibrium values of a quantum system, Eq. (2.5), are equivalent to values obtained from the microcanonical ensemble, Eq. (2.6). This result ultimately lead us to the eigenstate thermalisation hypothesis (ETH) (123, 124, 125), which seeks to explain thermalisation of many-body interacting quantum systems.

Integrability

Extending the definition of integrability from classical to quantum systems requires some care. A classical integrable system is defined as a system which possess an extensive number of conserved integrals of motion, as well as energy, and may be identified by an extensive number of operators which form a commuting Poisson bracket with the Hamiltonian function. One may be tempted to

define a quantum integrable system as one which possesses an extensive number of conserved quantities, such that the Hamiltonian of the system commutes with an extensive number of symmetry operators. However, by this definition, any quantum system would be quantum integrable, as there trivially exist exponential many operators which commute with the Hamiltonian; the projectors onto arbitrary eigenstates of the Hamiltonian.

It is known however that certain quantum systems are exactly solvable, in the sense the eigenvectors and eigenvalues of their Hamiltonians may be calculated analytically, by a technique known as the Bethe Ansatz (67). We will not discuss the details of the Bethe Ansatz here, it is sufficient to know that as a consequence of the Bethe ansatz, there arises an extensive set of commuting observables which are not trivially the projectors onto eigenstates. It is this property, being Bethe ansatz solvable, that defines quantum integrability. The formal definition of a non-integrable quantum system is therefore a quantum system which is not Bethe ansatz solvable.

Note this does not mean that a non-integrable quantum system is one for which an analytical solution is not known - the definition applies specifically to the solvability by the Bethe ansatz. If a non-integrable Hamiltonian is not solvable by the Bethe ansatz, it will still commute with an exponential number of operators (projectors onto eigenstates), however, there will not exist an extensive set of non-trivial integrals of motion (such as projectors onto eigenstates) which commute with with the non-integrable Hamiltonian.

2.2.1 Random matrix theory

It has been found that many of the properties of non-integrable, interacting quantum systems may be understood using random matrices (75). Experimental results pertaining to the energy levels of heavy nuclei suggested eigenvalues of strongly interacting quantum systems appeared rather random (120). Wigner (139) proposed that to understand these systems, the particular details of an interacting Hamiltonian are irrelevant, such that various properties of the Hamiltonian may be calculated from ensemble averages over appropriate set of random matrices. This includes matrix elements of observables in the energy basis,

which are necessary to evaluate long time equilibrium values. For real, symmetric Hamiltonians, the relevant ensemble of random matrices is the Gaussian orthogonal ensemble (GOE). These are matrices which are invariant under orthogonal transformation, with the individual matrix elements being continuous Gaussian random variables. Likewise, for complex, hermitian Hamiltonians, one would consider the Gaussian unitary ensemble (GUE), which consists of random matrices invariant under unitary transformations.

Level statistics

Results from random matrix theory are particularly useful in identifying if a quantum system is non-integrable. One quantity which may be predicted from random matrix theory of non-integrable systems is the distribution of level spacings. This distribution is different for integrable and non-integrable systems, providing a 'smoking gun' to identify if a system is non-integrable.

Assuming no degeneracies (resolve all necessary symmetries), define the normalised level spacings of a Hamiltonian, S_n, as:

$$S_n = \frac{E_{n+1} - E_n}{\langle S \rangle}, \quad \langle S \rangle = \frac{1}{N_s - 1} \sum_{n=1}^{N_s - 1} (E_{n+1} - E_n) \tag{2.7}$$

where N_s is the number of eigenstates in a given symmetry sector. If a non-integrable Hamiltonian is effectively no different from a random matrix drawn from the either the GUE or GOE, the level spacings S_n will be random variables.

To illustrate how one would derive the probability density function for the distribution of level spacings S_n using random matrix theory, consider an orthogonal 2×2 random matrix drawn from the GOE (139):

$$H = \begin{pmatrix} \frac{\Delta}{2} & \frac{V}{2} \\ \frac{V}{2} & -\frac{\Delta}{2} \end{pmatrix} \tag{2.8}$$

where Δ, V are (real) continuous random variables drawn from a Gaussian distribution centred around zero with variance σ^2. The eigenvalues of this matrix may be trivially calculated as $\pm\sqrt{\Delta^2 + V^2}/2$. The level spacing, as a function of the random variables Δ, V, is simply $S(\Delta, V) = \sqrt{\Delta^2 + V^2}$. The probability density

function describing the distribution of level spacings S may be calculated using a convolution:

$$P_{\text{GOE}}(\omega) = \frac{1}{2\pi\sigma^2} \int \delta\left(\sqrt{\Delta^2 + V^2} - \omega\right) e^{-\frac{\Delta^2+V^2}{2\sigma^2}} d\Delta dV \qquad (2.9)$$

$$= \frac{\omega}{\sigma^2} e^{-\frac{\omega^2}{2\sigma^2}} \qquad (2.10)$$

Likewise suppose H was a 2×2 hermitian matrix drawn from the GUE:

$$H = \begin{pmatrix} \frac{\Delta}{2} & \frac{\alpha+i\beta}{2} \\ \frac{\alpha-i\beta}{2} & -\frac{\Delta}{2} \end{pmatrix} \qquad (2.11)$$

with Δ, α, β continuous random Gaussian variables with variance σ^2. An analogous derivation results in the following probability density for the level spacing:

$$P_{\text{GUE}}(\omega) = \frac{1}{(2\pi\sigma^2)^{\frac{3}{2}}} \int \delta\left(\sqrt{\Delta^2 + \alpha^2 + \beta^2} - \omega\right) e^{-\frac{\Delta^2+\alpha^2+\beta^2}{2\sigma^2}} d\Delta d\alpha d\beta \qquad (2.12)$$

$$= \sqrt{\frac{2}{\pi}} \frac{\omega^2}{\sigma^3} e^{-\frac{\omega^2}{2\sigma^2}} \qquad (2.13)$$

Eqs. (2.10),(2.13) are the Wigner-Surmise distributions for level spacings of a random matrix drawn from either the GOE or GUE. The level spacing distribution for larger matrices are found to be well approximated by the result obtained from 2×2 matrices (140). A distinguishing feature of the level spacing distribution for a non-integrable Hamiltonian is the presence of level repulsion, indicated by the property that $P(\omega) \to 0$ as $\omega \to 0$. This is in stark contrast to integrable systems, for which adjacent energy levels will also differ in an extensive number of conserved quantities, resulting in an absence of level repulsion. The level spacing distribution for integrable systems are instead found to follow a Poisson distribution (8). The distribution of level spacings therefore provides a relatively simple criteria for distinguishing integrable and non-integrable systems.

A scalar quantity obtained from level spacing distributions may also be used to distinguish integrable and non-integrable systems. This is the mean ratio of

level spacings (90). Consider the following dimensionless quantity:

$$r_n = \frac{\min(S_n, S_{n+1})}{\max(S_n, S_{n+1})} \tag{2.14}$$

The mean average of all r_n, $\langle r \rangle$, may be calculated from the level spacing distribution. For a non-integrable system obeying the Wigner-Surmise of the GOE, it is found $\langle r \rangle = 0.5295$. On the other hand, for an integrable system whose level spacings follow a Poisson distribution, $\langle r \rangle = 0.386$.

Matrix elements of observables

In order to calculate the long time equilibrium values of observables, we require the diagonal elements of the observable in the energy basis of the system, Eq. (2.5). For non-integrable systems, these diagonal matrix elements are in fact consistent with microcanonical ensemble averages (29, 123). Random matrix theory provides a way in which we can sketch why this would be the case.

Consider a non-integrable Hamiltonian H obtained from some small perturbation to an integrable system H_0:

$$H = H_0 + \epsilon H_1 \tag{2.15}$$

It may be shown using random matrix theory that the eigenstates of H, $|E_n\rangle$ are equivalent to some random superposition of the integrable eigenstates of H_0, $|E_i^0\rangle$, localised around some narrow energy shell:

$$|E_n\rangle = \sum_{E_i^0 \in E_n + \Delta E} c_{in} |E_i^0\rangle \tag{2.16}$$

where c_{in} are Gaussian random variables with mean zero.

We are interested in the diagonal element of an observable in the non-integrable energy basis. Expanding this quantity in terms of the integrable energy basis of H_0, we find:

$$Q_{nn} = \langle E_n|Q|E_n\rangle = \sum_{i,j} c_{in} c_{jn} \langle E_i^0|Q|E_j^0\rangle \tag{2.17}$$

Averaging this quantity over the random matrix ensemble, only the diagonal contribution will remain, as the off diagonal contributions are odd in the random Gaussian variables. This results in the following ensemble average:

$$\langle Q_{nn}\rangle_{\mathrm{r}} = \sum_i \langle c_{in}^2\rangle_{\mathrm{r}} \langle E_i^0|Q|E_i^0\rangle \tag{2.18}$$

As the random variables c_{in} are clustered around the energy E_n, the ensemble average $\langle Q_{nn}\rangle_{\mathrm{r}}$ reproduces the microcanonical ensemble average, Eq. (2.6).

The above argument would also hold if we started at some non-integrable point and perturb the system, suggesting this property holds generally. Therefore, to leading order, the results of random matrix theory imply a strong connection between diagonal elements of observables in a non-integrable energy basis and the microcanonical ensemble.

2.2.2 Eigenstate thermalisation hypothesis

We have seen that many-body quantum systems will equilibrate at long times, Eq. (2.5), and general arguments about non-integrable Hamiltonians using random matrix theory suggest that for non-integrable systems, this equilibrium state will be consistent with the microcanonical ensemble. However, the random matrix theory approach is limited in its applicability to real systems. For example, correlation functions can violate random matrix theory predictions (58, 125). A generalisation of results obtained from random matrix theory was proposed by Srednicki (123, 124, 125), which modifies the expression for matrix elements of local observables, such that the resulting hypothesis adequately describes thermalisation in generic systems. This ansatz is known as the eigenstate thermalisation hypothesis (ETH) (25, 31). The ansatz is the following:

$$Q_{nm} = \langle E_n|Q|E_m\rangle = \langle Q\rangle_{\mathrm{micro}}(E)\delta_{nm} + e^{-S(E)/2}f_Q(E,\omega)R_{nm} \tag{2.19}$$

where $E = (E_n + E_m)/2$ is the average energy and $\omega = E_n - E_m$ the energy difference. The diagonal contribution corresponds to the microcanonical ensemble and is a smooth function in energy. The off-diagonal contribution describes fluctuations from the microcanonical ensemble. $S(E)$ is the thermodynamic entropy

(95) at the relevant energy which controls the scale of these deviations. $f_Q(E, \omega)$ is smooth envelope function, relevant for non-equal time correlation functions and linear response of a system to perturbations (58). R_{nm} is a random matrix belonging to either the GOE or GUE, dependant on whether the non-integrable Hamiltonian we have obtained the energy basis from is symmetric or hermitian respectively.

While no formal proof of this ansatz exists, it has been found in numerical simulations that the predictions of the ETH hold for many non-integrable systems (9, 10, 99, 100, 101, 110). However, the ansatz does not appear to hold for arbitrary observables, for example, matrix elements of projectors onto eigenstates do not satisfy the ETH. Nevertheless, it has generally been observed empirically that local, few body observables satisfy the predictions of the ETH ansatz.

The ETH is a statement about matrix elements of local observables of a non-integrable Hamiltonian in it's energy basis. Equivalently, this means the ETH is a statement about eigenstates of a non-integrable Hamiltonian. Consequences of the ETH are that diagonal matrix elements are smooth functions of energy. Furthermore, off-diagonal matrix elements are suppressed according to the thermodynamic entropy at the relevant energy scale. It also implies that the long time stationary values of observables after reaching equilibrium, Eq. (2.5), is a weighted sum of microcanonical ensemble averages. This equilibrium value is therefore independent of details of the initial state, depending only its energy, consistent with an ergodic hypothesis.

Bipartite entanglement entropy

An important quantity neglected in the previous analysis is the entropy of a system. Indeed, the thermodynamic entropy controls the scale of deviations from the microcanonical ensemble for the ETH ansatz, Eq. (2.19).

Entanglement spectrums and entropy measures are useful quantities for characterising quantum states (68, 85, 96). The bipartite entanglement entropy is one such measure, which is to be interpreted as a measure of mutual information between two systems. Consider partitioning an isolated system into two subsystems, A and B. Suppose the state of the system is a pure state, which may be

expressed as a density matrix ρ. Define the reduced density matrix of subsystem A as tracing out the environment of subsystem B:

$$\rho_A = Tr_B(\rho) \tag{2.20}$$

Bipartite entanglement entropy between these two subsystems is defined by the following entropy measure:

$$S = -Tr(\rho_A ln \rho_A) \tag{2.21}$$

ETH cannot be applied to this quantity, as it is not the expectation value of some local observable. Nevertheless, it has been shown through numerical works (32, 109) and theoretical arguments (30) that this entropy measure is related to the thermodynamic entropy. In particular, for a non-integrable system which satisfies the ETH, bipartite entanglement entropy of the systems eigenstates is found to be a smooth function of energy, much like the diagonal elements of matrix elements of local observables.

2.2.3 Example: longitudinal Ising model

Before discussing ergodicity breaking and violations of the ETH in many-body quantum systems, we will first consider a non-integrable model which is in agreement with the predictions of ETH. This will provide a benchmark for what is considered typical thermalising behaviour.

Consider the quantum Ising model with transverse and longitudinal fields (144), which is described by the following Hamiltonian:

$$H = \sum_n J\sigma_n^z \sigma_{n+1}^z + h_x \sigma_n^x + h_z \sigma_n^z \tag{2.22}$$

With $h_z = 0$, this is equivalent to the Ising model in transverse field, which is analytically solvable via a Jordan Wigner transformation (56) and is therefore integrable (69). Further, there is a well known critical point at $h_x = 1$ (106). For generic $h_z, h_x \neq 0$, the model is known to be non-integrable, although at the critical point $h_x = 1$ with $h_z << 1$ it remains integrable.
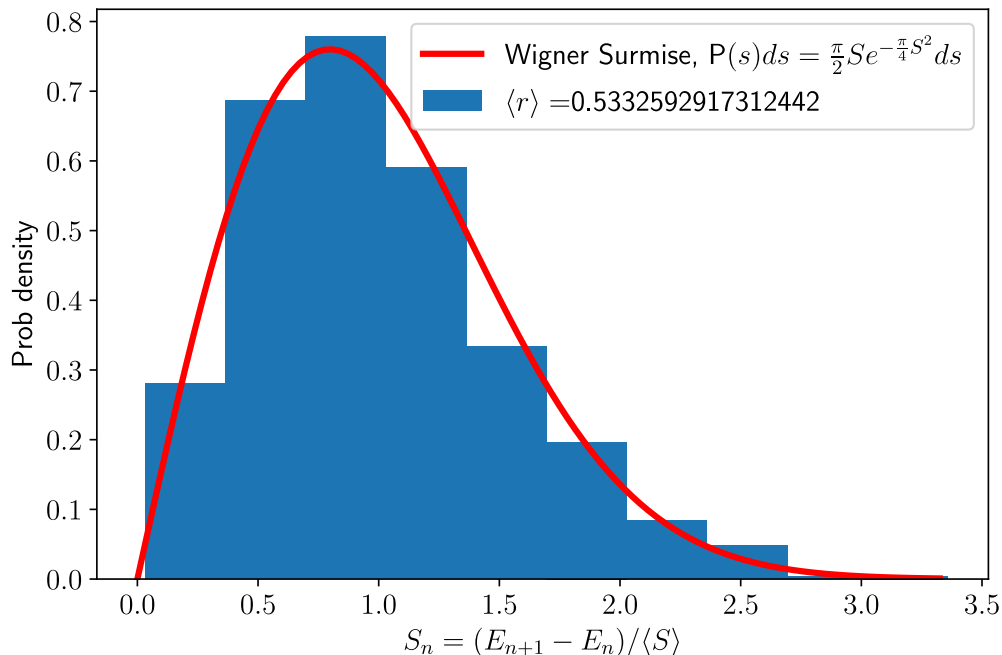
Figure 2.3: Level statistics for the longitudinal Ising model, Eq. (2.22), obtained for system size $N = 16$ using exact diagonalisation for model parameters $J = 1, h_x = 0.4, h_z = 0.7$. Eigenvalues were obtained by resolving both translation and spatial inversion symmetries, working in the momentum zero sector, that is, $[K, I] = [0, 0]$. The distribution of level spacings is in good agreement with a Wigner Surmise distribution describing level spacings of random matrices from the GOE, with the mean level spacing $\langle r \rangle \approx 0.54$. These results verify this model is non-integrable and should therefore agree with the predictions of the ETH.

We consider this model with periodic boundary conditions ($n + N \equiv N$) such that this system exhibits translational symmetry. The model is also symmetric with respect to spatial inversion, that is:

$$I : j \to N - j - 1. \tag{2.23}$$

Fig. 2.3 shows the level spacing distribution of this model at system size $N = 16$ with Hamiltonian parameters $J = 1, h_x = 0.4, h_z = 0.7$. Eigenvalues were obtained with exact diagonalisation, resolving both translation and spatial inversion symmetries, working in the zero momentum sector ($[K, I] = [0, 0]$). The level spacing distribution is converging to a Wigner-Surmise distribution, ex-

hibiting level repulsion. Furthermore, the mean level spacing may be computed as $\langle r \rangle = 0.5333$, in good agreement with the predictions of random matrix theory. These findings verify that at this point in parameter space, the longitudinal Ising model is indeed non-integrable and the predictions of ETH should be valid.

Fig. (2.4) shows exact diagonalisation results of the longitudinal Ising model for system size $N = 16$. Fig. 2.4(a) shows the expectation values of some some local observable, the spin polarisation in the Z direction on site 0, Z_0, with respect to the eigenstates of the system. As expected from the ETH ansatz, this is a smooth function of energy. Moreover, the bipartite entropy of eigenstates, shown in Fig. 2.4(b), is also a smooth function of energy. Finally, Fig. 2.4(c) shows the time evolution of the expectation value of Z_0, with the system initialised in the polarised state $|000...\rangle$. The expectation value quickly equilibrates to the value given by the diagonal ensemble, Eq. (2.5), confirming off-diagonal matrix elements of this operator in the energy basis are suppressed, in agreement with ETH. Finally, the dashed line indicates the prediction of the equilibrium value from the microcanonical ensemble, which is in good agreement with the numerical data. The numerics exhibits small fluctuations around this microcanonical value. These fluctuations are expected to be a finite size effect, whose magnitude should diminish as system size increases.

2.2.4 Ergodicity breaking

So far we've discussed how many-body quantum systems thermalise. Non-integrable systems are typically ergodic, such that quenches from initial states will equilibrate to stationary states whose expectation values depend only on their energy density, in agreement with the microcanonical ensemble, as predicted by the ETH.

We now turn our attention to systems which violate these predictions. This can be in either a strong or weak sense. Strong ergodicity breaking refers to a complete breakdown of the ETH, where no initial state exhibits an ergodic trajectory and all eigenstates are 'non-thermal', in the sense that they violate the predictions of the ETH. This is the case for integrable systems, where long time equilibrium states obtained from the diagonal ensemble, Eq. (2.5) must also conserve extensive number of additional symmetries. Furthermore, many-body
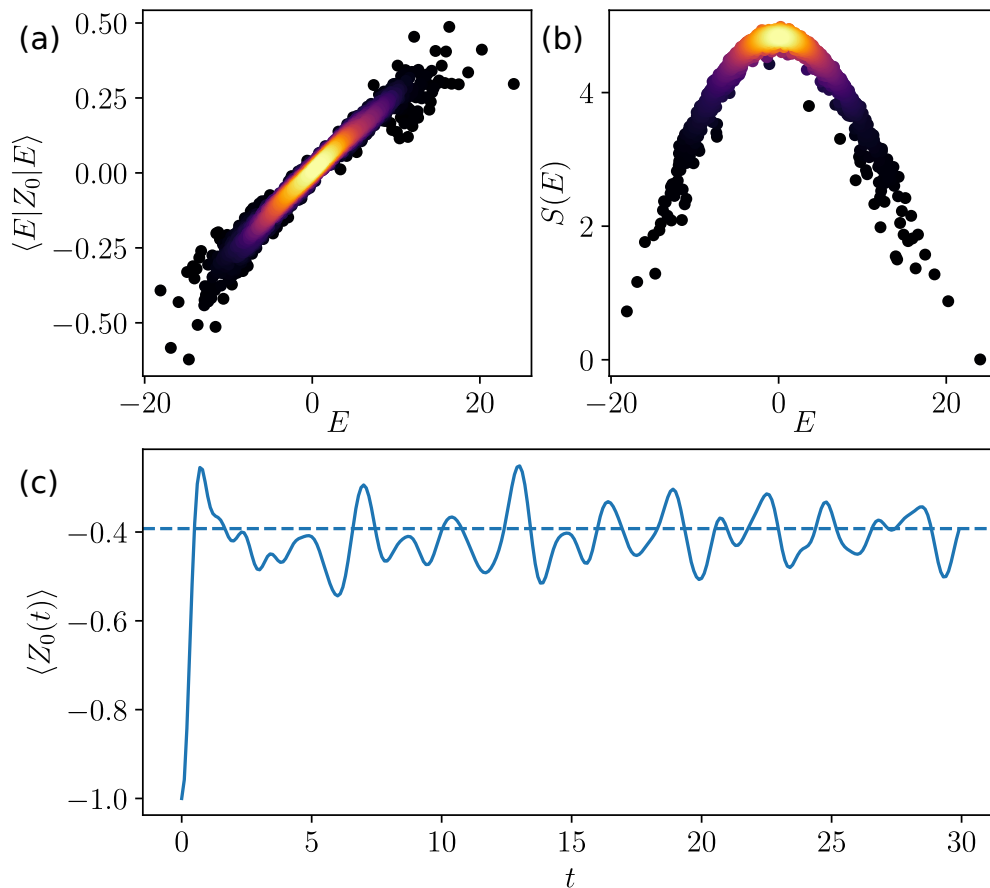
Figure 2.4: Longitudinal Ising model Eq. (2.22) numerical results at $N = 16$. (a) Is the expectation value of a local observable, the spin polarisation in the Z direction at site 0, Z_0, computed with respect to the eigenstates of the system. (b) The bipartite entanglement entropy of eigenstates, plotted as a function of energy. The colour scale in these panels indicate the density of points. (c) Shows the time evolution of the expectation value of Z_0 when the system is initialised in the polarised state $|000...\rangle$. The dashed line indicates the prediction of the equilibrium value obtained from the microcanonical ensemble, Eqs. (2.5),(2.6). These results are consistent with the predictions of the ETH ansatz, Eq. (2.19). These results therefore constitute typical behaviour of generic non-integrable system.

localised systems, a many-body analogue of Anderson localisation (1), exhibit strong ergodicity breaking. MBL occurs in many-body disordered systems, where there can emerge an extensive number of conserved local integrals of motion (21, 87, 105), resulting in the absence of thermalisation and the failure of eigenstates to agree with the ETH.

However, it is possible that some systems may only weakly violate the ETH. We already discussed weak ergodicity breaking in a classical setting in Section 2.1, where a system of billiards in a Bunimovich stadium hosts both ergodic and periodic trajectories. In quantum systems, weak ergodicity breaking refers to a breakdown of the ergodic hypothesis for only a few initial states, not all.

Single particle scarring

One particular class of systems which realise a form of weak ergodicity breaking in quantum systems are those exhibiting a phenomena known as single particle *quantum scarring*. This is an effect observed in quantum versions of classically chaotic systems exhibiting a mixed phase space (88), which means they host both ergodic and periodic trajectories in their phase space.

Consider again a classical system of billiards in a Bunimovich stadium. This system is chaotic, yet exhibits a mixed phase space. As shown in Fig. 2.2, most trajectories are ergodic, yet there exist certain trajectories corresponding to unstable periodic orbits. The quantum analogue of this system consist of a Hamiltonian which is simply the kinetic energy term of a free particle with boundary conditions corresponding to the geometry of the Bunimovich stadium. For the quantum system, it was found there exists a special subset of eigenstates which feature enhanced support clustered about the unstable periodic orbits of the corresponding classical model (46), Fig. 2.5. These eigenstates were termed *quantum scars*, as it appeared the classical orbit had left a 'scar' on the eigenstate.

The existence of scarred eigenstates has implications for the dynamics when the system is prepared in special initial states. For example, consider initialising the system in some arbitrary wavepacket. A cartoon picture of dynamics would suggest this wavefunction would spread out, bouncing off the boundary until it uniformly covers the space. Now consider initialising the system in a wavepacket
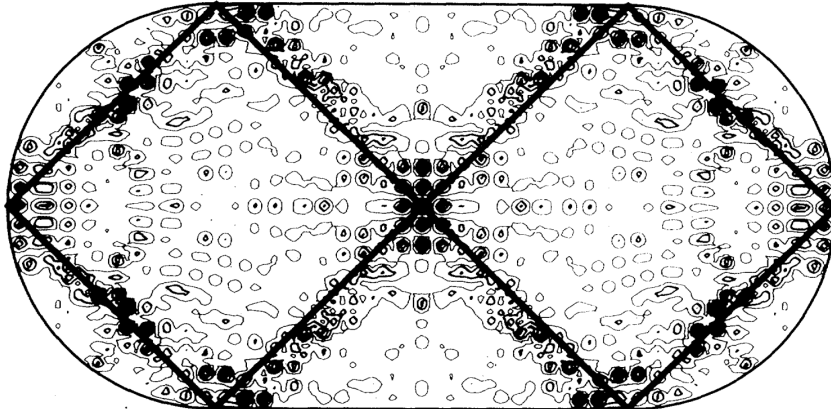
Figure 2.5: Single particle quantum scarring observed in the quantum version of a system of billiards bounded by a Bunimovich stadium. The Hamiltonian of this system is just the kinetic energy term of a free particle, with boundary conditions corresponding to the Bunimovich stadium. Scarring refers to certain eigenfunctions featuring enhanced support clustered around unstable periodic trajectories of the corresponding classical system. For example, the diamond trajectory, shown by a solid line, results in one particular scarred eigenfunction, whose support in position space is indicated by the contours which cluster around this orbit. Image obtained from Ref. (46).

localised on one of the unstable periodic orbits of the classical system, with momentum aimed along the orbit. This wavepacket would also eventually spread out, but would seem to 'cling' to the classical orbit for longer times than expected. This may be interpreted as a form of 'weak ergodicity breaking'.

2.3 Rydberg atom simulator

We will now review an experimental system which realises a non-integrable, many-body quantum system that appears to exhibit weak ergodicity breaking similar to single particle scarring. Attempts to understand the peculiar behaviour of this system resulted in the discovery of quantum many-body scars (130). The system exhibiting this strange behaviour was a 51-atom quantum simulator (7). The simulator was an experimental platform consisting of an array of trapped neutral cold atoms coupled to highly excited Rydberg states (55, 137) via a driving laser, such that the laser drives transitions between the ground state of the atom $|g\rangle$ and
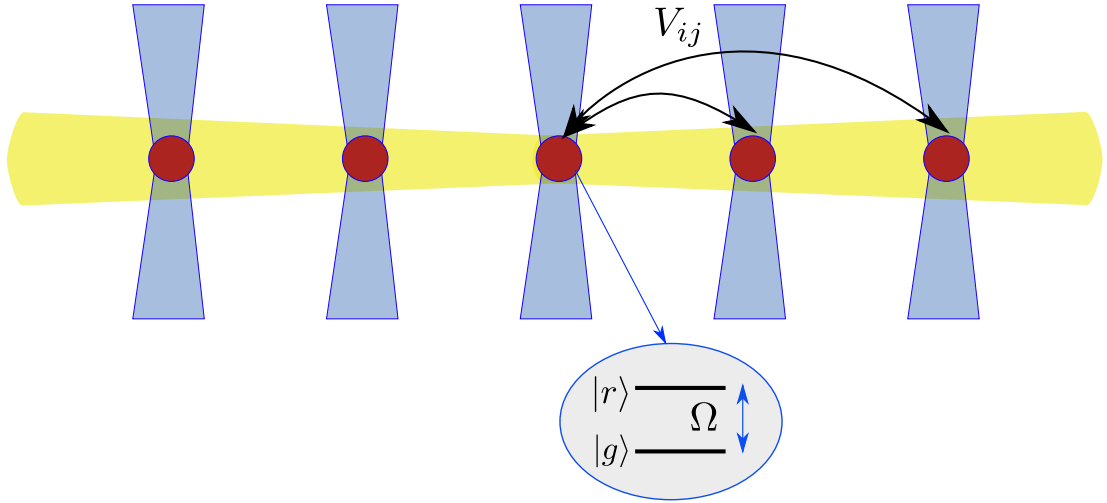
Figure 2.6: Experimental platform used to implement a 51-atom quantum simulator (7). The platform consists of cold atoms trapped by optical tweezers. A laser drives transitions between the ground state $|g\rangle$ and excited Rydberg state $|r\rangle$, with further long range, two body interactions present between Rydberg atom pairs due to Van der Waals forces. This interaction is of magnitude V_{ij}, where the subscripts indicate atoms position. It gives rise to an effect known as the 'Rydberg blockade', which, depending on the interaction strength V_{ij}, imposes a constraint that a unit cell of a given size cannot contain more than one Rydberg excitation.

the excited Rydberg state $|r\rangle$. Furthermore this setup results in a repulsive Van der Waals interaction between Rydberg atom pairs with strength $V_{ij} = C/R_{ij}^6$ ($C > 0$), where R_{ij} is the distance between pairs of atoms. A schematic of this experimental platform is shown in Fig. 2.6. The system may be described by the following Hamiltonian:

$$H = \sum_i \frac{\Omega_i}{2}\sigma_i^x - \sum_i \Delta_i n_i + \sum_{i<j} V_{ij} n_i n_j \tag{2.24}$$

where Ω_i are the effective Rabbi frequencies, Δ_i the detunings of the driving laser from the Rydberg state, $\sigma_i^x = |g_i\rangle\langle r_i| + |r_i\rangle\langle g_i|$ describes the transition from ground state to excited Rydberg state and $n_i = |r_i\rangle\langle r_i|$ the occupation of the excited Rydberg state.

The interacting term whose strength is given by V_{ij} produces an effect known

as the 'Rydberg blockade' (55). The interaction strength V_{ij} may be controlled by manipulating the distance between the atoms and for strong interactions resulting from large V_{ij}, states with sufficiently close Rydberg excitations $|r_i\rangle$ receive a heavy energy penalty, effectively prohibiting the occurrence of such states. This effective blockade may be characterised by the blockade radius R_b, which describes how large a unit cell is that is only permitted to contain a single Rydberg excitation. It is defined as the distance between atoms for which $V_{ij} = \Omega$.

The experimentalist were free to vary the parameters Ω_i, Δ_i, allowing them to prepare specific states by letting the system evolve under specific parameter regimes while switching the optical traps on and off (7). This approach meant they were easily able to prepare 'Rydberg crystal' states. These are ground states of the simulators Hamiltonian in a given ordered phase $\mathbb{Z}_n$, determined by the Rydberg blockade radius, when Δ/Ω is taken to be large and positive. When Δ/Ω is large and positive, the ground state will want to maximise the number of Rydberg excitations, yet the state must still respect the constraint imposed by the Rydberg blockade. For example, consider the case when the Rydberg blockade radius effectively imposes that every two site unit cell may only contain a single Rydberg excitation, which corresponds to the $\mathbb{Z}_2$ phase. The ground state with Δ/Ω large and positive will be an antiferromagnetic Néel state $|Z_2\rangle = |rgrg...\rangle$, which is a Rydberg crystal of order two. Likewise, if the Rydberg blockade radius is increased, further Rydberg crystal states of higher orders become ground states, such as $|Z_3\rangle = |rggrgg...\rangle$ or $|Z_4\rangle = |rgggrggg...\rangle$.

One of the experiments carried out with the 51-atom simulator in Ref.(7) was to perform a quantum quench. The experimentalist prepared a Rydberg crystal state of a given order, then quenched the detuning $\Delta \to 0$ before letting the system evolve under the resulting Hamiltonian. During this evolution, the experimentalist were able to measure a local observable; the density of domain walls (7).

Now the Hamiltonian in Eq. (2.24) is non integrable, therefore at late times the system should equilibrate into a thermal state whose energy density is the same as the initial state, in agreement with the predictions of ETH. While the results obtained appeared to be consistent with this prediction for nearly all initial states simulated under this quench, something rather different was observed when

the simulator was initialised in a Rydberg crystal of order two, that is, the Néel state $|Z_2\rangle = |rgrg...\rangle$. Instead, persistent, coherent oscillations in the measured local observable were observed for times much greater than the thermalisation timescale. This is particularly strange, as the Néel state has zero energy with respect to the Hamiltonian in Eq. (2.24) with $\Delta = 0$. This would imply the Néel state would be expected to rapidly thermalise (7, 31), due to the exponentially suppressed off-diagonal matrix element of local observables predicted by the ETH. The fact that arbitrary quenches resulted in local observables thermalising to values in agreement with the microcanonical ensemble prediction of ETH, yet only a single quench did not, constitutes a form of weak ergodicity breaking. This sensitivity to initial state is reminiscent of the weak ergodicity breaking exhibited by single-particle scarring, as discussed in Section 2.2.4. The dynamics of the Néel state in this system was largely a mystery which prompted further study, eventually resulting in the discovery of quantum many-body scars.

2.3.1 PXP model

We now derive an effective model (131) of the 51-atom quantum simulator, whose Hamiltonian is given in Eq. (2.24), so as to study the anomalous dynamics from the Néel state numerically. Consider the post quench Hamiltonian that governs the dynamics of the simulator, that is, let $\Delta \to 0$. In addition, as we are considering the oscillatory dynamics observed when the system is initialised in the $|Z_2\rangle$ state, we assume Hamiltonian parameters are chosen such that the Rydberg blockade radius is of the order of the distance between neighbouring atoms, such that we are in the $\mathbb{Z}_2$ phase. Due to the reduced Rydberg blockade radius, we truncate the Van der Waals interaction term to a nearest neighbour interaction. Furthermore, we assume we are in the strongly interacting limit, that is, $V = V_{i,i+1} >> \Omega$. Rescaling the Hamiltonian by $1/V$, we arrive at the following Hamiltonian which describes the dynamics of the quantum simulator in the $\mathbb{Z}_2$ phase:

$$H = \underbrace{\sum_i n_i n_{i+1}}_{H_0} + \underbrace{\epsilon \sum_i \sigma_i^x}_{H_1} \qquad (2.25)$$

Where $\epsilon = \Omega/(2V) << 1$ is a small parameter.

The above Hamiltonian consists of a dominant, diagonal term H_0 and small perturbation H_1. The initial state $|\mathbb{Z}_2\rangle$ belongs to the lowest energy sector of H_0, namely $H_0 = 0$. We utilise a Schrieffer-Wolff transformation (14, 114) to derive an effective Hamiltonian which describes dynamics within this zero energy subspace.

The zero energy subspace of H_0 consists of product state configurations with no neighbouring excitations $|rr\rangle$. The global projector into this subspace takes the following form:

$$\mathcal{P} = \prod_i \left(\mathbb{I} - n_i n_{i+1}\right) \tag{2.26}$$

The effective Hamiltonian within this subspace is then

$$H_{eff} = \mathcal{P}(H_0 + H_1)\mathcal{P} \tag{2.27}$$

Trivially $\mathcal{P}H_0\mathcal{P} = 0$, as $\mathcal{P}$ is a projector into the zero energy subspace of H_0. This may be seen from the following calculation:

$$\mathcal{P}H_0\mathcal{P} = \prod_i (\mathbb{I} - n_i n_{i+1}) \left(\sum_k n_k n_{k+1}\right) \prod_j (\mathbb{I} - n_j n_{j+1}) \tag{2.28}$$

Now all the operators in Eq. (2.28) commute. Therefore

$$\mathcal{P}H_0\mathcal{P} = \prod_i (\mathbb{I} - n_i n_{i+1}) \prod_{j \neq k} (\mathbb{I} - n_j n_{j+1}) \sum_k n_k n_{k+1} (\mathbb{I} - n_k n_{k+1}) \tag{2.29}$$

$$= \prod_i (\mathbb{I} - n_i n_{i+1}) \prod_{j \neq k} (\mathbb{I} - n_j n_{j+1}) \sum_k (n_k n_{k+1} - n_k n_{k+1}) \tag{2.30}$$

$$= 0 \tag{2.31}$$

It follows the effective Hamiltonian governing dynamics within the zero energy subspace is $H_{eff} = \mathcal{P}H_1\mathcal{P} = \mathcal{P}\left(\epsilon \sum_i \sigma_i^x\right)\mathcal{P}$. Neglecting the constant factor ϵ, this

becomes:

$$H_{eff} = \mathcal{P} \left(\sum_i \sigma_i^x \right) \mathcal{P} \tag{2.32}$$

$$= \prod_j (\mathbb{I} - n_j n_{j+1}) \left(\sum_i \sigma_i^x \right) \prod_k (\mathbb{I} - n_k n_{k+1}) \tag{2.33}$$

Now $[n_i, \sigma_i^x] \neq 0$. To proceed, commute all the projectors $(\mathbb{I} - n_j n_{j+1})$ and $(\mathbb{I} - n_k n_{k+1})$ to the right which do not have support on site i:

$$H_{eff} = \sum_i (\mathbb{I} - n_{i-1} n_i)(\mathbb{I} - n_i n_{i+1}) \sigma_i^x (\mathbb{I} - n_{i-1} n_i)(\mathbb{I} - n_i n_{i+1}) \prod_{j \neq i-1, i} (\mathbb{I} - n_j n_{j+1})^2 \tag{2.34}$$

Note that $(\mathbb{I} - n_j n_{j+1})^2 = (\mathbb{I} - n_j n_{j+1})$ as this operator is a projector. Expanding out the product of terms inside the sum, H_{eff} becomes

$$H_{eff} = \sum_i (\mathbb{I} - n_{i-1} n_i)(\mathbb{I} - n_i n_{i+1}) \sigma_i^x (\mathbb{I} - n_{i-1} n_i)(\mathbb{I} - n_i n_{i+1}) \prod_{j \neq i-1, i} (\mathbb{I} - n_j n_{j+1}) \tag{2.35}$$

$$= \sum_i \left(\sigma_i^x - n_{i-1} \sigma_i^x - \sigma_i^x n_{i+1} + n_{i-1} \sigma_i^x n_{i+1} \right) \prod_{j \neq i-1, i} (\mathbb{I} - n_j n_{j+1}) \tag{2.36}$$

Introduce the projector onto the the ground state $P_i = |g_i\rangle\langle g_i| = (\mathbb{I} - n_i)$. Rewriting the term in the sum in terms of P_i rather than n_i, H_{eff} simplifies:

$$H_{eff} = \sum_i \left(\sigma_i^x - n_{i-1} \sigma_i^x - \sigma_i^x n_{i+1} + n_{i-1} \sigma_i^x n_{i+1} \right) \prod_{j \neq i-1, i} (\mathbb{I} - n_j n_{j+1}) \tag{2.37}$$

$$= \sum_i \left(\sigma_i^x - (\mathbb{I} - P_{i-1}) \sigma_i^x - \sigma_i^x (\mathbb{I} - P_{i+1}) + (\mathbb{I} - P_{i-1}) \sigma_i^x (\mathbb{I} - P_{i+1}) \right) \prod_{j \neq i-1, i} (\mathbb{I} - n_j n_{j+1}) \tag{2.38}$$

$$= \sum_i \left(-\sigma_i^x + P_{i-1} \sigma_i^x + \sigma_i^x P_{i+1} + (\sigma_i^x - P_{i-1} \sigma_i^x)(\mathbb{I} - P_{i+1}) \right) \prod_{j \neq i-1, i} (\mathbb{I} - n_j n_{j+1}) \tag{2.39}$$

$$= \sum_i P_{i-1} \sigma_i^x P_{i+1} \prod_{j \neq i-1, i} (\mathbb{I} - n_j n_{j+1}) \tag{2.40}$$

2. QUANTUM ERGODICITY AND ITS BREAKDOWN

Now implicitly assume we work in the constrained Hilbert space consisting of no neighbouring excitations, such that the projector $\prod_{j\neq i-1,i}(\mathbb{I} - n_j n_{j+1}) = \mathbb{I}$ within this constrained Hilbert space, allowing us to drop this term from the right hand side of H_{eff}. The final effective Hamiltonian governing the 51-atom quantum simulator is therefore the following:

$$H_{PXP} = \sum_{i=0}^{N-1} P_{i-1}\sigma_i^x P_{i+1} \tag{2.41}$$

This model is known as the 'PXP' model. We interpret this model as a kinetically constrained spin half chain, changing notation from $|g\rangle = |0\rangle$ and $|r\rangle = |1\rangle$. The basic action of the Hamiltonian is to flip between spin down states $|0\rangle$ and spin up states $|1\rangle$, providing such an action does not violate the Rydberg constraint of no neighbouring excitations (configurations $|11\rangle$ are not permitted). An example of a permitted transition would be the following:

$$|000\rangle \leftrightarrow |010\rangle$$

Assuming periodic boundary conditions ($N + n \equiv n$), the model exhibits translational symmetry. However, the PXP model also exhibits other discrete symmetries. It commutes with the spatial inversion operator I, Eq. (2.23) and anti-commutes with a particle-hole operator ρ, which is defined as follows

$$\rho = \prod_{j=0}^{N-1} \sigma_j^z \tag{2.42}$$

The anti-commutation relation $\{H_{PXP}, \rho\} = 0$ ensures the spectrum of the PXP model is symmetric about $E = 0$, whilst it is also responsible for an exponential degeneracy of the eigenstates at $E = 0$ (130, 131). Finally we note the PXP model is non-integrable, as verified by its level spacing distribution converging to the Wigner-Surmise as system size increases (130).

Dynamics in the PXP model

Armed with an effective Hamiltonian describing the 51-atom simulator, we now perform time evolution numerically, using exact diagonalisation (108), to verify the weak ergodicity breaking reported from experimental observations (7).
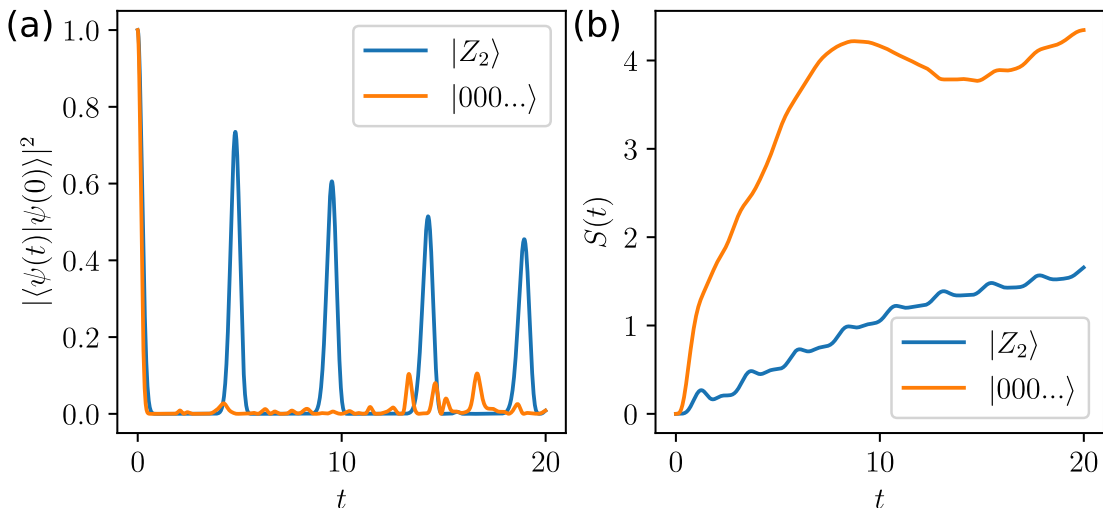
Figure 2.7: Weak ergodicity breaking observed in the PXP model, Eq. (2.41). The PXP model exhibits ergodic trajectories from arbitrary initial states, yet periodic dynamics is observed when the system is initialised in the Néel state $|Z_2\rangle = |0101...\rangle$. Results are for system size $N = 22$, obtained via exact diagonalisation (108). Numerics for such a large system size are obtained by working only within the constrained Hilbert space consisting of basis states with no neighbouring excitations, which has dimension $39,603$ at $N = 22$. In addition, we resolve both translation and spatial inversion symmetry (108), further reducing the dimension of the matrices which need diagonalising. Panel (a) shows the the many-body wavefunction fidelity (Eq. (2.43)), (b) the bipartite entanglement entropy of the evolved state. Initialising the system in the Néel state results in decaying fidelity revivals and suppressed entropy growth, relative to the expected thermalising behaviour, which is indicated by the dynamics of the polarised state $|000...\rangle$. These two states have the same energy density, so would be expected to have similar dynamics according to the ETH. Revivals in the many-body fidelity indicate a periodic trajectory in the exponentially large Hilbert space.

To probe for the presence of non-ergodic trajectories, we compute the many-body wavefunction fidelity, or 'Loschmidt echo', defined as:

$$f(t) = |\langle \psi(0)|\psi(t)\rangle|^2 \tag{2.43}$$

2. QUANTUM ERGODICITY AND ITS BREAKDOWN

The fidelity quantifies the support of the time evolved state on the initial state. For a non-integrable system obeying the predictions of the ETH, we expect a time evolved wavefunction following an ergodic trajectory would quickly acquire support on exponentially many states in the Hilbert space, resulting in a fidelity which would generically decay exponentially fast to zero.

Fig. 2.7(a) shows $f(t)$ computed when we initialise the system in either the Néel state $|Z_2\rangle = |1010...\rangle$ or the polarised state $|000...\rangle$ for system size $N = 22$. Both these states have zero energy with respect to the PXP Hamiltonian and are therefore expected to thermalise on the same timescale. The fidelity from the polarised state, which is representative of some generic initial state, quickly drops to zero as the wavefunction spreads throughout the Hilbert space, indicating a fast equilibration of local observables to their equilibrium values predicted by ETH. On the other hand, the fidelity from the Néel state exhibits decaying revivals, revealing a periodic trajectory in the exponentially large Hilbert space, resulting in robust oscillations in any local observable. These findings are consistent with observations of weak ergodicity breaking from the 51-atom simulator experiment, indicating the PXP model provides a good description of the physics of the $\mathbb{Z}_2$ phase.

Furthermore, in Fig. 2.7(b), we compute the bipartite entanglement entropy, Eq. (2.21), of the time evolved wavefunction. As both the Néel state and polarised state have the same energy density, we would expect this quantity to equilibrate on the same timescale and to the same value for both quenches. However, the Néel state $|\mathbb{Z}_2\rangle$ exhibits suppressed linear entropy growth relative to the polarised state, while also exhibiting small oscillations superimposed on top, as a result of the wavefunctions periodic trajectory.

It is apparent from these numerical simulations of the PXP model and also experimental data obtained from the 51-Rydberg atom simulator that the PXP model exhibits weak ergodicity breaking, with strong sensitivity of dynamics to the initial state. While generic initial states follow ergodic orbits, special initial states exhibit oscillatory dynamics which slowly decays in time, although on timescales much longer than the thermalisation timescale. This is reminiscent of weak ergodicity breaking observed in single-particle quantum scarred systems, as discussed in Section 2.2.4. In the next chapter, we will attempt to understand

why this weak ergodicity breaking is present in the PXP model.

Chapter 3

An overview of quantum many-body scars

In this chapter we review quantum many-body scars (QMBS), a mechanism for avoiding thermalisation via a weak violation of the ETH. By studying the spectral properties of the 'PXP' model introduced in the previous chapter (Eq. (2.41)), we demonstrate the existence of a subset of atypical non-thermal eigenstates, the so called 'scarred eigenstates', responsible for the weak ergodicity breaking observed in this model (130).

Next, we consider other mechanisms which result in the coexistence of thermal and non-thermal eigenstates in the same model. These include projector embedding techniques (119) and Krylov-restricted thermalisation (80). While similar to QMBS, it is found the distinguishing feature of these systems is that their Hamiltonians fracture into block-diagonal forms, hosting both integrable and non-integrable subspaces simultaneously. Nevertheless, we will argue that something similar occurs in QMBS models, although the fracturing is only approximate. This inevitably leads us to discuss an idealised limit of QMBS, termed 'exact scarring', where this fracturing can be made exact, in contrast to the 'approximate scarring' observed in the PXP model.

Finally we will discuss in more detail the distinction between exact and approximate scarring. By considering the necessary algebraic conditions for exact scarring, spectrum generating algebras, we lay the foundation necessary to under-

stand the remainder of this thesis, which aims to construct theories to understand 'approximate' scarring.

3.1   Quantum many-body scars in the PXP model

In the previous section, we demonstrated the PXP model, Eq. (2.41), exhibits weak ergodicity breaking when initialised in particular initial states (Fig. 2.7). Specifically, dynamics of generic initial states behave in accordance with predictions from the ETH, but initialising the system in the Néel state $|Z_2\rangle = |0101...\rangle$ results in a periodic trajectory in the exponentially large Hilbert space, indicated by decaying revivals in the many-body wavefunction fidelity, Eq. (2.43). Furthermore, the dynamics from the Néel state results in suppressed linear entropy growth relative to ETH predictions.

We now turn our attention to spectral properties of the PXP model, in an attempt to understand the peculiar dynamics when the system is initialised in the Néel state. As the PXP model is non-integrable, we expect the predictions of ETH (Section 2.2.2) should apply to it's eigenstates. Specifically, these eigenstates should appear thermal, in the sense that both their bipartite entanglement entropy and expectation values of local observables should be smooth functions of energy.

Fig. 3.1 shows spectral properties of the eigenstates of the PXP model at system size $N = 22$, as a function of energy. Panel (a) is the overlap of the eigenstates with the Néel state $|Z_2\rangle = |1010...\rangle$, panel (b) the bipartite entanglement entropy of the eigenstates. Both these quantities should be smooth functions of energy according to the ETH. It turns out, the statement that eigenstates are thermal appears to be true for *nearly* all eigenstates of the PXP model. However, there exist a linear subset of $N + 1$ eigenstates which appear non-thermal. In this sense the PXP model can be said to weakly violate the ETH. One observes a band of $N + 1$ eigenstates, coloured in red, with atypical thermal properties, namely their entropy is much smaller than expected from the ETH. Furthermore, this same band of eigenstates exhibits enhanced support on the Néel state and also feature the property that they are approximately equidistant in energy.

It is apparent that weak ergodicity breaking in the PXP model is a conse-
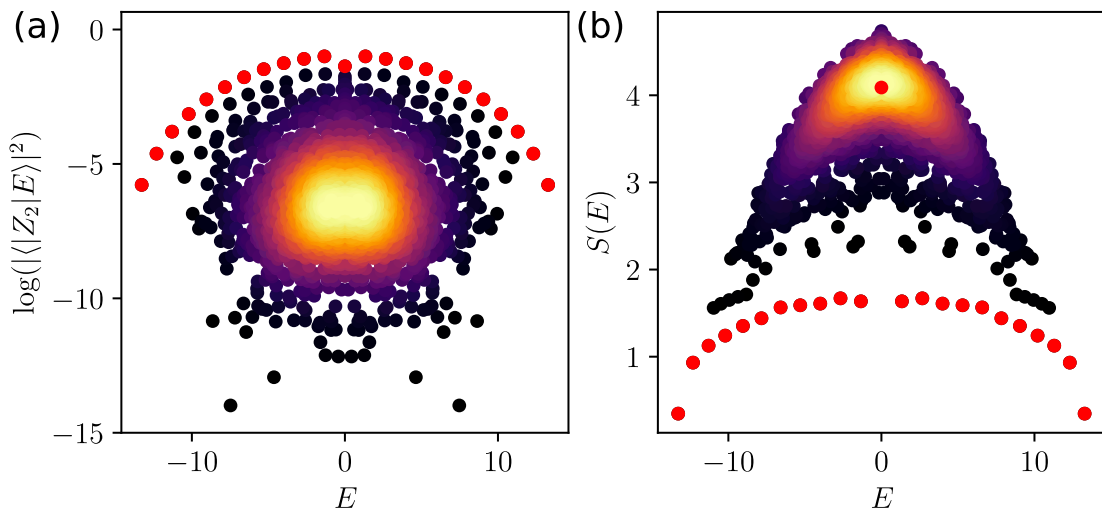
Figure 3.1: ETH violating eigenstates in the PXP model, responsible for the weak ergodicity breaking observed in dynamics when the system is initialised in the Néel state $|Z_2\rangle = |0101...\rangle$ (see Fig. 2.7). Results are for system size $N = 22$. Plotted are various properties of the eigenstates of the PXP model, Eq. (2.41) as a function of energy. (a) Shows the overlap of the eigenstates with the Néel state, (b) the bipartite entanglement entropy of the eigenstates. The colour scale indicates the density of points. As the PXP model is non-integrable (130), according to the ETH, the quantities depicted in plots (a),(b) should be smooth functions of energy. However, there exist $N+1$ eigenstates, coloured in red, which disagree with this prediction. These are the 'scarred eigenstates' (see text), which are roughly equidistant in energy and characterised by anomalously large overlap with the Néel state and atypical, sub-thermal entropy. As a consequence of the Néel states large support on these scarred eigenstates, initialising the system in the Néel state results in persistent oscillatory dynamics.

quence of these ETH violating eigenstates. Decaying fidelity revivals observed when the system is initialised in the Néel state, Fig 2.7(a), which indicates a periodic, non ergodic trajectory in the Hilbert space, follows simply as a consequence of the Néel's state enhanced support on these atypical eigenstates which are approximately equidistant in energy. Furthermore, the entropy of the evolved wavefunction when quenching from the Néel state, Fig 2.7(b), may also be understood from the properties of these atypical eigenstates. The oscillatory component of the entropy dynamics is a result of the large support of the Néel state on the roughly equidistant, non-thermal eigenstates, while the small but non-zero support on the remaining thermal eigenstates, Fig. 3.1, contributes to the linear growth observed in the entropy.

The ETH violating eigenstates in the PXP model have being given the name '*scarred eigenstates*', in analogy with single particle quantum scars (46). Due to the existence of the ETH violating eigenstates in the PXP model, it is possible to prepare special initial states whose time evolution generates some oscillatory trajectory in the Hilbert space while the wavefunction also slowly spreads out, resulting in long lived coherent dynamics, a form of weak ergodicity breaking. As discussed in Section 2.2.4, similar weak ergodicity breaking is also observed for single particle scarred systems, such as quantum billiards. Due to the existence single particle scarred eigenfunctions in these systems, it would also be possible to construct special initial states which would exhibit long lived oscillatory dynamics. The analogy is made even more concrete when one considers that for single particle scarring, the scarred eigenfunctions are characterised by concentrated support in the position basis along unstable periodic trajectories of the corresponding chaotic classical system. While the classical limit of the PXP model is not known, a form of semiclassical limit has been studied using the time-dependent variational principle (TDVP) (64, 92). TDVP constructs classical equations of motion which approximate the dynamics of a quantum system by projecting the time dependent Schrodinger equation along some manifold of variational states. TDVP equations of motion have been obtained for the PXP model for a specific manifold consisting of matrix product states (MPS) (47, 76). The resulting classical equations of motion indicate this semiclassical limit of the PXP model exhibits a mixed phase space, possessing both ergodic and periodic

trajectories, just as the classical limit of single particle quantum scarred systems do. By plotting the support of the ETH violating eigenstates on the variational manifold for which the TDVP equations of motion generates trajectories, one also observes enhanced support along a periodic trajectory originating from the Néel state (129). Therefore atypical eigenstates in both the PXP model and single particle scarred systems are both related to periodic orbits present in classically chaotic systems. In this sense, the PXP model can be said to realise a many-body version of single particle quantum scarring.

Non-ergodic behaviour in the PXP model is ultimately a consequence of the existence of few atypical thermal eigenstates. With this in mind, we now give a formal definition of quantum many-body scarring. Quantum many-body scarring is a form of weak ETH violation in non-integrable quantum systems, where there exist a subset of atypical, non-thermal eigenstates with suppressed entropy which are nearly equidistant in energy. Preparing special initial states which feature enhanced support on these scarred eigenstates results in coherent oscillatory dynamics and suppressed entropy growth for timescales much greater than the thermalisation time.

3.2 Exact embeddings of non-thermal eigenstates

While many-body scars are an example of weak ETH violation where only a few eigenstates of a non-integrable system are non-thermal, there exist other phenomena where non-thermal eigenstates are found to coexist alongside thermal ones (80, 116, 119). We briefly summarise these alternate scenarios, contrasting them with QMBS.

3.2.1 Projector embedding

Firstly, it is in fact possible to embed a subspace consisting of the span of an arbitrary set of states $|\psi_j\rangle$ into the eigenspace of a thermalising Hamiltonian. These arbitrary states may be chosen to be non-thermal, such that the resulting Hamiltonian may contain both thermal and non thermal eigenstates. This embedding is possible due to a method introduced by Shiraishi and Mori (119),

known as 'projector embedding'. Further extensions of this approach applied to topologically ordered systems have been developed in Ref. (91).

Consider a Hamiltonian describing some lattice system with Hilbert space $\mathcal{H}$ of the form:

$$H = \sum_{i=1}^{N} P_i h_i P_i + H', \tag{3.1}$$

where P_i are local projectors (which do not necessarily commute), h_i local Hamiltonians, and H' a Hermitian operator satisfying $[H', P_i] = 0$ for all i.

Now suppose there is a subspace $\mathcal{T} \subset \mathcal{H}$ spanned by a set of states $|\psi_j\rangle \in \mathcal{H}$, $\mathcal{T} = \mathrm{span}(|\psi_j\rangle)$, with $|\psi_j\rangle$ satisfying:

$$P_i|\psi_j\rangle = 0, \quad \forall\, i, j. \tag{3.2}$$

Subspace $\mathcal{T}$ is therefore equivalent to the null space of the total projector $P_T = \sum_i P_i$, ie $|\psi_\mathcal{T}\rangle \in \mathcal{T} \implies P_T|\psi_\mathcal{T}\rangle = 0$.

We will now demonstrate the subspace $\mathcal{T}$, which is the null space of P_T, is invariant under the action of the Hamiltonian in Eq. (3.1). Using the property of the states $|\psi_j\rangle$ given in Eq. (3.2) and the fact that $[H', P_i] = 0$, it follows that:

$$P_i H|\psi_j\rangle = P_i \left(\sum_n P_n h_n P_n \right) |\psi_j\rangle + P_i H'|\psi_j\rangle \tag{3.3}$$

$$= P_i H'|\psi_j\rangle \tag{3.4}$$

$$= H' P_i|\psi_j\rangle \tag{3.5}$$

$$= 0 \tag{3.6}$$

As $P_i H|\psi_j\rangle = 0, \forall\, i, j$, it trivially follows that $P_T H|\psi_j\rangle = \sum_i P_i H|\psi_j\rangle = 0$, such that the state $H|\psi_j\rangle \in \mathcal{T}$. This confirms the subspace $\mathcal{T}$ is invariant under the action of the Hamiltonian. The Hamiltonian in Eq. (3.1) must necessarily fracture into the block diagonal form:

$$H = H_\mathcal{T} \bigoplus H_{\perp \mathcal{T}}$$

With $H_\mathcal{T}$ corresponding to the projection of the Hamiltonian into the subspace $\mathcal{T}$

and $H_{\perp \mathcal{T}}$ the projection into the orthogonal space. Given this fracturing, Hamiltonians of the form Eq. (3.1) will contain $\dim \mathcal{T}$ eigenstates within $\mathcal{T}$ that may be thought of as having being embedded into the spectrum. Using this embedding procedure, ETH violating eigenstates may be embedded into the spectrum of an otherwise non-integrable model (119).

Models of this form generically embed eigenstates near the centre of the spectrum (119), unlike QMBS which host non-thermal eigenstates throughout the entire spectrum. Moreover there is no guarantee the embedded eigenstates are equidistant in energy and may even be degenerate, resulting in models which do not exhibit wavefunction revivals, as observed with QMBS. Further, note that, for periodic boundary conditions, the PXP model can be expressed in this 'projector embedded' form such that a single target state is embedded – namely the AKLT ground state at zero energy (118). However, the complete set of $N + 1$ scarred eigenstates with enhanced support on $|\mathbb{Z}_2\rangle$ state have not been understood through this embedding procedure.

3.2.2   Krylov restricted thermalisation

While 'projector embedding' illustrates how to embed an arbitrary integrable subspace into a non-integrable model, some systems are found to host both integrable and non-integrable sectors simultaneously without relying on the particular form of Hamiltonian given in Eq. (3.1). This effect is observed in a range of systems, such as in fractonic models (59, 93, 107) or models of bosons on an optical lattice (48, 147). These coexisting integrable and ergodic sectors arise as *Krylov subspaces* of a given Hamiltonian. We begin this section by discussing how to construct a basis for a disconnected component of a Hamiltonian, to motivate the definition of a Krylov subspace.

Suppose you have a Hamiltonian which fractures into a block diagonal form:

$$H = \bigoplus_n H_n \tag{3.7}$$

This would typically occur when the Hamiltonian commutes with certain symmetry operators, such that the block diagonal sectors may be labelled by the

symmetry quantum numbers. Now suppose one wished to construct a basis for a certain symmetry sector $\mathcal{S}$ which has dimension $\dim \mathcal{S} = D_{\mathcal{S}}$. Furthermore, say we are we already know a single vector which is in the symmetric subspace, $|\psi_{\mathcal{S}}\rangle \in \mathcal{S}$. By definition, since the Hamiltonian is symmetric with respect to this symmetry, states within a symmetry sector remain in that sector after applying the Hamiltonian, $|\psi_{\mathcal{S}}\rangle \in \mathcal{S} \implies H|\psi_{\mathcal{S}}\rangle \in \mathcal{S}$. It follows that we can generate a sequence of vectors which belong to the subspace $\mathcal{S}$ by repeated application of H onto the initial state $|\psi\rangle$. We can repeat this procedure until we have $D_{\mathcal{S}}$ states, which will span the subspace:

$$\mathcal{S} = \mathrm{span}\{|\psi_{\mathcal{S}}\rangle, H|\psi_{\mathcal{S}}\rangle, H^2|\psi_{\mathcal{S}}\rangle, ..., H^{D_{\mathcal{S}}-1}|\psi_{\mathcal{S}}\rangle\}$$

The vectors $H^n|\psi_{\mathcal{S}}\rangle$ will not generally be orthogonal, but one can always use a Gram-Schmidt procedure to produce an orthonormal basis if desired.

More generally, we introduce the notion Krylov subspaces $\mathcal{K}_D(H, |\psi\rangle)$, which is a $D+1$ dimensional subspace spanned by states obtained by repeated application of H onto an arbitrary vector $|\psi\rangle$:

$$\mathcal{K}_D(H, |\psi\rangle) = \mathrm{span}\{|\psi\rangle, H|\psi\rangle, ..., H^D|\psi\rangle\} \tag{3.8}$$

These subspaces are used extensively in numerical algorithms, particularly for finding eigenvalues (Lanczos recurrence (65)) and for time evolution.

Consider now time evolving a quantum state $|\psi\rangle$ with a small time step δt, expanding the propagator as a power series:

$$e^{-iH\delta t}|\psi\rangle = |\psi\rangle - i\delta t H|\psi\rangle - \frac{\delta t^2}{2}H^2|\psi\rangle + ...$$

We observe the basis states of a Krylov subspace, $H|\psi\rangle, H^2|\psi\rangle, ...$, arise naturally in this sum. Now lets assume $H^D|\psi\rangle = 0$ for some D smaller than the dimension of the Hilbert space. The time evolved state then becomes:

$$e^{-iH\delta t}|\psi\rangle = |\psi\rangle - i\delta t H|\psi\rangle - \frac{\delta t^2}{2}H^2|\psi\rangle + ... + H^{D-1}|\psi\rangle$$

The time evolution of the state $|\psi\rangle$ therefore occurs only within the Krylov sub-

space $\mathcal{K}_{D-1}(H, |\psi\rangle)$. This is not surprising if the Krylov subspace corresponds to a symmetry sector as discussed earlier, as the block diagonal form of the Hamiltonian in Eq. (3.7) implies dynamics only occurs within this symmetric subspace. However, for certain systems, it is possible that the Krylov subspace where the dynamics is localised is *not* a symmetry sector of the Hamiltonian! The Hamiltonian would still fracture into a block diagonal form, Eq. (3.7), with the separate blocks corresponding to dynamically disconnected sectors. Hamiltonians may fracture into an exponential number of dynamically disconnected Krylov sectors.

This phenomena is referred to as 'Hilbert space shattering' (80). Hilbert space shattering usually occurs when there are dynamical constraints present in a model, such as for fractonic systems, where the conservation of both charge and dipole symmetry imposes a dynamical constraint (107). When Hilbert space shattering occurs, the dimension of the dynamically disconnected Krylov sectors may range from being either one to exponentially large in system size (116). Crucially, when considering only the exponentially large Krylov subspaces, it is found that these dynamically disconnected sectors may be either integrable or non-integrable, resulting in Hamiltonians which possess both thermal and non-thermal eigenstates. This fracturing of the Hamiltonian into both integrable and non-integrable sectors is referred to as 'Krylov-restricted thermalisation' (80).

While Krylov restricted thermalisation illustrates a way in which integrable and non-integrable sectors may coexist in the same model, it does not offer an explanation for why non-thermal eigenstates are present in scarred models such as the PXP model. If one were to compute the largest Krylov subspace generated by repeated application of the PXP Hamiltonian, Eq. (2.41), onto the Néel state $|Z_2\rangle = |1010...\rangle$, one would not obtain an integrable sector corresponding to a subspace of scarred eigenstates, rather they would obtain the full Hilbert space, as the Néel state is not dynamically disconnected from all other product states under the action of the PXP Hamiltonian. Indeed, the non-integrable sectors hosted in a model exhibiting Krylov restricted thermalisation may themselves host QMBS (78), such that Krylov restricted thermalisation offers a way to realise QMBS, but does not explain them.

3.3 QMBS as approximate embedding of an integrable subspace

The two methods we have just discussed, projector embeddings and Krylov-restricted thermalisation, result in Hamiltonians which fracture into block diagonal forms hosting both integrable and non-integrable sectors simultaneously. These approaches are analytically tractable and present a simple picture of how thermal and non-thermal eigenstates may coexist in the same model. Fig. 3.2(a),(b) summarises the two approaches graphically, showing the fracturing of Hamiltonians into block diagonal forms when the Hamiltonian is expressed with respect to a suitably chosen basis. However, these two approaches do not directly apply to the non-thermal eigenstates observed in the PXP model (7), as the scarred eigenstates do not reside in some integrable sector which is orthogonal to some thermalising sector.

Nevertheless, by constructing a special basis, it is in fact possible to demonstrate that the PXP Hamiltonian *approximately* fractures into a block diagonal form containing both integrable and non integrable sectors,

$$H_{PXP} \approx H_{int} \bigoplus H_\perp \tag{3.9}$$

Fig. 3.2(c) demonstrates this fracturing graphically. The fracturing is approximate in the sense that the block diagonal component corresponding to the integrable sector is weakly coupled to a larger thermal sector via sparse matrix elements in the off diagonal block.

One gains further insight into the scarred non thermal eigenstates of the PXP model by projecting its Hamiltonian into this approximate integrable subspace and diagonalising the resulting matrix. The states produced by this procedure are very accurate approximations to the true scarred eigenstates of the full Hamiltonian (23, 131). This suggests that the scarred eigenstates have the majority of their support within this approximate integrable subspace, hence why they appear non-thermal. The scarred dynamics observed from the Néel state may therefore be interpreted as an oscillation within some integrable subspace, while the decaying component to the fidelity revivals is a consequence of this subspace
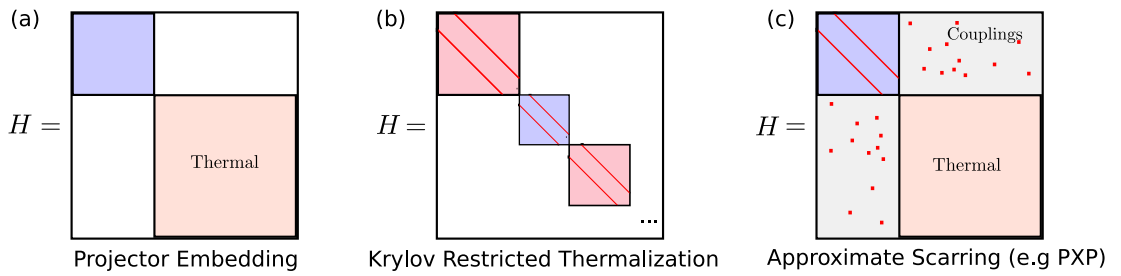
Figure 3.2: Graphical interpretation of various schemes in which Hamiltonians may host both thermal and non thermal eigenstates. Hamiltonians matrices are expressed in a particular basis which explicitly reveals block diagonal structures of integrable (blue) and non-integrable (red) sectors. (a) Corresponds to Shiraishi and Mori's 'projector embedding' (119), where a target integrable subspace is embedded into the spectrum of a non-integrable Hamiltonian. (b) Corresponds to Krylov-restricted thermalisation (80), where Hamiltonians may fracture into integrable and non-integrable subspaces, and a suitable basis (see Section. (3.3.1)) for each block diagonal sector may be chosen such that each sector is tridiagonal (red lines indicate non-zero matrix elements). (c) Corresponds to QMBS as observed in the PXP model, where, with a suitably chosen basis, it becomes apparent that the scarred eigenstates can be seen to arise from a 'loosely embedded' integrable subspace, with the Hamiltonian approximately fracturing into a block diagonal form, where an integrable subspace is weakly coupled to an orthogonal thermal subspace via sparse matrix elements.

not being exact, such that some component of the wavefunction leaks out of this subspace into the orthogonal thermal sector. We will now detail how to construct this special basis, using a procedure known as the forward scattering approximation (FSA), which bears a strong resemblance to the construction of Krylov subspaces introduced in the previous section.

3.3.1 Forward scattering approximation (FSA)

The Forward scattering approximation (FSA) applied to the PXP model constructs a subspace for which the PXP Hamiltonian approximately fractures into a block diagonal form. The subspace is obtained by constructing an orthonormal basis via repeated application of some operator. This procedure is very similar to the construction of Krylov subspaces, Eq. (3.8). We will first discuss how an orthonormal basis for a Krylov subspace is generated, deriving the well known Lanczos recurrence (4), in order to later demonstrate how the FSA subspace may be viewed as an approximate Krylov subspace.

Krylov subspace orthonormal basis - Lanczos recurrence

Recall a Krylov subspace, $\mathcal{K}_{\mathcal{D}}(H, |v_0\rangle)$, generated by a Hamiltonian H and arbitrary state $|v_0\rangle$, is the subspace spanned by the following states:

$$\mathcal{K}_D(H, |v_0\rangle) = \text{span}\{|v_0\rangle, H|v_0\rangle, ..., H^D|v_0\rangle\}$$

The basis for the subspace, $\{|v_0\rangle, H|v_0\rangle, H^2|v_0\rangle....\}$ is generally not orthonormal. One can obtain an orthonormal basis for the subspace by performing a Gram-Schmidt orthonormalisation on the basis vectors $H^n|v_0\rangle$.

However, an orthonormal basis may be constructed recursively using the well known Lanczos recurrence (4). Instead of producing all the basis vectors $\{|v_0\rangle, H|v_0\rangle, H^2|v_0\rangle....\}$ and performing a single orthonormalisation at the end, the Lanczos iteration orthonormalises the basis every time a new basis vector is obtained. This results in a recursion relation for the basis states, which we will now derive.

We will demonstrate how the usual Lanczos recurrence arises by considering

the first few steps of this process. Consider the first step. One obtains the first orthonormal vector $|v_1\rangle$ from $|v_0\rangle$ by applying the Hamiltonian H, orthogonalising the resulting vector and normalising it:

$$|u_1\rangle = H|v_0\rangle - \langle v_0|H|v_0\rangle|v_0\rangle \tag{3.10}$$

$$|v_1\rangle = \frac{1}{\beta_1}|u_1\rangle, \;\; \beta_1 = \sqrt{\langle u_1|u_1\rangle} \tag{3.11}$$

We have introduced the coefficient β_1, which is simply the normalisation of the orthogonalised vector $|u_1\rangle$. To obtain the next orthonormal vector $|v_2\rangle$, we apply the Hamiltonian H to $|v_1\rangle$, orthogonalise it with respect to both $|v_0\rangle$ and $|v_1\rangle$ using a Gram-Schmidt procedure, and finally normalise the state:

$$|u_2\rangle = H|v_1\rangle - \langle v_0|H|v_1\rangle|v_0\rangle - \langle v_1|H|v_1\rangle|v_1\rangle \tag{3.12}$$

For simplicity, let us introduce the notation $\alpha_i = \langle v_i|H|v_i\rangle$, such that:

$$|u_2\rangle = H|v_1\rangle - \alpha_1|v_1\rangle - \langle v_0|H|v_1\rangle|v_0\rangle \tag{3.13}$$

Note $H|v_0\rangle = \beta_1|v_1\rangle + \alpha_0|v_0\rangle$, such that the last term becomes:

$$|u_2\rangle = H|v_1\rangle - \alpha_1|v_1\rangle - (\beta_1\langle v_1| + \alpha_0\langle v_0|)|v_1\rangle|v_0\rangle \tag{3.14}$$

$$= H|v_1\rangle - \alpha_1|v_1\rangle - \beta_1|v_0\rangle \tag{3.15}$$

due to the orthogonality $\langle v_0|v_1\rangle = 0$. The second orthonormal vector is found by normalising the state $|u_2\rangle$, such that we find:

$$|v_2\rangle = \frac{1}{\beta_2}|u_2\rangle, \;\; \beta_2 = \sqrt{\langle u_2|u_2\rangle} \tag{3.16}$$

$$\beta_2|v_2\rangle = H|v_1\rangle - \alpha_1|v_1\rangle - \beta_1|v_0\rangle \tag{3.17}$$

In general, one can show that the relation given in Eq. (3.17) holds more generally at every step, due to the orthogonality of the vectors begin iteratively obtained, $\langle v_i|v_j\rangle = \delta_{ij}$. The resulting recurrence relation is the famous Lanczos recurrence

(4):

$$\beta_{j+1}\,|v_{j+1}\rangle = H\,|v_j\rangle - \alpha_j\,|v_j\rangle - \beta_j\,|v_{j-1}\rangle,\tag{3.18}$$

$\alpha_j = \langle v_j|H|v_j\rangle$ removes the component of the vector $H|v_j\rangle$ along $|v_j\rangle$. The coefficients $\beta > 0$ are simply normalisation coefficients, and are computed in practice by just calculating the norm of the orthogonal vectors $|u_n\rangle$ obtained after applying the Gram-Schmidt procedure, as demonstrated earlier with β_1, β_2.

We may rearrange the Lanczos recurrence in Eq. (3.18), interpreting it as an equation for the action of the Hamiltonian within the Krylov subspace:

$$H|v_j\rangle = \alpha_j|v_j\rangle + \beta_{j+1}|v_{j+1}\rangle + \beta_j|v_{j-1}\rangle,\tag{3.19}$$

This equation demonstrates that in the basis $|v_j\rangle$ for the Krylov subspace, obtained from the Lanczos recurrence, the Hamiltonian will be tridiagonal.

Forward scattering approximation

The Lanczos recurrence in Eq. (3.18) demonstrates how to iteratively construct an orthonormal basis for a Krylov subspace. We now introduce the forward scattering approximation, an iterative way of constructing an orthonormal basis for the so called FSA subspace. By considering the relation between the two iterative approaches, we will establish a connection between FSA subspaces and Krylov subspaces.

Start with a *product* state $|v_0^{fsa}\rangle$ which is a basis state of a Fock space. Now consider a Hamiltonian which is bipartite with respect to the Fock basis (no odd cycles: $\langle v_0^{fsa}|H^{2n+1}|v_0^{fsa}\rangle = 0, n \in \mathbb{Z}$). If this is the case, it is possible to decompose the Hamiltonian H into 'forward' and 'backward' propagating components H^+ and H^-, subject to the following criteria:

$$H = H^+ + H^- \tag{3.20}$$

$$H^- = (H^+)^\dagger \tag{3.21}$$

$$H^-|v_0^{fsa}\rangle = 0 \tag{3.22}$$

$$\langle n|m\rangle = 0, \text{ where } |n\rangle = (H^+)^n|v_0^{fsa}\rangle \tag{3.23}$$

The last two criteria state that H^- must annihilate $|v_0^{fsa}\rangle$, and the states produced by repeated application of H^+ on $|v_0^{fsa}\rangle$ are all orthogonal (though not normalised). These criteria are sufficient to uniquely specify the form of $H^\pm$, given a particular Hamiltonian H and product state $|v_0^{fsa}\rangle$.

An orthonormal basis may be constructed iteratively from repeatedly applying H^+ to $|v_0^{fsa}\rangle$ and normalising at each step:

$$\beta_{j+1}^{fsa}|v_{j+1}^{fsa}\rangle = H^+|v_j^{fsa}\rangle \tag{3.24}$$

$$\beta_{j+1}^{fsa} = \sqrt{\langle v_j^{fsa}|H^-H^+|v_j^{fsa}\rangle} \tag{3.25}$$

Eq. (3.28) is the FSA recurrence procedure to generate an orthonormal basis. This recurrence is repeated until it naturally terminates, $|v_{D-1}^{fsa}\rangle = 0$ for some D, such that the basis will consist of D states. The D dimensional subspace spanned by the set of states $|v_j^{fsa}\rangle$ is referred to as the FSA subspace. The advantage of this approach is the subspace generated will be linear in system size, allowing for efficient computations within it.

The form of the recurrence in Eq. (3.28) is similar to the Lanczos recurrence in Eq. (3.18), although the two procedures generate different basis and therefore different subspaces. However, the two approaches are in fact equivalent if the backwards propagator H^- satisfies $H^-|v_j^{fsa}\rangle = \beta_j^{fsa}|v_{j-1}^{fsa}\rangle$. To see this, introduce the FSA error vector:

$$|\delta_j^{fsa}\rangle = H^-|v_j^{fsa}\rangle - \beta_j^{fsa}|v_{j-1}^{fsa}\rangle \tag{3.26}$$

$|\delta_j^{fsa}\rangle$ is generically not zero. But assuming it is, we could add it to the FSA recurrence in Eq. (3.28) without it affecting the basis vectors:

$$\beta_{j+1}^{fsa}|v_{j+1}^{fsa}\rangle = H^+|v_j^{fsa}\rangle + |\delta_j^{fsa}\rangle \tag{3.27}$$

$$= H^+|v_j^{fsa}\rangle + H^-|v_j^{fsa}\rangle - \beta_j^{fsa}|v_{j-1}^{fsa}\rangle \tag{3.28}$$

$$= (H^+ + H^-)|v_j^{fsa}\rangle - \beta_j^{fsa}|v_{j-1}^{fsa}\rangle \tag{3.29}$$

$$= H|v_j^{fsa}\rangle - \beta_j^{fsa}|v_{j-1}^{fsa}\rangle \tag{3.30}$$

This is of the same form as the Lanczos recurrence in Eq. (3.18), with $\alpha_j =$

0 automatically satisfied as we have assumed H is bipartite. This reveals the connection between the FSA recurrence and the Lanczos recurrence. If the FSA error vectors $|\delta_j^{fsa}\rangle = 0 \, \forall$J, the FSA subspace is in fact equivalent to a Krylov subspace.

Recall from Section 3.2.2 that disconnected components of a Hamiltonian may be obtained as Krylov subspaces. Now if all the FSA error vectors $|\delta_j^{fsa}\rangle$ vanish such that the FSA subspace is equivalent to a Krylov subspace, this small subspace that is linear in the system size will correspond to some disconnected component of the Hamiltonian, such that the Hamiltonian will fracture into the block diagonal form $H = H_{fsa} \bigoplus H_{\perp}$, where H_{fsa} corresponds to projecting the Hamiltonian into the FSA subspace. This will not be the case if the error vectors are non zero, but if they remain sufficiently small, the Hamiltonian will approximately fracture into form $H \approx H_{fsa} \bigoplus H_{\perp}$. Therefore if the FSA error vectors are small, diagonalising H_{fsa} results in an accurate approximation to a linear set of eigenstates of the system.

FSA applied to PXP model

For the PXP Hamiltonian, we are interested in constructing a FSA subspace associated with the scarred oscillatory dynamics observed from the Néel state $|Z_2\rangle = |0101...\rangle$. Therefore, we make the specific choice that $|v_0\rangle = |Z_2\rangle$. The unique forward propagating component of the PXP Hamiltonian in Eq. (2.41), chosen to satisfy the conditions in Eq. (3.20-3.23) is the following:

$$H^+ = \sum_{n=0}^{N-1} P_{2n-1}\sigma_{2n}^+ P_{2n+1} + P_{2n-2}\sigma_{2n-1}^- P_{2n} \tag{3.31}$$

$$H^- = (H^+)^\dagger = \sum_{n=0}^{N-1} P_{2n-1}\sigma_{2n}^- P_{2n+1} + P_{2n-2}\sigma_{2n-1}^+ P_{2n} \tag{3.32}$$

The form of H^+ such that $H = H^+ + H^-$ is chosen so that repeated application of H^+ on $|Z_2\rangle$ generates an orthogonal basis. This convention of the FSA uniquely specifies H^+ given H and $|Z_2\rangle$. Why this particular H^+ is relevant for scarring is not apparent from this criteria. In this section we simply verify numerically the FSA subspace produced by this H^+ captures properties of the scarred eigenstates.

Nevertheless, there is a physical motivation for this choice of H^+ which gives some insight about the scarred eigenstates. This particular H^+ 'approximately' behaves as an su(2) raising operator, and the subspace spanned by the states $(H^+)^n|Z_2\rangle$ 'approximately' corresponds to some $s = N/2$ spin sector. We will not dwell on these facts here, or clarify what we mean by 'approximate' in this context - this topic will be the sole focus of Chapter. 4, where we will demonstrate scarred eigenstates in the PXP model are intimately related to su(2) Lie algebras.

The FSA recurrence, Eq. (3.28), starting from the Néel state with H^+ given in Eq. (3.31), terminates naturally after N steps, where N is the system size, such that $(H^+)^{N+1}|Z_2\rangle = 0$. The resulting FSA subspace therefore has dimension $\mathcal{D} = N + 1$. In addition, for this particular FSA recurrence, the normalisation coefficients β may be calculated analytically (131), allowing one to construct much larger subspaces than if one were to carry out this procedure numerically.

By projecting the PXP Hamiltonian to the FSA subspace generated from the Néel state, the PXP Hamiltonian will fracture into the approximate block diagonal form $H_{PXP} \approx H_{FSA} \bigoplus H_\perp$ as shown schematically in Fig. 3.2(c). The FSA subspace is not an exact subspace of the PXP Hamiltonian, as the error vectors $|\delta_j\rangle$ of the FSA approximation, Eq. (3.26), are non-zero, resulting in off diagonal matrix elements which couple the block diagonal component corresponding to the FSA subspace to the orthogonal thermalising component. However, error analysis of the error vectors $|\delta_j\rangle$ indicate these vectors are small for a FSA recurrence starting from the Néel state, justifying the FSA approximation (23, 131). As a consequence of these small errors, the FSA subspace is nearly decoupled from the orthogonal thermal sector.

Due to the approximate decoupling of the PXP Hamiltonian in the FSA subspace from the remaining orthogonal space, one should be able to diagonalise the PXP Hamiltonian projected to this FSA subspace, with the resulting $N+1$ eigenstates approximating some $N+1$ eigenstates of the full Hamiltonian. Fig. 3.3(a),(b) shows spectral properties of the approximate eigenstates obtained by this procedure at $N = 20$, indicated by red crosses. Results are obtained using exact diagonalisation, where we construct the FSA basis numerically. (a) shows the overlap of these approximate eigenstates with the Néel state while (b) shows their bipartite entanglement entropy. One observes these approximate eigenstates
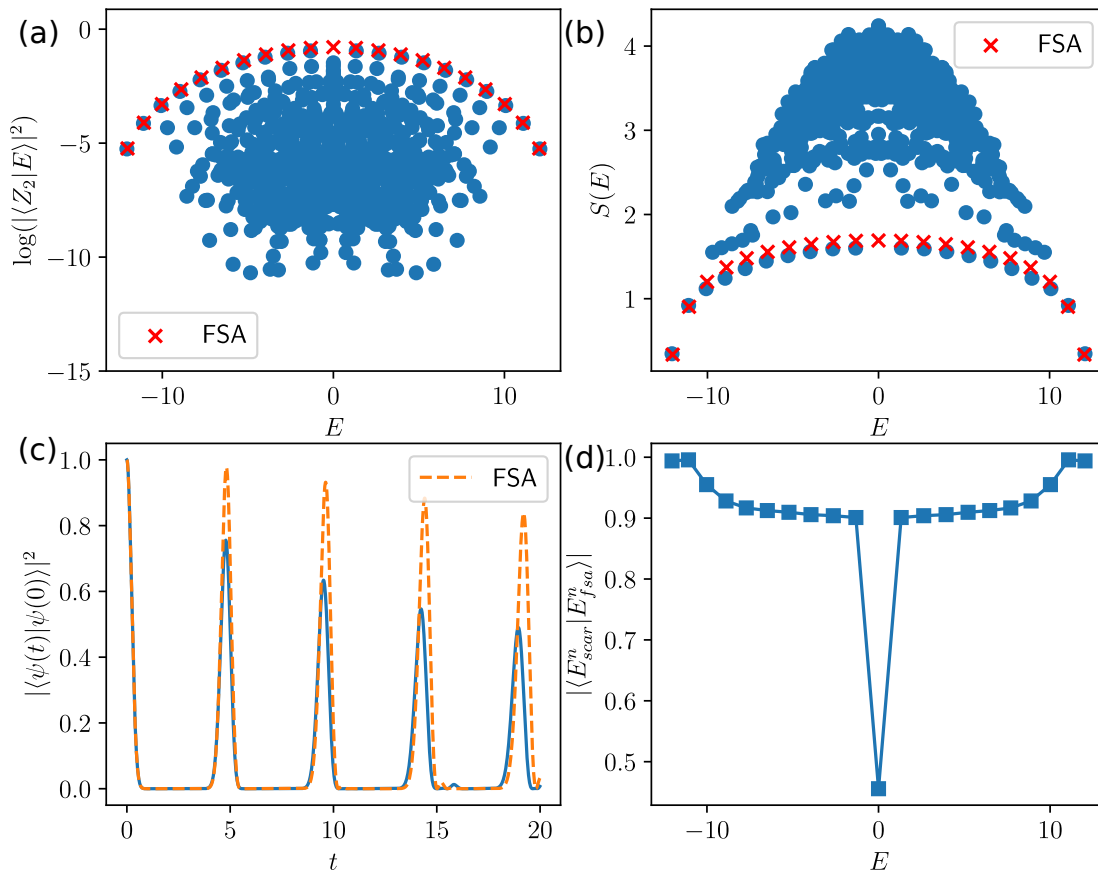
Figure 3.3: Numerical results showing the performance of the forward scattering approximation (FSA) applied to the PXP model. Results are for system size $N = 20$ and are obtained with exact diagonalisation. An FSA subspace is generated by repeated application of the operator H^+ (Eq. (3.31)) on the Néel state $|Z_2\rangle = |0101...\rangle$. By projecting the PXP Hamiltonian (Eq. (2.41)) into this subspace and diagonalising, one can approximate $N + 1$ eigenstates of the PXP Hamiltonian. Plots (a),(b) shows the overlap with the Néel state and entanglement entropy respectively of these approximate eigenstates, indicated by red crosses, contrasted with the true eigenstates of the PXP model, indicated by blue points. One observes that the approximate eigenstates capture the properties of the scarred eigenstates, which are states with anomalously large overlap with the Néel state and atypical, sub thermal entropy. Plot (d) shows the overlap of the approximate eigenstates in the FSA subspace with the scarred eigenstate at the same energy, which is O(1), indicating the approximate eigenstates indeed correspond with the scarred eigenstates. Plot (c) compares the many-body fidelity (Eq. (2.43)) of the PXP model when initialised in the Néel state $|\psi(0)\rangle = |Z_2\rangle = |0101...\rangle$ with the dynamics generated by constraining the evolution to only occur in the FSA subspace (see text). The approximate evolution in the FSA subspace provides a good description of the dynamics, capturing the fidelity of revivals and some component of the decay, due to dephasing within this subspace.

provide a very accurate description of the $N + 1$ scarred eigenstates of the PXP model, as it's found their energy, overlap with Néel state and entropy all match that of the actual scarred eigenstates of the full PXP Hamiltonian. This is verified in Fig. 3.3(d), which shows the overlap of the approximate eigenstates with the scarred eigenstates at the same energy density, where it's found this overlap is $O(1)$ for all $N + 1$ states, with the exception of the scarred eigenstate at $E = 0$. This is simply a consequence of the exponential degeneracy at $E = 0$ generated by the particle-hole symmetry of the PXP model, Eq. (2.42), therefore this overlap is a basis dependant quantity. It is expected with a suitable linear combination of the $E = 0$ eigenstates, this overlap would also be $O(1)$. These results indicate the scarred eigenstates are well described by a linear superposition of the $N + 1$ FSA basis states (131).

Further, by time evolving the Néel state within the FSA subspace, that is, by applying the projected propagator $U(t) = e^{-iP^{\dagger}_{FSA}HP_{FSA}t}$, where P_{FSA} is a projection to the FSA basis, one observes a reviving wavefunction fidelity resembling the oscillatory scarred dynamics of the PXP model, see Fig. 3.3(c). The only distinct difference between the true evolution of the Néel state and the approximate evolution restricted to the FSA subspace is that the fidelity revivals decay much slower when dynamics is restricted to the FSA subspace. Fidelity revivals within the FSA subspace decay as the approximate eigenstates within this subspace are still not exactly equidistant, resulting in dephasing. One can therefore associate two components to the decay of the fidelity during the true evolution. One is the dephasing within the FSA subspace, while another contribution is the leakage out of this FSA subspace into the orthogonal thermalising space, as a consequence of the non-zero off diagonal matrix elements coupling these two sectors.

3.4 Exact scars

In the previous section we have seen how QMBS in the PXP model may be interpreted in light of an approximate subspace, which results in the PXP Hamiltonian approximately fracturing into a block diagonal form, with an integrable sector weakly coupled via sparse matrix elements to a thermal sector. Furthermore, by projecting the PXP Hamiltonian into this subspace, one obtains a tridiagonal

matrix with eigenvalues which are nearly equidistant and eigenvectors which well approximate the scarred eigenstates (23, 131) of the full Hamiltonian.

This picture of QMBS in terms of an approximate, loosely embedded integrable subspace, suggests an idealised limit of QMBS, where, similar to projector embedding and Krylov-restricted thermalisation, this integrable subspace would become an exact subspace. However, in contrast to these two other methods, this idealised limit of QMBS would carry the property that the scarred eigenstates within this integrable subspace are exactly equidistant. We refer to this idealised limit of QMBS as 'exact scarring', in contrast to the QMBS observed in the PXP model, which we now refer to as 'approximate scarring', with the nomenclature chosen due to the approximately equidistant eigenvalues of the scarred eigenstates in the PXP model.

Exact scarring has been realised in a variety of models, such as spin-1 XY models (22, 112) and a spin 1/2 model with emergent kinetic constraints (51). As a consequence of the equidistant scarred eigenstates, it is possible to prepare special initial states with support only on these scarred eigenstates which exhibit perfect revivals in the many-body fidelity for all time, in contrast to the PXP model's decaying fidelity revivals. Furthermore, even though some arbitrary combination of eigenstates is usually some complicated entangled state, for exact scarred systems, a suitable linear superposition of all the scarred eigenstates tends to itself be some relatively simple state, for example, a Nematic Néel state (112).

The purpose of this thesis is to understand the origin of approximate scarring. We will spend the remainder of this chapter reviewing exact scarring and the algebraic structures which give rise to this physics, as this will lay the foundation necessary to understand the algebraic origin of approximate scarring discussed in Chapter 4.

3.4.1 Spectrum generating algebras

The defining characteristic of exact scarred models is that the scarred eigenstates (atypical low entropy eigenstates) are exactly equidistant in energy. Models hosting many sets of equidistant eigenstates may be seen to possess a *spectrum gen-*

erating algebra (SGA) (12, 50, 143). A generalisation of the SGA, known as a *restricted spectrum generating algebra* (RSGA) (82), results in Hamiltonians which possess only a single set of equidistant eigenstates.

A Hamiltonian H is said to possess a SGA if for some raising operator Q^+ it satisfies the following relation:

$$[H, Q^+] = \omega Q^+ \tag{3.33}$$

Typical examples of raising operators Q^+ in physical many-body systems may be spin raising operators or quasiparticle creation operators, which may be either fermionic or bosonic. Regardless of the physical origin of Q^+, if a Hamiltonian possesses a SGA with respect to the operator Q^+, $[H, Q^+] = \omega Q^+$, it follows that for every eigenstate $|E\rangle$ of H with eigenvalue E, there will exist a set of connected eigenstates, $(Q^+)^n|E\rangle$ with eigenvalues separated by multiples of ω. This follows trivially from the commutation relation:

$$\begin{aligned} HQ^+|E\rangle &= (\omega Q^+ + Q^+ H)|E\rangle \\ &= (E + \omega)Q^+|E\rangle \\ &\implies H(Q^+)^n|E\rangle = (E + n\omega)(Q^+)^n|E\rangle \end{aligned}$$

Call the set of n linearly independent eigenstates of H which are annihilated by the lowering operator $Q^- = (Q^+)^\dagger$ *root states* $|E_0^n\rangle$:

$$Q^-|E_0^n\rangle = 0 \; \forall n$$

The number of root states n depends on the details of the particular Hamiltonian H and raising operator Q^+. We group all the eigenstates obtained by acting with the raising operator Q^+ on a specific root state $|E_0^n\rangle$ together and refer to this set of connected eigenstates as a *tower*. A Hamiltonian possessing a SGA therefore contains multiple towers of eigenstates, where eigenstates in a single tower are all equidistant in energy with spacing ω.

3. AN OVERVIEW OF QUANTUM MANY-BODY SCARS

Restricted spectrum generating algebra

A restricted spectrum generating algebra (RSGA) (82) is analogous to a SGA, but rather than resulting in a Hamiltonian possessing multiple towers of equidistant eigenstates, the Hamiltonian will instead possess a single tower of equidistant eigenstates. Higher order generalisations of a RSGA exist (82), but here we will only consider a first order RSGA, in order to illustrate how such structures give rise to a single tower . A Hamiltonian is said to possess a RSGA, to first order, if it satisfies the following conditions:

$$H|\psi_0\rangle = E_0|\psi_0\rangle \tag{3.34}$$

$$[H, Q^+]|\psi_0\rangle = \omega Q^+|\psi_0\rangle \tag{3.35}$$

$$[[H, Q^+], Q^+] = 0 \tag{3.36}$$

Eq. (3.34) guarantees the existence of a single root state $|\psi_0\rangle$ with energy E_0. Eqs. (3.35),(3.36) guarantee repeated application of the raising operator Q^+ on the root state $|\psi_0\rangle$ generates a set of equidistant eigenstates of H. Note this proof runs in both directions. If a model is found to possess a single tower of equidistant eigenstates $|E_n\rangle$ such that $H|E_n\rangle = (E_0 + n\omega)|E_n\rangle$, one could construct an operator $Q^+ = \sum_n |E_{n+1}\rangle\langle E_n|$ which would satisfy the requirements of a RSGA, Eqs. (3.34)-(3.36). A model hosting a single tower of equidistant eigenstates therefore necessarily possesses an RSGA.

While a Hamiltonian possessing a RSGA results in a single set of equidistant eigenstates, to claim such a Hamiltonian hosts exact scars, the eigenstates generated by the RSGA must be atypical thermal eigenstates, in the sense their entropy deviates from the ETH prediction for eigenstates of similar energy. The next section presents a particularly simple construction for a Hamiltonian possessing a RSGA whose tower of equally spaced eigenstates are ETH violating. Note it is not the only way of engineering an exact scarred model, (89), however, a wide variety of exact scarred systems previously studied follow this formula (22, 51, 112).

Exact scarred model construction

Consider a Hamiltonian of the form:

$$H = H_0 + H'. \tag{3.37}$$

We assume the operator H' possess a spectrum generating algebra with respect to some *local* operator Q^+, i.e.

$$[H', Q^+] = \omega Q^+, \tag{3.38}$$

such that, for any eigenstate $|\Omega\rangle$ of H', $H'|\Omega\rangle = \Omega|\Omega\rangle$, H' will also possess an equally spaced tower of eigenstates $|\Omega_n\rangle$, defined as

$$|\Omega_n\rangle = \frac{1}{\sqrt{\mathcal{N}}}(Q^+)^n|\Omega\rangle \tag{3.39}$$

$$H'|\Omega_n\rangle = (\Omega + n\omega)|\Omega_n\rangle \tag{3.40}$$

where $\mathcal{N}$ is some normalisation factor.

Now suppose H_0 is chosen so that one particular tower of eigenstates of H' are degenerate eigenstates of H_0:

$$H_0|\Omega_n\rangle = E_\Omega|\Omega_n\rangle \;\forall n \tag{3.41}$$

It follows that, for the total Hamiltonian H in Eq. (3.37), H' will split the degeneracy such that $|\Omega_n n\rangle$ are equidistant eigenstates of the full Hamiltonian:

$$H|\Omega_n\rangle = (E_\Omega + \Omega + n\omega)|\Omega_n\rangle$$

Further, if $|\Omega\rangle$ is a weakly entangled state, due to the locality of Q^+, states $|\Omega_n\rangle$ are also expected to be weakly entangled. Given an appropriate choice of H_0 such that the model is non-integrable, the states $|\Omega_n\rangle$ will be weakly entangled scarred eigenstates which violate the ETH. Due to the presence of a single tower of equidistant eigenstates, models satisfying this construction must necessarily posses a RSGA.

In the next section we give an example of an exact scarred model which may be understood from this construction.

3.4.2 Example: longitudinal Ising model with additional 3-body interaction

Consider the following Hamiltonian, studied in Ref. (51), corresponding to a longitudinal Ising model with an additional 3-body interaction:

$$H = \sum_{i=0}^{N-1} \underbrace{\lambda(\sigma_i^x - \sigma_{i-1}^z \sigma_i^x \sigma_{i+1}^z)}_{H_\lambda} + \underbrace{\Delta\sigma_i^z}_{H_z} + \underbrace{J\sigma_i^z \sigma_{i+1}^z}_{H_{zz}} \qquad (3.42)$$

$$\sigma_i^z = \begin{pmatrix} 1 & 0 \\ 0 & -1 \end{pmatrix}, \ \sigma_i^x = \begin{pmatrix} 0 & 1 \\ 1 & 0 \end{pmatrix}$$

where σ_i^z, σ_i^x are the Pauli matrices. Throughout this section, we assume periodic boundary conditions, and we will consider parameters $\lambda = 1, \Delta = 0.1, J = 1$. The level statistics of this model with these parameters has been shown to be in agreement with a Wigner-Surmise distribution (51) confirming it is non-integrable.

By calling $H_0 = H_\lambda, H' = H_z + H_{zz}$, we see this Hamiltonian is of the form given in Eq. (3.37), that is, $H = H_0 + H'$. Trivially, the eigenstates of H' are simply all product states in the Z basis.

Now consider the local raising operator defined as:

$$Q^+ = \sum_{n=0}^{N-1} (-1)^n P_{n-1}^0 \sigma_n^+ P_{n+1}^0 \qquad (3.43)$$

Note that H' possess a spectrum generating algebra with respect to Q^+. Explicitly computing the commutator, one finds:

$$[H', Q^+] = (2\Delta - 4J)Q^+ \qquad (3.44)$$

Therefore, the eigenstates of H' may be grouped into equally spaced towers, connected by the application of the raising operator Q^+. To complete the analogy with the construction of exact scarred models in Section (3.4.1), all that remains

is to show a single tower of eigenstates of H' are degenerate eigenstates of H_0. Consider the tower of states generated by the application of Q^+ on the polarised state:

$$|S_n\rangle = \frac{1}{n!\sqrt{\mathcal{N}(N,n)}}(Q^+)^n|000...\rangle \tag{3.45}$$

The prefactor is simply a normalisation factor, with the quantity $\mathcal{N}(N,n)$ taking the following form for PBC:

$$\mathcal{N}(N,n) = \frac{N}{n}\binom{N-n-1}{n-1} \tag{3.46}$$

This is just a combinatorial factor which counts the number of states produced by the spin flips generated by Q^+.

Physically, $|S_n\rangle$ correspond to a state containing n magnons, with each magnon carrying momentum $k = \pi$. Moreover, for this particular tower of eigenstates of H', one can prove H_0 annihilates this entire tower of eigenstates (51):

$$H_0|S_n\rangle = 0 \ \forall n \tag{3.47}$$

It follows that the states $|S_n\rangle$ are eigenstates of the full Hamiltonian in Eq. (3.42) which are equally spaced in energy. Their energies may be computed explicitly as:

$$E_n = (2\Delta - 4J)n + (J - \Delta)N \tag{3.48}$$

Since the states $|S_n\rangle$ consist of quasiparticle excitations atop the polarised state, they are weakly entangled, relative to states nearby in energy. Moreover, as the model is non-integrable, the states $|S_n\rangle$ are exact scarred eigenstates of the Hamiltonian in Eq. (3.42).

Fig. 3.4(a) shows the entropy of eigenstates of this model at $N = 14$, obtained using exact diagonalisation. The exact scarred eigenstates are coloured in red. Similar to the PXP model, we see these are characterised by having sub-thermal entropy relative to states nearby in energy, in violation of the ETH. However,

$$H = \sum_{i=0}^{N-1} \lambda(\sigma_i^x - \sigma_{i-1}^z \sigma_i^x \sigma_{i+1}^z) + \Delta\sigma_i^z + J\sigma_i^z \sigma_{i+1}^z$$
$$\lambda = 1, \Delta = 0.1, J = 1, N = 16$$
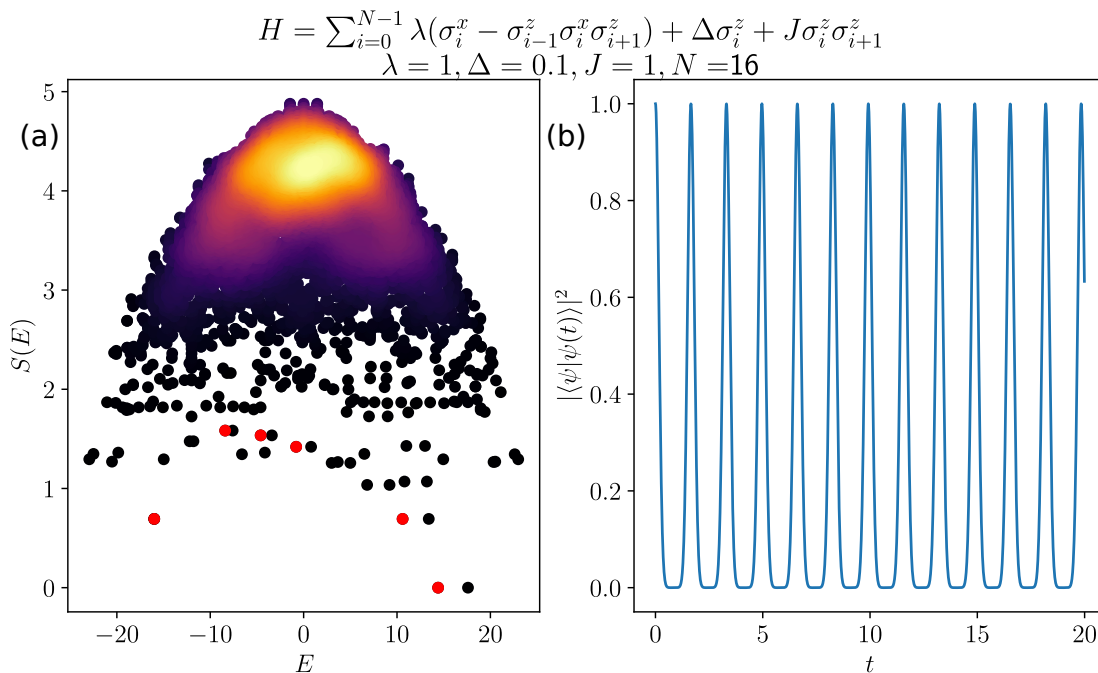
Figure 3.4: Exact scarring observed in the longitudinal Ising model with additional three body interaction (Eq. (3.42)) at system size $N = 16$. Results are obtained with exact diagonalisation. Plot (a) shows the entropy of eigenstates of the model, with the scarred eigenstates coloured in red. The scarred eigenstates are exactly equidistant in energy and are characterised by sub-thermal entropy relative to the predictions of ETH. As a consequence of the exact scarring, one can prepare special initial states which will undergo perfect oscillations for all times. Plot (b) shows the many-body fidelity (Eq. (2.43)) for one such initial state, a Rokshar-Kivelson state given in Eq. (3.49) with $\epsilon = 1$, which exhibits perfect revivals for all times.

they are equidistant in energy. This implies one can prepare an initial state with support only on the scarred eigenstates which would exhibit perfect fidelity revivals for all times. One family of initial states with this property are are Rokshar-Kivelson states (104), which may be expressed as:

$$|\epsilon\rangle = \frac{1}{\sqrt{\mathcal{Z}(\epsilon)}} \prod_{n=0}^{N-1} (1 + \epsilon(-1)^n P_{n-1}^0 \sigma_n^+ P_{n+1}^0)|000...\rangle \qquad (3.49)$$

$$= \frac{1}{\sqrt{\mathcal{Z}(\epsilon)}} \sum_{n=0}^{N/2} \epsilon^n \sqrt{\mathcal{N}(N,n)}|S_n\rangle \qquad (3.50)$$

where $\mathcal{Z}(\epsilon)$ is a normalisation factor:

$$\mathcal{Z}(\epsilon) = \sum_{n=0}^{N/2} \epsilon^{2n} \, \mathcal{N}(N, n) \tag{3.51}$$

These initial states are weakly entangled (51), unlike the reviving initial state in the PXP model, which was simply a product state (130). Fig. 3.4(b) shows the evolution of the wavefunction fidelity when this system is initialised in the state $|\epsilon = 1\rangle$. As expected due to the exact scarring present in this model, the wavefunction exhibits perfect revivals which persist for all time.

3.5 Summary

In this chapter we have introduced the concept of quantum many-body scars (QMBS), a form of weak ergodicity breaking occurring due to the presence of a subset of special eigenstates which violate the ETH. For the PXP model introduced in Eq. (2.41), it's scarred eigenstates are found to be approximately equidistant in energy, such that special initial states may be prepared that exhibit oscillatory dynamics for long times.

However, for the PXP model, these oscillations decay over time. To understand why this is the case, we introduced the forward scattering approximation (FSA), Eq. (3.28). This subspace was found to be 'approximately' invariant under the action of the PXP Hamiltonian. This result indicates that, in a suitable basis, the PXP Hamiltonian in fact consists of an integrable component weakly coupled via sparse matrix elements to a thermal component, as shown schematically in Fig. (3.2)(c). The scarred eigenstates were found to have their dominant support in this integrable subspace. The decaying component to the oscillatory scarred dynamics may then be understood as a leakage out of this integrable subspace into the exponentially large thermal sector.

Motivated by these findings, we introduced the concept of 'exact' QMBS. Systems hosting exact QMBS have Hamiltonians which fracture into an exact block diagonal form, with an integrable sector completely disconnected from the thermal sector. Scarred eigenstates reside completely in the integrable sector

and are exactly equidistant in energy. As a consequence, scarred dynamics from special initial states in exact scarred systems realise perfect oscillations for all times, with no decaying component. In order for a Hamiltonian to host exact scars, it must possess some underlying algebraic structure, Eq. (3.33). Using insights from these requirements, we introduced a particular construction which results in Hamiltonians realising exact QMBS.

Throughout the rest of this thesis, we wish understand the origin of approximate QMBS, as observed in the PXP model. Motivated by the necessary algebraic structure to realise exact QMBS, we seek similar conditions necessary to realise approximate QMBS. By understanding the requirements for approximate scarring, we will develop recipes to construct new scarred models. Exact scars, the idealised limit of approximate scarring, necessarily have Hamiltonians which possess spectrum generating algebras (SGA), $[H, Q^+] = \omega Q^+$. By interpreting exact scarring as an idealised limit of approximate scarring, a natural first step to understand the latter is to search for commutation relations of this form. However, given the scarred eigenstates in approximate scarred models do not strictly have equal energy spacing, we would not expect commutation relations like this to hold exactly, otherwise equidistant eigenstates would be present in the model. One can make progress if they relax the criteria of a SGA, instead searching for an approximate SGA such that

$$[H, Q^+] \approx \omega Q^+ \tag{3.52}$$

for some operator Q^+. The sense in which this relation is approximate is yet to be defined, and we will consider this question in more detail in the next Chapter. Indeed, we find the PXP model does in fact satisfy this relation, with the raising operator being intimately related to an approximate SU(2) symmetry.

Chapter 4

Weakly-broken Lie algebras: a mechanism for approximate scars

In this chapter, based on our work in Ref. (16), we outline how an approximate SGA may emerge which gives rise to QMBS, as a consequence of 'weakly broken Lie algebras'. The approximate SGA emerges due to the root structure of these Lie algebras. We discuss several different representations of these algebras found in the PXP model, highlighting the special case of a broken su(2) Lie algebra. Furthermore, we introduce a systematic method for which higher order corrections to these broken Lie algebras may be successively calculated. These successive corrections 'fix' the broken Lie algebra, in the sense they iteratively perturb the broken Lie algebra towards an exact Lie algebra. This results in Hamiltonians which possess an exact SGA corresponding to the relevant symmetry group generated by the Lie algebra. In this sense, the approximate scarred eigenstates may be interpreted as eigenstates which still possess a strong resemblance to the eigenstates of a proximate Hamiltonian hosting an exact symmetry generated by a Lie algebra.

4.1 Broken Lie algebra representations

We start by recalling some basics of Lie algebras and representation theory (45).
Infinitesimal generators g_i of a Lie group $\mathcal{G}$ form a Lie Algebra $\mathcal{A}$:

$$[g_i, g_j] = f_{ij}^k g_k. \tag{4.1}$$

The algebra is encoded in the structure constants f_{ij}^k, which are antisymmetric
with respect to lower indices, $f_{ij}^k = -f_{ji}^k$. A set of $n \times n$ matrices $\{M_i\}$ satisfy-
ing $[M_i, M_j] = f_{ij}^k M_k$ forms an n-dimensional representation of the Lie algebra.
Verifying these commutation relations is sufficient to verify the set $\{M_i\}$ form a
valid representation.

Given a set of infinitesimal generators of a Lie Group, define $\{H^i\}$ as the
largest set of mutually commuting generators. By taking linear combinations
of the remaining generators, one can construct a set of ladder operators, $\{E^\alpha\}$,
which satisfy:

$$[H^i, E^\alpha] = \alpha^i E^\alpha. \tag{4.2}$$

The coefficients α^i are called the *roots* of the Lie algebra. Verifying the roots
structure of the matrices $\{H^i\}, \{E^i\}$ is sufficient to check they form a valid rep-
resentation of the Lie algebra.

Together, the sets $\{H^i\}, \{E^\alpha\}$ are known as the Cartan-Weyl basis (146). As
the set $\{H^i\}$ are mutually commuting by definition, there exists a basis which
simultaneously diagonalises every H^i such that we can label basis states of a
representation by their H^i quantum numbers. On application of E^α, the change
in H^i quantum numbers is just the roots α^i:

$$\begin{aligned}
H^i|\psi\rangle &= \lambda_i|\psi\rangle, \tag{4.3} \\
H^i E^\alpha|\psi\rangle &= (E^\alpha H^i + \alpha^i E^\alpha)|\psi\rangle = (\lambda_i + \alpha^i)E^\alpha|\psi\rangle. \tag{4.4}
\end{aligned}$$

Given a single basis state which is an eigenstate of every H^i, one can systemati-
cally construct the remaining basis states via repeated applications of the ladder
operators E^α. This construction will prove useful for forming approximate basis

states of broken Lie algebra representations, which can be used to approximate many-body scar states.

Consider the set of operators $\{E^\alpha\}$ which are raising and lowering operators of some Lie algebra $\mathcal{A}$ in the Cartan-Weyl basis. One can expand the commutator $[E^\alpha, E^\beta]$ as a linear superposition of all the generators of the Lie algebra:

$$[E^\alpha, E^\beta] = \sum_\gamma c_\gamma E^\gamma + \sum_\gamma d_\gamma H^\gamma, \tag{4.5}$$

where the coefficients c_γ, d_γ, follow from the properties of the Lie algebra. However, one could consider inverting these equations, treating them as a definition for the operators $H^i(E^\alpha, [E^\alpha, E^\beta])$.

Now we are in position to introduce our notion of a 'broken' Lie algebra. Let the set of operators $\{\bar{E}^\alpha\}$ be of equal size as the previous set $\{E^\alpha\}$, but we do not assume they are raising/lowering operators of any Lie algebra. Taking Eq. (4.5) as a definition for H^i, we can express the latter as some linear combination of $\{E^\alpha, [E^\alpha, E^\beta]\}$. Then, define $\bar{H}^i$ as the *same* linear combination of $\{\bar{E}^\alpha, [\bar{E}^\alpha, \bar{E}^\beta]\}$. If the sets $\{\bar{E}^\alpha\}, \{\bar{H}^i\}$ satisfy:

$$[\bar{H}^i, \bar{E}^\alpha] = \alpha^i \bar{E}^\alpha + \delta^\alpha, \tag{4.6}$$

where α^i match the roots coefficients of the Lie algebra $\mathcal{A}$, we say $\{\bar{E}^\alpha\}, \{\bar{H}^i\}$ form a *broken representation* of the Lie algebra $\mathcal{A}$. It is understood δ^α contain no terms proportional to the generators $\bar{E}^\alpha$.

Now consider a Hamiltonian consisting of a linear combination of the diagonal generators $\{\bar{H}^i\}$ rotated to some other basis:

$$H = \sum_n a_n U^\dagger \bar{H}^n U, \tag{4.7}$$

where U is an arbitrary unitary rotation. Consider quenching from a simultaneous eigenstate $|\psi_0\rangle$ of the operators $\{\bar{H}^i\}$. Construct a basis for the broken representation by repeated application of the raising operators $\bar{E}^\alpha$ on $|\psi_0\rangle$. We refer to this basis as the representation basis. If the algebra were exact, the Hamiltonian would fracture into the block diagonal form $H = H_{\text{rep basis}} \bigoplus H_\perp$, where

$H_{\text{rep basis}}$ corresponds to projecting the Hamiltonian to the representation basis. Furthermore, there would exist several spectrum generating algebras of $H_{\text{rep basis}}$, corresponding to the rotated ladder operators, $Q_\alpha = U^\dagger E^\alpha U$. For a broken Lie algebra, these relations only hold approximately, with the error controlled by δ^α in Eq. (4.6).

It is possible the dynamics can resemble a quench with additional decoherence from the related system $H(\bar{H}^i, \bar{E}^\alpha) \to H(H^i, E^\alpha)$. For example, if the embedded algebra was su(2), it is possible the wavefunction will revive with a single frequency. The conditions necessary for the quench to resemble that of the proximate model with exact algebraic structure $H(H^i, E^\alpha)$ are the following are:

1. The variance of the approximate basis with respect to $\bar{H}^i$ is sufficiently small.

2. The spacing of expectation values with respect to $\bar{H}^i$ after applications of $\bar{E}^\alpha$ to $|\psi_0\rangle$ approximately obeys the root structure of the desired Lie algebra, i.e.,

$$\frac{\langle\phi|\bar{H}^i|\phi\rangle}{\langle\phi|\phi\rangle} \approx \lambda_i + \alpha^i, \qquad (4.8)$$

where $\bar{H}^i|\psi_0\rangle = \lambda_i|\psi_0\rangle$ and $|\phi\rangle = \bar{E}^\alpha|\psi_0\rangle$.

3. Repeated application of $\bar{E}^\alpha$ on $|\psi_0\rangle$ will terminate after a finite number of steps, thus generating a subspace of the full Hilbert space. In general, this subspace does not correspond to an exact symmetry sector of the Hamiltonian. To see signatures of the exact Lie algebra, this subspace must be sufficiently disconnected from the orthogonal space under the action of the Hamiltonian.

4.2 Derivation of perturbative corrections

By perturbing the operators $\bar{E}^\alpha$ with terms that appear in the error δ^α, it is possible to improve the broken Lie algebra, in the sense that decoherence in the quench described in the previous section is reduced.

Consider some broken representation of a Lie algebra:

$$[\bar{H}^i, \bar{E}^\alpha] = \alpha^i \bar{E}^\alpha + \delta^\alpha, \quad \delta^\alpha = \sum_n V_n^\alpha, \tag{4.9}$$

where the error δ^α has been decomposed into linearly independent terms V_n^α. Now perturb the raising/lowering operators as follows:

$$\bar{E}^\alpha_{(1)} = \bar{E}^\alpha + \sum_n c_n V_n^\alpha. \tag{4.10}$$

The coefficients c_n are to be understood as variational parameters, which we will seek to solve for so as to minimise the second order error terms arising from commutations involving the perturbed raising/lowering operators.

The first order raising and lowering operators $E^\alpha_{(1)}$ in turn defines the first order diagonal elements of the Lie algebra, $\bar{H}^i_{(1)}$, following the same definition of H^i in Eq. (4.5). The root structure of the broken Lie algebra at first order may then be computed as follows:

$$[\bar{H}^i_{(1)}, \bar{E}^\alpha_{(1)}] = \alpha^i \bar{E}^\alpha_{(i)} + \delta^\alpha{}_{(2)}(\vec{c}), \tag{4.11}$$

The magnitude of the second order error term $\delta^\alpha_{(2)}(\vec{c})$ will be a function of the variational parameters c_n. If coefficients c_n can be obtained such that the second order error becomes smaller than the first order error, $||\delta^\alpha_{(2)}||_F < ||\delta^\alpha||_F$, we would say the broken Lie algebra has been 'improved'. If the higher order error term can be made zero, we would say the broken Lie algebra has been corrected completely and is now exact. If the error term does not completely vanish, one can use the same procedure described at first order to obtain second order perturbations to the raising and lowering operators, such that the process can be iteratively repeated to obtain higher and higher order correction terms. Fig. 4.1 schematically shows this process of identifying corrections to the algebra. We will demonstrate that this procedure of iteratively correcting a broken Lie algebra results in many-body scarred models with long-lived coherent dynamics in the subsequent sections.

Before illustrating this approach with examples, we briefly discuss ways of

4. WEAKLY-BROKEN LIE ALGEBRAS: A MECHANISM FOR APPROXIMATE SCARS
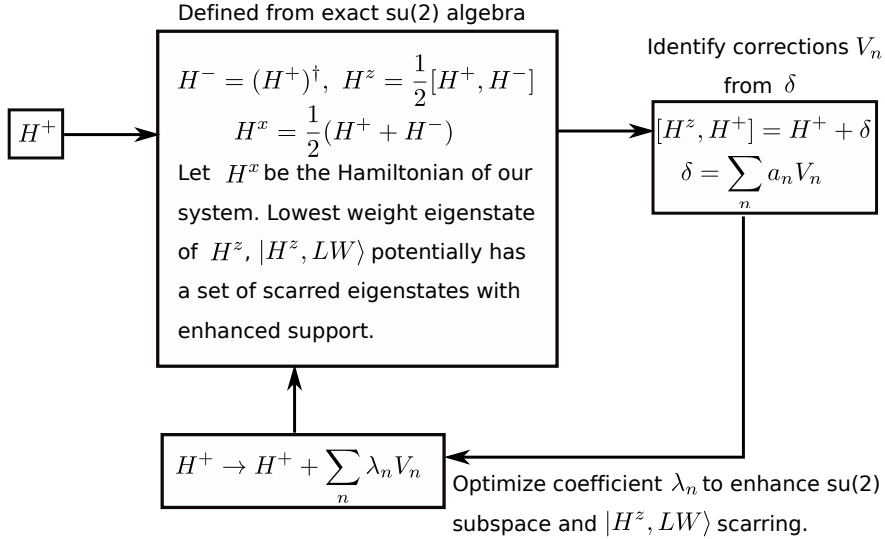
Figure 4.1: Schematic illustration of an iterative scheme which identifies corrections to broken Lie algebras, specifically an su(2) Lie algebra in this case. The optimisation of λ_n is with respect to the error measures described in the text, such as maximising the first fidelity peak $|\langle H^z, LW | e^{-iHt} | H^z, LW \rangle|^2$ or minimising the subspace variance of H w.r.t. to the su(2) basis defined in Eq. (4.13).

quantifying how much the approximate Lie algebra representation differs from an exact representation. From now on we explicitly restrict to the case of an su(2) Lie algebra for simplicity. Therefore the broken Lie algebra consists of the operators $\{\bar{H}^z, \bar{H}^+, \bar{H}^-\}$, which are assumed to satisfy the conditions of a broken su(2) Lie algebra:

$$[\bar{H}^z, \bar{H}^\pm] = \pm \bar{H}^\pm + \delta^\pm. \tag{4.12}$$

As a possible error measure, we consider $\max\{\text{var}(\bar{H}^z)_n\}$, where $\text{var}(\bar{H}^z)_n$ is defined as the variance of the operator $\bar{H}^z$ with respect to the state $|n\rangle$:

$$|n\rangle = \frac{1}{\sqrt{\mathcal{N}}} (\bar{H}^+)^n |\text{LW}\rangle, \tag{4.13}$$

$$var(\bar{H}_z)_n = \langle n | (\bar{H}_z)^2 | n \rangle - (\langle n | \bar{H}_z | n \rangle)^2 \tag{4.14}$$

with $|\text{LW}\rangle$ the lowest weight eigenstate of $\bar{H}^z$ and $\mathcal{N}$ a normalisation factor. If an algebra were exact, $\max\{\text{var}(\bar{H}^z)_n\} = 0$.

Furthermore, for an exact su(2) algebra, we expect the basis states $|n\rangle$ should have harmonic (equal) energy spacing. To quantify the deviation from harmonic spacing we introduce the quantity K:

$$K = ||M||_F, \quad M_{nm} = |\Delta E_n - \Delta E_m|, \tag{4.15}$$

which represents the Frobenius norm of the matrix of level spacings. The latter are given by

$$\Delta E_n = \langle \bar{H}^z \rangle_{n+1} - \langle \bar{H}^z \rangle_n, \quad \langle \bar{H}^z \rangle_n = \langle n|\bar{H}^z|n\rangle. \tag{4.16}$$

For an exact su(2) Lie algebra, we would also expect $K = 0$.

Finally, we may consider as an error measure how disconnected the subspace spanned by $|n\rangle$ is from its orthogonal subspace under the action of the Hamiltonian $H = H^+ + H^-$. For an exact su(2) Lie algebra, these subspaces would remain disconnected under the action of H, as H possesses su(2) symmetry. To quantify this property, we use the subspace variance σ:

$$\sigma = \text{tr}\left((U_{\text{rep}}^\dagger H^2 U_{\text{rep}}) - (U_{\text{rep}}^\dagger H U_{\text{rep}})^2 \right), \tag{4.17}$$

where U_{rep} is a projector onto the basis $|n\rangle$. This quantity can be interpreted as being proportional to the Frobenius norm of the block labelled couplings in Fig. 3.2(c).

4.3 Example: Fixing a 'trivial' broken su(2) algebras

We have introduced in a general fashion both broken Lie algebras and how to find their corrections, however we now consider specific cases. Before considering broken Lie algebras which emerge due to kinetic constraints, specifically broken Lie algebras which offer insight into the scarred dynamics of the PXP model, we will first consider a trivial case of a broken su(2) Lie algebra, which is simply a small perturbation of an exact su(2) algebra. While it is immediately obvious how

4. WEAKLY-BROKEN LIE ALGEBRAS: A MECHANISM FOR APPROXIMATE SCARS

to 'correct' this algebra (remove the perturbation), we nevertheless go through the process of deriving the corrections, to demonstrate how the procedure outlined in the previous section would work in practice.

Consider the following operators, to be interpreted as raising and lowering operators, defined for a Hilbert space of dimension 2:

$$H^+ = \begin{pmatrix} \epsilon & 0 \\ 1 & \epsilon \end{pmatrix} \quad H^- = (H^+)^\dagger = \begin{pmatrix} \epsilon & 1 \\ 0 & \epsilon \end{pmatrix} \tag{4.18}$$

Where ϵ is some small (real) parameter. It is apparent that one may write $H^\pm = S^\pm_{1/2} + \epsilon \mathbb{I}$, where $\mathbb{I}$ is the identity matrix and $S^\pm_{1/2}$ are the conventional su(2) raising and lowering operators of a spin half representation:

$$S^+_{1/2} = \begin{pmatrix} 0 & 0 \\ 1 & 0 \end{pmatrix}, \quad S^-_{1/2} = \begin{pmatrix} 0 & 1 \\ 0 & 0 \end{pmatrix} \tag{4.19}$$

Therefore it is somewhat trivial that the operators $H^\pm$ should form a broken su(2) Lie algebra, and we would expect our procedure to correct the Lie algebra to produce the operators $S^\pm_{1/2}$. Nevertheless, we will demonstrate this explicitly in order to illustrate the process.

To show $H^\pm$ are elements of a broken su(2) Lie algebra, we must calculate the Z element of the algebra, which is defined from the properties of a conventional su(2) Lie algebra:

$$H^z \equiv \frac{1}{2}[H^+, H^+] = \frac{1}{2}\begin{pmatrix} -1 & 0 \\ 0 & 1 \end{pmatrix} \tag{4.20}$$

Verifying the root structure of the Lie algebra, we find:

$$[H^z, H^+] = \begin{pmatrix} 0 & 0 \\ 1 & 0 \end{pmatrix} = H^+ - \underbrace{\epsilon \mathbb{I}}_{V^+_{(1)}} \tag{4.21}$$

$$[H^z, H^-] = -\begin{pmatrix} 0 & 1 \\ 0 & 0 \end{pmatrix} = -H^- - \underbrace{\epsilon \mathbb{I}}_{V^-_{(1)}} \tag{4.22}$$

70

These commutation relations verify that the operators $\{H^+, H^-, H^z\}$ realise a broken su(2) Lie algebra, according to the definition given in Eq. (4.6). This is because the coefficient of $H^\pm$ on the right hand side of these equations are ± 1 respectively, the correct coefficient for the root structure of a su(2) Lie algebra.

Corrections to this broken Lie algebra at first order follow from perturbing the raising and lowering operators $H^\pm$ by the first order error terms $V^\pm_{(1)}$, multiplied by a variational parameter, λ. Absorbing the coefficient ϵ into this variational parameter, the first order raising and lowering operators become:

$$H^+_{(1)} = H^+ + \lambda V^+_{(1)} = H^+ + \lambda \mathbb{I} \tag{4.23}$$

$$H^-_{(1)} = H^- + \lambda V^-_{(1)} = H^- + \lambda \mathbb{I} \tag{4.24}$$

In this trivial case it is possible to find the optimal λ by calculating the second order errors terms of the broken Lie algebra and minimising them:

$$H^z_{(1)} \equiv \frac{1}{2}[H^+_{(1)}, H^-_{(1)}] = \frac{1}{2}\begin{pmatrix} -1 & 0 \\ 0 & 1 \end{pmatrix} \tag{4.25}$$

$$[H^z_{(1)}, H^+_{(1)}] = H^+_{(1)} - \underbrace{(\epsilon + \lambda)\mathbb{I}}_{V^+_{(2)}} \tag{4.26}$$

$$[H^z_{(1)}, H^-_{(1)}] = -H^-_{(1)} - \underbrace{(\epsilon + \lambda)\mathbb{I}}_{V^-_{(2)}} \tag{4.27}$$

Therefore by setting $\lambda = -\epsilon$, the second order error terms $V^\pm_{(2)}$ vanish completely and the algebra is completely fixed at first order. The first order corrected raising and lowering operators are nothing but the conventional spin half raising and lowering operators defined earlier, $H^\pm_{(1)} = S^\pm_{(1/2)}$. It must be admitted that this case is rather trivial, but it serves to illustrate how one would derive corrections to a broken Lie algebra when the proximate generators of an exact algebra are not obvious.

4.4 PXP model and weakly broken su(2) algebra

We now exemplify our general embedding scheme outlined in Section 4.1 by using the PXP model, Eq. (2.41). We demonstrate how to identify and improve the broken su(2) algebra associated with $\mathbb{Z}_2$ revivals.

4.4.1 $\mathbb{Z}_2$ revivals and su(2) algebra

First we focus on the well-known case of $\mathbb{Z}_2$ revivals in the PXP model. Define the su(2) spin raising operator

$$\bar{H}^+ \equiv \sum_n \left(\tilde{\sigma}^+_{2n} + \tilde{\sigma}^-_{2n-1} \right), \tag{4.28}$$

where we have introduced the shorthand notation

$$\tilde{\sigma}^\alpha_n \equiv P_{n-1} \sigma^\alpha_n P_{n+1}. \tag{4.29}$$

Recall this is the same operator used in the forward scattering approximation (FSA) in Section 3.3.1. However, the motivation for choosing this form of $\bar{H}^+$ is rather different from why it was chosen for the FSA procedure, which we will discuss below.

For the above representation, we have $H_{\text{PXP}} = \bar{H}^+ + \bar{H}^-$ such that $H_{\text{PXP}} = \bar{H}^x$, ie the PXP Hamiltonian itself may be considered the X element of this Lie algebra. However, note the choice of $\bar{H}^+$ such that $H_{PXP} = \bar{H}^+ + \bar{H}^-$ is not unique. The reason we choose this particular $\bar{H}^+$ in this instance is we want a specific su(2) representation which is relevant for revivals from the Néel state $|Z_2\rangle = |0101...\rangle$ when evolving under the action of $\bar{H}^x = H_{PXP}$. We seek a representation for which $|\mathbb{Z}_2\rangle$ is the lowest weight state of the Z element of the Lie algebra, $\bar{H}^z = 1/2[\bar{H}^+, \bar{H}^-]$, such that by analogy with an exact su(2) algebra we can think of this state as being a large spin along the negative Z direction. Decaying revivals may then be loosely understood as a precession of this large spin around the X axis, generated by $\bar{H}^x = H_{PXP}$.

We verify the Néel state is indeed the lowest weight eigenstate of $\bar{H}^z$ by computing it explicitly:

$$\bar{H}^z \equiv \frac{1}{2}[\bar{H}^+, \bar{H}^-] = \sum_n \left(\tilde{\sigma}^z_{2n} - \tilde{\sigma}^z_{2n-1} \right). \tag{4.30}$$

Note the minus sign in the second equation, which tells us that $\bar{H}^z$ acts as a staggered magnetisation in the constrained Hilbert space. Since $\bar{H}^z$ is a staggered magnetisation, it follows that the Néel state $|0101...\rangle$ is the lowest weight eigenstate of this operator, while the anti-Néel state $|1010...\rangle$ would correspond to a large spin in the positive Z direction.

Computing the root structure arising from the operators $\{\bar{H}^+, \bar{H}^-, \bar{H}^z\}$ verifies they do realise a broken Lie su(2) algebra:

$$\left[\bar{H}^z, \bar{H}^+\right] = \bar{H}^+ + \delta^+_{(1)}, \tag{4.31}$$

$$\left[\bar{H}^z, \bar{H}^-\right] = -\bar{H}^- + \delta^-_{(1)}, \tag{4.32}$$

where the error terms that break the algebra are

$$\delta^+_{(1)} = -\frac{1}{2}(PP\sigma^+_{2n}P + P\sigma^+_{2n}PP + P\sigma^-_{2n+1}PP + PP\sigma^-_{2n+1}P), \tag{4.33}$$

$$\delta^-_{(1)} = \frac{1}{2}(PP\sigma^-_{2n}P + P\sigma^-_{2n}PP + P\sigma^+_{2n+1}PP + PP\sigma^+_{2n+1}P). \tag{4.34}$$

For brevity, we have suppressed a summation over the lattice sites in the definition of $\delta^{+/-}_{(1)}$, and terms like $PP\sigma^+_{2n}P$ stand for $\sum_n P_{2n-2}P_{2n-1}\sigma^+_{2n}P_{2n+1}$ (i.e., strings of P's act on consecutive neighbouring sites).

From the expressions in Eqs. (4.31)-(4.32), we see that $\{\bar{H}^z, \bar{H}^+, \bar{H}^-\}$ form a broken representation of su(2). In this language, the forward scattering approximation (FSA) (130) (Section 3.3.1) is rephrased as projecting the Hamiltonian H to the broken representation basis in Eq. (4.13), with $|\text{LW}\rangle \equiv |\mathbb{Z}_2\rangle$, and diagonalising. This procedure gives very accurate approximations to the special eigenstates of the full PXP model – see red crosses in Fig. 4.2 (a), (b), (c), (e).

Next, we identify perturbations which can potentially improve the su(2) rep-
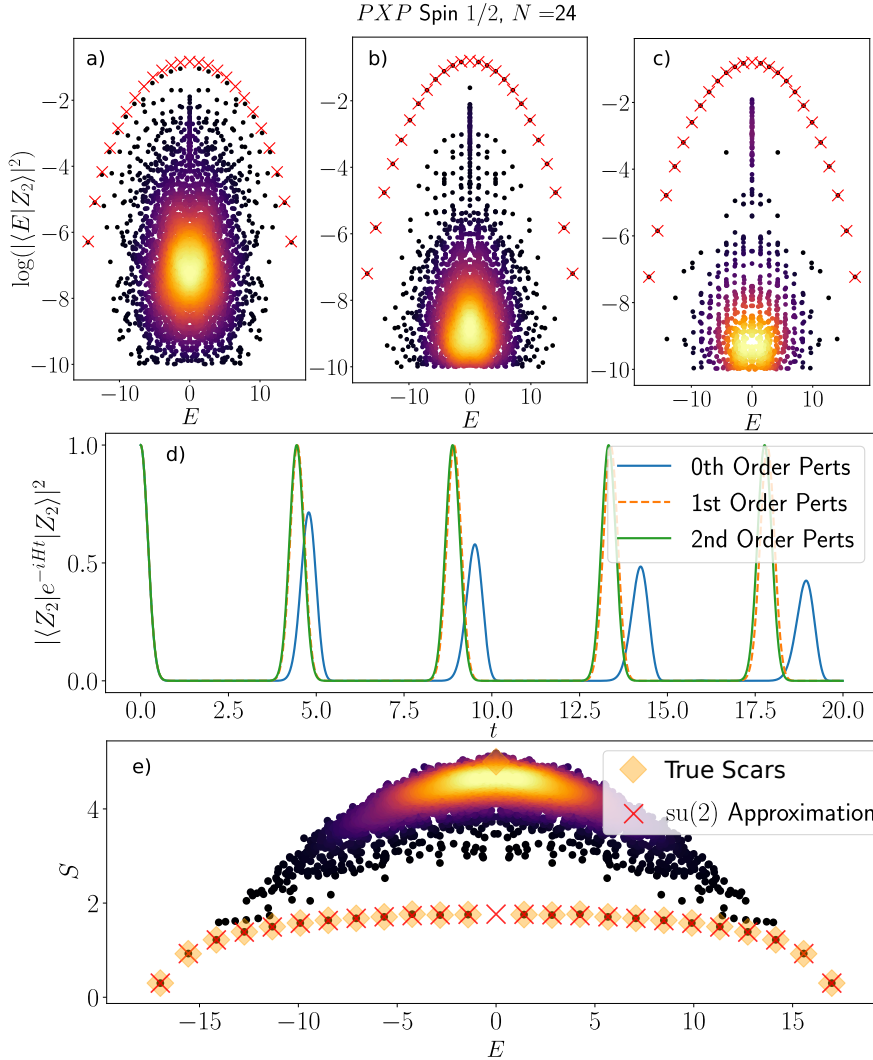
Figure 4.2: $\mathbb{Z}_2$ revival in PXP model originating from a broken su(2) Lie algebra. (a) Eigenstate overlap with the Néel $|\mathbb{Z}_2\rangle$ state. (b) Eigenstate overlap after including the first order su(2) correction, Eq. (4.37). (c) Eigenstate overlap after including the second order su(2) correction, Eqs. (4.40)-(4.47). (d) Quantum fidelity in $\mathbb{Z}_2$ quench, with and without perturbations. Perturbation coefficients are those that maximise the first fidelity revival peak. (e) Bipartite entropy, Eq. (2.21), of the eigenstates of PXP model after including second order $\mathbb{Z}_2$ su(2) corrections. The states labelled 'True Scars' are exact diagonalisation results identified from the top band of states in (c). Red crosses in (a), (b), (c), (e) indicate approximate scar states obtained by projecting the Hamiltonian to the broken su(2) basis and diagonalising. Colour scale in (a), (b), (c), (e) indicates the density of data points, with lighter regions being more dense.

Order	$1 - f_0$	$\sigma/D_{\text{su}(2)}$	$max(var(H^z)_n)$	K
$n = 0$	$2.853{\times}10^{-1}$	$1.116{\times}10^{-1}$	$2.711{\times}10^{-1}$	$9.310{\times}10^{0}$
$n = 1$	$6.760{\times}10^{-4}$	$2.190{\times}10^{-4}$	$9.694{\times}10^{-4}$	$6.008{\times}10^{-1}$
$n = 2$	$3.113{\times}10^{-6}$	$3.303{\times}10^{-6}$	$2.355{\times}10^{-5}$	$8.090{\times}10^{-2}$

Table 4.1: Error metrics for the $\mathbb{Z}_2$ su(2) subspace of the PXP model at various perturbation orders for $N = 24$. Subspace variance σ is normalised by the dimension of the su(2) representation, $N + 1$. See text for details of the perturbations.

resentation. First, define $\bar{H}^{\pm}_{(1)} = \bar{H}^{\pm} + \lambda\delta^{\pm}_{(1)}$. This gives us

$$\bar{H}^x_{(1)} = \bar{H}^+_{(1)} + \bar{H}^-_{(1)} \tag{4.35}$$

$$= H_{PXP} + \lambda(\delta^+_{(1)} + \delta^-_{(1)}) \tag{4.36}$$

$$= P\sigma^x_n P + \lambda(P\sigma^x_n PP + PP\sigma^x_n P). \tag{4.37}$$

In order to find the optimal perturbation strength λ, we maximise the first fidelity revival as a function of λ,

$$f_0(\lambda) = f(\lambda, t_0) = |\langle\psi(0)|e^{-iH(\lambda)t_0}|\psi(0)\rangle|^2, \tag{4.38}$$

where t_0 is the time at which the first revival occurs. Note that t_0 is λ-dependent. This minimisation was carried out using the Python SciPy routine that employs the 'Sequential Least Squares Programming' (SLSQP) method. After optimisation, we recover the perturbation that was previously empirically found in Ref. (60) to enhance the revivals following a $|\mathbb{Z}_2\rangle$ quench with maximal f_0 when $\lambda = 0.108$ (at system size $N = 18$). It was previously demonstrated the PXP model remains non-integrable after including this perturbation (23). Note that the first order perturbation improves all error metrics of the broken representation, see Table 4.1.

Second order perturbations can be obtained in a similar fashion, although algebraic manipulations become very laborious to perform by hand. Our analytical results have been tested against a custom-designed software for symbolic computations of the nested commutators involving projectors [1]. Fig. 4.2 summarises

---

[1]K. Bull (https://github.com/Cable273/comP).

4. WEAKLY-BROKEN LIE ALGEBRAS: A MECHANISM FOR APPROXIMATE SCARS

the differences between models after including first and second order perturbations. We find the scarred eigenstates become increasingly decoupled from the thermal bulk and can also be characterised by their anomalously low bipartite entanglement entropy S, Eq. (2.21).

The second order error term $\delta_{(2)}^+$, evaluated by computing the root structure $[\bar{H}_{(1)}^z, \bar{H}_{(1)}^+] = \bar{H}_{(1)}^+ + \delta_{(2)}^+$, is found to be a linear combination of linearly independent error terms:

$$\delta_{(2)}^+ = \sum_n \alpha_n \delta_{(2),n}^+ \tag{4.39}$$

Restricting to terms $\delta_{(2),n}^+$ with only a single spin flip, we identify the following linearly independent second order error terms $\delta_{(2),n}^+$:

$$\delta_{(2),1}^+ = P\sigma^z P\sigma_{2n}^+ P + P\sigma_{2n}^+ P\sigma^z P + P\sigma^z P\sigma_{2n+1}^- P + P\sigma_{2n+1}^- P\sigma^z P, \tag{4.40}$$

$$\delta_{(2),2}^+ = P\sigma_{2n}^+ PPP + PPP\sigma_{2n}^+ P + P\sigma_{2n+1}^- PPP + PPP\sigma_{2n+1}^- P, \tag{4.41}$$

$$\delta_{(2),3}^+ = PP\sigma_{2n}^+ PP + PP\sigma_{2n+1}^- PP, \tag{4.42}$$

$$\delta_{(2),4}^+ = PP\sigma_{2n}^+ P\sigma^z P + P\sigma^z P\sigma_{2n}^+ PP + PP\sigma_{2n+1}^- P\sigma^z P + P\sigma^z P\sigma_{2n+1}^- PP, \tag{4.43}$$

$$\delta_{(2),5}^+ = PPP\sigma_{2n}^+ PP + PP\sigma_{2n}^+ PPP + PPP\sigma_{2n+1}^- PP + PP\sigma_{2n+1}^- PPP, \tag{4.44}$$

$$\delta_{(2),6}^+ = P\sigma_{2n}^+ P\sigma^z PP + PP\sigma^z P\sigma_{2n}^+ P + PP\sigma^z P\sigma_{2n+1}^- P + P\sigma_{2n+1}^- P\sigma^z PP, \tag{4.45}$$

$$\delta_{(2),7}^+ = PPPP\sigma_{2n}^+ P + P\sigma_{2n}^+ PPPP + PPPP\sigma_{2n+1}^- P + P\sigma_{2n+1}^- PPPP, \tag{4.46}$$

$$\delta_{(2),8}^+ = PP\sigma_{2n}^+ P\sigma^z PP + PP\sigma^z P\sigma_{2n}^+ PP + PP\sigma_{2n+1}^- P\sigma^z PP + PP\sigma^z P\sigma_{2n+1}^- PP. \tag{4.47}$$

Putting these terms together, we obtain the second order perturbations, $\bar{H}_{(2)}^+ = \bar{H}^+ + \lambda_0 \delta_{(1)}^+ + \sum_{i=1}^8 \lambda_i \delta_{(2),i}^+$ and $\bar{H}_{(2)}^- = \bar{H}^- + \lambda_0 \delta_{(1)}^- + \sum_{i=1}^8 \lambda_i \delta_{(2),i}^-$, which in turn define $\bar{H}_{(2)}^x = \bar{H}_{(2)}^+ + \bar{H}_{(2)}^-$. Coefficients λ_i optimising the fidelity were found to be:

$$\lambda_i^* = [0.11135, 0.000217, -0.000287, -0.00717, 0.00827, 0.00336, 0.00429, 0.0103, 0.00118],$$

where the first value is the optimal coefficient for the first order term Eq. (4.33), while the remaining coefficients correspond to the terms in order of appearance in Eqs. (4.40)-(4.47). These values have been found via numerical optimisation

at system size $N = 16$. Note that previous work in Ref. (23) only considered $PXPIP + PIPXP$ as a second order perturbation to H_{PXP}. By including all spin flip terms obtained from the Lie algebra error, fidelity can be enhanced to $1 - f_0 \approx O(10^{-6})$, while if we only retain $PXPIP + PIPXP$ we obtain infidelity that is a few orders of magnitude higher, $1 - f_0 \approx O(10^{-3})$ (data for $N = 16$). In Ref. (23) fidelity on the order $1 - f_0 \approx O(10^{-6})$ was found by including only terms $P_{n-1}X_nP_{n+1}P_{n+d} + P_{n-d}P_{n-1}X_nP_{n+1}$ up to high order $d \leq 10$, which are expected to arise as corrections in higher orders of our method. While these terms alone appear sufficient to reach very high fidelity values, our analysis suggests that, strictly speaking, these terms do not fully fix the su(2) algebra.

As discussed earlier, the decomposition of $H_{\text{PXP}} = \bar{H}^+ + \bar{H}^-$ used to identify the broken su(2) algebra associated with $\mathbb{Z}_2$ revivals is not unique. In the following section, we discuss additional decompositions leading to an additional su(2) representation which can be enhanced to fix revivals from $|\mathbb{Z}_3\rangle$. Furthermore, in Appendix A.1.2, we discuss a su(2) representation which may be enhanced to generate new models exhibiting revivals from the $|\mathbb{Z}_4\rangle$ state, even though quenches from this state were found to be generically thermalising in the original PXP model (131).

4.5 $\mathbb{Z}_3$ revivals from $\mathrm{su}(2)$ algebra

In addition to $\mathbb{Z}_2$ revivals, the PXP model was also shown numerically to exhibit wave function revivals following a quench from $|\mathbb{Z}_3\rangle = |100100...\rangle$ state (130, 131). Unlike $|\mathbb{Z}_2\rangle$ state, the revivals from $|\mathbb{Z}_3\rangle$ sharply decay even in numerical simulations on fairly small systems (131), suggesting the model is even further away from any exact Lie algebra representation furnished by $|\mathbb{Z}_3\rangle$ state.

The $\mathbb{Z}_3$ revivals originate from $2N/3 + 1$ scarred eigenstates with enhanced support on the $|\mathbb{Z}_3\rangle$ state. We stress that out of these $2N/3+1$ scarred eigenstates, only two eigenstates coincide with the $N + 1$ scarred eigenstates with enhanced support on $\mathbb{Z}_2$, which are the ground and most excited eigenstates of the model. Thus, we interpret the $\mathbb{Z}_3$ scarred subspace as a distinct embedded $\mathrm{su}(2)$ subspace as compared to the $\mathbb{Z}_2$ scarred subspace.

There has been no FSA method to describe the $2N/3 + 1$ $\mathbb{Z}_3$ scar states and, consequently, the perturbations that improve the $\mathbb{Z}_3$ revival are not known. Here we demonstrate that it is possible to deform the PXP model to stabilise a *different* $\mathrm{su}(2)$ algebra representation compared to the $\mathbb{Z}_2$ case, which results in robust $\mathbb{Z}_3$ revivals.

We follow our general approach and start by introducing raising and lowering operators compatible with $|\mathbb{Z}_3\rangle$ state:

$$\bar{H}^+ = \sum_n \left(\tilde{\sigma}_{3n}^- + \tilde{\sigma}_{3n+1}^+ + \tilde{\sigma}_{3n+2}^+ \right), \tag{4.48}$$

$$\bar{H}^- = \sum_n \left(\tilde{\sigma}_{3n}^+ + \tilde{\sigma}_{3n+1}^- + \tilde{\sigma}_{3n+2}^- \right), \tag{4.49}$$

where, as before, we have $H_{\mathrm{PXP}} = \bar{H}^+ + \bar{H}^-$. The $\mathrm{su}(2)$ diagonal generator is then given by $\bar{H}^z = \frac{1}{2}[\bar{H}^+, \bar{H}^-]$, which can be shown to take the form

$$\bar{H}^z = \sum_n -\tilde{\sigma}_{3n}^z + \tilde{\sigma}_{3n+1}^z + \tilde{\sigma}_{3n+2}^z + \frac{1}{2} \sum_n \left(P_{3n}\sigma_{3n+1}^+\sigma_{3n+2}^- P_{3n+3} + P_{3n}\sigma_{3n+1}^-\sigma_{3n+2}^+ P_{3n+3} \right). \tag{4.50}$$

The lowest weight state of $\bar{H}^z$ is $|\mathbb{Z}_3\rangle$, as it should be, although it is degenerate. The first order perturbation will lift this degeneracy such that $|\mathbb{Z}_3\rangle$ is the unique

ground state of $\bar{H}^z_{(1)}$. We find the $\bar{H}^z, \bar{H}^+, \bar{H}^-$ obey the commutation relations:

$$[\bar{H}^z, \bar{H}^+] = \bar{H}^+ + \delta^+_{(1)}, \tag{4.51}$$

$$\delta^+_{(1)} = -\frac{1}{2} \sum_n \left(P_{3n-1} P_{3n} \sigma^+_{3n+1} P_{3n+2} + P_{3n-2} \sigma^+_{3n-1} P_{3n} P_{3n+1} \right.$$

$$+ \left. P_{3n-1} \sigma^-_{3n} P_{3n+1} P_{3n+2} + P_{3n+1} P_{3n+2} \sigma^-_{3n+3} P_{3n+4} \right)$$

$$+ \frac{1}{2} \sum_n \left(P_{3n-1} \sigma^-_{3n} \sigma^+_{3n+1} \sigma^-_{3n+2} P_{3n+3} + P_{3n} \sigma^-_{3n+1} \sigma^+_{3n+2} \sigma^-_{3n+3} P_{3n+4} \right)$$

$$+ \sum_n \left(P_{3n} \sigma^+_{3n+1} P_{3n+2} P_{3n+3} + P_{3n} P_{3n+1} \sigma^+_{3n+2} P_{3n+3} \right). \tag{4.52}$$

Similarly, we find $[\bar{H}^z, \bar{H}^-] = -\bar{H}^- + \delta^-_{(1)}$, such that $\{\bar{H}^z, \bar{H}^+, \bar{H}^-\}$ form a broken representation of su(2). We identify the following first order perturbations to the PXP model which improve the representation:

$$V_1 = \sum_n \left(P_{3n-2} \sigma^x_{3n-1} P_{3n} P_{3n+1} + P_{3n-1} P_{3n} \sigma^x_{3n+1} P_{3n+2} \right.$$

$$+ \left. P_{3n-1} \sigma^x_{3n} P_{3n+1} P_{3n+2} + P_{3n-2} P_{3n-1} \sigma^x_{3n} P_{3n+1} \right), \tag{4.53}$$

$$V_2 = \sum_n \left(P_{3n} P_{3n+1} \sigma^x_{3n+2} P_{3n+3} + P_{3n} \sigma^x_{3n+1} P_{3n+2} P_{3n+3} \right), \tag{4.54}$$

$$V_3 = \sum_n \left(P_{3n} \sigma^x_{3n+1} \sigma^x_{3n+2} \sigma^x_{3n+3} P_{3n+4} + P_{3n-1} \sigma^x_{3n} \sigma^x_{3n+1} \sigma^x_{3n+2} P_{3n+3} \right). \tag{4.55}$$

We emphasise that perturbations that improve $\mathbb{Z}_3$ revival, even at first order, break the full translation symmetry of the model to a subgroup of translations by a unit cell of size 3. This is different from $\mathbb{Z}_2$ revivals where the first-order corrections respect the full translation symmetry of the chain. We next discuss two interesting limits, corresponding to weak and strong magnitude of these perturbations.

4.5.1 Weak limit

By numerical optimisation of the revival amplitude under perturbations in Eqs. (4.53),(4.54) and (4.55), bounding coefficients to satisfy $|\lambda_i| < 0.5$, we find that revivals from

Order	$1 - f_0$	$\sigma/D_{\mathrm{su}(2)}$	$max(var(H^z)_n)$	K
$n = 0$	$6.397{\times}10^{-1}$	$3.358{\times}10^{-1}$	$9.300{\times}10^{-1}$	$1.234{\times}10^{1}$
$n = 1$	$1.338{\times}10^{-2}$	$3.349{\times}10^{-2}$	$1.717{\times}10^{-1}$	$4.957{\times}10^{0}$
$n = 2$	$1.852{\times}10^{-5}$	$7.082{\times}10^{-3}$	$2.357{\times}10^{-2}$	$2.124{\times}10^{0}$

Table 4.2: Error metrics for the $\mathbb{Z}_3$ su(2) subspace of the PXP model at various perturbation orders for system size $N = 24$. Subspace variance σ is normalised by the dimension of the su(2) representation, $2N/3 + 1$. See text for details of the perturbations.

$|\mathbb{Z}_3\rangle$ can be enhanced with optimal perturbation coefficients

$$\lambda^* = [0.18244, -0.10390, 0.05445]. \tag{4.56}$$

Similar to $|\mathbb{Z}_2\rangle$ revival, we can find second order perturbations which improve revivals further (see Appendix A.1.1 for the terms and optimal coefficients). A summary of the effect of successive perturbations on $|\mathbb{Z}_3\rangle$ is given in Fig. 4.3, while error metrics at various orders are given in Table 4.2. Despite long-lived coherent oscillations when the system is initialised in the $|\mathbb{Z}_3\rangle$ state, we verify the model including second order perturbations is still ergodic by calculating the mean level spacing (90) $\langle r \rangle = 0.5256$ at $N = 24$, consistent with the Wigner-Surmise distribution one would expect in an ergodic system.

4.5.2 Strong limit: exact spectrum generating algebra

A curious feature of $\mathbb{Z}_3$ revivals is that the su(2) algebra can be made exact for the model

$$H = \sum_n \tilde{\sigma}_n^x - V_1, \tag{4.57}$$

which is the PXP model from which we subtracted the V_1 perturbation defined previously in Eq. (4.53). As the strength of V_1 is order unity, this model should not be called a 'perturbation' to the PXP model. For the model in Eq. (4.57),
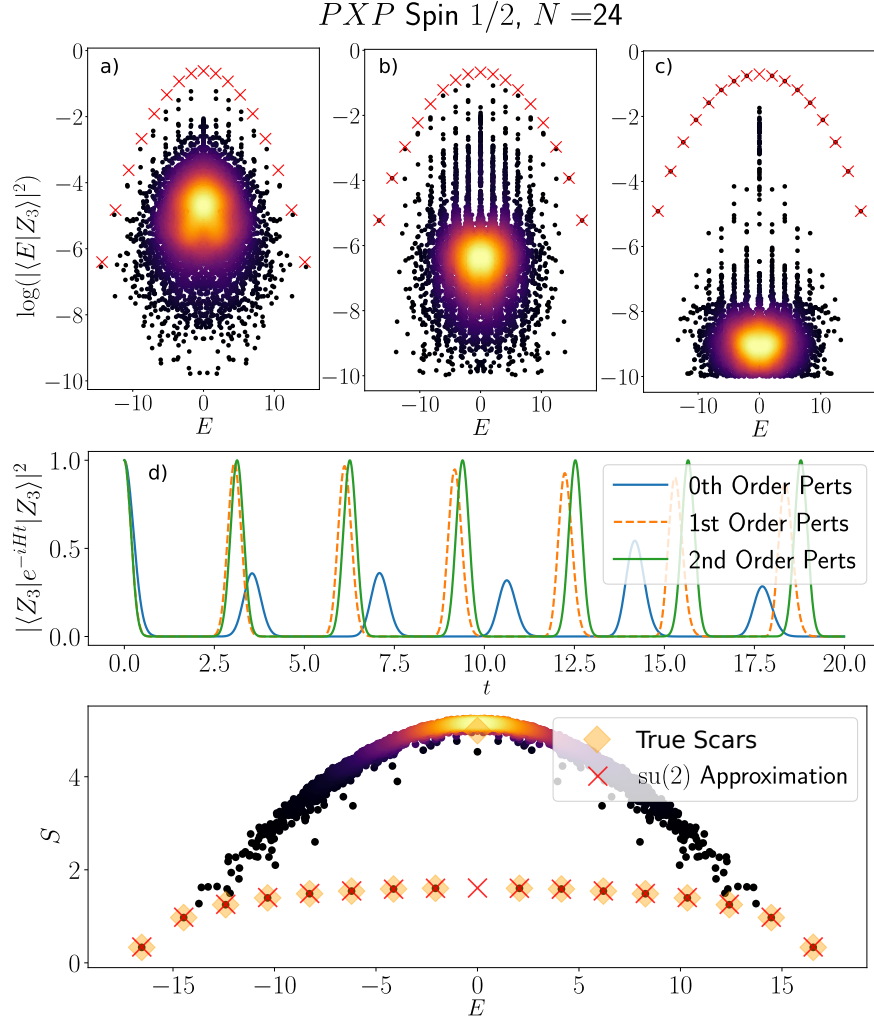
Figure 4.3: Improving the $\mathbb{Z}_3$ revival in the PXP model. (a) Eigenstate overlap with $|\mathbb{Z}_3\rangle$ state for PXP model. (b) Eigenstate overlap after including first order correction in Eqs. (4.53)-(4.55). (c) Eigenstate overlap after including second order perturbations listed in Appendix A.1.1. (d) Quantum fidelity when the system is quenched from $|\mathbb{Z}_3\rangle$ state at various perturbation orders. The perturbation coefficients are those which maximise the first fidelity revival peak. (e) Bipartite entropy, Eq. (2.21), of eigenstates of the PXP model after including second order $\mathbb{Z}_3$ su(2) corrections. Points labelled 'True Scars' are exact diagonalisation results identified from the top band of states in (c). Red crosses in (a), (b), (c), (e) indicate approximations to the scar states obtained by projecting the Hamiltonian to the broken representation basis and diagonalising. Colour scale in (a), (b), (c), (e) indicates the density of data points, with lighter regions being more dense.

4. WEAKLY-BROKEN LIE ALGEBRAS: A MECHANISM FOR APPROXIMATE SCARS

the raising operator is

$$\bar{H}^+ = \sum_n \left((\mathbb{I} - (P_{3n-2} + P_{3n+2}))\bar{\sigma}_{3n}^- + (\mathbb{I} - P_{3n-1})\bar{\sigma}_{3n+1}^+ + (\mathbb{I} - P_{3n+4})\bar{\sigma}_{3n+2}^+ \right),$$

(4.58)

and, as before, $\bar{H}^- = (\bar{H}^+)^\dagger$, $\bar{H}^z = \frac{1}{2}[\bar{H}^+, \bar{H}^-]$, $H = \bar{H}^+ + \bar{H}^-$. By inspection, it is easy to see the projectors $(\mathbb{I} - P_{3n-1}), (\mathbb{I} - P_{3n+4})$ evaluate to zero when $\bar{H}^+$ is applied to $|\mathbb{Z}_3\rangle = |100100...\rangle$. Thus, the terms containing $\bar{\sigma}_{3n+1}^+, \bar{\sigma}_{3n+2}^+$ never generate a spin flip and spins pointing down at these sites are frozen. It follows that the action of $\bar{H}^+$ on $|\mathbb{Z}_3\rangle$ is equivalent to:

$$(\bar{H}^+)^n|\mathbb{Z}_3\rangle = \left(-\sum_n \tilde{\sigma}_{3n}^- \right)^n |\mathbb{Z}_3\rangle,$$

(4.59)

which implies that, within this subspace, the su(2) algebra is exact. Dynamics is just a free precession of spins located at positions $3n$ along the chain, $|100100...\rangle \rightarrow |000000...\rangle \rightarrow |100100..\rangle \rightarrow ....$ The model now possesses an exact SGA within the su(2) subspace, namely

$$\left[P_{\text{su}(2)}^\dagger H P_{\text{su}(2)}, P_{\text{su}(2)}^\dagger Q^+ P_{\text{su}(2)} \right] = P_{\text{su}(2)}^\dagger Q^+ P_{\text{su}(2)},$$

(4.60)

$$Q^+ = e^{-i\frac{\pi}{2}\bar{H}^y} \bar{H}^+ e^{i\frac{\pi}{2}\bar{H}^y}, \quad \bar{H}^y = \frac{1}{2i}(\bar{H}^+ - \bar{H}^-),$$

(4.61)

where $P_{\text{su}(2)}$ is the basis transformation which projects to the subspace spanned by the su(2) basis states $|n\rangle = (\bar{H}^+)^n|\mathbb{Z}_3\rangle$.

The Hamiltonian in Eq. (4.57) fractures the Hilbert space in the computational basis even further than the pure PXP model. We find the number of sectors grows exponentially with system size, in a similar fashion to fractonic systems (93) exhibiting Kyrlov-restricted thermalisation. While one sector is the desired embedded representation of su(2), various other sectors emerge due to the projectors blocking access from one configuration to another based on the decomposition of the state into unit cells of three consisting of $\{|000\rangle, |001\rangle, |010\rangle, |100\rangle, |101\rangle\}$.

We find it is also possible for a model to feature an exactly embedded su(2) representation for which the Hamiltonian in the computational basis does not

fracture into exponentially many sectors as seen in the $\mathbb{Z}_3$ case. In Appendix A.1.2 we discuss one su(2) representation which allows us to identify such a model.

4.6 Summary

We have argued that, up to a rotation, many-body scars in kinetically constrained spin models can be interpreted as forming an approximate basis of a broken Lie algebra representation. This results in a loosely embedded integrable subspace with approximate SGA, which acts as an approximate representation of the Lie algebra. Seeking deformations of the Hamiltonian which improve this broken Lie algebra we have identified several perturbations to the PXP model such that the resulting systems feature near perfect revivals from the simple product states $|\mathbb{Z}_2\rangle$, $|\mathbb{Z}_3\rangle$. In addition, we have found by seeking corrections to severely broken broken Lie algebras, one can engineer revivals from initial states which do not revive in the original model, rather they just generically thermalise (see Appendix A.1.2, where we construct a new model, related to the PXP model, which features revivals from the $|\mathbb{Z}_4\rangle$ product state). Further, we have constructed two models with exactly embedded su(2) representations, thus obtaining 'exact scars' in a similar spirit to 'Krylov-restricted thermalisation' (80) and 'projector embedded' scar states (119).

The identification of embedded su(2) subspaces followed from identifying decompositions of the Hamiltonian $H = \bar{H}^+ + \bar{H}^-$, with $\bar{H}^- = (\bar{H}^+)^\dagger$. Thus, the representation is fixed by the choice of $\bar{H}^+$. This choice is not unique and many other possible decompositions of H exist, but many of these decompositions would result in embedded representations whose subspace variance is too large to give rise to scarred dynamics. However, from the examples considered in this chapter, it appears that aspects of an su(2) algebra can generically be improved in models like PXP, no matter how broken the representation is to begin with, by considering errors of a suitably defined broken representation. An obvious question is how 'broken' can these representations be such that we would see signatures of su(2) dynamics (revivals) following quenches from states in the su(2) subspace. In the examples considered in this chapter, subspace variance of the approximate representation basis seems to be the best indicator of scarred dynamics.

Chapter 5

Quantum many-body scars from embedded hypercube subgraphs

In the previous chapter we demonstrated how approximate scarring can occur due to a weakly broken Lie algebra. In this chapter, we focus on the case of an su(2) Lie algebra, but offer a complementary interpretation. Rather than interpreting the proximity of one Hamiltonian to another with an exact SU(2) symmetry via the algebra of generators, we instead study the Hamiltonian interpreted as an adjacency matrix of a graph, investigating whether it contains large regular subgraphs which are hypercubes. This graph-theoretic approach, based on our work in Ref. (27), is motivated by the fact that a Hamiltonian whose adjacency matrix is a hypercube is isomorphic to the free paramagnet. As the free paramagnet possesses an exact SU(2) symmetry, the existence of a hypercube subgraph would signal the presence of a subset of states with an approximate SU(2) structure. This approach is useful when the particular decomposition of the Hamiltonian into generators of the broken Lie algebra, as discussed in Chapter 4, is not obvious. Furthermore, this approach allows us to construct new models which contain quantum many-body scars. While such models may be expected to possess a broken su(2) Lie algebra, the form of the generators are likely very complicated.

In this chapter we begin by introducing the concept of an adjacency matrix and its associated graph. We demonstrate that quantum dynamics of many-

body interacting systems may be interpreted as a quantum walk on a particular
graph. Our primary example will be the Hamiltonian of a free paramagnet, which
gives rise to a hypercube graph. We then review well known results pertaining the
dynamics of a free paramagnet in order to develop intuition for how the trajectory
of a quantum walk on a hypercube behaves. In particular, we will demonstrate a
quantum walk on a hypercube realises 'perfect corner-to-corner' transmission

Having established the relationship between quantum walks on hypercubes
and SU(2) symmetry via the connection between this graph and the free para-
magnet, we then introduce the concept of embedded hypercubes. The primary
example used will be the 'two joined hypercube' model, which plays the role of
a parent model which captures the main features of the scarred dynamics ob-
served in the PXP model. Furthermore, we demonstrate that the PXP model is
'generic', in the sense that it is just one of many scarred models whose adjacency
graphs interpolate between the free paramagnet and the two joined hypercubes.
Finally, we show how the embedded hypercubes approach allow us to formulate
new scarred models with local constraints.

5.1 Hamiltonians as adjacency matrices: quantum walks on graphs

Graphs describe the connectivity between a set of vertices. They are usually
represented graphically. Vertices are drawn as a set of dots, while lines connecting
pairs of vertices indicates their connectivity. An example of a graph with four
vertices is shown in Fig. 5.1. Graphs may also be represented using *adjacency
matrices*. These are off-diagonal, symmetric matrices A_{ij} with matrix elements
either 0 or 1. Row and column indices i, j label vertices of a graph. If $A_{ij} = 1$,
this indicates a link between the vertex i and vertex j. For example, for the graph

Figure 5.1: An example of a graph, which is a collection of vertices (dots) connected by links. This graph may also be described by the *adjacency matrix* given in Eq. (5.1).

shown in Fig. 5.1, it's adjacency matrix would be the following:

$$
A = \begin{array}{c} \\ 0 \\ 1 \\ 2 \\ 3 \end{array}
\begin{array}{cccc}
0 & 1 & 2 & 3 \\
\left(\begin{array}{cccc}
0 & 1 & 1 & 0 \\
1 & 0 & 1 & 0 \\
1 & 1 & 0 & 1 \\
0 & 0 & 1 & 0
\end{array} \right)
\end{array}
\tag{5.1}
$$

The row and column indices refer to four vertices, labelled as $0, 1, 2, 3$. By drawing four dots, labelling them as $0, 1, 2, 3$ and connecting pairs of dots (i, j) with a line when $A_{ij} = 1$, we would reproduce the graph in Fig. 5.1, such that there is a one to one correspondence between the adjacency matrix and the graph.

Graphs have primarily been studied in the context of quantum mechanics by considering quantum walks along a graph . Given classical random walks have yielded various search algorithms, it has been hoped that quantum analogous of these walks may yield useful algorithms. A continuous quantum walk on a graph is a single particle hopping problem where a particle may hop between neighbouring vertices on a graph. Formally, let A be an adjacency matrix of a graph with vertices labelled by an index i. The vertices of the graph, i, are to be understood as forming an orthogonal basis $|i\rangle$ of a Hilbert space, $\langle i|j\rangle = \delta_{ij}$. The system may therefore be in a state which is some superposition of

the states localised at different vertices, $|\psi\rangle = \sum_i c_i |i\rangle$. A continuous quantum walk corresponds to evolving the state of the system $|\psi(t)\rangle = e^{-iHt}|\psi\rangle$ with a Hamiltonian H which is obtained by treating the adjacency matrix as the Hamiltonian, $H = \sum_{ij} A_{ij} |i\rangle\langle j|$. This Hamiltonian generates hoppings between neighbouring vertices of the graph, permitting transitions between states $|i\rangle \rightarrow |j\rangle$ only if $A_{ij} = 1$. The propagator of a continuous quantum walk on a given graph is therefore obtained by exponentiation of the adjacency matrix of the graph: $U(t) = e^{-iHt} = e^{-iAt}$.

Now consider a many-body Hamiltonian expressed with respect to a Fock space basis. Let us assume that in this basis, the Hamiltonian is purely off-diagonal, and all non-zero matrix elements are uniform. Without loss of generality, we may rescale the Hamiltonian such that all matrix elements are either 0 or 1. A Hamiltonian of this form may be interpreted as an adjacency matrix of a graph, with the particular graph been implied by the Hamiltonian. The Fock basis states are to be understood as the vertices of the graph, while the connectivity of the vertices represents allowed transitions between basis states under the action of the Hamiltonian. The propagator of this complicated interacting system is $U(t) = e^{-iHt}$. We observe, by interpreting H as an adjacency matrix of a graph, the evolution of this many-body system is equivalent to a single particle quantum walk occurring on the graph implied by the Hamiltonian.

An important example is the graph associated with the Hamiltonian of a free paramagnet. The relevant Fock space is a tensor product space of N spin half degree of freedoms. This Hilbert space is spanned by a basis of Z product states labelled by bit strings of length N:

$$|\vec{\sigma}_z\rangle = \bigotimes_{n=0}^{N-1} |\sigma_n^z\rangle, \quad |\sigma_n^z\rangle = \{|0\rangle, |1\rangle\}, \tag{5.2}$$

where states $|0\rangle$ and $|1\rangle$ refer to spin up and down in the Z direction respectively. The Hamiltonian of a free paramagnet is the following:

$$H = \sum_{i=0}^{N-1} \sigma_i^x \tag{5.3}$$
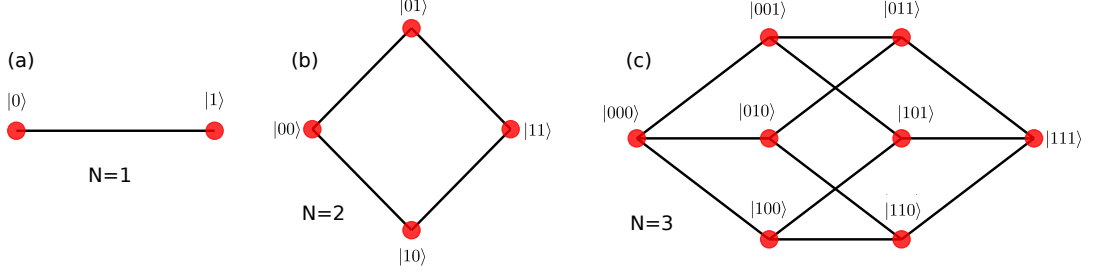
Figure 5.2: Graphs implied by the Hamiltonian of a free paramagnet are N dimensional hypercubes. These graphs show the connectivity of basis states under the action of the Hamiltonian. The Hamiltonian of a free paramagnet, Eq. (5.3) permits transitions between product states in the Z basis, Eq. (5.2), which differ by a single spin flip. At $N = 2$, the graph of the free paramagnet is a square, while at $N = 3$, the graph is a cube. It follows the dynamics of the free paramagnet of N spin half degree of freedoms is equivalent to a quantum walk on a N dimensional hypercube.

where σ_i^x is the conventional Pauli σ^x acting on site i, whose action is to flip a spin at site i in the Z direction:

$$\sigma^x|0\rangle = |1\rangle, \quad \sigma^x|1\rangle = |0\rangle \tag{5.4}$$

The Hamiltonian of the free paramagnet simply connects basis states $|\vec{\sigma}^z\rangle$ which differ by a single spin flip. For example, a permitted transition at $N = 3$ would be $|101\rangle \rightarrow |111\rangle$. The graph for which the equivalent quantum walk will take place consists of 2^N vertices, each labelled by a bit string of length N representing a product state $|\vec{\sigma}^z\rangle$, with lines connecting states differing by a single spin flip. The resulting graph is a N dimensional hypercube, which has been studied extensively due to possessing several desirable properties for quantum walks.

To gain an intuitive understanding why the graph of the free paramagnet results in a hypercube, let us construct the graphs for various small system sizes sequentially, starting from $N = 1$.

For $N = 1$, the Hilbert space has dimension 2, with the basis being spanned by the states $|0\rangle$ and $|1\rangle$. The Hamiltonian of a free paramagnet is simply the

Pauli X matrix, $H_{N=1} = \sigma_0^x$:

$$
H_{N=1} = \begin{array}{c} \\ |0\rangle \\ |1\rangle \end{array} \begin{array}{cc} |0\rangle & |1\rangle \\ \left(\begin{array}{cc} 0 & 1 \\ 1 & 0 \end{array} \right) \end{array} \tag{5.5}
$$

The two states $|0\rangle$ and $|1\rangle$ are connected under the action of the Hamiltonian, therefore the free paramagnet at $N = 1$ is equivalent to a quantum walk on a graph consisting of two vertices connected by a single line, Fig. 5.2(a).

For $N = 2$, the Hilbert space is spanned by 4 states, namely $|00\rangle, |01\rangle, |10\rangle, |11\rangle$. Writing the free paramagnet Hamiltonian explicitly as a 4×4 matrix, we find:

$$
H_{N=2} = \begin{array}{c} \\ |00\rangle \\ |01\rangle \\ |10\rangle \\ |11\rangle \end{array} \begin{array}{cccc} |00\rangle & |01\rangle & |10\rangle & |11\rangle \\ \left(\begin{array}{cccc} 0 & 1 & 1 & 0 \\ 1 & 0 & 0 & 1 \\ 1 & 0 & 0 & 1 \\ 0 & 1 & 1 & 0 \end{array} \right) \end{array} \tag{5.6}
$$

By treating this Hamiltonian matrix as an adjacency matrix, we can draw the associated graph. This graph is shown in Fig. 5.2(b), where we observe the graph is a 2 dimensional square whose 4 vertices correspond to the 4 basis states, and only basis states differing by a single spin flip are connected.

Likewise, at $N = 3$, the Hilbert space is spanned by 8 basis states, $|000\rangle$, $|001\rangle, |010\rangle, |011\rangle, |100\rangle, |101\rangle, |110\rangle, |111\rangle$. For brevity, we do not produce here the full 8×8 Hamiltonian matrix for the $N = 3$ free paramagnet. However, to construct the graph implied by treating the Hamiltonian as an adjacency matrix, one would draw 8 vertices corresponding to the 8 basis states, and connect those states differing by a single spin flip with a line. The resulting graph is shown in Fig. 5.2(c), where it is apparent the that the $N = 3$ free paramagnet Hamiltonian connects basis states into a graph corresponding to a 3 dimensional cube.

In general, it follows that the dynamics generated by the Hamiltonian of a free paramagnet for N spin half degree of freedoms is equivalent to a continuous quantum walk on a N dimensional hypercube. In the following section we will

study the dynamical properties of the free paramagnet in more detail, translating between the language of spins and quantum walks on hypercubes, to gain some intuition for the unique properties quantum walks on hypercubes possess.

5.2 Free paramagnet: Quantum walks on hypercubes

In the previous section we have introduced the Hamiltonian of the free paramagnet in Eq. (5.3) and demonstrated the equivalence between this system and a quantum walk on a hypercube. We now consider the dynamics of the free paramagnet model, to see what this implies for trajectories of quantum walks on hypercubes. In particular, we are interested in demonstrating a unique property of quantum walks on hypercubes, that they feature perfect transmission from an arbitrary initial vertex to the vertex opposite it on the hypercube. This will enable the reader to develop some intuition for trajectories on hypercube graphs, which is essential for understanding the remainder of this chapter. Analytical calculations of more complicated many-body scarred systems are not possible, but one can get a feel for what is occurring by considering the scarred system as a quantum walk on a graph containing large hypercube subgraphs.

5.2.1 Dynamics of the free paramagnet: corner-to-corner transmission of hypercubes

The dynamics of a free paramagnet in the language of spins is simply the free precession of each spin half degree of freedom, independent of it's neighbours. However, as noted in the previous section, the dynamics may be interpreted as a quantum walk on a hypercube. By working in the spin language, many time dependent properties of this system may be calculated analytically, given the simplicity of the model. In this section we derive an expression for the time evolved wavefunction initialised on an arbitrary vertex of the hypercube graph.

For clarity, we reproduce the Hamiltonian of the free paramagnet, Eq. (5.3)

5. QUANTUM MANY-BODY SCARS FROM EMBEDDED HYPERCUBE SUBGRAPHS

here:

$$H = \sum_{i=0}^{N-1} \sigma_i^x \tag{5.7}$$

An arbitrary vertex of the hypercube graph corresponds to an arbitrary product state in the Z direction, $|\vec{\sigma}_z\rangle = \bigotimes_n |\sigma_n^z\rangle$. Initialising the system in one of these arbitrary product states $|\psi(t=0)\rangle = |\vec{\sigma}_z\rangle$ results in the independent precession of each spin in the chain around the x-axis. This can be seen from the action of the propagator, which may be decomposed into a tensor product of single site unitaries, given the Pauli matrices at each site commute:

$$U(t) \quad = e^{-iHt} = e^{-i\sum_n \sigma_n^x t} = \bigotimes_n e^{-i\sigma_n^x t} = \bigotimes_n \left(\cos(t)\mathbb{I} - i\sin(t)\sigma_n^x \right) \tag{5.8}$$

Applying this propagator to the initial state $|\vec{\sigma}_z\rangle = \bigotimes_n |\sigma_n^z\rangle$, we find the time evolved state is:

$$|\psi(t)\rangle \quad = U(t)|\vec{\sigma}_z\rangle = \bigotimes_n \left(\cos(t)|\sigma_n^z\rangle - i\sin(t)\sigma_n^x|\sigma_n^z\rangle \right). \tag{5.9}$$

Now in the language of a quantum walk on a hypercube, the initial state $|\vec{\sigma}_z\rangle$ corresponds to an arbitrary vertex on the hypercube. The opposite corner to this initial vertex on the hypercube is the state with all the local spin half degree of freedoms flipped (see Fig. 5.2). Therefore the opposite corner to this initial vertex will be the product state $|\vec{\sigma}_z'\rangle = \bigotimes_n \sigma_n^x|\sigma_n^z\rangle$. Using the expression for the time evolved wavefunction starting from an arbitrary state $|\vec{\sigma}_z\rangle$, Eq. (5.9), the probability the time evolved wavefunction is found on the initial vertex or the vertex opposite it, $P_{initial}(t), P_{opposite}(t)$, may be computed as follows:

$$P_{initial}(t) = |\langle \vec{\sigma}_z|U(t)|\vec{\sigma}_z\rangle|^2 = |\cos^N(t)|^2 \tag{5.10}$$

$$P_{opposite}(t) = |\langle \vec{\sigma}_z'|U(t)|\vec{\sigma}_z\rangle|^2 = |\sin^N(t)|^2 \tag{5.11}$$

Significantly, these functions are periodic, with the probability to be found on the initial vertex or the opposite vertex being 1 at various times. Therefore for a quantum walk on a hypercube, an intuitive picture of the dynamics is as follows: initialising the system in an arbitrary vertex will result in the wavefunction propagating away from the initial vertex and spreading out, before refocusing perfectly

to the opposite corner. After this perfect transmission, the wavefunction reflects back, repeating the process and refocusing back onto the initial vertex. We refer to this property of a quantum walk on a hypercube as 'perfect corner-to-corner transmission' and 'perfect reflection'.

5.2.2 Hypercubes and SU(2) symmetry: FSA

We continue our program of studying the free paramagnet in order to gain intuition about quantum walks on hypercubes. We have already demonstrated that hypercubes realise perfect corner-to-corner trajectories along their quantum walks. We now wish to investigate further how the SU(2) symmetry of the free paramagnet model may be interpreted from the hypercube point of view. It turns out equal weight superpositions of all states the same distance away from an arbitrary vertex of the hypercube is in fact a SU(2) symmetric state. To understand why this is the case, we will consider mapping the Hamiltonian of the free paramagnet to a tight binding chain, using the forward scattering approximation (FSA) introduced in Section 3.3.1. The basis states of this equivalent tight binding chain will be the desired equal weight superpositions of all states the same distance from an arbitrary vertex of the graph, which we will demonstrate are SU(2) symmetric.

The FSA procedure produces an orthogonal basis, the FSA basis, which spans some subspace of the full Hilbert space. Projecting the Hamiltonian into this subspace yields a tridiagonal matrix such that the dynamics within this subspace is equivalent to a tight-binding chain. Recall the recurrence procedure which generates the FSA basis:

$$\beta_{j+1} |v_{j+1}\rangle = H |v_j\rangle - \alpha_j |v_j\rangle - \beta_j |v_{j-1}\rangle \tag{5.12}$$

$$= (H^+ + H^-) |v_j\rangle - \alpha_j |v_j\rangle - \beta_j |v_{j-1}\rangle \tag{5.13}$$

$$= H^+ |v_j\rangle - \alpha_j |v_j\rangle + |\delta_j\rangle \tag{5.14}$$

$$|\delta_j\rangle = H^- |v_j\rangle - \beta_j |v_{j-1}\rangle \tag{5.15}$$

As described in Section 3.3.1, Eq. (5.12), is just Lanczos recursion (Eq. (3.18)). By repeated application of the Hamiltonian H, we obtain new states $|v_{j+1}\rangle$. The

term with coefficients α ensures the new vector is orthogonalised against the previous vector, whereas the β coefficients are present to ensure the vectors are correctly normalised.

H^+, H^- correspond to forward and backward propagating parts of the Hamiltonian $H = H^+ + H^-$, with respect to the initial vector $|v_0\rangle$. It is worth considering what these operators mean from the graph point of view. Recall these operators are uniquely specified given a Hamiltonian H and an initial state $|v_0\rangle$, by requiring that the Hamiltonian may be decomposed as $H = H^+ + H^-$, with $H^- = (H^+)^\dagger$, such that the states $|n\rangle = (H^+)^n |v_0\rangle$ are all orthogonal $\langle n|m\rangle = \delta_{nm}$. For the free paramagnet, the operator H^+ which satisfies this condition from an arbitrary vertex $|v_0\rangle$ is the operator which always increases the *Hamming distance* from $|v_0\rangle$. Hamming distance between a pair of vertices on the hypercube graph labelled by bit strings is the number of bits which differ between the two strings. In other words, it counts how many spin flips are necessary to get from one vertex state to another. As H^+ always increases the Hamming distance from the initial vertex $|v_0\rangle$, repeated application of the operator H^+ on the initial state $|v_0\rangle$ may be understood from the graph point of view as forming an equal weight superposition of all vertices which are the same Hamming distance away from the initial vertex. We refer to this collection of vertices with the same distance away from the initial vertex as a 'Hamming layer'. The role of H^+ is shown graphically Fig 5.3(a), with a particular Hamming layer of a hypercube circled in blue.

$|\delta_j\rangle$ defined in Eq. (5.15) is the FSA error vector, which is assumed to be small and neglected for the FSA approximation. For a single hypercube in Eq. (5.3), the FSA scheme is fully analytically tractable and *exact*. By *exact*, we mean the FSA error vectors $|\delta_j\rangle$ is always zero for a hypercube, regardless of the initial vertex $|v_0\rangle$, such that the obtained FSA subspace is an exact symmetric subspace of the Hamiltonian.

Let $|v_0\rangle = |\vec{\sigma}_z\rangle = \bigotimes_n |\sigma_n^z\rangle$ be an arbitrary vertex of the hypercube graph. The forward and backward propagating components of the Hamiltonian with respect
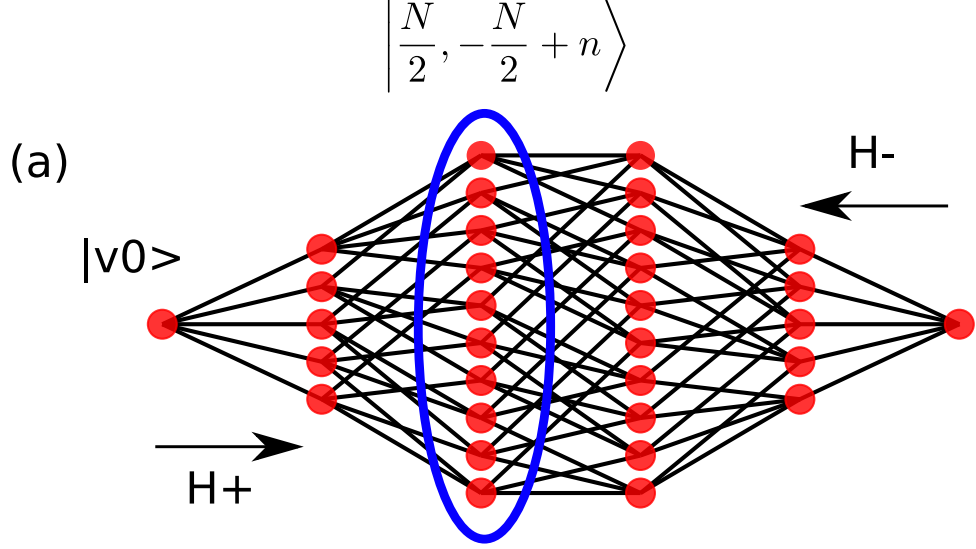
Figure 5.3: Forward scattering approximation applied to the hypercube graph, which reveals how a hypercube graph implies SU(2) symmetry.
$|v_0\rangle = |\vec{\sigma}_z\rangle = \bigotimes_n |\sigma_n^z\rangle$ is an arbitrary vertex of the graph. The forward propagator with respect to $|v_0\rangle$ is H^+, given in Eq. (5.16). When H^+ is applied n times on the initial vertex $|v_0\rangle$, it produces an equal weight superposition of all states with Hamming distance n from the initial vertex, ie. a superposition of all vertices in a vertical line in panel (a), such as the column circled in blue.
For a hypercube of dimension N, the forward propagator from an arbitrary vertex H^+ coincides with a spin $s = N/2$ raising operator $\bar{S}^+$, Eq. (5.16), such that equal weight superpositions of vertices in vertical columns of the graph in panel (a) are SU(2) symmetric states $|s = N/2, \bar{S}^z = -N/2 + n\rangle$.

to $|v_0\rangle$, subject to the criteria discussed above, are found to be:

$$H^+ = \bar{S}^+ = \sum_n \sigma_n^{\text{sgn}(n)}, \quad H^- = \bar{S}^- = \sum_n \sigma_n^{-\text{sgn}(n)}, \quad \text{sgn}(n) = \begin{cases} + & |\sigma_n^z\rangle = |0\rangle \\ - & |\sigma_n^z\rangle = |1\rangle \end{cases},$$

$$(5.16)$$

Note that the operators $\bar{S}^+$, $\bar{S}^-$ in fact realise some representation of su(2). To demonstrate this, construct the Z element of the Lie algebra:

$$\bar{S}^z = \frac{1}{2}[\bar{S}^+, \bar{S}^-] = \frac{1}{2} \sum_n \text{sgn}(n)\sigma_n^z. \tag{5.17}$$

5. QUANTUM MANY-BODY SCARS FROM EMBEDDED HYPERCUBE SUBGRAPHS

It is trivial to verify the operators $\{\bar{S}^+, \bar{S}^-, \bar{S}^z\}$ realise the root structure of an su(2) Lie algebra, $[\bar{S}^z, \bar{S}^\pm] = \pm \bar{S}^\pm$. It is this property, that the forward and backward propagators of a hypercube graph from *any* vertex are equivalent to su(2) raising and lowering operators, which establishes the connection between hypercube graphs and su(2) symmetry. Furthermore, one can verify the state $|v_0\rangle = |\vec{\sigma}_z\rangle$ is the lowest weight eigenstate of $\bar{S}^z$, $\bar{S}^z |v_0\rangle = -N/2 |v_0\rangle$, such that the state $|v_0\rangle$ may be identified with a large spin $s = N/2$ pointing in the negative Z direction, $|v_0\rangle = |S = N/2, \bar{S}^z = -N/2\rangle$. These facts can be used to immediately map the Hamiltonian of the free paramagnet to a $N + 1$ dimensional subspace where it is tridiagonal, using well known results from the theory of angular momentum. Nevertheless, we will derive the Hamiltonian matrix in the FSA subspace by analytical calculation of the β coefficients. This approach directly generalises to more complicated models, even if the β coefficients must be calculated numerically .

Consider the first step of the recurrence. Operator H^- annihilates the state $|\vec{\sigma}_z\rangle$, and we obtain the vector $\beta_1 |v_1\rangle = H^+ |\sigma_z\rangle$, which is an equal-weight superposition of all single-spin flips on top of $|\vec{\sigma}_z\rangle$,

$$\beta_1 |v_1\rangle = \sum_{n=0}^{N-1} \left(\bigotimes_{m \neq n} |\sigma_m\rangle_z \right) \otimes \sigma_n^x |\sigma_n\rangle_z. \tag{5.18}$$

The vector $|v_1\rangle$ is automatically orthogonal to $|v_0\rangle$, thus we set $\alpha_0 = 0$, and $\beta_1 = \sqrt{N}$ by normalisation, where N is the number of spins.

In the second step, we observe that the action of H^+ on $|v_1\rangle$ will produce an equal weight superposition of all states containing a pair of spin flips atop the product state $|\vec{\sigma}_z\rangle$, which is thus orthogonal to both $|v_1\rangle$, and $|v_0\rangle$. Furthermore, the action of the backward-scattering part gives us the original state $|v_0\rangle$, $H^- |v_1\rangle = \beta_1 |v_0\rangle$, where we explicitly used the value of β_1. For a hypercube, one can show that

$$|\delta_j\rangle = H^- |v_j\rangle - \beta_j |v_{j-1}\rangle = 0 \tag{5.19}$$

holds more generally at *every* step of the iteration. This allows one to cancel

$H^- |v_j\rangle$ with the last term in Eq. (**??**), yielding the usual FSA recurrence:

$$\beta_{j+1} |v_{j+1}\rangle = H^+ |v_j\rangle , \qquad (5.20)$$

where we also omitted the $\alpha_j |v_j\rangle$ term since all $\alpha_j{=}0$. This follows from the fact that $H^\pm$ operators change the Hamming distance from $|\vec{\sigma}_z\rangle$ state by ± 1. Hence, the new state $|v_{j+1}\rangle$ is always orthogonal to $|v_j\rangle$. Moreover, by the same argument, the FSA recurrence closes after $N{+}1$ steps as it reaches the vector at the opposite corner on the hypercube, $|\vec{\sigma}'_z\rangle = \bigotimes \sigma_n^x |\sigma_n^z\rangle$ that vanishes under the action of H^+.

Finally, using induction one can show

$$\beta_j = \sqrt{j(N-j+1)}, \qquad (5.21)$$

which, as anticipated, is the well-known matrix element of a spin ladder operator. This results in the effective tridiagonal matrix form in the basis of $|v_j\rangle$:

$$H_{\text{hypercube}} = \sum_{j=1}^{N} \beta_j \, |v_j\rangle \langle v_{j-1}| + \text{H.c.} \qquad (5.22)$$

This allows to one reduce the dynamics of an arbitrary product state $|\vec{\sigma}_z\rangle$ to that of a tight-binding chain with the corresponding hopping strength. Taking into account the expression for β_j, we see that this matrix coincides with the $2\bar{X}$ operator for a spin of size $N/2$, resulting in a set of $N{+}1$ equidistant energy levels.

The FSA basis states may be expressed as:

$$|v_n\rangle = \frac{1}{\sqrt{\mathcal{N}}}(H^+)^n|v_0\rangle \qquad (5.23)$$

with $\mathcal{N}$ being a combinatorial factor necessary for normalisation. We noted earlier that the FSA basis states $|v_n\rangle$ correspond to an equal weight superposition of all states with a Hamming distance of n from the initial vertex on the hypercube $|v_0\rangle$. However, crucially, for a hypercube graph, the forward propagator H^+ is equivalent to a su(2) raising operator, such that equal weight superpositions of all

vertices in a given Hamming layer of a hypercube graph may be identified with large spin $s = N/2$ z-basis states of an su(2) representation:

$$|v_n\rangle = |N/2, -N/2 + n\rangle_{\bar{z}}.$$

This establishes the relationship between a hypercube graph and SU(2) symmetry. Forward propagation on a N dimensional hypercube graph is equivalent to an $s = N/2$ su(2) raising operator, and equal weight superpositions of states an equal distance away from an arbitrary vertex is a SU(2) symmetric state. These properties are summarised graphically in Fig. 5.3. It follows that whenever a graph contains a hypercube subgraph, this implies the presence of SU(2) symmetric states. Speaking loosely, if the adjacency graph of a Hamiltonian contains large hypercube subgraphs, this indicates the structure of the graph is 'almost' SU(2) symmetric, as the graph is close to a hypercube. Therefore, rather than probing how well a Hamiltonian approximately hosts an SU(2) symmetry by studying the algebra of generators, as we did in Chapter 4 when considering broken Lie algebras, an equivalent metric would be to look for the presence of large hypercube subgraphs in the graph implied by the Hamiltonian. Throughout the remainder of this chapter, we will study how the presence of embedded hypercube graphs may be understood to give rise to the oscillatory scarred dynamics, such as observed in the PXP model. Furthermore, by constructing models explicitly which feature large hypercube subgraphs, we construct new families of many-body scarred models.

5.3 The model of two joined hypercubes

We now move away from a quantum walk on a full hypercube, corresponding to the free paramagnet, to study quantum walks on different graphs containing large hypercubes. An essential graph which plays the role of a parent model capturing the essential features of the PXP model is model of two hypercubes joined at a single vertex.

From a graph point of view, the model for a system size N is defined as a quantum walk on two hypercubes (of dimension $N/2$), sharing a single vertex -

the corresponding graph for $N = 6$ dimensional cubes is shown in Fig 5.4.
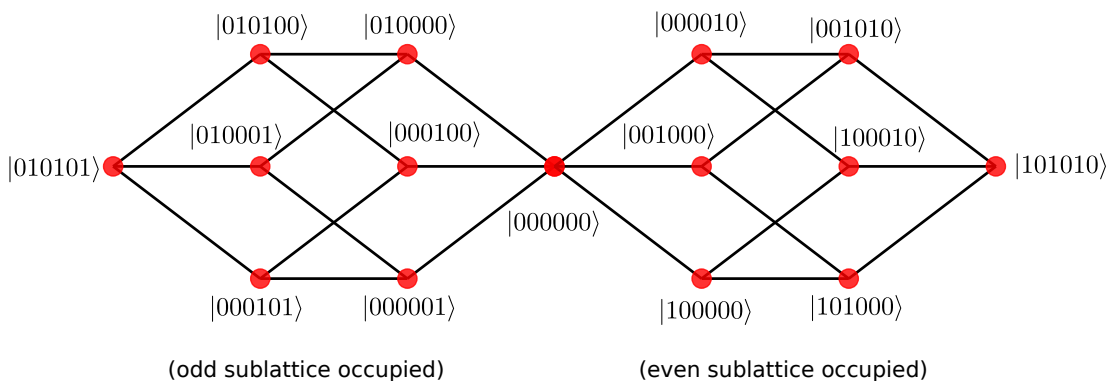
Figure 5.4: Quantum walk on two joined hypercubes model at $N = 6$, which is equivalent to the kinetically constrained Hamiltonian in Eq (5.24). The kinetic constraint enforced by this spin Hamiltonian is that even and odd sublattices may not simultaneously host spin excitations. The Hamiltonian simply flips spins if this constraint is not violated. Each even and odd sublattice behaves as a free paramagnet with $N/2$ sites, therefore realising a $N/2$ dimensional hypercube in the graph. These two hypercubes are joined at the shared vertex $|000...\rangle$.

This two-hypercube model can be written as a translation-invariant spin Hamiltonian:

$$H_{\text{2HC}} = \sum_j \cdots P_{j-3} P_{j-1} X_j P_{j+1} P_{j+3} \cdots , \qquad (5.24)$$

obtained by dressing each Pauli matrix X_j by an infinite string of projectors onto the spin down state $P_j = (1 - Z_j)/2$. For a finite system, the length of the string can be limited to $N/2$ on each side.

Physically, this Hamiltonian may be understood as a kinetically constrained free paramagnet. The kinetic constraint is that the sublattices consisting of only even or odd sites may not both simultaneously host a spin excitation. The action of this Hamiltonian is to flip a spin if this constraint is not violated. For example, the transition $|100000\rangle \rightarrow |100010\rangle$ is permitted, as the resulting state only has excitations on the even sublattice. On the other hand, the transition $|100000\rangle \rightarrow |100100\rangle$ is not permitted, as the final state has excitations on both the even and odd sublattice. All possible transitions for system size $N = 6$ are summarised in

the Hamiltonian graph in Fig. 5.4, where we observe the graph indeed realises two 3 dimensional cubes joined at a single vertex. For general N, each even and odd sublattice will realise a $N/2$ free paramagnet, as spin flips restricted to a single sublattice are not further constrained. Therefore for general N, the graph of this Hamiltonian will consist of the two $N/2$ dimensional hypercubes, corresponding to the two sublattices, while these two hypercubes will share a single state $|000...\rangle$, corresponding to no excitations on either the even and odd sublattices.

This formulation of the two-hypercube graph in terms of a kinetically constrained free paramagnet reveals that this graph emerges as a subgraph of both the PXP model and the free spin-1/2 model, as can be seen in Fig. 5.5. Both the PXP model and two hypercube model are kinetically constrained free paramagnets, so their Hamiltonian graphs are naturally subgraphs of a full hypercube. Furthermore, the kinetic constraint is similar for both the two hypercube model and the PXP model. But in the case of two hypercubes, the kinetic constraint encompasses *all sites* on the other sublattice, whereas the kinetic constraint only effects the nearest neighbours in the PXP model. The two hypercube model may therefore be considered as a more strongly constrained variant of the PXP model, such that all the states in the two-hypercube model satisfy the PXP constraint but not the other way round.

Fig. 5.5 also shows the dynamics of both the two hypercube model and the PXP model initialised in the Néel state $|0101...\rangle$. While the two hypercube model is a simpler model than the PXP model, from the point of view of its graph, the dynamics in both these models from Néel state is remarkably similar, indicating the two hypercube model is capturing the main features of the scarred dynamics in the PXP model, such as the decaying fidelity revivals and the revival frequency. We investigate this relationship between an embedded two hypercube subgraph and many-body scarring further in Section 5.4

5.3.1   FSA and dynamics of two joined hypercubes - numerical results

For the two-hypercube model, the FSA introduced in Section 3.3.1 remains exact for certain initial states (FSA error vector is zero). Indeed, when starting
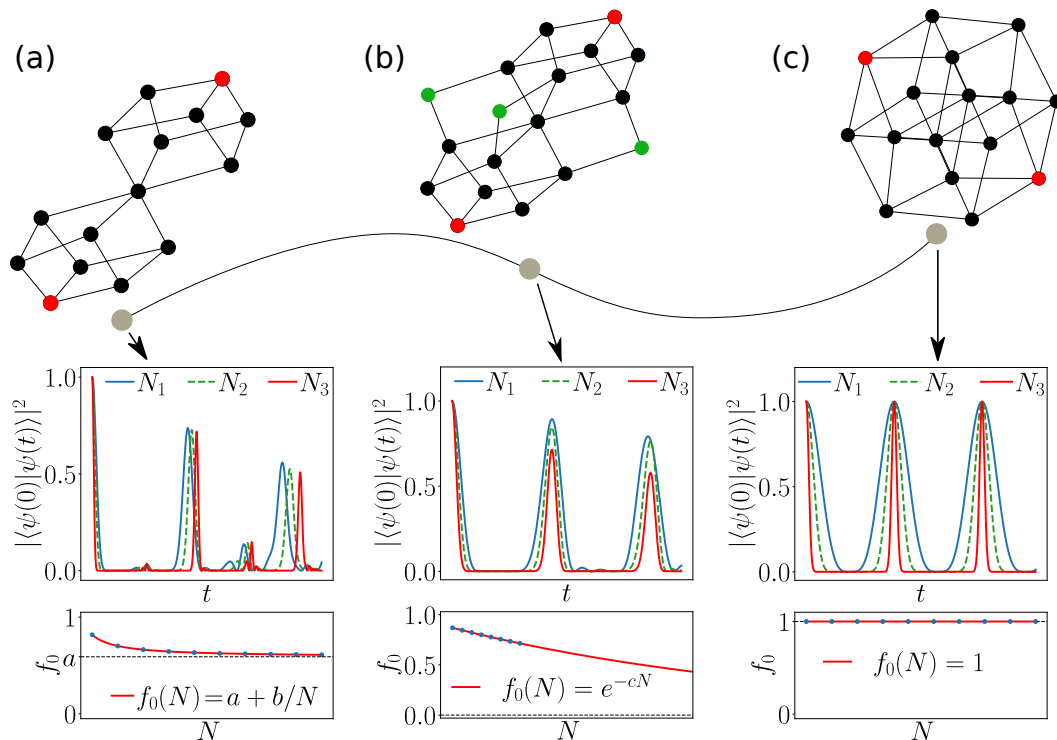
Figure 5.5: Hamiltonian adjacency graphs of three models- from left to right: (a) two hypercubes model, Eq. (5.24) with N=6; (b) PXP model, Eq. (2.41), with N=6; (c) the spin-1/2 free paramagnet model, Eq. (5.3) with N=4, whose adjacency graph corresponds to a hypercube. From a graphical point of view, the PXP model may be interpreted as an intermediate model between (a) and (c), as it contains the two hypercube model as a subgraph, while the adjacency graph of the PXP model is itself a subgraph of a full hypercube. Red vertices in the graphs denote the two Néel states. The black vertices in the PXP graph highlight the embedded subgraph corresponding to two hypercubes. The two hypercubes are connected via 'bridges' (green vertices), i.e., vertices and edges present in the PXP model but not contained within the two hypercubes. The behaviour of the wave function fidelity revivals $|\langle\psi(0)|\psi(t)\rangle|^2$ for three different system sizes $N_1 < N_2 < N_3$ is sketched below the models, along with the system size scaling of the first revival peak f_0. We observe the two hypercube model is a minimal model which captures the main phenomenology of the PXP model.
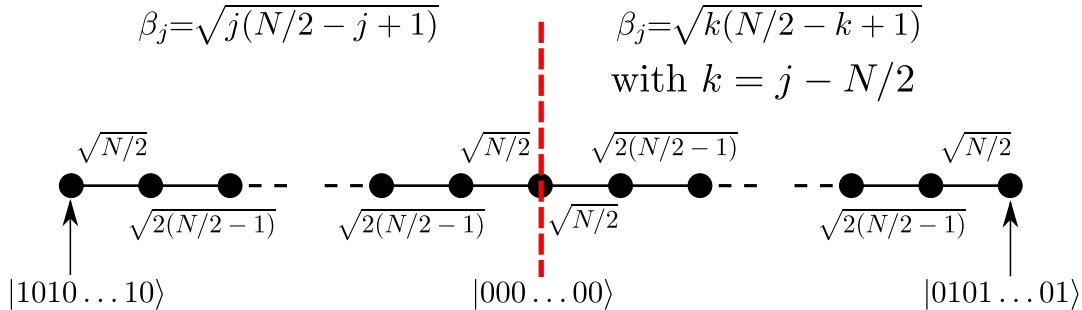
Figure 5.6: Equivalent tight-binding chain describing the dynamics from the Néel state for the two-hypercube model, Eq. (5.24), at arbitrary N. The many-body dynamics can be reduced to a single-particle hopping on a 1D tight-binding chain, with the site-dependent hopping amplitudes indicated on the chains. From these amplitudes, it can be seen that the two-hypercube model with N sites (N-even) simply corresponds to 'sewing' together two free paramagnets with $N/2$ sites each.

from the $|\mathbb{Z}_2\rangle = |1010\ldots\rangle$ state (which is the extremal vertex at the maximal distance away from the shared vertex), the FSA procedure mirrors that of a single hypercube until the shared vertex is reached (after $N/2$ steps), such that β coefficients representing the tight binding hopping amplitudes are the same as a regular hypercube (Fig. 5.6). At the central vertex, the second half of the FSA procedure happens exclusively in the second hypercube until the translated $|\bar{\mathbb{Z}}_2\rangle = |0101\ldots\rangle$ state is reached, such that the β coefficients obtained are a mirror of those obtained during the first half of the FSA procedure – see Fig. 5.6 for an illustration. As a consequence, the FSA for the model in Eq. (5.24) is exact for the $|\mathbb{Z}_2\rangle$ initial state and the tridiagonal Hamiltonian corresponds to two copies of Eq. (5.22) joined together. Unfortunately, analytical diagonalisation of this Hamiltonian in the FSA subspace is no longer trivial. Nevertheless, due to the complexity of the problem growing only linearly with N, numerical simulations on large systems $N \lesssim 10^5$ are possible. The finite-size scaling analysis in Fig. 5.7 for the two-hypercube model in Eq. (5.24) shows that this model supports revival of the wave function in the thermodynamic limit. We evaluated the quantum fidelity, $|\langle\psi(0)|e^{-iH_{\text{2HC}}t}|\psi(0)\rangle|^2$, which is seen to rapidly decay to zero and then rise to a value $f_0 \approx 0.7159$ around the time $T = 6.282$, corresponding to the first revival.
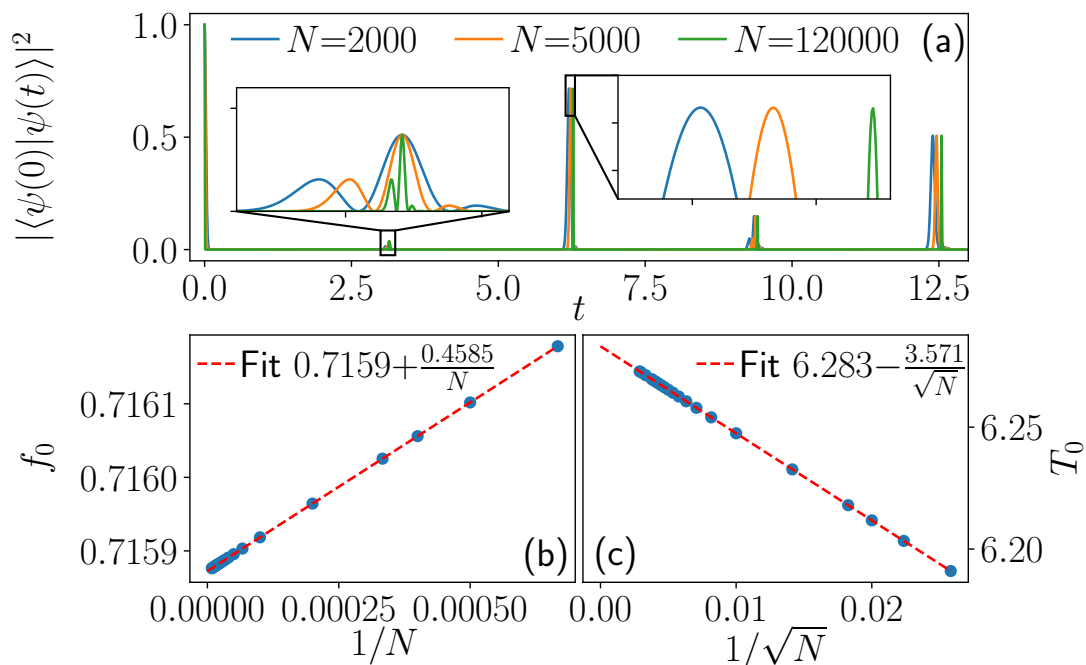
Figure 5.7: Dynamics in the two-hypercube model in Eq. (5.24). (a) Time evolution of the return probability, $|\langle\psi(0)|\psi(t)\rangle|^2$, for the Néel state, $|\psi(0)\rangle=|1010\ldots\rangle$ and several system sizes N. The insets zoom in on the first revival at time T and on the reflection peak at $T/2$. (b)-(c) Finite size scaling analysis of the first revival amplitude f_0 (b) and period T_0 (c). Extrapolation to $N\to\infty$ yields a finite revival peak f_0.

Another interesting feature of the revivals in Fig. 5.7 is the presence of a small but visible peak at *half* the revival period. In order to understand this, it is convenient to decompose the problem into a symmetric superposition of the two hypercubes and their antisymmetric superposition. The symmetric sector has $N+1$ states and its Hamiltonian is the one from Eq. (5.22) except that the last term of the sum is multiplied by a factor of $\sqrt{2}$. In the antisymmetric sector, the contribution of the two chains cancel at the middle vertex $|000\ldots\rangle$. Therefore, this sector has only N states and its Hamiltonian is the one of Eq. (5.22) without the last term in the sum. On their own, both sectors revive (although imperfectly) with a period close to $T=\pi$. However, at each revival the antisymmetric sector picks up a phase of -1. This is why the first revival of the full system only happens at $T\approx2\pi$. The symmetric sector also has a slightly longer revival period that the

antisymmetric one. The difference of frequency and amplitude of revivals means that they do not exactly cancel at $T \approx \pi$, hence the reflection peak.

5.4 Interpolating between two hypercubes and the PXP model

As shown in the previous section, the PXP model contains two embedded hypercubes of dimension $N/2$ which, on their own, support a revival from the $|\mathbb{Z}_2\rangle$ state in the thermodynamic limit. Here we explore a possible connection between the two-hypercube model and the full PXP model. Interpolation between the two models can be done naturally by varying the range of the projectors dressing the Pauli X operator in Eq. (5.24). Specifically, the class of models interpolating between the PXP and two hypercubes are defined by

$$H_r = \sum_j P_{j-2r+1} \cdots P_{j-3} P_{j-1} X_j P_{j+1} P_{j+3} \cdots P_{j+2r-1}, \qquad (5.25)$$

where r labels the number of projectors to the one side of X. Setting $r=1$ simply gives back the PXP model, whereas $r \geq N/4$ corresponds to the two-hypercube model in Eq. (5.24).

Physically, this Hamiltonian may be understood as a kinetically constrained free paramagnet. The constraint realised by this Hamiltonian for a given r is to forbid the occupation of even and odd sublattices of local unit cells of length $4r - 2$. For example, at $r = 1$, the constraint acts on unit cells of length 2, such that states containing the pattern 11 on any two neighbouring sites are forbidden. This is equivalent to the PXP constraint, and hence $r = 1$ is equivalent to the PXP model. For $r = 2$, the unit cell is of length 6. Any states which contain a local pattern of 6 sites with occupation on even and odd sublattices will be forbidden. For example, a state containing the local pattern 100100 on any 6 consecutive sites will be forbidden. Therefore as r increases, the number of forbidden states grows, corresponding to removing additional vertices from the graph of the PXP model. Eventually, at $r > N/4$, the length of the unit cell is larger than the size of the system, recovering the constraint corresponding to the two hypercubes. In

the language of graphs at $r > N/4$, all the vertices of the PXP model not present on the two hypercube graph, have been removed.

All the models in Eq. (5.25) have the two-hypercube as a subgraph and we compare the revivals from the Néel state in all of them in Fig. 5.8(a) for a fixed value of N=32. We observe the fidelity at the first revival peak remains in the ballpark of $f_0 \sim 0.7-0.8$ for all values of r, with a slight increase of the revival period with r. Moreover, for all values of r, we can identify a band of N+1 eigenstates with anomalously high-overlap on $|\mathbb{Z}_2\rangle$, see Fig. 5.8(b)-(d). The energy separation between these eigenstates is approximately constant in the middle of the spectrum and matches the frequency of revivals in Fig. 5.8(a). For r=$N/4$, the Hamiltonian exactly corresponds to the two-hypercubes model and the spectrum contains only N+1 states. As r is decreased, this band of states evolves smoothly, while an increasing number of thermal eigenstates start to appear in the system – see Fig. 5.8 (c) and (d).

In Fig. 5.8 (e) and (f) we compare the revivals from all states in the computational basis, i.e., we probe the revivals from *all* graph vertices. To make a fair comparison between different models, instead of fixing the system size, we take a different value of N for each model that gives roughly the same Hilbert space dimension. While for the Néel states there are few changes with r, this is not the case for most other initial states, whose revivals get worse as the constraint is relaxed. This can be understood by considering new vertices and edges that appear in the graph as r is decreased.

In the rest of this work we will refer to these graph elements (vertices and corresponding edges) as 'bridges' as they are effectively bridging between the hypercubes. For example, the 'bridges' present in the PXP model are shown as green vertices in Fig. 5.5.

When only the two hypercubes are present, the dynamics for the majority of vertices consists of perfect corner-to-corner transmission followed by a reflection back to the initial vertex occurring within single hypercube, with a small leakage to the other hypercube. However, if a bridge is added close to a vertex, this will drastically enhance the state transfer to the other hypercube. Thus the dynamics is no longer well described by perfect state transfer with some leakage, and the revivals consequently get worse.
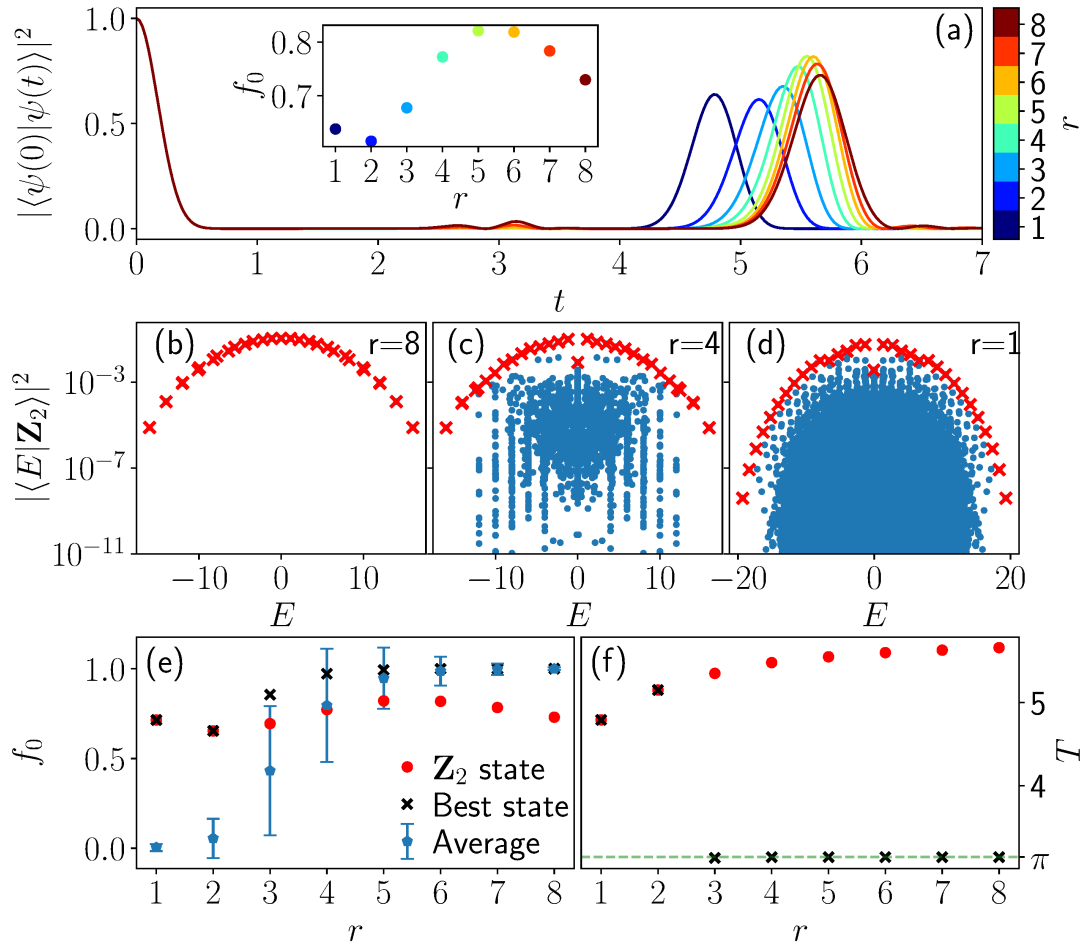
Figure 5.8: Revivals and scarred eigenstates in models defined in Eq. (5.25) for different values of r. (a) Fidelity for the $|\mathbb{Z}_2\rangle$ initial state for $N=32$. The inset shows the fidelity at the first revival peak f_0 as a function of r. (b)-(d) Overlap between $|\mathbb{Z}_2\rangle$ and the energy eigenstates for three different values of r with $N=32$. Panel (b) corresponds to the two-hypercube model while (d) is PXP. The red crosses highlight the top band of $N+1$ eigenstates with anomalously high overlap with the $|\mathbb{Z}_2\rangle$ state. (e)-(f) f_0 and revival period T for different r values. In panels (e)-(f), we compare the revival period and the first revival peak f_0 for $|\mathbb{Z}_2\rangle$ initial state with the computational basis state having the highest f_0 ('best state') as well as the average over all initial basis states (with the standard deviation shown by an error bar). The value of N changes with r in order to keep the Hilbert space dimensions comparable and in the range $10^5 < \mathcal{D} < 1.5 \times 10^5$.

On the other hand, for the Néel state the dynamics is relatively unchanged as we always have state transfer to the translated Néel state and back. Due to the form of the constraint, no bridge is added closer than at Hamming distance equal to 2 measured from that state. Because of this, during the interpolation the dynamics is left relatively unchanged by the bridges. It also means that the first two steps of the FSA are identical and exact for all values of $r \geq 1$.

For all values of r, the top band of $N+1$ states is present and states belonging to it are decoupled from the bulk of the spectrum. These states can be well approximated by the FSA. As we change r, we see that the magnitude and period of the revival smoothly varies. These results suggest there is a form of 'adiabatic continuity' that protects the scarred subspace in the family of models in Eq. (5.25). However, unlike the usual notion of adiabatic continuity, where the energy gap protects the smooth evolution of the ground state, here we are looking at a subspace spanning a finite range of energy densities, which remains protected due to a combined effect of constraint and many-body scarring.

5.5 Weakening the constraint: interpolating between PXP and free spin $1/2$ model via $(k, k+1)$ models

Instead of making the PXP constraint stronger as we did in the previous section, therefore interpolating between the PXP model and the two joined hypercube model, one may wonder if by *weakening* the constraint it might be possible to relate the many-body scarring in the PXP model with the free spin-1/2 model.

This can be achieved by introducing a class of $(k, k+1)$ models with the constraint that each cell of $k+1$ sites can contain *at most k* excitations. The Hamiltonian for this series of models is given by the Rabi flip term compatible with the constraint, i.e.,

$$H_{(k,k+1)} = \mathcal{P}_k \left(\sum_j X_j \right) \mathcal{P}_k,\tag{5.26}$$

where $\mathcal{P}_k$ projects out any configuration with more than k contiguous excitations anywhere in the chain. Varying k then allows to tune the effective strength of the constraint, with $k=1$ corresponding to the PXP model and $k=N$ being the free spin-1/2 model.

Fig. 5.9 summarises the dependence of revivals in the models defined by Eq. (5.26) as a function of k. In the limit of large k, the behaviour is dominated by the proximity to the free spin-1/2 model, where many basis states revive. Intriguingly, we observe that the PXP model ($k=1$) is not smoothly connected to this large-k limit. For example, the fidelity at the first revival peak, Fig. 5.9(b), first increases in going from $k=1$ to $k=2$, but then drops precipitously from $k=2$ to $k=3$. The drop is sharp for the Néel initial state, but somewhat less pronounced if we look at *all* initial basis states and choose the 'best' one. Nevertheless, this implies that scarred $|\mathbb{Z}_2\rangle$ dynamics in the PXP model cannot be understood by smoothly turning off the constraint to reach the free spin-1/2 model. From the FSA point of view, we expect $1<k \ll N$ models to support poorer revivals compared to the PXP model. Indeed, as more and more configurations are allowed, the graph starts to differ from the one of the two hypercubes as we get closer to the Néel state. This means that the FSA steps will start to become inexact due to backscattering after fewer steps . For $k>3$, new states appear in the graph already in the first Hamming layer, and this is expected to strongly destabilise the revivals (23). Similarly, for $k=2$ new states will appear in the second Hamming layer, in theory causing similar effects. However, this expectation is clearly not in agreement with Fig. 5.9 which shows that the $k=2$ model has more robust revival compared to the PXP model, for the same $|\mathbb{Z}_2\rangle$ initial state. In the remainder of this section, we study in detail the $k=2$ model, identifying its scarred eigenstates in order to understand why revivals are better than the PXP model. We further expand on differences between the $k=2$ model and PXP model from a graph theoretic point of view in Appendix A.2.1, where we demonstrate an underlying *hypergrid* subgraph is responsible for scarred dynamics from the Néel state, in contrast to the embedded hypercubes present in the PXP model.
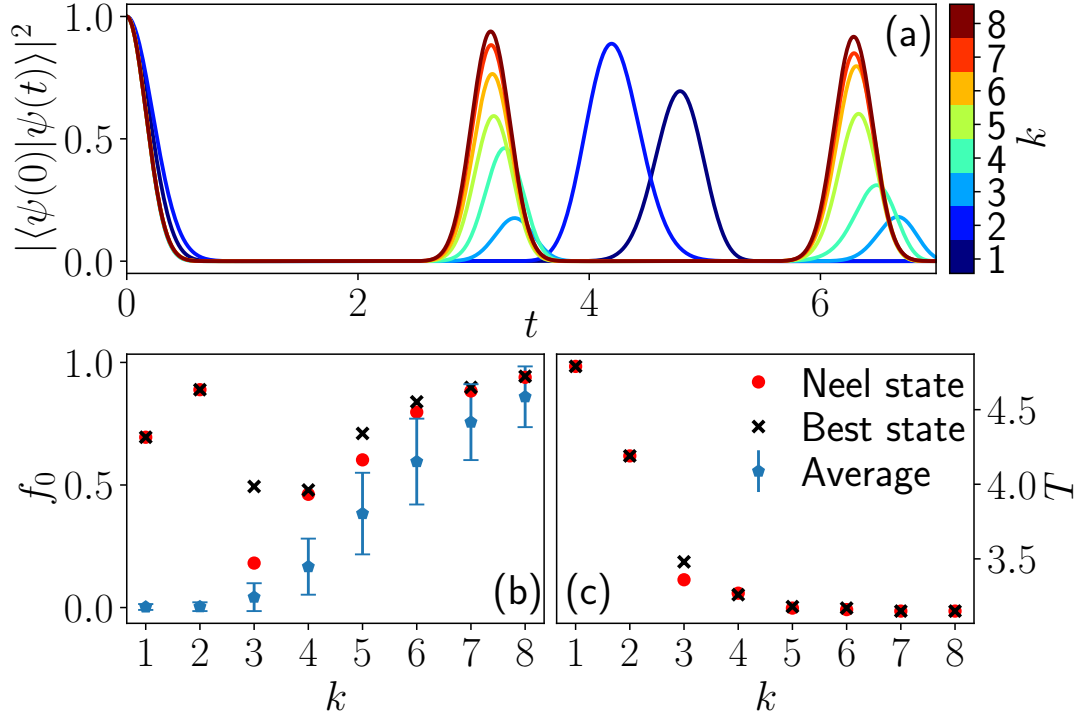
Figure 5.9: Revival fidelity for $(k, k+1)$ models in Eq. (5.26). (a) Fidelity time series for the $k, k+1$ models when initialised in the Néel state $|Z_2\rangle = |1010...\rangle$ for various k. (b)-(c) Height of the first fidelity revival peak f_0 and the associated revival period T for various initial product states. In order to compare different models at approximately the same Hilbert space dimension, the system sizes are chosen according to the value of k in such a way that the Hilbert space dimension is in the range $1.3 \times 10^5 < \mathcal{D} < 2.8 \times 10^5$. Shown is the Néel state (red), the best reviving basis state (black cross) and the average over all computational basis states (blue - with the standard deviation shown as an error bar). Going from the $k = 1$ to the $k = 2$ model improves revivals from the Néel state, but progressing to $k = 3$ results in a discontinuity, where revivals get worse and the Néel state is no longer the best reviving state. At intermediate k, the distribution of reviving states is roughly binomial, with many states reviving well (with the same f_0) and many states not reviving at all. This produces the large variance seen in (b) at $k = 4, 5, 6$)

5.5.1   Quantum many-body scars in the (2,3) model

The (2,3) model – a special case of Eq. (5.26) where each consecutive triplet of
sites can have at most two excitations – bears many similarities with the PXP
model. For example, we will show that the (2,3) model is non-integrable yet it
hosts a band of $N+1$ scarred eigenstates with large support on the Néel state,
$|1010\ldots10\rangle$, reminiscent of the PXP model. However, despite this similarity
between the two models, we find the revivals and scarred eigenstates are more
robust in the (2,3) model, even though the Hilbert space is larger in the latter
model for the same size N, due to the weaker kinetic constraint (27). A more
striking difference, which arises in sizes N divisible by 4, is the existence of
additional reviving states, $|11001100\ldots\rangle$ and its three translated equivalents in
the (2,3) model.

We first demonstrate that the (2,3) model is non-integrable and it supports
revivals due to the existence of $N+1$ towers of scarred eigenstates. The aver-
age energy level spacing $\langle r \rangle$ (90) is found to approach 0.53 in large systems,
see Figs. 5.10 (a)-(b), as expected from a thermalising system. Moreover, the
distribution of energy level spacings is consistent with the Wigner-Surmise dis-
tribution (75), demonstrating that physical properties of the model cannot be
explained by its proximity to the full hypercube.

The fidelity density at the first revival, $\ln(f_0)/N$, is computed for the Néel
and $|11001100\ldots\rangle$ initial states and several values of N in Fig. 5.10(c). For the
Néel state, the fidelity density quickly saturates to ≈ -0.00591. For a random
initial state one would expect the saturation value to be $-\ln(D)/N = -\ln(\alpha)$,
where D is the dimension of the Hilbert space and α is the 'quantum dimension',
which measures the exponential scaling of the Hilbert space $D = \alpha^N$. For the
$k = 2$ constrained Hilbert space, we find the fidelity density of a random state
should saturate to ≈ -0.609. As this is two orders of magnitude larger than
the value obtained for the Néel state, it shows that the revivals are not simply
fluctuations due to a small finite size of the system. For comparison, we also
study the other reviving state, $|1100\ldots1100\rangle$, whose fidelity density converges to
≈ -0.0304. While larger than for the Néel, this value is still an order of magnitude
smaller than for a random state, signalling that this initial state is also atypical
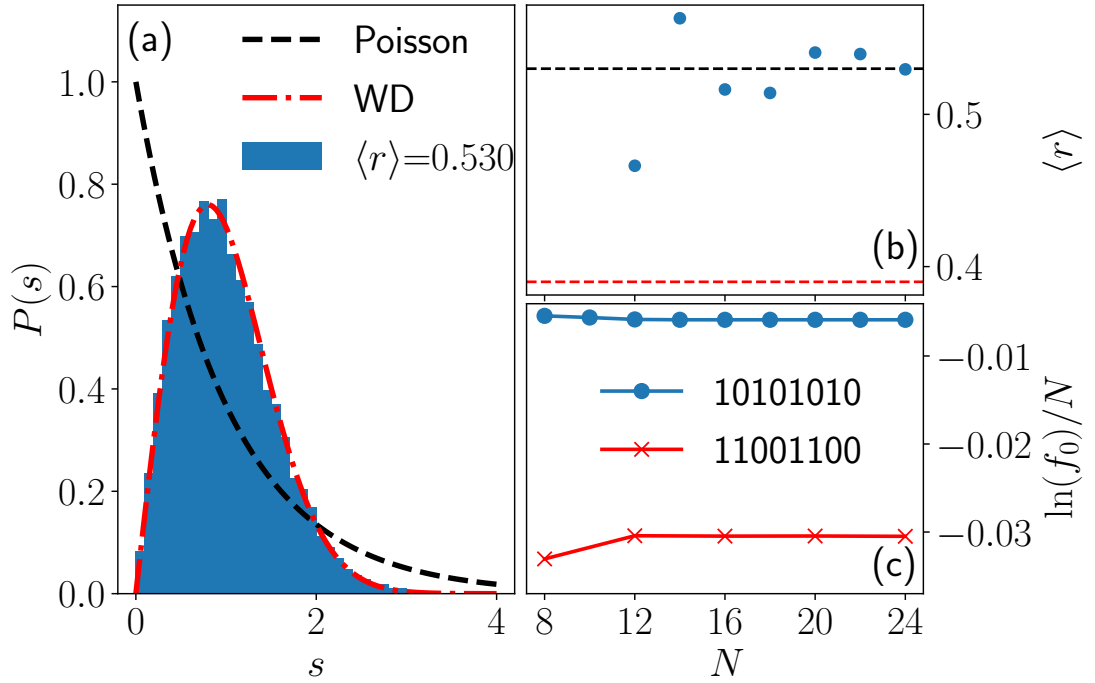
Figure 5.10: Level statistics of the (2,3) model, confirming it is non-integrable. (a) Statistics of energy level spacings $P(s)$ in the (2,3) model in a large system size $N=24$ is consistent with the Wigner-Surmise distribution. The average r-value is close to 0.53. The level statistics is computed in the momentum sector $K=0$ and inversion sector $I=+1$, after performing the spectrum unfolding. (b) Convergence of $\langle r \rangle$ with system size. (c) Fidelity density at the first revival from the Néel state in the (2,3) model saturates to a non-ergodic value -0.00591. For comparison, we also show the fidelity density of $|11001100\ldots\rangle$ initial state. Both of these fidelity densities are much larger than expected for a random initial state, signalling they are strongly atypical initial conditions for the (2,3) model.

for the (2,3) model.

In Fig. (5.11) we study the scarred dynamics present in the $(2,3)$ model. Fig. 5.11(a) shows the overlap between the reviving Néel state and the eigenstates of the (2,3) model. Similar to the PXP model studied in Ref. (131), we observe that eigenstates form tower structures. At the top of each tower is a scarred state with high overlap on the Néel state. The FSA subspace provides a very good estimate of the energy of each tower, as indicated by crosses in Fig. 5.11(a). The FSA also captures the revival dynamics, as shown in Fig. 5.11(c), in particular it accurately estimates its frequency, while somewhat overestimating the amplitude of the revival.

Moreover, as usual scarred eigenstates can also be identified as having much lower entanglement than other eigenstates at the similar energy density. To quantify entanglement, we compute the bipartite entanglement entropy, Eq. (2.21). Entanglement entropy of eigenstates of the (2,3) model in momentum sectors $K=0$ and $K=\pi$ is shown in Fig. 5.11(b). Entanglement entropy reveals the scarred eigenstates as some of the most weakly entangled states in the spectrum. While in smaller systems entropy distribution shows a large spreading, similar to the PXP model as pointed out in Ref. (60), in larger system sizes like $N=24$ shown in Fig. 5.11(b), we observe that entropy distribution becomes quite narrow, starting to look more similar to models such as AKLT (81) and constrained clock models (17). In particular, constrained clock models exhibit very narrow towers densely populated with eigenstates, as also seen in Fig. 5.11(a). Such towers enhance the hybridisation between the top $N+1$ scarred eigenstates and the rest of the spectrum, resulting in relatively high entropy of scarred eigenstates, Fig. 5.11(b).

5.6 Numerical interpolation between two hypercubes and free spin $1/2$ model: adding bridges

In Sections 5.4, 5.5 we studied two classes of models which were shown to contain hypergrid subgraphs. These two classes of models were obtained from physical Hamiltonians corresponding to strengthening or weakening the PXP constraint.
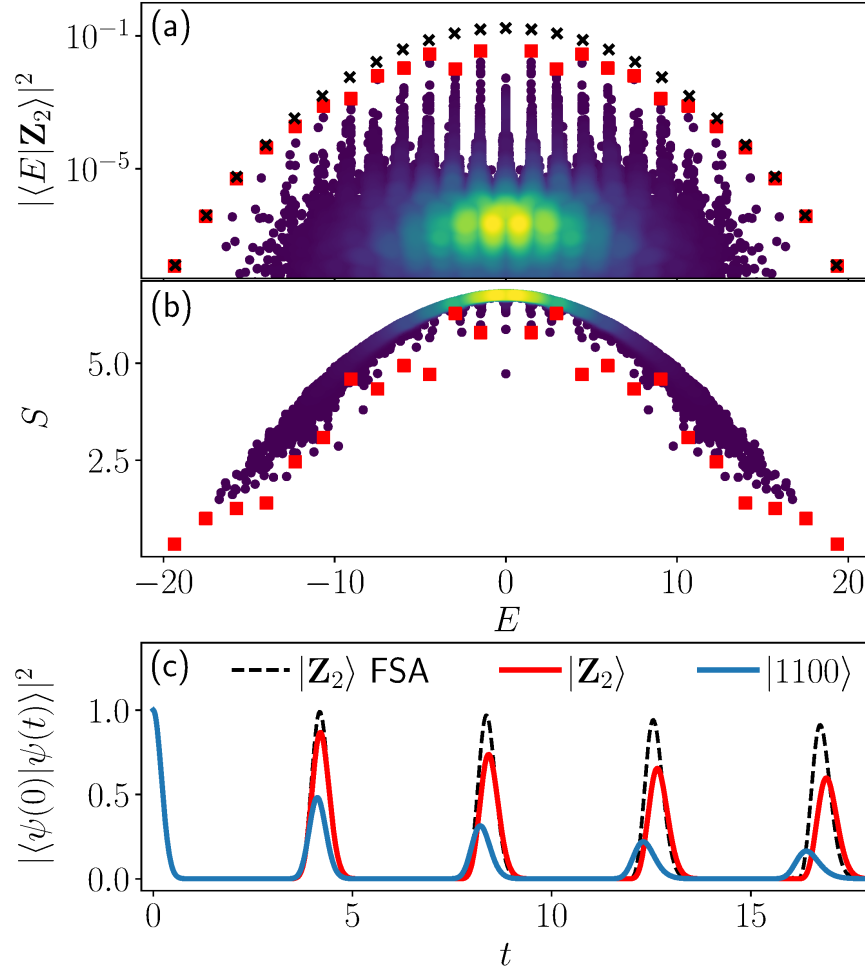
Figure 5.11: QMBS in the $(2, 3)$ $k, k+1$ model. The $(2, 3)$ model realises scarred oscillatory dynamics from the states $|Z_2\rangle$, $|11001100...\rangle$. (a) Shows the overlap of eigenstates with $|\mathbb{Z}_2\rangle$ state, verifying the presence of scarred eigenstates responsible for the scarred dynamics. $N+1$ scarred eigenstates with anomalously high overlap are labelled by red squares. The FSA approximation (Section. 3.3.1) is applied to produce approximations for the scarred eigenstates (black crosses). (b) Entanglement entropy of all eigenstates in momentum sectors $K=0$ and $K=\pi$, with the same $N+1$ scarred eigenstates highlighted in red. (c) Fidelity revivals indicating scarred dynamics from the states $|Z_2\rangle$, $|11001100...\rangle$, whose exact dynamics generated by the $(2, 3)$ models Hamiltonian are the bold face lines. The dashed line corresponds to an approximate time evolution generated by restricting the evolution to only occur within a subspace produced by the FSA approximation. The FSA provides a good estimate of the revival frequency from $|\mathbb{Z}_2\rangle$ initial state, although it somewhat overestimates the revival amplitude. For comparison All data is for system size $N=24$. In (a) and (b) the colour scale indicates the density of data points.

5. QUANTUM MANY-BODY SCARS FROM EMBEDDED HYPERCUBE SUBGRAPHS

We now turn towards building new constrained models by instead constructing different graphs, considering quantum walks occurring on these graphs. The graphs we consider will all be partial cubes, that is, they will all be subgraphs of a full hypercube, obtained by removing vertices from the full hypercube. Therefore a Hamiltonian of the form $H = \mathcal{P} \sum_n X_n \mathcal{P}$ will exists for these graphs, with $\mathcal{P}$ a global projector.

We start from the graph of two joined hypercubes and add back states from the unconstrained spin-1/2 chain of the same length. Recall that we refer to vertices and links from the full hypercube that are not present on the two joined hypercube graph as 'bridges'. For example, the green vertices on the PXP graph in Fig. 5.5 are bridges. Our method will consist of an algorithm which adds back these bridges in a systematic fashion.

When adding back vertices from the full hypercube onto the graph of the two joined hypercube, we will also add all translationally equivalent vertices, such that the models sampled will also be invariant under translation. The algorithm we use to grow the graph is the following: A new basis state with m excitations is randomly chosen. After that, all vertices corresponding to this state, its translations, or states that can be obtained by removing excitations from these, are added along with the relevant edges. The value of m is initialised at 2 and increased after a step if some conditions are met. Full details of this algorithm can be found in Appendix A.2.2. After each addition, the first revival and the revival period are computed.

In order to monitor closeness to the two hypercubes or to the free spin-1/2 model, we introduce the bridge-density parameter λ defined as

$$\lambda = \frac{\ln(|G|) - \ln(2^{N/2+1} - 1)}{\ln(2^N) - \ln(2^{N/2+1} - 1)}, \tag{5.27}$$

where $|G|$ is the number of states in the graph. Note that the two joined hypercube graph has $2^{N/2+1} - 1$ vertices, whereas the full hypercube graph has 2^N vertices. Therefore this quantity is a normalised measure of how many vertices have been added to the two hypercube graph. When no vertices have been added such that G is still the two hypercube graph, $\lambda=0$, while when G is a single large hypercube $\lambda=1$. The logarithms ensure that λ is properly normalised in large
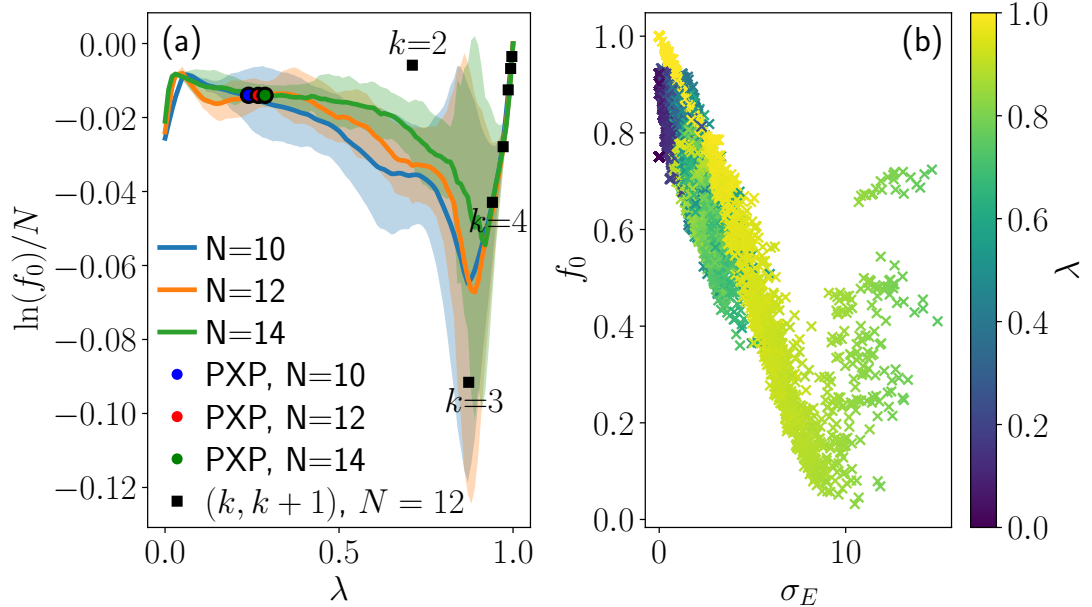
Figure 5.12: Interpolating between the two hypercube model and the free paramagnet via the addition of bridges, resulting in QMBS models. (a) Revival fidelity density when random bridges of density λ are added to the two-hypercube model in a few system sizes N. The shaded areas represent standard deviation over different realisations of the bridges with the given density. This analysis reveals that the PXP model falls in the middle of the distribution, thus it is a 'generic' model with the given density of bridges. The behaviour of most $(k, k+1)$ models is also close to the expected average, with $k=2$ being a notable outlier. (b) Revival fidelity for random bridges added to the two-hypercube model with $N=12$. The subspace variance of the FSA, σ_E, correlates well with the fidelity at the first revival.

systems.

The result of adding bridges is summarised in Fig. 5.12 for chains of length $N=10, 12, 14$. Fig. 5.12 shows that the PXP model represents a typical model with the given density of bridges added to the two hypercubes. The presence of the two hypercubes explains why this model revives, and the bridges only weakly affect the fidelity and period of the revivals. For larger values of k, the corresponding $(k, k+1)$ models generally fall very close to the average of random models for the same value of λ due to their proximity to the free spin-1/2 model. A notable exception is $k=2$, which has significantly better revivals than expected

from our random sampling analysis. As we argued previously, this is likely due
to the presence of the 2HG subgraph and the special structure of the bridges in
that model.

Another notable feature of Fig. 5.12 is that there is always an improvement
of the revivals when a small number of bridges are added to the two hypercubes.
Intuitively, we would expect the fidelity to decay as the graph gets further away
from the two hypercubes, until it becomes close enough to the full hypercube of
a larger size, which also has good revivals. The enhancement of revivals at low
values of λ can be understood as 'correcting' the frequency mismatch between
the symmetric (resp. antisymmetric) superpositions of the two hypercubes, as
we discussed in Section 5.3. In this regime the bridges only affect the frequency
of the symmetric sector, bringing it closer to the frequency of the antisymmetric
sector, thus improving the revival fidelity (see Appendix A.2.3 for further details).
It is also important to note that the range of λ where this improvement happens
goes to zero in the thermodynamic limit, meaning that the slope of the curve in
the limit $\lambda \to 0$ in Fig. 5.12(a) becomes steeper with the increase in system size.

For all graphs sampled during the process in Fig. 5.12 the dimension of the
FSA subspace remains unchanged. Indeed, the FSA process from the Néel states
always terminates on the anti-Néel state after N steps, leading to $N+1$ states. In
addition, for the two joined hypercubes and for the full hypercube, this subspace
is exact, meaning that it is disconnected from the rest of the Hilbert space. For
the random graphs sampled, the FSA is generally not exact, and this can be
quantified using the subspace variance σ_E introduced in the previous chapter,
Eq. (4.17). Among all graph properties, the subspace variance was found to best
correlate with the existence of revivals, see Fig. 5.12(b). This correlation implies
that the FSA revivals are generally good, and that the leakage out of it is the
main factor that destabilises the revivals in the full system. As the algorithm
adds back states with incrementally more excitations, these new vertices can get
closer and closer to the Néel state. This means that they can affect the FSA at
earlier steps and thus exert a stronger effect on the revivals.

5.7 Summary

In this chapter we explored a complementary interpretation of broken Lie algebras, giving a graph-theoretic perspective on the origin of many-body scars and associated wave function revivals in the PXP model. We studied the properties of the Hamiltonian adjacency graph, in particular the existence of large regular subgraphs, as we varied the constraint in the PXP model. We considered two simple limiting cases, the free spin-1/2 model and the model of two hypercubes joined at a single vertex, which naturally arise when the constraint is either completely turned off or made stronger to penalise not only nearest-neighbour excitations, but an entire sublattice of the chain. While both of these limits support revivals in the thermodynamic limit, we argued that only the two hypercube model faithfully captures the many-body scarring phenomenology in the PXP model. To demonstrate the connection between the two, we introduced a family of models with a variable range of the constraint, showing that the scarred subspace remains preserved under this interpolation. By contrast, such a smooth interpolation was not found between PXP and the free spin-1/2 model. Nevertheless, the exploration of this connection led us to new constrained models, such as the (2,3) model, which were shown to have unique scarring phenomenology of their own.

We note that the Hamiltonian adjacency graph have recently been linked to quantum many-body scars in a few models (28, 48, 126, 132, 145). However, these studies focus on regular subgraphs with *weak* connectivity to the the rest of the Hilbert space. In contrast, the subgraphs identified in this work do not have this property. For example, in the PXP and (2,3) models, the bridges form an essential part of the scarred dynamics and even enhance it, as opposed to simply destabilising revivals.

Our approach sheds light on the relation between constrained systems and many-body scarring. Indeed, constraints have the effect of removing vertices and edges from the graph. If the constraint removes enough bridges while leaving the substructure intact, then it can create the right conditions for scarring and revivals.

In much of the existing literature, quantum many-body scars and other kinds

of non-stationary dynamics have been understood from the su(2) algebra point of view, where the non-thermalising eigenstates form a representation of the algebra (15, 72, 74, 81, 89, 112). This eigenstate-based picture, however, does not directly allow to predict the existence of many-body scars without diagonalisation of the Hamiltonian – an exponentially difficult task. By utilising a graph-theoretic approach, one can instead focuses on the Hamiltonian matrix and its properties in the computational basis. While in general we expect there is no easy way to directly relate the two points of view, we found that in many scarred models the existence of regular subgraphs, judiciously perturbed by bridges, correlates with the emergence and enhancement of su(2) algebra, as captured by the forward scattering approximation.

Chapter 6

Systematic construction of quantum many-body scars using kinetic constraints

The previous two chapters have introduced two complementary theories that attempt to understand *why* approximate quantum many-body scars arise in interacting quantum systems. We have proposed that approximate quantum many-body scarring, as seen in the PXP model, is a reflection of the fact that scarred eigenstates possess a strong resemblance to eigenstates of a proximate Hamiltonian which possesses some exact symmetry. This notion is made more rigorous by the introduction of 'broken Lie algebras' (Chapter 4), for which scarred Hamiltonians approximate elements of a Lie algebra of the appropriate symmetry. Furthermore, rather than probing the proximity of a scarred Hamiltonian to another Hamiltonian possessing an exact symmetry by studying the algebra of generators, we have shown one can also utilise a graph theoretic point of view, inspecting the proximity of the Hamiltonian, interpreted as an adjacency matrix of a graph, to that of another graph which possesses the relevant symmetry group. For instance, the PXP model adjacency matrix consists of two large embedded hypercubes, where a hypercube graph is known to possesses SU(2) symmetry. The hypercube graph has the property that it permits perfect transmission and reflection on a quantum walk from any node, shedding light on the anomalous

oscillatory dynamics observed in the PXP model.

These two approaches are useful in understanding the origin of quantum many-body scars and their insight have resulted in the construction of new scarred models (16, 27). However, these approaches may not always be a practical way of understanding the scarred eigenstates or constructing new scarred Hamiltonians when considering more complicated systems. From the algebraic point of view, to understand the scarred eigenstates, one must first decompose the scarred Hamiltonian into a linear combination of generators of the broken Lie algebra (16), and this decomposition may not be obvious. Furthermore, from the graph point of view, the hypercube graph is not the only one which features perfect transmission and reflection and thus perfect oscillatory dynamics (111). There even exist weighted graphs with this property of perfect transmission (34), which falls outside the scope of the previous chapter. Identifying generic embedded graphs which permit perfect transmission and reflection quickly becomes an unfeasible problem.

The purpose of this chapter is to introduce a general construction, via the use of kinetic constraints, which yield quantum many-body scarred models. Our construction, which we introduced in Ref. (17), is based on the systematic embedding of a single-site unitary dynamics into a kinetically-constrained many-body system. Utilising this construction, we scan the phase space of kinetically constrained models of a given local Hilbert space dimension for hosting many-body scars. Due to the nature of the construction, it is apparent there is likely an underlying broken Lie algebra structure responsible for scarring in the obtained models, but this construction does not rely on the details of this algebra being known. This construction results specifically in approximate scarred models. Given the only experimentally realised many-body scarred models have hosted approximate scars (7), this construction may prove useful in experimentally realising weak ETH violating systems with periodic oscillatory dynamics.

6.1 Construction of scarred models

Our construction produces interacting lattice models that exhibit periodic quantum revivals when quenched from a Néel state. The basic building block has

a Hilbert space containing N_c states ('colours') and a time-independent local Hamiltonian that yields periodic unitary dynamics, $\mathcal{U}(t + T) = \mathcal{U}(t)$. The interacting models are defined by coupling these building blocks under a kinetic constraint. Intriguingly, the dynamics in these models decomposes into periods of nearly free precession, in which the local degrees of freedom coherently cycle through the available states on a single site, followed by an interacting segment of dynamical evolution, reminiscent of a kicked quantum top (43). In all cases, the existence of atypical scarred eigenstates underpins the revivals. We show that our construction includes known models, such as chiral clock models (36), which are shown to support scars, and also gives a way of enhancing the revivals in spin-s generalisations of the Rydberg chain (47). In selected cases for small values of N_c, we numerically explore general deformations of the models, verifying that our construction yields optimal models with the highest amplitude of the wave function revivals.

Specifically, consider a system with a local basis $|0\rangle$, $|1\rangle$, ..., $|N_c - 1\rangle$, and an arbitrary time independent Hamiltonian h whose unitary dynamics is periodic, such that $\mathcal{U}^T \equiv \exp(-ihT) = \mathbb{I}$ for arbitrary period T. The eigenvalues of $\mathcal{U}$ are $\lambda_n = \exp(i2\pi k_n / T)$, with the corresponding eigenvectors $|\psi_n\rangle$, where k_n are arbitrary integers. We obtain candidate Hamiltonians h by choosing particular $\{\lambda_n\}$ which guarantee a periodic $\mathcal{U}$ and taking its logarithm:

$$h = i \sum_{n=0}^{N_c-1} \frac{2\pi i}{T} k_n |\psi_n\rangle\langle\psi_n|. \tag{6.1}$$

The many-body lattice Hamiltonian is defined by taking a tensor product of h and imposing the kinetic constraint that h only acts on sites whose neighbours are in some unlocking state $|\chi\rangle$:

$$H = \sum_{j=0}^{N-1} P_{j-1} h_j P_{j+1}, \quad P_j \equiv |\chi_j\rangle\langle\chi_j|, \tag{6.2}$$

where N is the number of lattice sites. Note that if the operator $\sum_j h_j$ is itself some linear combination of elements of a Lie algebra, the local projector dressing in Eq. (6.2) will result in a broken Lie algebra when considering the commutation

of these dressed elements, as is the case with the PXP model (Chapter 4).

The only other condition we place on h is that the many-body system possesses a particle-hole symmetry ρ, which anticommutes with H, $\{H, \rho\} = 0$, leading to the symmetry $E \leftrightarrow -E$ of the energy spectrum. This is motivated by the fact that PXP model in Eq. (2.41) possesses such a symmetry: $\rho = \prod_i Z_i$ anticommutes with the Hamiltonian of the PXP model. Moreover, the PXP revivals were found to be improved by perturbations which preserve this symmetry (23, 60). Indeed, the perturbations we derived in Chapter 4 by correcting errors in a broken su(2) Lie algebra all preserved this particle-hole symmetry. We thus focus on cases where $\{k_n\}$ are symmetric around zero, resulting in h being off diagonal and compatible with some ρ. A particularly illustrative example of this construction is when $\mathcal{U}$ is interpreted as the shift operator of a quantum clock (36, 134, 138), as we explain next.

6.2   Example: clock models

Consider a specific periodic unitary $\mathcal{U}$ which implements a cyclic precession through the N_c coloured basis states:

$$\mathcal{U} = e^{-iC} = \left(\sum_{n=0}^{N_c-2} |n+1\rangle\langle n| \right) + |0\rangle\langle N_c - 1| \tag{6.3}$$

In this case, $\lambda_n = \exp(2\pi i k_n/N_c)$ and $|\psi_n\rangle = \sum_{j=0}^{N_c-1}(1/\lambda_n^j)|j\rangle$. For odd N_c, k_n takes the values $-\frac{N_c-1}{2}, \ldots, 0, \ldots, \frac{N_c-1}{2}$. For N_c-even, we need to double the period, $T = 2N_c$, in order to make h off-diagonal in the $|j\rangle$ basis. This allows to choose $k = -\frac{N_c-1}{2}, \ldots, -\frac{1}{2}, \frac{1}{2}, \ldots, \frac{N_c-1}{2}$, and Eq. (6.3) continues to be valid for N_c-even after performing a gauge transformation, $|j\rangle \rightarrow e^{i\pi j/N_c}|j\rangle$.

The single site clock operator C is obtained by taking the logarithm of the unitary in Eq. (6.3). We also utilise the convention that C is rescaled such that the magnitude of the largest matrix element is 1. For example, for $N_c = 3, 4$ the

single site clock operator C takes the following forms:

$$C^{N_c=3} = \begin{pmatrix} 0 & i & -i \\ -i & 0 & i \\ i & -i & 0 \end{pmatrix}, \tag{6.4}$$

$$C^{N_c=4} = \begin{pmatrix} 0 & i & -i/\sqrt{2} & i \\ -i & 0 & i & -i/\sqrt{2} \\ i/\sqrt{2} & -i & 0 & i \\ -i & i/\sqrt{2} & -i & 0 \end{pmatrix}. \tag{6.5}$$

The inspiration behind Eq. (6.3) is that local dynamics is a cyclic rotation around the basis of N_c 'clock' states $|j\rangle$, Fig. 6.1(a). With h in Eq. (6.1) denoted by C, Eq. (6.2) defines a many-clock 'PCP' Hamiltonian,

$$H_{\text{clock}} = \sum_j P^0_{j-1} C_j P^0_{j+1}. \tag{6.6}$$

Without loss of generality, the projector can be chosen onto any of the clock basis states, e.g., $P^0 = |0\rangle\langle 0|$. Thus, each site precesses around the clock if both its neighbours are in $|0\rangle$ state, otherwise it remains frozen, Fig. 6.1(a). Note that the PXP model in Eq. (2.41) is equivalent to $N_c = 2$ clock.

The PCP model, by construction, possesses the desired (anti-unitary) particle-hole symmetry, which for an arbitrary N_c coloured clock model generalises to charge conjugation symmetry. Our clock model actually possesses several discrete unitary and anti-unitary symmetries, originating from charge conjugation, parity and time reversal. We define single-site charge conjugation as the following $N_c \times N_c$ operator (138):

$$\mathcal{C}_i = \begin{pmatrix} 1 & 0 & 0 & ... & 0 \\ 0 & 0 & ... & \pm 1 & 0 \\ 0 & ... & \pm 1 & 0 & 0 \\ ... & & & & \\ 0 & \pm 1 & 0 & ... & 0 \end{pmatrix}, \tag{6.7}$$

where $+$ corresponds to odd N_c while $-$ corresponds to even N_c. Further, we
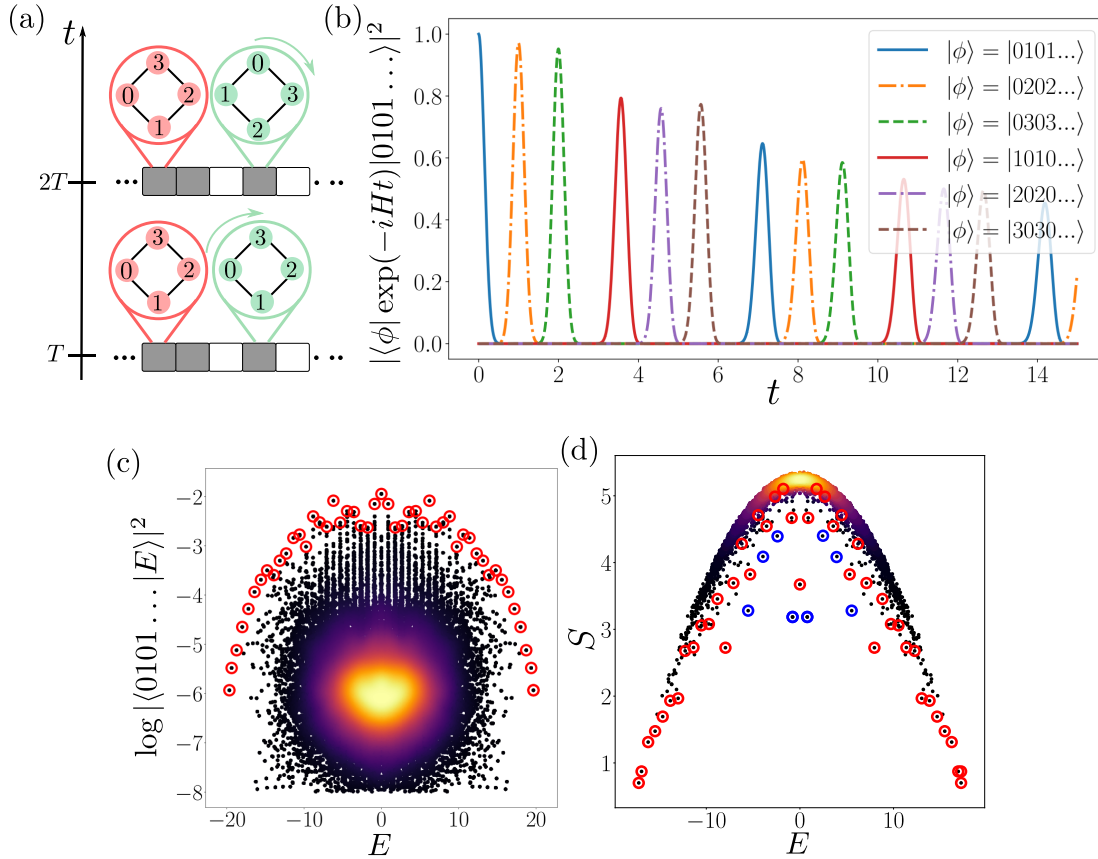
Figure 6.1: QMBS observed in a kinetically constrained clock model, constructed by embedding periodic single site dynamics into a kinetically constrained model. (a) A schematic of scarred clock models. Green clock can precess because both of its neighbours are in the unlocking state $|0\rangle$ (white), unlike the frozen red clock. (b) Dynamics of fidelity, $|\langle\phi|e^{-itH}|1010\ldots\rangle|^2$, for $N_c = 4$-colour clock model in Eq. (6.6). Different curves correspond to several choices of $|\phi\rangle$ indicated in the legend. (c) Overlap of all eigenstates of $N_c = 4$-colour clock model with the Néel state $|0101\ldots\rangle$. Each dot corresponds to a single eigenstate $|E\rangle$ with energy E shown on the x-axis. colour scale indicates the density of data points. Scarred states are marked by red circles. (d) Entanglement entropy S of all eigenstates of $N_c = 4$-colour clock model, plotted as a function of their energy E. Red circles indicate the matching scarred states from (c), while a few additional scar states, associated with the a 'defected $\mathbb{Z}_4$' state, $|20002030103000\rangle$, are marked by blue circles. Plots (b), (c) are for system size $N = 16$, while (d) is for $N = 14$. In all cases, we resolve translation and spatial inversion symmetry, and plot both $[k = 0, P = +]$ and $[k = \pi, P = -]$ sectors.

define spatial inversion P and time reversal T operators in the conventional way:

$$P: \quad j \to L - j - 1, \tag{6.8}$$

$$T: \quad \hat{K}, \tag{6.9}$$

where $\hat{K}$ corresponds to complex conjugation. It then follows that the PCP models possess the following discrete symmetries:

$$[H, I] = 0, \tag{6.10}$$

$$[H, \mathcal{C}T] = 0, \tag{6.11}$$

$$\{H, \mathcal{C}\} = 0, \tag{6.12}$$

$$\{H, \mathcal{C}I\} = 0, \tag{6.13}$$

where $\mathcal{C} = \prod_i \mathcal{C}_i$.

We have studied the PCP model in Eq. (6.6) with periodic boundary conditions using exact diagonalisation, resolving both translation and spatial inversion symmetries. For any $N_c \leq 12$ accessible to us numerically, we find long-lived oscillatory dynamics when the system is quenched from any Néel-like state, $|0101...\rangle$, $|0202...\rangle$, etc. Fig. 6.1(b) summarises the result for $N_c = 4$. The dynamics proceeds in two steps. First, each unfrozen clock nearly freely cycles through its states, $|1\rangle \to |2\rangle \to \ldots |N_c - 1\rangle$. After this coherent process is complete, the many-clock state shifts, $|N_c - 1, 0, N_c - 1, 0 \ldots\rangle \to |0101 \ldots\rangle$. In this second step, interactions kick in and some fidelity is lost to thermalisation. We now see that the PXP model is special in that it lacks free-precession dynamics. On the other hand, similar to the PXP case, in scarred clock models coherence also remains protected to a large degree during the interacting part of the process, allowing the wave function to keep returning to the initial state.

In order to visualise the dynamics, in Fig. 6.1(b) we plot the generalised fidelity

$$|\langle\phi| \exp(-itH)|1010\ldots\rangle|^2 \tag{6.14}$$

with respect to several product states $|\phi\rangle$, corresponding to either the initial state,

the internal shift of each clock, or to the overall translation of the initial state. The duration of individual clock ticks (e.g., $|1010\ldots\rangle \rightarrow |2020\ldots\rangle$) matches that of the *unconstrained* clock model. Following the convention that C is rescaled such that nearest neighbour hoppings have magnitude one, the frequency of the putative free precession is found to be ≈ 0.902 (in units $\hbar = 1$) while the frequency of the single site precession (in the absence of a constraint) is ≈ 0.900.

Fig. 6.1(c) shows the overlap of all eigenstates with the Néel state $|0101\ldots\rangle$, while Fig. 6.1(d) shows the bipartite entanglement entropy, Eq. (2.21). The scar states are easily identifiable as a band of special eigenstates (circled in red) that extend throughout the entire spectrum. The total number of special states is $(N_c - 1)N + 1$. Similar to the PXP model, the special eigenstates are distinguished by their high overlap with the Néel state, or alternatively as ones with atypically low entanglement. Note that some of the eigenstates with small entanglement belong to a different band of scarred states associated with a 'defected $\mathbb{Z}_4$' state $|20002030103000\rangle$ [blue circles in Fig. 6.1(d)]. Apart from these special states, there are tower structures in the spectrum which reflect the clustering of neighbouring eigenstates around the energies of the scarred eigenstates. Deep in the bulk of the spectrum, the density of states [indicated by colour scheme in Fig. 6.1(c)] appears uniform, as expected from the ETH. Indeed, at $N = 14$ we find a mean level spacing ratio (90) of $\langle r \rangle = 0.5218$, consistent with a Wigner-Surmise distribution. We have confirmed that the frequency of the revival to the initial state matches the energy separation between special eigenstates in Fig. 6.1(c).

While we have demonstrated a reviving wavefunction by computing the generalised fidelity in Eq. (6.14), this quantity is formidable to measure experimentally. However, one can demonstrate that the same picture of the dynamics can be inferred from studying revivals in local observables. For example, measuring a colour on a given site, $Q \equiv P^n = |n\rangle\langle n|$ shows the same pattern of dynamics, see Fig. 6.2. Consider the two sublattices, corresponding to even and odd sites. When the system is quenched from the Néel state $|0101...\rangle$, even sites initially cycle through the basis set $1 \rightarrow 2 \rightarrow 3...$ while odd sites are locked at 0 by the constraint. These sublattices exchange and the process repeats after a full precession $1 \rightarrow 0$ has been completed. This trajectory is captured in Fig. 6.2, with

smaller oscillations present under the main peaks, which emerge due to the longer range hoppings present in the single site clock operator, i.e., $\langle n + d|C|n \rangle \neq 0$.

6.3 Additional scarred models via kinetic constraints

6.3.1 Larger spin PXP models

It is apparent that larger spin generalisations of the PXP model may be obtained via the construction outlined in Section 6.1. Similar to the spin-1/2 PXP model, these are models of the form:

$$H = \sum_j P^0_{j-1} X_j P^0_{j+1} \tag{6.15}$$

However the local Hilbert space dimension, N_c, is now arbitrary, with X_j being a spin-s ($s = (N_c - 1)/2$) representation of the X element of an su(2) Lie algebra. P^0_j is still to be understood as being a projector onto the spin down state, that is, the state $|0\rangle$ corresponds to the lowest weight eigenstate of Z_j. Given the eigenvalues of X_j are equidistant, it follows that $U(t) = e^{-iX_j t}$ is a periodic unitary $U(t+T) = U(t)$ for some T, such that Hamiltonians of the form Eq. (6.15) follow from our general construction.

Ref. (47) has studied a semiclassical limit of larger spin-s PXP models using the time dependant variational principle (TDVP), as discussed in Section 3.1. Periodic revivals were numerically demonstrated for $s = 1, 2$. Indeed, using exact diagonalisation, we verify that large spin-s PXP models exhibit quantum many-body scarring. Fig. 6.3 shows the fidelity revivals observed in spin-s PXP models initialised in the Néel state $|0, N_c - 1, 0, N_c - 1, ...\rangle$ for system size $N = 12$. Revivals in the many-body wavefunction persist to larger s, though the amplitude of revivals decays as s increases. This is likely due to the growing Frobenius norm of the error δ of the broken Lie algebra, as defined in Eq. (4.6). Indeed one can understand this fact intuitively, as the projection onto a single basis state, the spin down state, becomes a stronger constraint as the local Hilbert space dimension
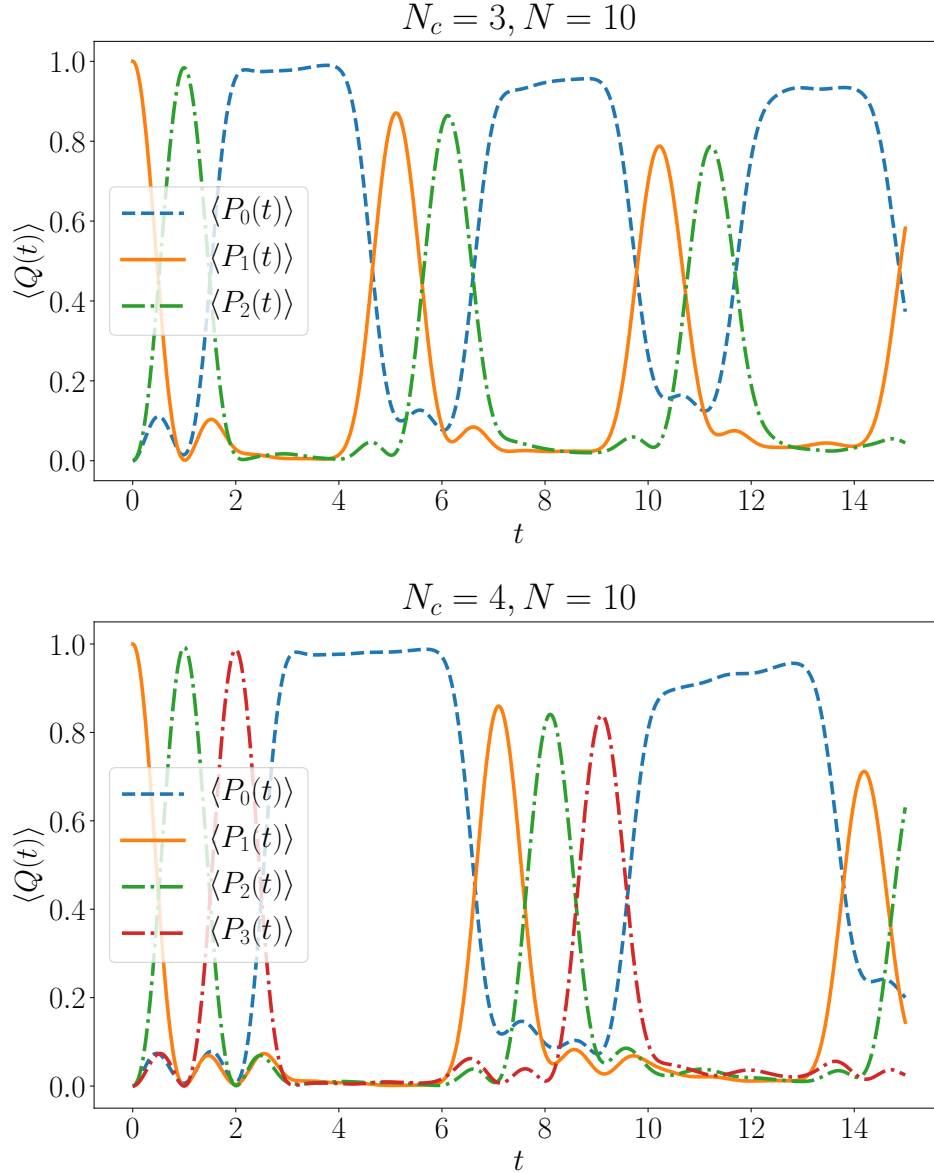
Figure 6.2: Time evolution of local observables when the PCP model is quenched from the Néel state $|0101...\rangle$. Plots show the time evolution of the average colour on a given site, $\langle P^n(t)\rangle$, as a function of time. Top plot is for $N_c = 3$ and bottom plot is $N_c = 4$, with system size $N = 10$. A period of free precession can be observed where the sublattice containing 1 cycles through the clock basis, followed by a period of time where the colour on the site is locked to 0 while the other sublattice cycles through the clock basis.
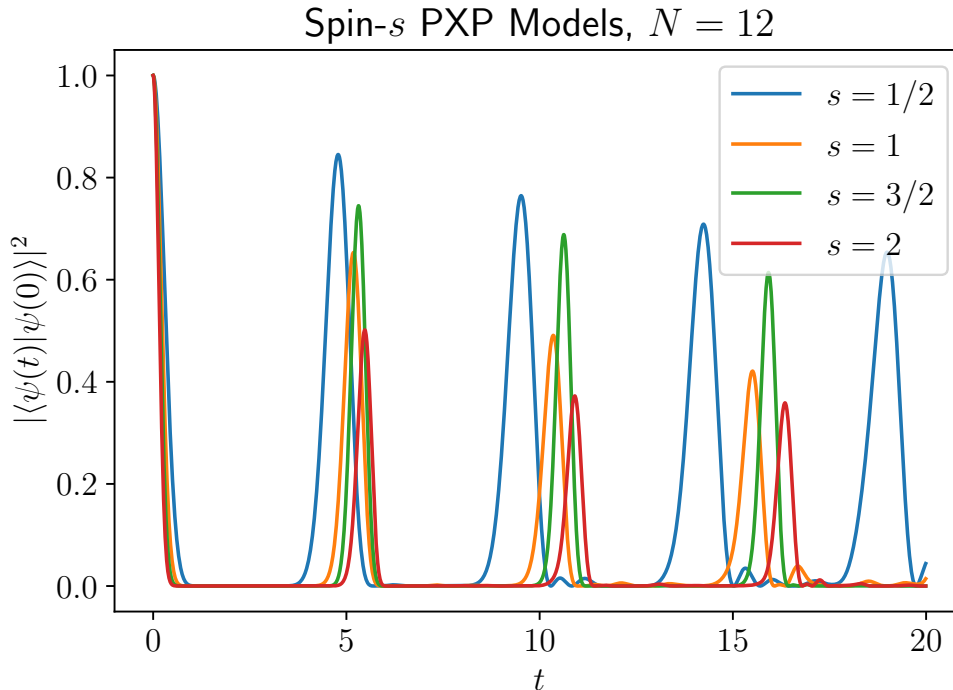
Figure 6.3: Fidelity revivals in the many-body wavefunction observed in arbitrary spin-s PXP models, initialised in the Néel state $|0, N_c - 1, 0, N_c - 1, ...\rangle$. Results for system size $N = 12$. Spin-s PXP models exhibit quantum many-body scarring and as such realise oscillatory dynamics in the many-body wavefunction for arbitrary s. Amplitude of revivals decays as s increases, and this is believed to be due to a growing error in the broken Lie algebra (Chapter 4).

grows, which results in larger spin-s PXP models being further from an exact SU(2) symmetric model. Fig. 6.4 shows the overlap of eigenstates of the $s = 2$ and $s = 5/2$ PXP models with the Néel states, where one can observe a band of $2sN + 1$ scarred eigenstates responsible for the oscillatory dynamics when the system is initialised in these states.

Relation between spin-s PXP and clock models

Both spin-s PXP model and $N_c = 2s + 1$ coloured PCP clock models are obtained from our construction in Eq. (6.2) by taking $k = -s, ..., s$, such that the unconstrained models have the same spectrum. Indeed, the spin X operator and the clock operator C are equivalent by a change of basis. The distinction between the

constrained clock and spin models therefore lies entirely in the kinetic constraint, i.e., the choice of the projector $P = |\phi\rangle\langle\phi|$.

By performing a basis rotation, the clock Hamiltonian can be expressed in the spin basis, $H_{\text{clock}} = \sum_j P'_{j-1} X_j P'_{j+1}$, where P' corresponds to a rotation of the projector P^0 in Eq. (6.6). To give an explicit example, at $N_c = 3$, we find:

$$H_{clock} = \sum_n P^0_{n-1} C_n P^0_{n+1}, \quad P^0 = \begin{pmatrix} 1 & 0 & 0 \\ 0 & 0 & 0 \\ 0 & 0 & 0 \end{pmatrix} \tag{6.16}$$

$$= \sum_n P'_{n-1} X_n P'_{n+1}, \quad P' = \begin{pmatrix} 1/6 & 1/3 & -1/6 \\ 1/3 & 2/3 & -1/3 \\ -1/6 & -1/3 & 1/6 \end{pmatrix}. \tag{6.17}$$

We have numerically found that the number of scarred states remains the same for PXP models expressed in terms of either the spin P^0 or P'; however, for N_c-odd the amplitude of the revivals is always higher when using P' instead of P^0. One can see why this occurs by inspecting the overlap of the initial state with the eigenstates of the system, as shown in Fig. 6.4. The scarred eigenstates remain better separated from the thermal bulk in the clock models for odd N_c when compared to the spin models, resulting in better fidelity revivals. Thus, our construction shows how to improve the revivals in the standard PXP models by modifying the kinetic constraint. In addition, when using P', mapping to the clock representation allows to clearly delineate nearly-free precession from the interacting part of the dynamics, which is not transparent in the spin representation.

6.3.2 Chiral clock models

Our construction additionally yields a new class of scarred models, for which C is not related to spin or clock models via a change of basis. We refer to this class of models as 'chiral clock models' (CCM). Here we give a definition of the models and present numerical results verifying they host quantum many-body scars.

CCM models emerge in analogy with the quantum Ising model in a transverse
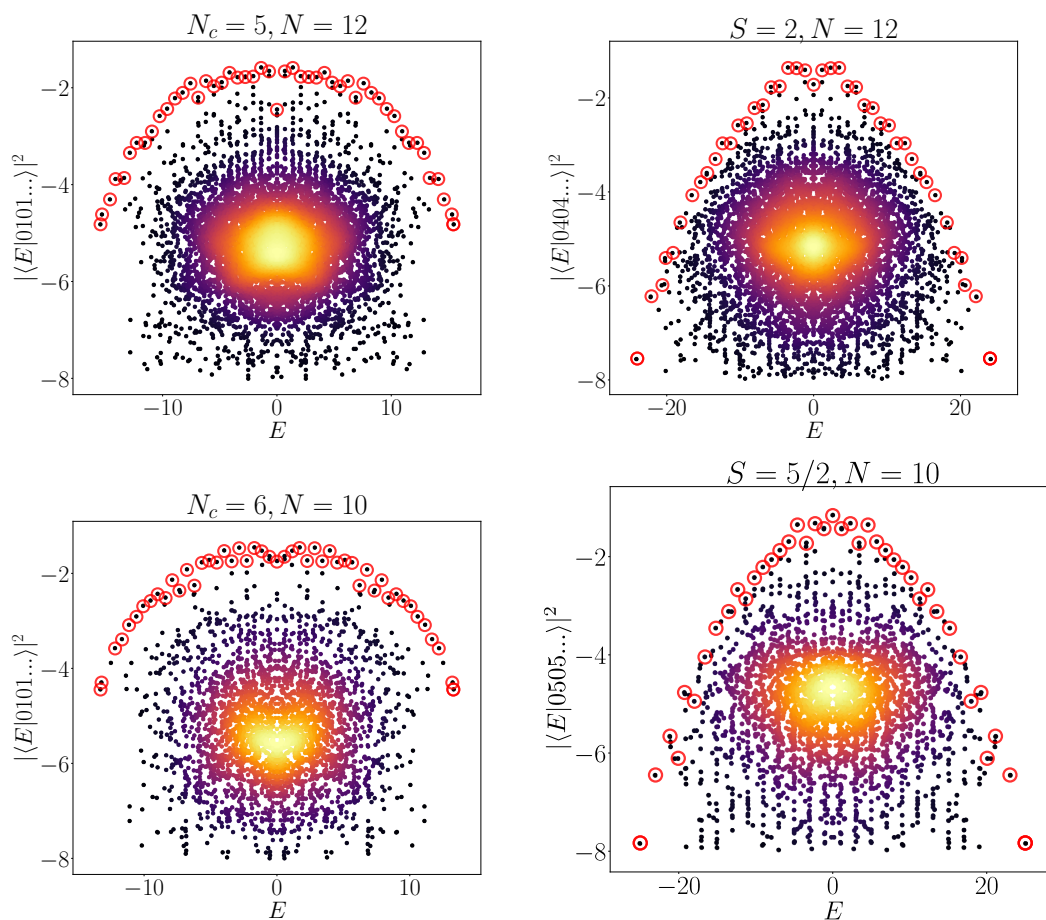
Figure 6.4: Comparison of the scarred band of states for 5-colour clock model and PXP spin-2 model. Each plot shows overlap of all eigenstates with the product state $|0404\ldots\rangle$. While the total number of scarred states is the same in the two models, the shape of the scarred band is different. The larger degree of separation between the scarred eigenstates and thermal bulk in the clock models as compared to the spin models results in better fidelity revivals in clock models.

6. SYSTEMATIC CONSTRUCTION OF QUANTUM MANY-BODY SCARS USING KINETIC CONSTRAINTS

field (6, 36). Instead of focusing on critical properties of such models, we mainly focus on their fixed point, where only a shift operator is present in the Hamiltonian. The first non-trivial case that is distinct from our clock operators occurs for $N_c = 4$ CCM (36), with the Hamiltonian defined as:

$$H = f \sum_{j=1}^{N} \tau_j^\dagger e^{-i\phi} + J \sum_{j=1}^{N-1} \sigma_j^\dagger \sigma_{j+1} e^{-i\theta} + h.c, \qquad (6.18)$$

The operators σ and τ generalise the spin-1/2 Pauli matrices, σ_z and σ_x, respectively. They are given by

$$\sigma_j = \begin{pmatrix} 1 & 0 & 0 & 0 \\ 0 & \omega & 0 & 0 \\ 0 & 0 & \omega^2 & 0 \\ 0 & 0 & 0 & \omega^3 \end{pmatrix}, \qquad \tau_j = \begin{pmatrix} 0 & 1 & 0 & 0 \\ 0 & 0 & 1 & 0 \\ 0 & 0 & 0 & 1 \\ 1 & 0 & 0 & 0 \end{pmatrix}, \qquad (6.19)$$

where (for $N_c = 4$) we have $\omega = i$. Taking $J = 0$, $\phi = -\pi/2$, the Hamiltonian in Eq. (6.18) becomes non-interacting, with the on-site Hamiltonian reducing to:

$$H^{site} = \begin{pmatrix} 0 & -i & 0 & i \\ i & 0 & -i & 0 \\ 0 & i & 0 & -i \\ -i & 0 & i & 0 \end{pmatrix}. \qquad (6.20)$$

We construct an interacting CCM model hosting quantum many-body scars by introducing the same Rydberg-like constraint:

$$H_{chiral} = \sum_j P_{j-1}^0 H_j^{site} P_{j+1}^0, \qquad (6.21)$$

where as usual $P_j^0 = |0_j\rangle\langle 0_j|$. This Hamiltonian can be obtained via our construction in Eq. (6.2) by choosing choosing $k = -2, -1, -1, 2$.

The $N_c = 4$ kinetically constrained CCM model in Eq. (6.18) exhibits two types of oscillatory behaviour: quenches from $|0202...\rangle$ result in slowly decaying fidelity revivals, while quenches from $|1010...\rangle$, $|3030...\rangle$ essentially freeze out the

0 sublattice and the system oscillates like a nearly free paramagnet, see Fig. 6.6.
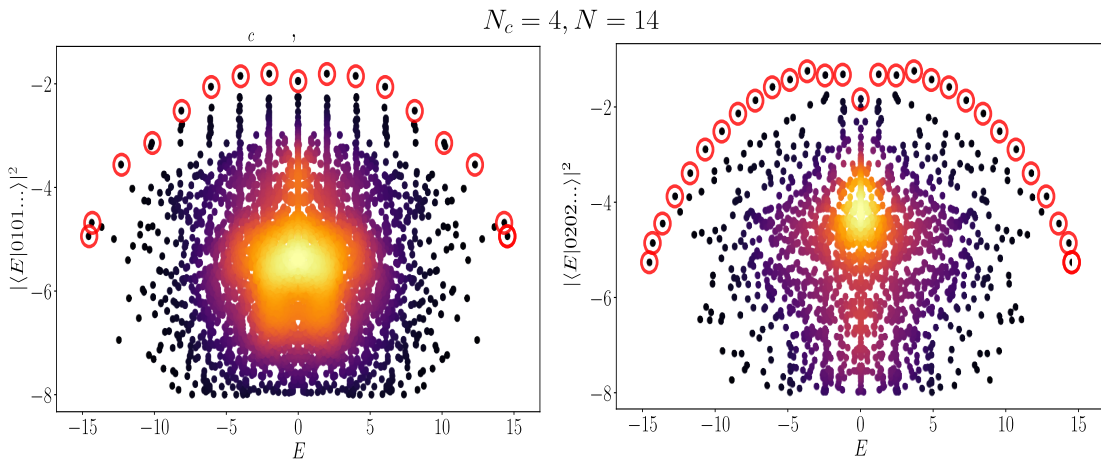
Figure 6.5: Overlap of all eigenstates of the $N_c = 4$ CCM, Eq. (6.21), with product state $|0101\ldots\rangle$ (left) and $|0202\ldots\rangle$ (right). System size $N = 14$. $|0101...\rangle$ has $N + 1$ scars, while $|0202...\rangle$ has $N + 2$ scars.

In Fig. 6.5 we plot the overlap of all eigenstates of the Hamiltonian in Eq. (6.21) with two product states states: $|1010\ldots\rangle$ (left) and $|2020\ldots\rangle$ (right). System size is $N = 14$ with periodic boundary conditions. These plots show that the model is not completely ergodic and supports a band of scarred states. However, the scarred bands look rather different in the two cases, with a stronger clustering of eigenstates into towers for the case of $|1010\ldots\rangle$ state. This stronger preservation of a perfect tower structure for the $|1010\ldots\rangle$ suggests the broken su(2) Lie algebra responsible for oscillations from the $|1010...\rangle$ state has a smaller error, Eq. (4.6), hinting at why oscillations are more robust from this state. We note that the structure of the scarred band in the right panel of Fig. 6.5, corresponding to the state $|2020...\rangle$, is quite reminiscent of the PXP spin-1/2 model (131). In fact, as we show next, the dynamics in this case reduces to the same type of oscillation that was found in the PXP spin-1/2 model.

Fig. 6.6 shows the single-site precession of H^{site} in the absence of a constraint. We see that the dominant dynamics is $0 \to 2$ flips and $1 \to 3$ flips. Thus, when the constrained model, dressed with P^0, is quenched from $|0101...\rangle$, the dominant dynamics is just oscillation between $|0101...\rangle \to |0303...\rangle$, as $0 \to 2$ is blocked due to the constraint. Neglecting leakage, this is just a decoupled free paramagnet,
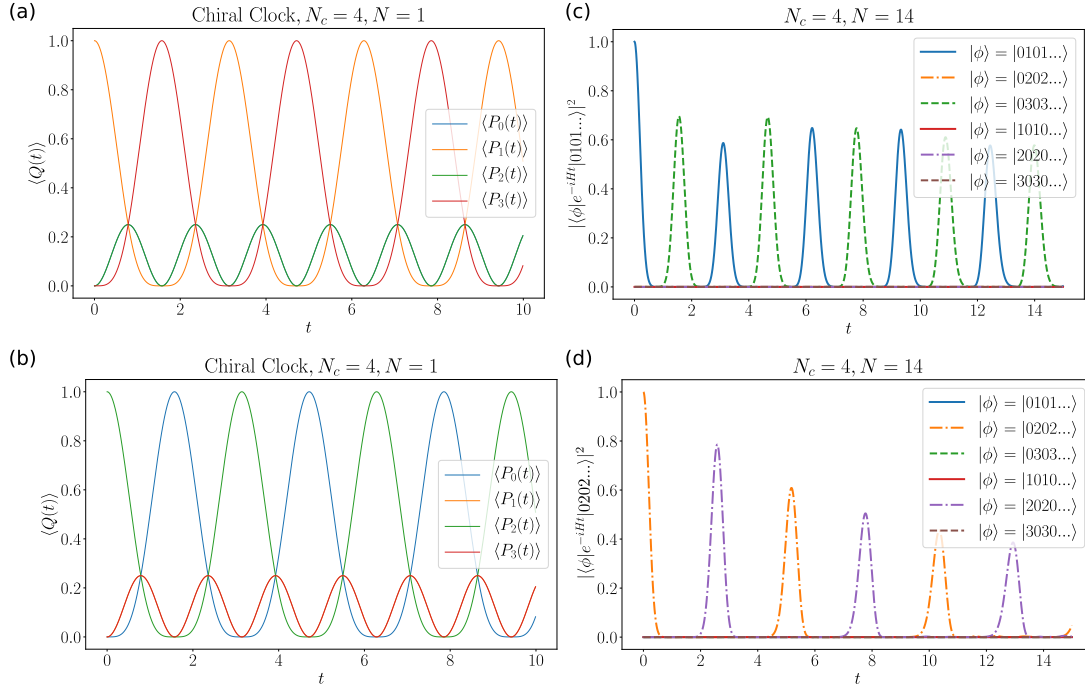
Figure 6.6: Dynamics of chiral clock models, exhibiting QMBS. Left column: Single site precession of the unconstrained H_{site} model in Eq. (6.20). The dominant dynamics is $0 \to 2$ flips and $1 \to 3$ flips. Right column: Fidelity of revivals in CCM, Eq. (6.18), from the initial states $|1010\ldots\rangle$ (top) and $|2020\ldots\rangle$ (bottom). System size $N = 14$. The plots show $|\langle\phi|\exp(-itH)|\psi_0\rangle|^2$, where for $|\phi\rangle$ is any of $|n0n0\ldots\rangle$, $n = 1, 2, 3$, and their translated copies, $|0n0n\ldots\rangle$.

where every other site precesses freely. However, when quenched from $|0202...\rangle$, a transition through the polarised state $|0000...\rangle$ is permitted and we see transitions like $|0202...\rangle \to |2020...\rangle$, reminiscent of spin-1/2 PXP.

We confirm this by studying the fidelity time series, shown in Fig. 6.6, for the two initial states, $|\psi_0\rangle = |1010\ldots\rangle$ (top) and $|\psi_0\rangle = |2020\ldots\rangle$. To get a clearer insight into the dynamics, we plot the generalised fidelity, $|\langle\phi|\exp(-itH)|\psi_0\rangle|^2$, where for $|\phi\rangle$ we do not necessarily pick the initial state, but any $|n0n0\ldots\rangle$, $n = 1, 2, 3$, and their translated copies, $|0n0n\ldots\rangle$. Indeed, we observe when the system is quenched from $|1010...\rangle$, there is an initial shedding of fidelity followed by a relative perfect oscillation between the states $|1010...\rangle$ and $|3030...\rangle$. This dynamics is just a free precession of the decoupled spin-1/2 chain, with a small leakage. In contrast, $0 \to 2$ flips are permitted when quenching from the state

$|2020\ldots\rangle$. This allows the state to evolve through the polarised state $|0000...\rangle$ and exchange sublattices, undergoing oscillations between $|0202...\rangle \rightarrow |2020...\rangle$. This is precisely the same dynamics of spin-1/2 PXP, neglecting the leakage. As we see in Fig. 6.6, we obtain non-zero fidelity only with the states $|2020\ldots\rangle$ and $|0202\ldots\rangle$, suggesting that the 4-colour chiral clock model contains an embedded PXP spin-1/2.

Finally, we note that CCMs, as defined in Ref. (36), appear to have scars only in $N_c \leq 4$ cases. For odd $N_c \geq 5$, we did not find revivals from Néel-type initial states. However, we note that for N_c-even it is possible to construct a special case of our clock models by choosing $k_n \in \{-N_c/2, ..., -1, 1, ...N_c/2\}$. These models *do* appear to support scars, and for $N_c = 4$ this choice of k's reduces to CCM in Eq. (6.18). Nevertheless, for $N_c > 4$ longer range couplings are introduced and the models are no longer equivalent to Ref. (36). The scarring in these models can similarly be explained by studying the single-site free precession, where dominant cyclic transitions between basis states emerge, with cycles shorter than N_c.

6.4   Map of models hosting scarring

We now perform an extensive search for scarred models of the form Eq. (6.6) with a fixed kinetic constraint P^0. By considering models of the form Eq. (6.6) with arbitrary C (ie not obtained from our procedure of logging a unitary), we verify that models of this form which host QMBS are only those for which $e^{-iCT} = \mathbb{I}$, justifying our original assumption for the construction of scarred models. By varying the matrix elements of C, we map out a diagram of scarred models based on the robustness of scars, inferred from the first revival maximum of the fidelity from the Néel-like states. We restrict the matrix C to be purely imaginary and off diagonal, as this preserves the desired particle-hole symmetry.

6.4.1 $N_c = 3$ Scarred models

For $N_c = 3$, it is straightforward to visualise the entire span of models of the form Eq. (6.2) with fixed projector P^0 and C purely imaginary and off diagonal. There are two couplings to vary, as by a rescaling of C we are free to fix the value
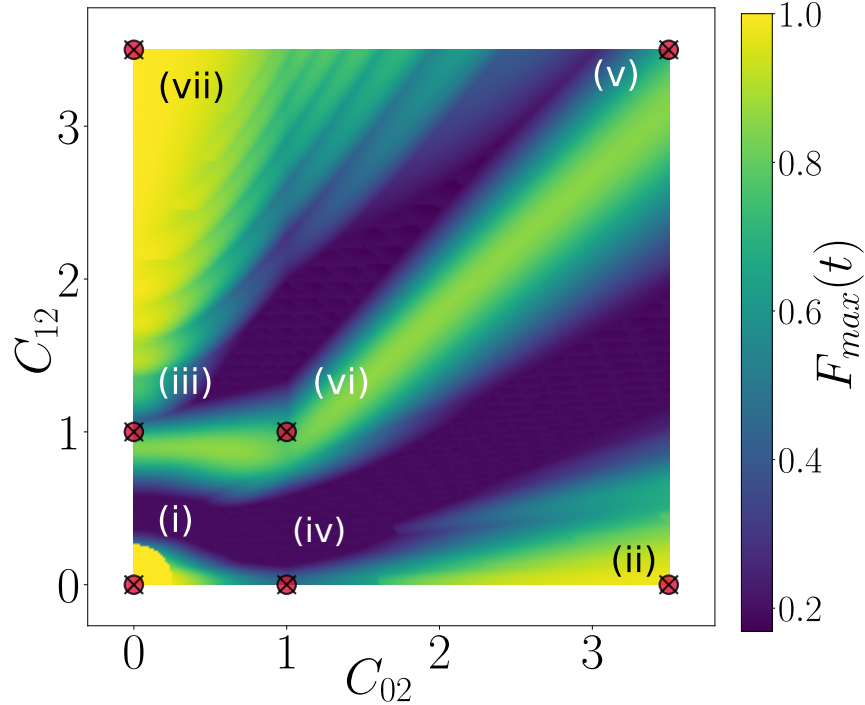
Figure 6.7: Kinetically constrained models of the form Eq. (6.2) with local Hilbert space dimension $N_c = 3$ which realise QMBS. Models were obtained by varying the two matrix elements, C_{02} and C_{12}, Eq. (6.22). Since the matrix elements are assumed to be purely imaginary, the label on each axis refers to the modulus of the corresponding matrix element. The colour scale indicates the average maximum of the first fidelity revival quenched from the Néel states $|0101\ldots\rangle$ and $|0202\ldots\rangle$. A value close to 1 indicates the presence of fidelity revivals and hence QMBS. These fidelity values were obtained at $N = 12$. All regions associated with strong scarring can be identified with either spin or clock models previously discussed.

of one of the three couplings. To be explicit, the form of C we consider is the following:

$$
C = \begin{pmatrix} 0 & -i & iC_{02} \\ i & 0 & iC_{12} \\ -iC_{02} & -iC_{12} & 0 \end{pmatrix}
\tag{6.22}
$$

The fidelity revivals for all possible models at $N_c = 3$ is shown in Fig. 6.7 as a function of C_{02} and C_{12} matrix elements. All the regions in the diagram that

have large fidelity revivals and hence display strong scarring can be interpreted as deformations of one of our previously discussed models. Specifically, in Fig. 6.7 we identify the representative points as: (i) and ii) are spin-$\frac{1}{2}$ PXP, (iii) is spin-1 PXP, with $P = |S_z = -1\rangle\langle S_z = -1|$, (iv) spin-1 PXP, with $P = |S_z = 0\rangle\langle S_z = 0|$, (v) spin-1 PXP, with $P = |S_z = 1\rangle\langle S_z = 1|$, (vi) $N_c = 3$-colour clock model, (vii) free paramagnet. From this we conclude that for the on-site Hilbert space dimension $N_c = 3$, for Hamiltonians of the form Eq. (6.6), the only scarred models are obtained by various ways one can constrain a free paramagnet. As mentioned in the previous section, the maximum fidelity of the clock model, 0.724, is greater than the spin-1 model, 0.653. This improvement in the revival fidelity is seen in all N_c-odd models. For example, at $N_c = 5$, $N = 10$, spin: 0.563, clock: 0.766. Thus, by constraining the free paramagnet with P' as opposed to P^0 leads to better revivals for N_c odd. Finally, although still expressible as spin models, the clock basis provides a much simpler interpretation of the dynamics, clearly showing a period of free precession followed by an interacting segment of the evolution.

6.4.2 $N_c = 3$ Scarred models

Next we consider the $N_c = 4$ case. Allowed deformations involve varying the 5 matrix elements in C, so we take slices where only two parameters are simultaneously varied. We consider two cases, (A) vary the next-nearest-neighbour hoppings $C_{02} = C_{13} = \alpha i$, while also varying $C_{03} = -\beta i$, or (B) switch off next-nearest-neighbour hoppings, while varying $C_{12} = -\alpha i$ and $C_{03} = -\beta i$. Explicitly:

$$C_n^{(A)} = \begin{pmatrix} 0 & -i & \alpha i & -\beta i \\ i & 0 & -i & \alpha i \\ -\alpha i & i & 0 & -i \\ \beta i & -\alpha i & i & 0 \end{pmatrix}, \tag{6.23}$$

$$C_n^{(B)} = \begin{pmatrix} 0 & -i & 0 & -\beta i \\ i & 0 & -\alpha i & 0 \\ 0 & \alpha i & 0 & -i \\ \beta i & 0 & i & 0 \end{pmatrix}. \tag{6.24}$$
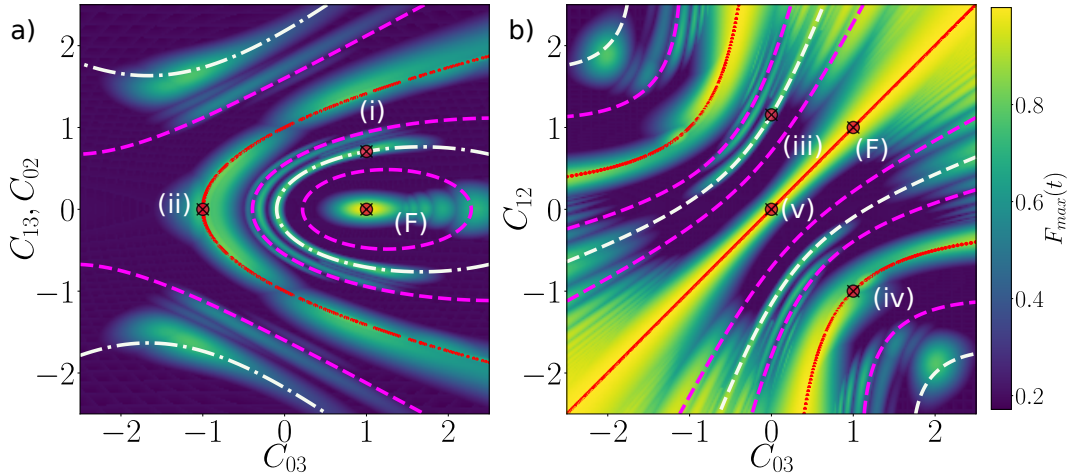
Figure 6.8: Kinetically constrained models of the form Eq. (6.2) with local Hilbert space dimension $N_c = 4$ which realise QMBS. Shown in (a), (b) are two slices of the parameter space obtained by varying the matrix elements of C, defined in the text. The colour scale represents the maximum of the first fidelity revival for quenches from any of the states $|0101\ldots\rangle$, $|0202\ldots\rangle$, $|0303\ldots\rangle$. A value close to 1 indicates robust fidelity revivals and hence strong scarring. Results are for system size $N = 10$. Labels on the diagrams refer to special limiting cases defined in the text. Scarred models can be accurately predicted based on the commensurability of the eigenvalue spectrum of C, as denoted by lines and explained in the text.

The maximum fidelity revivals of the many-bodied models Eq. (6.6) with local Hilbert space dimension $N_c = 4$ and C given above are shown in Fig. 6.8. These diagrams include several limiting cases at special values of (β, α). For variation (A), we have: (i) $(1, 1/\sqrt{2})$ is $N_c = 4$ clock; (ii) $(-1, 0)$ is $N_c = 4$ CCM model. For variation (B): (iii) $(0, 2/\sqrt{3})$ is spin-$\frac{3}{2}$ PXP; (iv) $(1, -1)$ is also $N_c = 4$ CCM; (v) at $(0, 0)$, we have $C = i\sum_{j=0,2} |j\rangle\langle j+1| - \text{h.c.}$, which (with P^0) can be viewed as the sum of a spin-$\frac{1}{2}$ PXP and a free $s = \frac{1}{2}$ paramagnet. Points marked F correspond to decoupled free paramagnets.

In contrast to N_c odd, the maximum fidelity at first revival for N_c-even is generally comparable between clock and spin-s PXP models. For example, for $N_c = 4$ in Fig. 6.8, $F_{max} \approx 0.761$ (clock) and $F_{max} \approx 0.783$ for spin-$\frac{3}{2}$ PXP. For $N_c = 6$ and $N = 8$, we obtain $F_{max} \approx 0.813$ (spin) and $F_{max} \approx 0.802$ (clock), while for $N_c = 8$, $N = 8$ we find $F_{max} \approx 0.793$ (spin) and $F_{max} \approx 0.806$ (clock).

Since the diagram in Fig. 6.8 is quite rich, we look for a simple guiding principle that predicts the most robust scarring models. The commensurability of the

eigenvalue spectrum of C provides such a criterion – see lines and dots in Fig. 6.8. Appendix A.3 contains an analytical derivation of the equations describing these lines. White lines mark the models for which C has equidistant energy levels, $E_n = k\epsilon$, $k \in \mathbb{Z}$. Our $N_c = 4$ clock model lies on one of these lines, as shown in Fig. 6.8(a). We can consider further commensurability conditions where the energy spacings of C are in simple ratios such as 1:2 (purple lines). Finally, red points mark the cases where C contains one pair of degenerate eigenvalues, $E = E_0, E_0, E_1, E_1$. One of these points is the $N_c = 4$ CCM at its fixed point in the disordered phase. Another one, along the diagonal in Fig. 6.8(b), hosts a combination of the free paramagnet and spin-$\frac{1}{2}$ PXP model. In fact, revivals in models lying on red lines are generically due to the model effectively becoming a free paramagnet when quenched from specific Néel like states, due to one of the sublattices being frozen out.

For all of the lines on Fig. 6.8 which predict the scarred regions, given the commensurability of the eigenvalue spectrum of C along these lines, it follows that $e^{-iCT} = \mathbb{I}$ for some T. In other words, along these lines of scarred regions, the operator C may be obtained from logging a periodic unitary and hence these models may be found via our general construction introduced earlier in this chapter. The numerical work presented in this chapter therefore justifies the assumptions of our construction. We note, however, that our simple criterion based on the non-interacting spectrum of C only serves as a rough indicator of scarring models, i.e., it overpredicts the number of models as one would expect from a single-particle criterion. The precise parameter values where such models are realised are determined by the non-trivial interplay between this condition and the kinetic constraint, i.e., P^0.

6.5 Summary

We have presented a systematic construction of non-integrable PCP models exhibiting quantum many-body scars and decaying wavefunction revivals. The construction is based on embedding local unitary precession, $U^T = e^{-iCT} = \mathbb{I}$, into an interacting quantum system. The obtained models are expressed in terms of kinetic constraints which arise in quantum simulators in the Rydberg block-

ade regime (7, 57, 127). Kinetic constraints of this kind also emerge naturally in lattice gauge theories, which have recently been realised in periodically driven optical lattices (42, 115). The strongest reviving models are predicted by considering the commensurability of C's eigenvalues. For odd N_c and equidistant eigenvalues for C, the obtained models revive better than the corresponding spin $s = (N_c - 1)/2$ PXP model. Rotating $C \to X$, $P \to P'$, our construction thus provides a prescription for improving PXP revivals. If we do not restrict to equidistant eigenvalues of C, our construction yields further families of scarred models not related to PXP by rotation. Further, clock models provide a simple physical picture of the underlying dynamics – a period of nearly free precession followed by an interacting bottleneck. This 'effective drive' is reminiscent of kicked systems, where mixed phase space dynamics (both recurrent and thermalising behaviour) can emerge due to the presence of a continuous spectrum in the Floquet operator (77).

Our construction of many-body scarred models utilising kinetic constraints is particularly useful as it does not require any knowledge of the underlying mechanism to be known to yield further scarred models. In particular, one does not need to decompose a Hamiltonian into a sum of broken Lie algebra generators or identify embedded subgraphs of the Hamiltonian adjacency matrix, which was how we constructed further scarred models in previous chapters. While we believe the mechanism of a broken Lie algebra is still ultimately responsible for scarring in models obtained via kinetic constraints, due to the nature of the projector dressing, Eq. (6.2), predicting scarred models based on the commensurability of eigenvalues of a single site operator is practically much simpler, as evidenced by the rich diagram of scarred models we have obtained in Fig. 6.8. Indeed, given the only scarred model to have been realised in experiment is the PXP model (7), it seems likely that scarred models of the form given in Eq. (6.2) may stand a better chance of being realised in experiment, in contrast to the scarred models with non-local interactions obtained in previous chapters.

Chapter 7

Realising scarred dynamics on quantum hardware

Until now we have been concerned with the mechanisms which give rise to quantum many-body scars, in particular approximate scars, and have used these insights to construct new models exhibiting weak ETH violation. The purpose of this chapter, based on currently unpublished work, is to realise the dynamics of a scarred model experimentally, by utilising current noisy-intermediate scale quantum (NISQ) devices (11). Fault-tolerant quantum computers with large number of qubits which utilise error-correction (103) do not currently exist. However, NISQ devices with a few qubits are already being used to simulate quantum systems (2, 13, 84). Taking advantage of NISQ hardware in the context of many-body quantum systems (11) is an exciting prospect, nevertheless, given the lack of reliable error-correction (141), one issue in this approach is to identify candidate problems which are sufficiently interesting to warrant their implementation, while being sufficiently simple such that their implementation does not exceed current hardware limitations.

Quantum many-body scarred systems seem perfectly suited to NISQ devices: although these systems feature interesting collective phenomena, the dynamics when the system is initialised in special states, with large support on the scarred eigenstates, is a relatively simple oscillation with suppressed growth of entanglement entropy. The suppressed entropy growth exhibited during scarred dynamics

is particularly appealing from the perspective of NISQ hardware, as it suggests the states the system evolves into are weakly entangled, such that a shallow depth unitary circuit should be sufficient to describe them. In this chapter we focus on implementing the dynamics of the PXP model, initialised in the Néel state, on current quantum hardware. We begin by providing a numerical justification, using classical matrix product state (MPS) techniques (24, 113), for why we expect the dynamics of the PXP model to be simulable on current quantum devices. We then proceed to introduce a variational quantum algorithm (20, 35) to simulate time evolution on NISQ devices. We note we have previously used the same variational approach to successfully simulate a geometric quench of a fractional quantum hall system (FQH)) (62, 94). This approach was also fruitful for the FQH system due to suppressed entropy growth during dynamics, although the origin of this suppression for the FQH system, emerging from the geometric quench (41, 44, 142), is distinct from QMBS . Using our variational algorithm, we obtain dynamical results pertaining to the PXP model from current state of the art quantum hardware. Quantum computers have currently being implemented using a variety of architectures, such as IBMQ's superconducting qubit platform (52) and IONQ's trapped ion platform (54). Both of these platforms have shown promise in the implementation of quantum algorithms (37, 38, 39, 83, 122, 136). We will use IONQ's trapped-ion architecture (26) to implement the dynamics of the PXP model. The all-to-all connectivity of the trapped ion qubits (26) make this architecture appealing as we will consider the PXP model with periodic boundary conditions.

7.1 Numerical justification for quantum simulation of the PXP model

Implementing quantum algorithms on current quantum hardware essentially constitutes designing unitary quantum circuits which will be applied to a set of qubits (20). Each device will have a particular gateset for which the unitary circuit must be composed from. For example, common single qubit gates include Pauli rotations and Hadamard gates, while common two qubit entangling gates include

controlled NOT (CNOT) gates and swap gates (85), see Fig. 7.1. Circuit libraries including compilers exist, such as *Qiskit* (53) and *pyTKET* (98), which abstract away the details of particular gatesets for specific devices. This frees the end user to focus on designing the unitary circuits, while the compiler will decompose the circuit into one and two qubit gates which are available on the desired device the circuit is to be ran on. Throughout this chapter we use the *Qiskit* circuit library.

(a)

$$R_\alpha(\theta)$$

$$R_\alpha(\theta)|\gamma\rangle = e^{-i\sigma^\alpha\theta/2}|\gamma\rangle$$

(c)

$$Cx_{(0,1)}|00\rangle = |00\rangle$$
$$Cx_{(0,1)}|01\rangle = |01\rangle$$
$$Cx_{(0,1)}|10\rangle = |11\rangle$$
$$Cx_{(0,1)}|11\rangle = |10\rangle$$

(b)

$$H$$

$$H|0\rangle = \frac{1}{\sqrt{2}}(|0\rangle + |1\rangle)$$
$$H|1\rangle = \frac{1}{\sqrt{2}}(|0\rangle - |1\rangle)$$

(d)

$$\text{SWAP}|00\rangle = |00\rangle$$
$$\text{SWAP}|01\rangle = |10\rangle$$
$$\text{SWAP}|10\rangle = |01\rangle$$
$$\text{SWAP}|11\rangle = |11\rangle$$
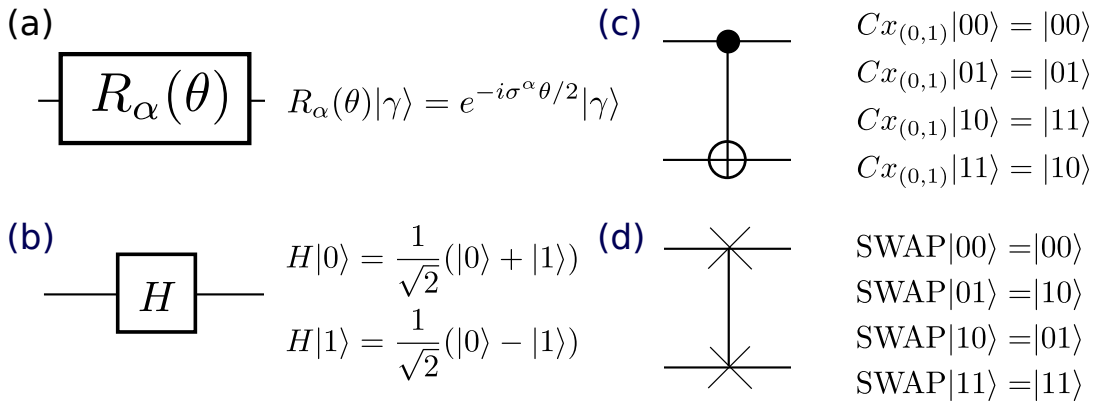
Figure 7.1: Definitions of various quantum gates used throughout this chapter. (a) is a single qubit Pauli rotation, where σ^α are the standard Pauli matrices for a spin half representation of su(2). (b) is a Hadamard gate, (c) a controlled not (cNOT) gate, with control on the 1st site and action on the 2nd site and (d) a swap gate. (c) and (d) are multi-qubit entangling gates, and the presence of such gates is the primary contribution to the hardware error on current NISQ devices (11), therefore one should try to minimise the number of these gates in a given circuit ansatz.

The primary limitation of current quantum devices is the quality of qubits, notably their effect on the fidelity of multi-qubit entangling gates. Gate fidelity, in the context of quantum computing, refers to how close the experimentally realised state, upon application of a quantum gate, is to the state that is to be expected in theory. It is quantified by the overlap of the expected state with the experimentally realised state. We refer to deviations from expected results due to gate fidelity as *hardware error*. Generally, the application of single qubit gates have a high fidelity and do not greatly contribute to hardware errors. It is only the application of multiple qubit entangling gates which are noisy. Therefore, for NISQ hardware, the likelihood a quantum circuit will produce sensible results as

opposed to pure noise is inversely proportional to the number of entangling gates present in the circuit, or, alternatively, the circuit depth. To take advantage of current NISQ hardware, it is essential to utilise shallow depth circuit, limiting the number of entangling gates.

We propose that if a many-body quantum system exhibits dynamics featuring suppressed entropy growth, as is the case for quantum many-body scarred models, then there will exist a shallow depth unitary circuit which is capable of describing the time evolution of the system. This follows from the fact that the entropy of a matrix product state (MPS) is bounded by it's bond dimension (24, 113). Therefore a weakly entangled state with relatively low entropy will be well approximated by a low bond dimension MPS. But a low bond dimension MPS state is equivalent to a low bond dimension matrix product operator (MPO) acting on a product state, which in turn is equivalent to a shallow depth unitary circuit acting on a product state.

Throughout the remainder of this section we provide explicit numerical evidence that a shallow depth unitary circuit should be sufficient for simulating scarred dynamics in the PXP model, by utilising the time-evolving block decimation (TEBD) algorithm (113). TEBD evolves a system by applying a trotterised matrix product operator, followed by a singular value truncation (113) of the resulting MPS down to the desired bond dimension. Accuracy of the TEBD algorithm is measured by the cumulative sum of discarded singular values, which we refer to as the truncation error. A small truncation error indicates the evolution obtained from TEBD is in close agreement with the true evolution of the system. If we were to evolve some system with TEBD, truncating to a *small* bond dimension, yet find a small cumulative truncation error, it follows that a small bond dimension MPS is capable of parameterising the evolved states. This would indicate a shallow depth unitary circuit should also be sufficient to describe the time evolved state.

Fig. 7.2 shows the TEBD cumulative truncation error as a function of system size and bond dimension for two quenches of the PXP model. Note, due to the nature of the TEBD algorithm (113), the PXP model considered in this plot has open boundary conditions. For clarity, the PXP model with open boundary
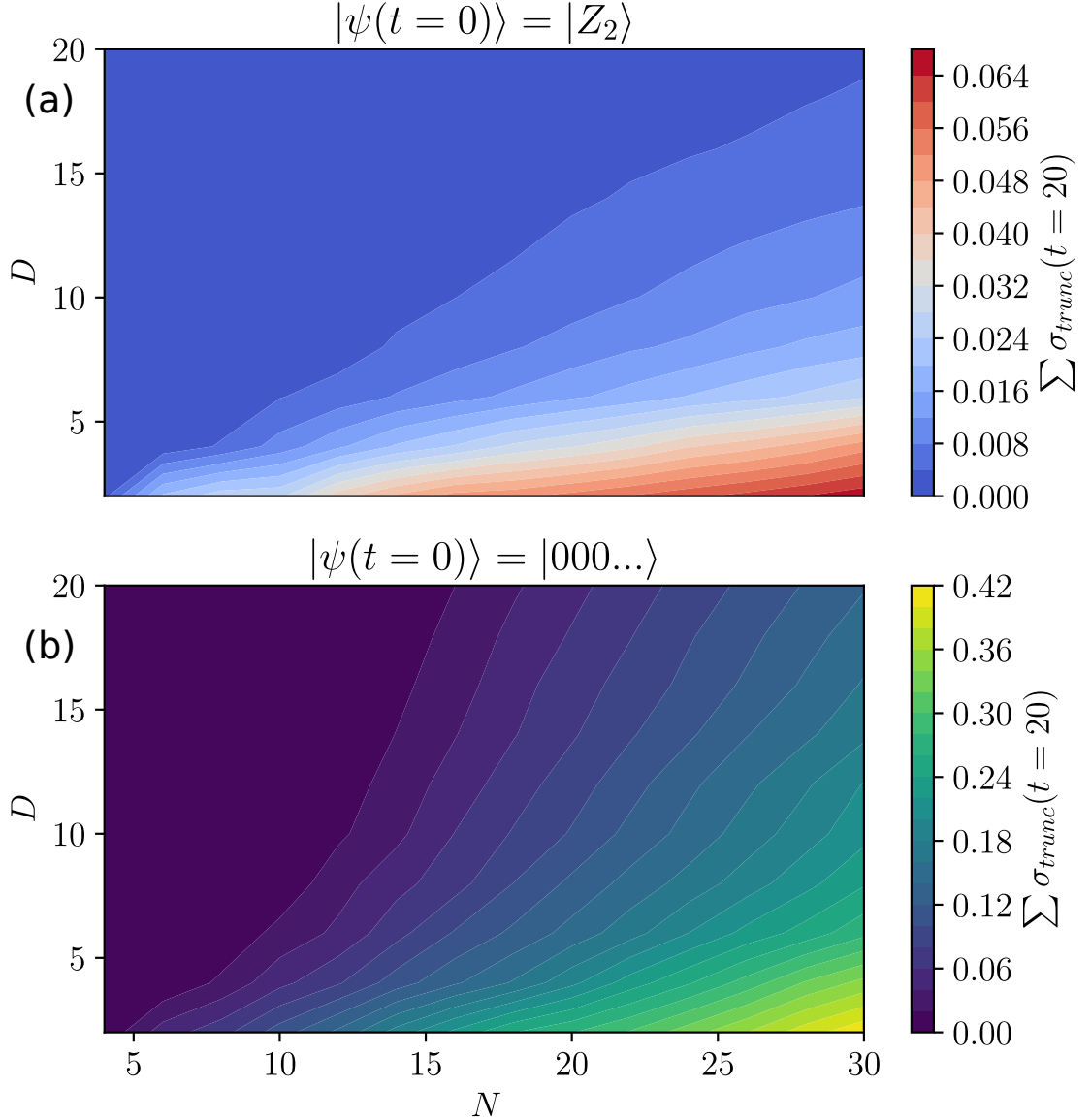
Figure 7.2: TEBD cumulative SVD truncation error at time $t = 20$, indicated by the colour scale, as a function of system size and bond dimension for the PXP model initialised in either the (a) Néel state $|10101....\rangle$ or (b) polarised state $|0000....\rangle$. The quench from the polarised state shown in panel (b) is generically thermalising, hence the truncation error becomes larger as entropy grows. However, the quench from the Néel state shown in panel (a) exhibits suppressed entropy growth and correspondingly has suppressed truncation error relative to a thermalising quench, indicating a low bond dimension MPO or equivalently a shallow unitary circuit should be able to express the time evolved states.

7. REALISING SCARRED DYNAMICS ON QUANTUM HARDWARE

condition has the following Hamiltonian:

$$H = \left(\sum_{n=1}^{N-2} P_{n-1} X_n P_{n+1} \right) + X_0 P_1 + P_{N-2} X_{N-1} \tag{7.1}$$

where the operators P, X have the same meaning as those given in Eq. (2.41). Throughout the remainder of this chapter all results will pertain to the PXP model with periodic boundary conditions, Eq. (2.41), only the TEBD results in Figs. 7.2, 7.3 correspond to open boundaries. However, given the negligible effect boundary conditions have as system size grows, the TEBD results still justify the use of shallow depth circuits for the PXP model with periodic boundaries.

Fig. 7.2(a) shows the TEBD truncation error when initialising the PXP model in the in the Néel state $|10101...\rangle$, which exhibits suppressed entropy growth. The quench shown in Fig. (7.2)(b) corresponds to initialising the PXP model in the polarised state $|000...\rangle$, which generically thermalises such that the entropy grows much faster. When quenching from the Néel state the truncation error for a fixed bond dimension D grows slowly with system size, relative to the thermalising quench from the polarised state. This indicates a shallow circuit should be sufficient to simulate dynamics at small system sizes. The truncation error, although growing slowly with system size, is however still growing, such that deeper circuits will be required for accurate simulations of larger systems. However, the necessary depth of a circuit which accurately captures the scarred dynamics will always be smaller than the depth of a circuit needed to capture thermalising dynamics at a given system size.

For example, shown in Fig. (7.3) is numerical results for the dynamics of the PXP model, up to time $t = 20$, from the two initial states $|000...\rangle$ and $|Z_2\rangle$ at system size $N = 72$. These results were obtained using the TEBD algorithm with bond dimension $D = 100$. Panel (a) shows the many-body fidelity, panel (b) the bipartite entanglement entropy and panel (c) the cumulative truncation error, which indicates how accurate the approximate evolution generated by TEBD is compared with the true evolution. When quenching from the Néel state, the truncation error with $D = 100$ remains small, indicating the simulated fidelity, including both the oscillatory and decaying components, are accurate up to the latest

7.1 Numerical justification for quantum simulation of the PXP model

time sampled. Note that while simulations of the PXP model using low bond dimension have been found to sufficiently capture the frequency of oscillations of the scarred dynamics (76), it is necessary to go to larger bond dimensions if one wants to capture the decaying component of the fidelity revivals. On the other hand, the truncation error of the thermalising quench from the polarised state $|000...\rangle$, obtained with $D = 100$ begins to grow significantly at time $t = O(10)$. This indicates the TEBD simulation with $D = 100$ is not accurate after $t \propto 10$ for the polarised state, whereas $D = 100$ was sufficient to accurately capture the scarred dynamics of the Néel state up to times $t > 20$. Understanding bond dimension as a measure of how deep a unitary circuit would be necessary for accurate simulation, these results indicate that scarred dynamics will always be more favourable to simulate vs thermalising dynamics on quantum hardware.
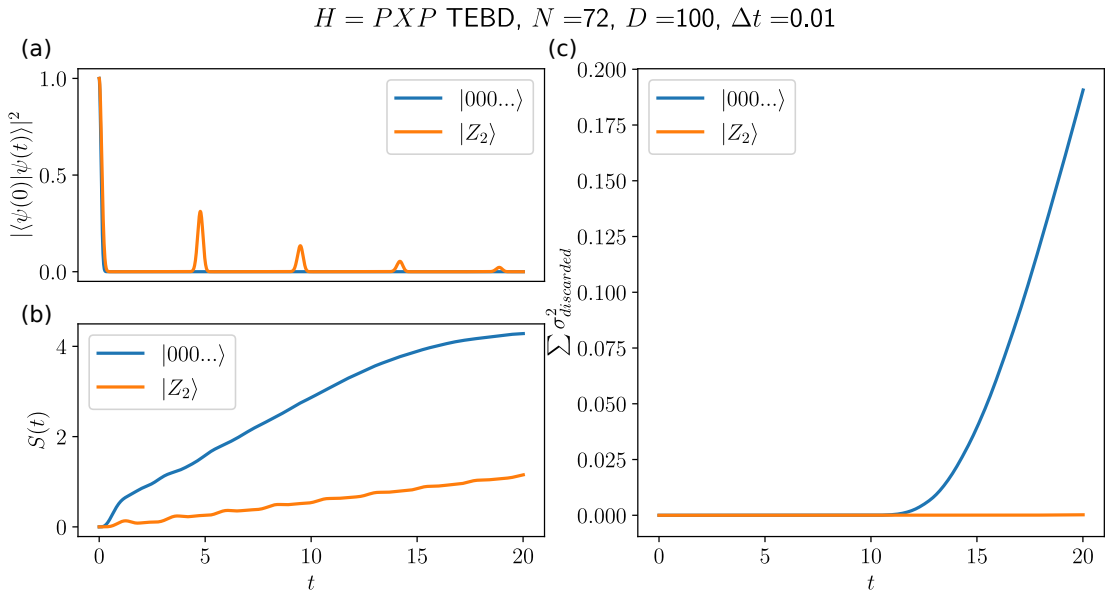
Figure 7.3: PXP dynamics (OBC) at large system size $N = 72$, obtained using the TEBD algorithm with bond dimension $D = 100$ and timestep $\Delta t = 0.01$. (a) is the many-body wave function fidelity, (b) the bipartite entanglement entropy and (c) the TEBD cumulative SVD truncation error. Even at such a large system size, we still observe suppressed growth of entropy and cumulative truncation error when the system is initialised in the Néel state $|1010...\rangle$, relative to a generically thermalising quench such as from the polarised state $|0000...\rangle$.

7.2   PXP quantum hardware implementation

We wish to construct a unitary circuit which approximates the action of the propagator for arbitrary times t:

$$e^{-iHt}|\psi(t=0)\rangle \approx U(L, \vec{x}(t))\,|000...\rangle \tag{7.2}$$

$\vec{x}(t)$ are time dependant variational parameters, whereas L is a fixed integer quantifying the depth of the circuit ansatz. The MPO which is equivalent to this variational circuit has bond dimension which scales exponentially in L (see Appendix A.4). Therefore increasing L should yield a more accurate simulation at later times, when entropy has grown.

There are two sources of error in this approach. First the simulation error, or how well this unitary circuit approximates the true action of the propagator. This error is independent of quantum hardware, and may be quantified by the co-moving fidelity:

$$C(L,t) = |U(L, \vec{x(t)})|000...\rangle - e^{-iHt}|\psi(t=0)\rangle| \tag{7.3}$$

To find the unitary circuit which best approximates the true dynamics, for every time t, we minimise the co-moving fidelity, treating $\vec{x}(t)$ as variational parameters. Note increasing L should lead to a smaller global minima from this optimisation procedure, due to the increasing bond dimension of the matrix product state manifold this ansatz is sampling.

In addition, there is also the hardware error, which will be affected by the specific platform we choose to implement the variational circuit ansatz on. While the quality of qubits and resulting gate fidelity is outside of our control, we can reduce this error by designing $U(\vec{x}(t))$ to minimise the number of multi-qubit entangling gates.

7.2.1 Variational circuit ansatz

To simulate the PXP model initialised in the Néel state, we use the following circuit ansatz:

$$U_{\text{PXP}}(L, \vec{x}(t)) = \prod_{l=1}^{L} \left[\prod_{i=0}^{N-1} e^{-iP_{i-1}X_iP_{i+1}\phi_i^l(t)} \right] \qquad (7.4)$$

Here $\phi_i^l(t)$ are time dependent variational parameters which are different at each site i and in each layer l. The local PXP phase gate present in this ansatz may be implemented as a Toffoli R_x rotation (doubly controlled Rx), see Fig. 7.4. Note however that this circuit will act on the polarised state $|000....\rangle$, Eq. (7.2). It follows that some of the controls in the first layer of this ansatz may be discarded, as they are automatically satisfied with respect to the state they are acting on. More specifically, both controls may be dropped from the first PXP phase gate (with phase $\phi_0^1(t)$), while a single control may be dropped from all other phase gates in the first layer except the last one, which requires two controls due to periodic boundary conditions (ie the controls may be dropped from the gates with phases $\phi_i^1(t), i \in [1, N-2]]$). Dropping these controls results in a decrease of the number of entangling gates, reducing the hardware error. We further reduce the CNOT count by using a particular decomposition of the Toffoli PXP phase gate utilising Hadamard gates (Fig. 7.4), such that each PXP phase gate contains 4 CNOTs. The total CNOT count of the ansatz after these considerations is:

$$\#_{\text{CNOT}}^{\text{PXP}}(N, L) = 2N(2L - 1) \qquad (7.5)$$

The circuit ansatz considered in Eq. (7.4) is inspired by a parameterised MPS ansatz used to simulate a semiclassical limit of the PXP model using the time dependent variational principle (TDVP) (76), which we discussed in Section 3.1. In the next section we will map the unitary circuit in Eq. (7.4) to an MPS representation to illustrate this connection. Furthermore the unitary circuit is structurally very similar to trotterisation (71, 92, 97). The structure of the trotterised propagator is equivalent to the variational circuit described in Eq. (7.4),
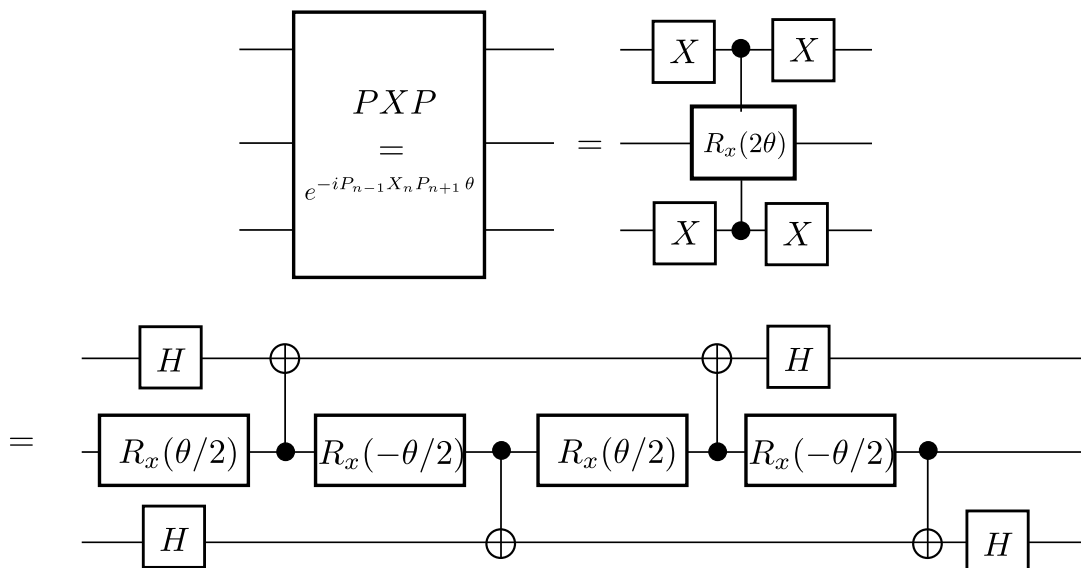
Figure 7.4: Decomposition of the local PXP unitary gate, used to implement the PXP variational ansatz, Eq. (7.4) on IONQ hardware.

with the trotter circuit corresponding to fixing all the variational parameters $\vec{x(t)} = t/L$. We find that allowing variational freedom in the phases greatly decreases the simulation error relative to typical trotterisation, without introducing any extra hardware error, due to the enhanced optimisation landscape.

7.2.2 Circuit ansatz MPS mapping: relation with PXP TDVP semiclassical limit

In this section we will demonstrate the single layer $L = 1$ variational circuit ansatz, Eq. (7.4), is equivalent to a MPS manifold previously considered to simulate a semi-classical limit of the PXP model using TDVP. This illustrates why the ansatz works well with only a few layers, as dynamics in the PXP model is known to be well approximated by an evolution constrained along a manifold consisting of small dimension MPS states (76).

To find the MPS state corresponding to the $L = 1$ circuit ansatz, consider the state produced by the $L = 1$ circuit explicitly:

$$|\psi(\vec{\phi})\rangle = e^{-i\phi_{N-1}P_{N-2}X_n}...e^{-i\phi_1 P_0 X_1}e^{-i\phi_0 X_0}|000...\rangle \tag{7.6}$$

As we are only considering an circuit of depth $L = 1$, the subscript l indicating the circuit layer of the variational parameters ϕ_l^i in Eq. (7.4) are redundant, so we drop them in the above notation.

Note here we consider the ansatz with open boundary conditions, in contrast to the periodic form used in Eq. (7.4). This is to make analytical calculations more tractable, but is sufficient to illustrate the relationship with the previously considered TDVP MPS ansatz (76), as the difference between boundaries becomes negligible for increasing system sizes.

We will construct a MPO corresponding to the application of this sequence of unitaries and from this it is trivial to construct the $L = 1$ MPS state. To cast the unitary circuit into the form of a matrix product operator we are seeking a parametrisation of the tensors W such that the following equality is satisfied:

$$U(\vec{\phi}) = e^{-iP_{N-2}X_{N-1}\phi_{N-1}}...e^{-iP_0X_1\phi_1}e^{-iX_0\phi_0} \tag{7.7}$$

$$\overset{!}{=} \sum_{\sigma,\theta} W_{L,\theta_1}^{\sigma_0\sigma_0'} W_{\theta_1\theta_2}^{\sigma_1\sigma_1'}...W_{\theta_{N-2}\theta_{N-1}}^{\sigma_{N-2}\sigma_{N-2}'} W_{R,\theta_{N-1}}^{\sigma_{N-1}\sigma_{N-1}'}|\sigma\rangle\langle\sigma'|$$

Here $|\sigma\rangle = |\sigma_0\sigma_1...\sigma_{N-1}\rangle$ are product states in the spin basis, such that σ_n correspond to physical indices of dimension 2, whereas θ_n correspond to the virtual indices of the MPO, whose dimension is the bond dimension (113).

This parametrisation may be be achieved if the tensors W take the following form, resulting in an MPO of bond dimensions $D = 2$:

$$W_L^{00} = (\cos\phi_0, 0), \quad W_L^{01} = (-i\sin\phi_0, 0)$$
$$W_L^{10} = (0, -i\sin\phi_0), \quad W_L^{11} = (0, \cos\phi_0)$$
$$W^{00} = \begin{pmatrix} \cos\phi_n & 0 \\ 1 & 0 \end{pmatrix}, \quad W^{01} = \begin{pmatrix} -i\sin\phi_n & 0 \\ 0 & 0 \end{pmatrix}$$
$$W^{10} = \begin{pmatrix} 0 & -i\sin\phi_n \\ 0 & 0 \end{pmatrix}, \quad W^{11} = \begin{pmatrix} 0 & \cos\phi_n \\ 0 & 1 \end{pmatrix}$$
$$W_R^{00} = (\cos\phi_{N-1}, 1), \quad W_R^{01} = (-i\sin\phi_{N-1}, 0)$$
$$W_R^{10} = (-i\sin\phi_{N-1}, 0), \quad W_R^{11} = (\cos\phi_{N-1}, 1)$$

Note the bond dimension of the MPO U^L grows exponentially as 2^L. We

verify in Appendix A.4 that the bond dimension of the MPS $U^L|000...\rangle$ also grows exponentially as 2^L, by explicitly verifying it is not possible for a SVD compression to be carried out on the state $U^L|000...\rangle$.

From the unitary MPO of the circuit ansatz $U(\vec{\phi})$. Eq. (7.7), one can read off the bond dimension $D = 2$ MPS corresponding to the state $|\psi(\vec{\phi})\rangle = U(\vec{\phi})|000...\rangle$. The resulting MPS takes the following form:

$$|\psi(\vec{\phi})\rangle = \sum_{\sigma,\theta} A^{\sigma_0}_{\theta_0} A^{\sigma_1}_{\theta_0\theta_1} A^{\sigma_2}_{\theta_1\theta_2} ... A^{\sigma_{N-2}}_{\theta_{N-3}\theta_{N-2}} A^{\sigma_{N-1}}_{\theta_{N-2}} |\vec{\sigma}\rangle \tag{7.8}$$

$$A^{\sigma_0=0} = (\cos\phi_0, 0), \quad A^{\sigma_0=1} = (0, -i\sin\phi_0)$$

$$A^{\sigma_n=0} = \begin{pmatrix} \cos\phi_n & 0 \\ 1 & 0 \end{pmatrix}, \quad A^{\sigma_n=1} = \begin{pmatrix} 0 & -i\sin\phi_n \\ 0 & 0 \end{pmatrix}$$

$$A^{\sigma_{N-1}=0} = (\cos\phi_{N-1}, 1), \quad A^{\sigma_{N-1}=1} = (-i\sin\phi_{N-1}, 0)$$

Given the MPS representation of our $L = 1$ circuit ansatz, Eq. (7.8), it is now possible to reveal the connection with a semiclassical limit of the PXP model obtained via TDVP. For simplicity, consider the ansatz in Eq. (7.8) with uniform angles $\phi_n = \phi \; \forall n$ and insert the following gauge transformation:

$$U = \begin{pmatrix} 1 & 0 \\ 0 & \sin\phi \end{pmatrix} \tag{7.9}$$

$$|\psi(\phi)\rangle = \sum_{\sigma}(A^{\sigma_0})^{\dagger}U^{-1}(UA^{\sigma_1}U^{-1})(UA^{\sigma_2}U^{-1})... \tag{7.10}$$

such that the boundary and bulk tensors are mapped to the new representation:

$$\tilde{A}^{\sigma_0} = U^{-1}A^{\sigma_0}, \quad \tilde{A}^{\sigma_{N-1}} = UA^{\sigma_{N-1}} \tag{7.11}$$

$$\tilde{A}^{\sigma_n} = UA^{\sigma_n}U^{-1} \tag{7.12}$$

It follows the $L = 1$ circuit ansatz with uniform angles is equivalent to the

following MPS representation:

$$\tilde{A}^{\sigma_0=0} = (\cos\phi, 0), \quad \tilde{A}^{\sigma_0=1} = (0, -i) \tag{7.13}$$

$$\tilde{A}^{\sigma_{N-1}=0} = (\cos\phi, \sin\phi), \quad \tilde{A}^{\sigma_{N-1}=1} = (-i\sin\phi, 0) \tag{7.14}$$

$$\tilde{A}^{\sigma_n=0} = \begin{pmatrix} \cos\phi & 0 \\ \sin\phi & 0 \end{pmatrix}, \quad \tilde{A}^{\sigma_n=1} = \begin{pmatrix} 0 & -i \\ 0 & 0 \end{pmatrix} \tag{7.15}$$

In the large N limit, this is equivalent to an infinite MPS previously used to study TDVP dynamics in the PXP model (76), for which a mixed phase space was observed. By permitting site-dependent angles ϕ_n and considering ansatz with $L > 1$, we expect our ansatz to improve upon the semi-classical approximation of PXP's scarred dynamics previously considered with TDVP.

7.3 Results

7.3.1 Classical benchmarking

We benchmark the performance of the variational ansatz introduced in Eq. (7.4) against the more conventional approach of trotterisation. For every time t, we perform an optimisation which minimises the co-moving fidelity, Eq. (7.3), using the SciPy minimisation package, in particular using the Nelder-Mead method. Trotterisation on the other hand has no free parameters, thus an optimisation is not necessary. For both approximate methods of evolution, we consider two layer ansatz ($L = 2$). The circuit depth of both the variational ansatz and trotterisation are equivalent, ensuring that each method of evolution would suffer from the same hardware error.

Fig. 7.5 shows the resulting dynamics, obtained with classical techniques (exact-diagonalisation), after obtaining optimal variational parameters, at system size $N = 6$. In the limit of exact agreement between the true evolution and approximate evolution, the co-moving fidelity $C(L = 2, t) = 1$ for all times. We find trotterisation is only accurate up to times of the $O(1)$, after which the co-moving fidelity decays away from 1. The variational ansatz on the other hand is found to accurately approximate the true dynamics up to the largest time sam-
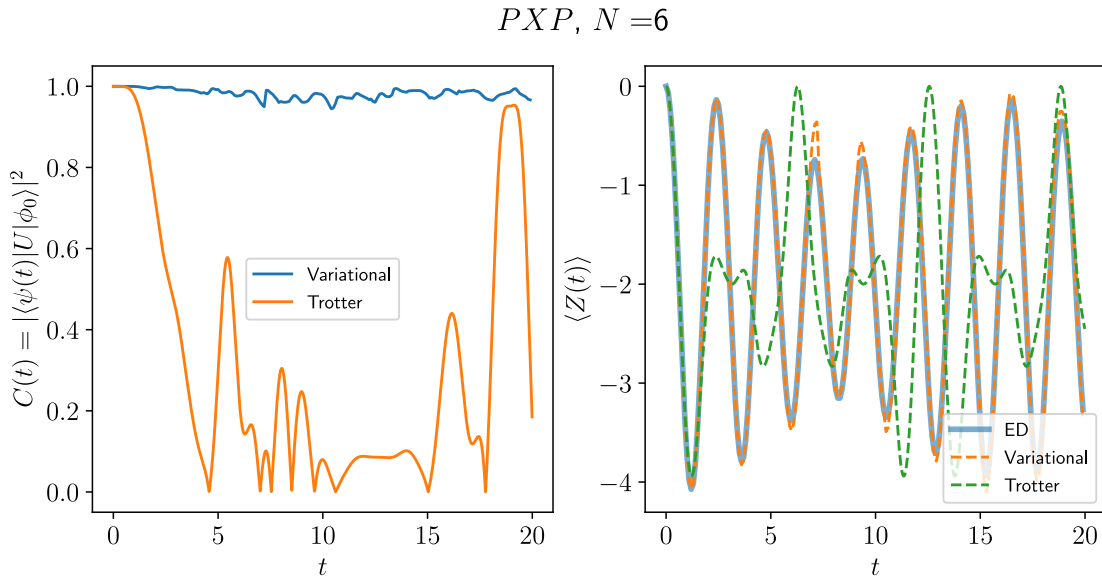
Figure 7.5: Classical benchmarking of the variational circuit ansatz, Eq. (7.4), with $L = 2$, for simulating scarred dynamics in the PXP model. Left plot corresponds to co-moving fidelity, which should equal 1 for perfect performance. The right plot shows a local observable ($Z = \sum_i Z_i$) and how well the various approximations agree with exact dynamics. Trotterisation (also with $L = 2$) is only accurate up to times O(1). While the variational circuit is the same depth as the trotter, it vastly outperforms trotterisation and provides a good approximation for dynamics, as expected from the suppressed entropy growth of these quenches.

pled, with $C(L = 2, t) \approx 1$. Although the variational ansatz is structurally the same circuit as the trotter circuit, the only difference being the phases of the local unitary gates, we typically wouldn't expect varying phases in the trotter circuit to lead to such a significant improvement in the quality of approximation. This procedure is working here due to the suppressed entropy growth, such that the expressibility of the variational ansatz, corresponding to a manifold of low bond-dimension MPS states, is sufficient to capture the trajectory.

Finally in Fig. 7.5 we also compute the dynamics of a local observable, namely the total Z magnetisation, $Z = \sum_i Z_i$. As expected, whenever the co-moving fidelity $C(L = 2, t) \approx 1$, there should be good agreement between true dynamics and approximate dynamics in any local observable. Indeed this is observed with the variational ansatz, where the co-moving fidelity remains close to 1. Furthermore, we find the variational ansatz is able to capture the decay of oscillations

observed in the PXP model, owing to the relevant low bond-dimension MPS manifold associated with the circuit ansatz.

7.3.2 Hardware result

We use IONQ's trapped-ion quantum computer to obtain the dynamics of the total Z magnetisation at $N = 6$ (Fig. 7.6). To obtain these results, we run the optimal variational circuits and measure either the wavefunction fidelity, Eq. (2.43) or the total Z magnetisation. Note it is only possible to measure the wavefunction fidelity here as the initial state is a simple product state $|Z_2\rangle = |1010...\rangle$, such that taking measurements in the Z basis is sufficient to compute this quantity. This process of applying the unitary circuit and performing measurements is repeated a number of times (known as the number of 'shots'), with the data then averaged over the shots to obtain the final result.

In general, as expected due to hardware error, we find mixed results from the quantum hardware. The best hardware result corresponds to the $L = 1$ variational Ansatz, showing good agreement between hardware result and exact diagonalisation results. In general, while increasing L should lead to an improvement in the agreement with exact diagonalisation, as demonstrated classically in Fig. 7.5, in practice, the $L = 2$ circuit performs worse than the $L = 1$ circuit, although it still captures the frequency of oscillations. This is due to the growing hardware error, as it appears the $L = 2$ ansatz has too large a circuit depth to give sensible results on current NISQ hardware. Therefore, although classical results indicate the variational ansatz is an efficient description of the dynamics for the PXP model, we find already at $N = 6, L = 2$ we are reaching the limit of the capabilities of current NISQ devices.

7.4 Summary

By taking advantage of the suppressed entropy growth typical of quantum many-body scarred systems, we have simulated the dynamics of one scarred model, the PXP model, on current NISQ hardware. Utilising a variational quantum algorithm and further optimising the obtained circuit for current NISQ hardware, by
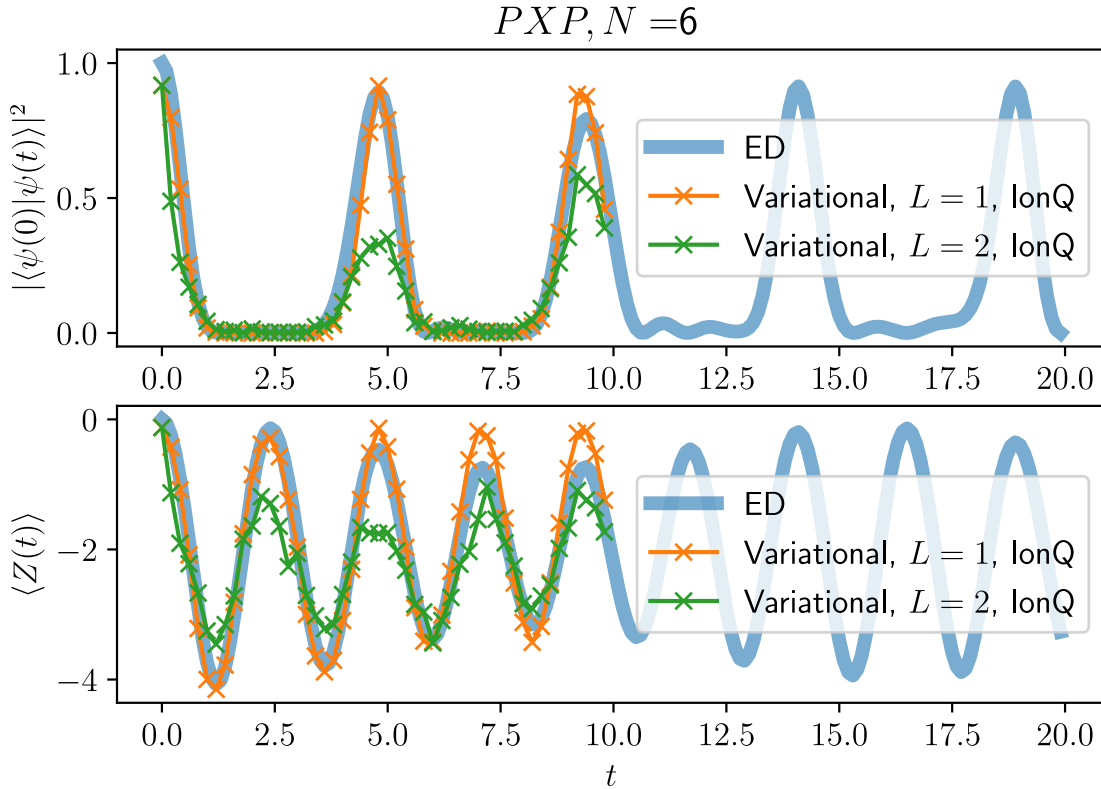
Figure 7.6: Hardware results of quench dynamics of the PXP model obtained from IONQ's trapped-ion quantum computer at $N = 6$, using 5000 shots. (Top) is the many-body wavefunction fidelity, Eq. (2.43). (Bottom) is the total Z magnetisation, $Z = \sum_n \sigma_n^z$. Bold blue lines correspond to results obtained from exact diagonalisation, such that they represent a benchmark for what a 'correct' result corresponds to. We see good agreement between hardware and theory with the $L = 1$ results, whereas the $L = 2$ results starts to deviate from the expected value. While deeper circuits (larger L) perform better in theory (see Fig. 7.5 for classical results), current qubits are too noisy so that adding additional layers to the ansatz actually makes performance worse.

removing redundant multi-qubit entangling gates and using a particular decomposition of the PXP phase gate (Fig. 7.4), we were able to obtain a time series of a local observable at $N = 6$ on IONQ's trapped ion platform, which has good agreement with theoretical results.

NISQ hardware is currently very limited as to what problems it can sufficiently handle. While we certainly have not demonstrated any quantum advantage (2) with our simulation, we believe quantum many-body scars are an interesting yet tractable problem to push the limits of current NISQ hardware. This is due in particular to the unique dynamical properties of quantum many-body scars - their suppressed entropy growth and coherent oscillatory revivals.

Chapter 8

Conclusions

Throughout this thesis, we have been concerned with the origin of quantum many-body scars, a mechanism for weak ergodicity breaking in which there exist a subset of ETH violating eigenstates in non-integrable models. The presence of these atypical scarred eigenstates result in the dynamics of QMBS systems being very sensitive to initial conditions; generic states thermalise and follow ergodic trajectories, whereas special initial states exhibit coherent oscillatory dynamics. This is in contrast to strong ergodicity breaking, as observed in integrable systems or in disordered models exhibiting many-body localisation, for which all initial states do not thermalise to canonical thermal values and all eigenstates violate the ETH.

As discussed in Chapter 3, two classes of QMBS models exist, 'exact scarred' models and 'approximate scarred' models. The former feature scarred eigenstates which are exactly equidistant in energy, resulting in oscillatory dynamics which persists up to arbitrarily long times. Approximate scarred systems on the other hand host scarred eigenstates which are only approximately equidistant in energy. As a consequence of this energy spacing and the fact that experimentally relevant initial states in approximate scarred systems also have non zero support on thermal eigenstates, oscillatory dynamics in these systems generally decay, although on timescales much longer than the thermalisation timescale. Nevertheless, approximate scarring is the only form of QMBS realised to date in experiment (7), and the first model studied which led to the discovery of QMBS, the PXP model, Eq. (2.41) , hosted approximate scarred eigenstates.

8. CONCLUSIONS

Exact scarred Hamiltonians, as a consequence of hosting eigenstates which are equidistant in energy, necessarily possess a spectrum generating algebra (SGA) with respect to some raising operator (Section 3.4.1). Scarred eigenstates are therefore generally much better understood in these models, as knowledge of this raising operator of the SGA typically allows one to construct analytical expressions for the scarred eigenstates (51, 112). For approximate scarred models, closed form expressions for the scarred eigenstates are typically not known, although high accuracy approximations to them have been constructed (23, 131).

In Chapter 4 we have proposed that approximate QMBS is a consequence of scarred Hamiltonians being proximate to some related system possessing a spectrum generating algebra. Specifically, we have introduced a theory of 'broken Lie algebras', where the spectrum generating algebra corresponds to the root structure of a Lie algebra. A broken Lie algebra consists of Lie algebra elements which satisfy the root structure of the appropriate conventional Lie algebra up to the inclusion of additional error terms, Eq. (4.6). We have introduced metrics which quantify this error and directly correlates with the quality of scarring, measured by the magnitude of wavefunction revivals. Hamiltonians of approximate QMBS are themselves elements of a broken Lie algebra. If no error terms were present in the commutation relations defining the Lie algebra, their Hamiltonians would fracture exactly into orthogonal integrable and non-integrable subspaces, due to a spectrum generating algebra. However, the presence of these error terms prohibits Hamiltonians of approximate QMBS systems from completely fracturing into this block diagonal form. Instead, they will host a 'loosely embedded' integrable subspace spanned by the scarred eigenstates which is coupled via sparse matrix elements to the orthogonal thermal subspace. This fracturuing provides a unifying framework in which the weak ergodicity breaking observed in QMBS models is similar to a high level of abstraction to other forms of weak ergodicity breaking, including Krylov-restricted thermalisation (80) and projector embedding techniques (119) (Fig. 3.2). Furthermore, we have proposed an iterative scheme which enables one to systematically derive perturbations to QMBS models which correct broken Lie algebras, providing a route to analytically connect approximate and exact scarred models.

Applying these insights to the PXP model, we have identified QMBS in this

model is a consequence of the PXP Hamiltonian being an element of a broken su(2) Lie algebra. Scarred eigenstates responsible for non-ergodic dynamics from the Néel state $|Z_2\rangle$ are found to reside in a 'loosely' embedded integrable subspace spanned by a basis for a particular representation of this Lie algebra. Using our iterative scheme to identify corrections to this broken Lie algebra, we have recovered perturbations to the PXP model which were previously known to enhance scarring from the Néel state (23). In addition, our method also allowed us to derive additional corrections, up to arbitrary order, enhancing scarring from this state further. By considering different representations of a su(2) Lie algebra, we have constructed deformations of the PXP model which result in persistent coherent dynamics from arbitrary charge density wave initial states $|Z_n\rangle$, even from those which did not exhibit non-ergodic dynamics in the original PXP model.

In Chapter 5, we have introduced a complimentary graph theoretic approach to study the proximity of QMBS systems to models hosting an exact spectrum generating algebra. Specifically, we consider QMBS whose scarring originates from broken su(2) Lie algebras. Instead of studying the algebra of generators, as we did in Chapter 4, we instead propose to investigate the proximity of the Hamiltonian, interpreted as the adjacency matrix of a graph, to that of a hypercube, which is isomorphic to a free paramagnet hosting an exact SU(2) symmetry. This approach to studying scarring revealed that QMBS is a somewhat generic property of quantum walks on partial cubes, that is, hypercubes with vertices removed, providing certain relevant embedded structures are left in tact, such as a model of two joined hypercubes relevant for scarring in the PXP model. By interpolating between the model of two joined hypercubes and the free paramagnet, we have discovered the PXP model is one of many models along this interpolation hosting QMBS. While most of these graphs correspond to highly non-local models, we have constructed families of kinetically constrained models with local interactions which host QMBS whose origin is intuitively understood from this graph theoretic approach, due to the relevance of embedded hypercubic subgraphs. While our analysis has been primarily numerical, it would be interesting to analytically affirm the connection between the emergent su(2) algebra and the underlying regular subgraph in future work.

Furthermore in Chapter 6, we introduced a systematic construction of approx-

imate QMBS models, which consisted of embedding the local periodic unitary dynamics of free models into kinetically constrained, interacting quantum systems using projector dressings. This resulted in a very simple criteria to predict if models of this form would host approximate scarring, one needs only consider the eigenvalues of a single site operator and determine if they are commensurate. Using this criteria it was possible to map out a phase space of scarred models with arbitrary local Hilbert space dimension, yielding many new QMBS models. Due to the form of Hamiltonians obtained via this construction, Eq. (6.2), it seems apparent that the approximate scarring in these models would also be consistent with broken Lie algebras, as without the projector dressings the Hamiltonians produced by this construction would be linear combinations of elements of an exact Lie algebra. The projector dressing will only serve to produce error terms from the relevant commutators, breaking the algebra. Nevertheless, an advantage of this construction is that detailed knowledge of the relevant broken Lie algebra or embedded graph structure is not necessary to determine if a model will host QMBS, rather only eigenvalues of a small dimensional matrix is relevant to predict scarring. Given the only QMBS which have been observed experimentally have been approximate scars in a kinetically constrained models (7), models obtained from this construction may yet prove to be relevant experimentally.

Finally in Chapter 7, we turned our attention from the origin of QMBS to potential implementations. By taking advantage of the weak ergodicity breaking and suppressed entropy growth typical of QMBS, we successfully implemented time evolution of the PXP model on a trapped ion quantum computer, using a variational quantum algorithm. Therefore QMBS, a non-trivial form of weak ergodicity breaking, corresponds to an interesting yet tractable problem for current near-intermediate scale quantum computers. Our success in this endeavour indicates the potential to realise additional scarred models on current quantum hardware. One interesting avenue is if an exact scarred model may be realised on quantum hardware. With traditional experimental platforms, it is not necessarily obvious which experimental systems are mappable to exact scarred models. Quantum computers however are universal platforms, with a first guess for the variational circuit necessary for simulation being obvious from trotterisation. Given the noisy qubits of current devices, implementation of exact scarred sys-

tems may even realise approximate scarred counterparts to these models.

The mechanism of broken Lie algebras introduced in this thesis has shed light on the origin of approximate QMBS, revealing the relationship between QMBS and other forms of weak ergodicity breaking. However, an important open question relates to the closure of the broken Lie algebra – will recursively feeding higher order error terms back into the broken generators result in an exact spectrum generating algebra, such that error terms of the broken lie algebra converge to zero? Indeed, we have identified two representations where an su(2) algebra can be made exact ($|\mathbb{Z}_3\rangle, |\mathbb{Z}_4\rangle$) after only considering first order error terms. This would be a difficult problem to tackle analytically, indeed, we had to resort to a custom symbolic code [1] to compute nested commutators in order to calculate higher order correction terms to the PXP model. The number of correction grows exponentially, such that the most fruitful approach would probably be a numerical scaling of the magnitude of errors. But even tackling this problem numerically is not trivial, as one would have to optimise the coefficients of the resulting corrections, minimising the magnitude of the error term. With exponential number of corrections, this classical optimisation becomes a numerically intensive problem.

More generally, there remain several open questions about QMBS. An interesting question for future work is if it is possible to engineer approximate spectrum generating algebras in a subspace without making use of a Lie algebra, but perhaps more general algebraic structures such as the quantum group $U_q(sl_2)$. Indeed, exact spectrum generating algebras which do not rely on a Lie algebra root structure has already been observed in the AKLT model (81). The model possesses a SGA $[H_{\text{AKLT}}, K^+] = \omega K^+$ and, while the operators $\{K^+, K^- = (K^+)^\dagger, H^z = \frac{1}{2}[K^+, (K^+)^\dagger]$ form an exact representation of su(2), the AKLT Hamiltonian itself H_{AKLT} is not a linear combination of the su(2) generators. Therefore, the SGA does not trivially follow from the root structure and further the scarred subspace, generated by repeated application of $K^\pm$ on the AKLT ground state, does not act as a representation of su(2) (81). Moreover, we have not considered embeddings of higher order su(n) Lie algebras throughout this thesis, instead restricting only to su(2). We expect this to be increasingly more difficult compared to su(2), due to the presence of more than one set of

---

[1] K. Bull (https://github.com/Cable273/comP).

raising operators, resulting in multiple error sources where there is no guarantee that improving errors of one set of raising operators will not exasperate errors in another set. However, it would seem the construction of scarred models of larger local Hilbert space dimension introduced in Chapter 6 may potentially give rise to such models.

In addition, it appears that kinetic constraints play an important role in the realisation of approximate scarred models. This is intuitively seen in the models hosting broken Lie algebras considered in this thesis, where kinetic constraint were directly responsible for the presence of error terms in the root structure of the algebra. Indeed, virtually all the approximate scarred models considered in this thesis, either from partial cubes of the free paramagnet (Chapter 5) or from the embedding of periodic unitary dynamics (Chapter 6) have being kinetically constrained models. Even for exact scarred models which are not intrinsically constrained systems, kinetic constraints have been found to emerge in the SGA raising (51). An interesting question is whether alternate, non trivial routes to QMBS exist.

Studying QMBS has resulted in a surge of interest in mechanisms of weak ergodicity breaking in many-bodied quantum systems. Indeed, the discovery of QMBS was a contemporary example of condensed matter research where new physics emerged from studying experiment, as opposed to experiment verifying theory. With the advancement of quantum computing as a platform for simulating many-bodied quantum systems, one can only hope many more exotic phenomena may be discovered.

Appendix A

Appendices

A.1 Broken Lie algebras

A.1.1 PXP $\mathbb{Z}_3$ second order su(2) corrections

Here we detail the second order corrections to the embedded su(2) algebra which improves $\mathbb{Z}_3$ revivals in the PXP model (Eq. (2.41)), obtained by our recursive scheme summarised in Fig. 4.1. As with the $\mathbb{Z}_2$ case (Section 4.4.1), the second order error term $\delta_{(2)}$ emerging from the commutator in Eq. (**??**) may be expressed as a linear combination of individual error terms $\delta_{(2),n}$:

$$\delta_{(2)}^+ = \sum_n \alpha_n \delta_{(2),n}^+ \tag{A.1}$$

A. APPENDICES

The individual error terms, only considering those which include a single spin flip, take the following form:

$$\delta^+_{(1),0} = PP\sigma^-_{3n}P + P\sigma^-_{3n}PP + PP\sigma^+_{3n+1}P + P\sigma^+_{3n+2}PP,$$

$$\delta^+_{(2),1} = PP\sigma^-_{3n}PP, \tag{A.2}$$

$$\delta^+_{(2),2} = P\sigma^-_{3n}P\sigma^z P + P\sigma^z P\sigma^-_{3n}P, \tag{A.3}$$

$$\delta^+_{(2),3} = P\sigma^-_{3n}P\sigma^z PP + PP\sigma^z P\sigma^-_{3n}P, \tag{A.4}$$

$$\delta^+_{(2),4} = P\sigma^+_{3n+1}PP + PP\sigma^+_{3n+2}P, \tag{A.5}$$

$$\delta^+_{(2),5} = PP\sigma^+_{3n+1}PP + PP\sigma^+_{3n+2}PP, \tag{A.6}$$

$$\delta^+_{(2),6} = P\sigma^+_{3n+1}PPP + PPP\sigma^+_{3n+2}P, \tag{A.7}$$

$$\delta^+_{(2),7} = P\sigma^+_{3n+1}P\sigma^z P + P\sigma^z P\sigma^+_{3n+2}P, \tag{A.8}$$

$$\delta^+_{(2),8} = P\sigma^+_{3n+1}PQP + PQP\sigma^+_{3n+2}P, \tag{A.9}$$

$$\delta^+_{(2),9} = PP\sigma^+_{3n+1}PPP + PPP\sigma^+_{3n+2}PP, \tag{A.10}$$

$$\delta^+_{(2),10} = PP\sigma^+_{3n+1}P\sigma^z P + P\sigma^z P\sigma^+_{3n+2}PP, \tag{A.11}$$

$$\delta^+_{(2),11} = P\sigma^+_{3n+1}P\sigma^z PP + PP\sigma^z P\sigma^+_{3n+2}P \tag{A.12}$$

$$\delta^+_{(2),12} = PP\sigma^+_{3n+1}PQP + PQP\sigma^+_{3n+2}PP, \tag{A.13}$$

$$\delta^+_{(2),13} = PP\sigma^+_{3n+1}P\sigma^z PP + PP\sigma^z P\sigma^+_{3n+2}PP, \tag{A.14}$$

$$\delta^+_{(2),14} = PPP\sigma^+_{3n+1}P + P\sigma^+_{3n+2}PPP, \tag{A.15}$$

where $Q \equiv |1\rangle\langle 1|$. $\delta_{(1),0}$ corresponds to the first order error term previously discussed in Section 4.5, while $\delta_{(2),n)}$ are the individual contributions to the second order error term. Perturbations to the PXP Hamiltonian follow from $V_{(n),m} = \delta^+_{(n),m} + (\delta^+_{(n),m})^\dagger$. Optimising the coefficients of these terms at $N = 16$, we find maximal wave-function revivals occur for the following values:

$$\lambda^*_i = [0.1630, 0.1129, 0.0228, 0.0409, 0.0871, 0.0046, -0.0303, -0.0144,$$
$$- 0.0592, 0.0005, 0.0223, -0.0185, -0.0451, 0.0101, 0.0035] \tag{A.16}$$

Thus, the dominant perturbations to the PXP Hamiltonian which enhance $\mathbb{Z}_3$ revivals up to second order are:

$$V_1 = PP\sigma^x_{3n}P + P\sigma^x_{3n}PP + PP\sigma^x_{3n+1}P + P\sigma^x_{3n+2}PP, \qquad (A.17)$$

$$V_2 = PP\sigma^x_{3n}PP. \qquad (A.18)$$

A.1.2 $\mathbb{Z}_4$ Revivals from su(2) Algebra

In Chapter 4, we have discussed how the PXP Hamiltonian, Eq. (2.41), hosts a broken Lie algebra, and by seeking corrections to this Lie algebra we have derived perturbations to the PXP Hamiltonian which enhance revivals from both the $|\mathbb{Z}_2\rangle$ and $|\mathbb{Z}_3\rangle$ states. However, unlike $|\mathbb{Z}_2\rangle$ and $|\mathbb{Z}_3\rangle$, quenches from $|\mathbb{Z}_4\rangle = |10001000...\rangle$ do not result in a reviving wavefunction beyond system size $N \gtrsim 20$ in the original PXP model. Furthermore, when quenching from $|\mathbb{Z}_4\rangle$, expectation values of local observables equilibrate as expected from the ETH (31, 131), such that there appear to be no scarred dynamics associated with the $|\mathbb{Z}_4\rangle$ state.

Nevertheless, in this appendix, we show that our Lie algebra approach identifies deformations to the PXP model which fixes a new su(2) algebra, engineered such that $|\mathbb{Z}_4\rangle$ is the lowest weight eigenstate of some $\bar{H}^z$, rather than $|\mathbb{Z}_2\rangle, |\mathbb{Z}_3\rangle$ as seen previously. While the subspace variance of this representation is too large to witness observable revivals in the PXP model, by fixing the algebra we realise new models which *do* exhibit $\mathbb{Z}_4$ revivals.

In direct analogy with the $\mathbb{Z}_2$ and $\mathbb{Z}_3$ cases, we define the raising and lowering operators of a broken su(2) Lie algebra associated with the $|\mathbb{Z}_4\rangle$ state as:

$$\bar{H}^+ = \sum_n \left(\tilde{\sigma}^-_{4n} + \tilde{\sigma}^+_{4n+1} + \tilde{\sigma}^+_{4n+2} + \tilde{\sigma}^+_{4n+3} \right), \qquad (A.19)$$

$$\bar{H}^- = \sum_n \left(\tilde{\sigma}^+_{4n} + \tilde{\sigma}^-_{4n+1} + \tilde{\sigma}^-_{4n+2} + \tilde{\sigma}^-_{4n+3} \right), \qquad (A.20)$$

which, in turn, define $\bar{H}^z = \frac{1}{2}[\bar{H}^+, \bar{H}^-]$ that evaluates to

$$
\begin{aligned}
\bar{H}^z &= \sum_n \left(-\tilde{\sigma}^z_{4n} + \tilde{\sigma}^z_{4n+1} + \tilde{\sigma}^z_{4n+2} + \tilde{\sigma}^z_{4n+3}\right) \\
&+ \frac{1}{2}\sum_n \left(P_{4n}\sigma^+_{4n+1}\sigma^-_{4n+2}P_{4n+3} + P_{4n}\sigma^-_{4n+1}\sigma^+_{4n+2}P_{4n+3} \right. \\
&+ \left. P_{4n+1}\sigma^+_{4n+2}\sigma^-_{4n+3}P_{4n+4} + P_{4n+1}\sigma^-_{4n+2}\sigma^+_{4n+3}P_{4n+4}\right).
\end{aligned} \tag{A.21}
$$

Similar to previous cases, $|\mathbb{Z}_4\rangle$ is the lowest weight state of $\bar{H}^z$ and it is found that $\{\bar{H}^z, \bar{H}^+, \bar{H}^-\}$ form a broken representation of su(2), as defined by Eq. (4.6). Errors in the root structure, for which we give an exhaustive list in Appendix A.1.3, suggest the following perturbations to the PXP model are necessary to stabilise $\mathbb{Z}_4$ revival:

$$
V_1 = \sum_n P_{4n}\sigma^x_{4n+1}\sigma^x_{4n+2}\sigma^x_{4n+3}P_{4n+4}, \tag{A.22}
$$

$$
V_2 = \sum_n \left(P_{4n-1}\sigma^x_{4n}\sigma^x_{4n+1}\sigma^x_{4n+2}P_{4n+3} + P_{4n+1}\sigma^x_{4n+2}\sigma^x_{4n+3}\sigma^x_{4n+4}P_{4n+5}\right) \tag{A.23}
$$

$$
\begin{aligned}
V_3 &= \sum_n \left(P_{4n}P_{4n+1}\sigma^x_{4n+2}P_{4n+3} + P_{4n}\sigma^x_{4n+1}P_{4n+2}P_{4n+3} \right. \\
&+ \left. P_{4n+1}P_{4n+2}\sigma^x_{4n+3}P_{4n+4} + P_{4n+1}\sigma^x_{4n+2}P_{4n+3}P_{4n+4}\right),
\end{aligned} \tag{A.24}
$$

$$
\begin{aligned}
V_4 &= \sum_n \left(P_{4n-2}\sigma^x_{4n-1}P_{4n}P_{4n+1} + P_{4n-1}P_{4n}\sigma^x_{4n+1}P_{4n+2} \right. \\
&+ \left. P_{4n-1}\sigma^x_{4n}P_{4n+1}P_{4n+2} + P_{4n+2}P_{4n+3}\sigma^x_{4n+4}P_{4n+5}\right).
\end{aligned} \tag{A.25}
$$

Explicit optimisation finds that the terms in Eqs. (A.22)-(A.25) can stabilise $\mathbb{Z}_4$ revivals, but some of the resulting optimal coefficients turn out to be of the order unity. Therefore we arrive at a model that cannot be viewed as a small deformation of the PXP Hamiltonian, but rather a new model in its own right. It is intuitive a strong deformation of the PXP model is necessary to engineer revivals from the $\mathbb{Z}_4$ state, given the original PXP model did not exhibit any revival from this state. Specifically, optimising V_i coefficients λ_i for fidelity we find (at $N = 16$)

$$
\lambda^*_i = [0.0008, -1.43, 0.0979, 0.0980], \tag{A.26}
$$
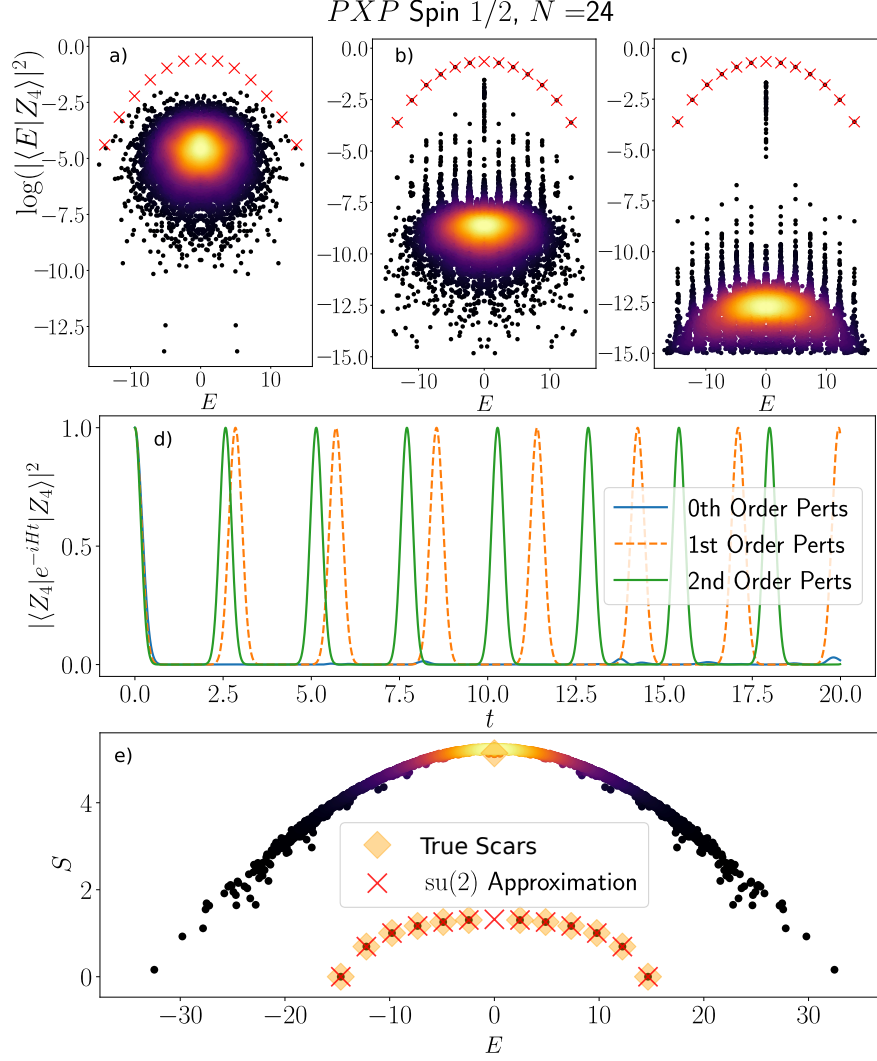
Figure A.1: $\mathbb{Z}_4$ revivals in PXP model, enhanced by terms which correct a particular representation of a broken su(2) Lie algebra. (a) Eigenstate overlap with $|\mathbb{Z}_4\rangle$ state for PXP model. (b) Eigenstate overlap with $|\mathbb{Z}_4\rangle$ state after including first order su(2) corrections, Eqs. (A.22)-(A.23). (c) Eigenstate overlap after including second order su(2) corrections (see Appendix A.1.3). (d) $\mathbb{Z}_4$ quench fidelity. $|\mathbb{Z}_4\rangle$ state does not revive in pure PXP model, but it does revive in the new model obtained by correcting the su(2) algebra. (e) Bipartite entropy, Eq. (2.21), of eigenstates of the PXP model after including second order $\mathbb{Z}_4$ su(2) corrections. Points labelled 'True Scars' are exact diagonalisation results identified from the top band of states in (c). Red crosses in (a), (b), (c), (e) indicate approximate scar states obtained by projecting the Hamiltonian to the broken representation basis and diagonalising. Colour scale in (a), (b), (c), (e) indicates the density of data points, with lighter regions being more dense.

A. APPENDICES

Order	$1 - f_0$	$\sigma/D_{\mathrm{su}(2)}$	$max(var(H^z)_n)$	K
$n = 0$	$9.993{\times}10^{-1}$	$3.333{\times}10^0$	$2.779{\times}10^0$	$4.323{\times}10^0$
$n = 1$	$5.814{\times}10^{-5}$	$6.722{\times}10^{-4}$	$7.902{\times}10^{-4}$	$3.258{\times}10^{-3}$
$n = 2$	$3.351{\times}10^{-9}$	$9.746{\times}10^{-6}$	$2.753{\times}10^{-4}$	$1.534{\times}10^{-3}$

Table A.1: Error metrics for the $\mathbb{Z}_4$ su(2) subspace of the PXP model at various perturbation orders for $N = 24$. Subspace variance σ is normalised by the dimension of the su(2) representation, $N/2+1$. See text for details of the perturbations. Errors at $n = 0$ are much worse than $n = 0$ $\mathbb{Z}_2, \mathbb{Z}_3$ errors (compare with Table 4.1 and Table 4.2), consistent with there being no revivals or $\mathbb{Z}_4$ scars in pure PXP model.

where we see the coefficient of optimal V_2 is $\sim O(1)$. Once again, second order perturbations can be identified from the Lie algebra and revivals enhanced further (see Appendix A.1.3 for details of the 36 terms and optimal coefficients – note only 3 terms contribute significantly with $O(1)$ coefficient after optimising for revivals). The effect of these perturbations is summarised in Fig. A.1. Error metrics at various perturbation orders are given in Table A.1. The second order deformations leave the model non-integrable, which we verify from the mean level spacing $\langle r \rangle = 0.5271$ at $N = 24$, consistent with an ergodic system.

Exact $\mathbb{Z}_4$ su(2) embedding

Here we note that similar to $\mathbb{Z}_3$ case in Section 4.5, there exists a deformation of the PXP model such that $|\mathbb{Z}_4\rangle$ is the lowest weight state of an *exact* su(2) representation. This model is obtained by redefining the raising operator in Eq. (A.19) according to

$$
\begin{aligned}
\bar{H}^+ &\to \bar{H}^+ - V_2 \\
&= \bar{H}^+ - \sum_n \left(P_{4n+3}\sigma^-_{4n+4}\sigma^+_{4n+5}\sigma^-_{4n+6}P_{4n+7} + P_{4n+1}\sigma^-_{4n+2}\sigma^+_{4n+3}\sigma^-_{4n+4}P_{4n+5} \right),
\end{aligned}
$$
(A.27)
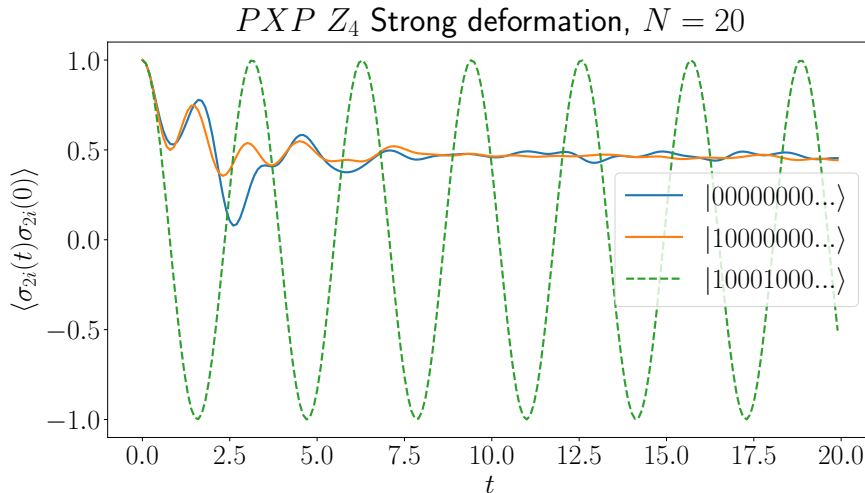
Figure A.2: Local autocorrelation function $\langle \sigma_{2i}^z(t)\sigma_{2i}^z(0)\rangle$ of the model given by Eq. (A.28), for various initial states given in the legend. Results are for $N = 20$. We consider sites $2i$ as the translation symmetry of Eq. (A.28) is broken to a subgroup corresponding to translations by two units. Generic initial states such as the polarised state $|000...\rangle$ equilibrate, whereas the autocorrelation function exhibits non stationary behaviour for all times when the system is initialised in the $|\mathbb{Z}_4\rangle = |10001000...\rangle$ state.

which yields the Hamiltonian:

$$
H \;=\; \sum_n P_{n-1}\sigma_n^x P_{n+1} - \sum_n \left(P_{4n+3}\sigma_{4n+4}^x \sigma_{4n+5}^x \sigma_{4n+6}^x P_{4n+7} + P_{4n+1}\sigma_{4n+2}^x \sigma_{4n+3}^x \sigma_{4n+4}^x P_{4n+5}\right).
$$

$$(A.28)$$

This model features an exact spectrum generating algebra (SGA), Eq. (3.33), within the su(2) subspace, with the symmetry generator taking the same form as Eq. (4.60). However, unlike the $\mathbb{Z}_3$ example of an exact SGA (Section 4.5.2), the computational basis which satisfies the Rydberg constraint does not fracture into exponentially many sectors. There still exists an exact Krylov subspace generated by repeated application of the Hamiltonian on $|\mathbb{Z}_4\rangle$ which is block diagonal with respect to the orthogonal thermalising subspace, such that this model fractures into the block diagonal form shown schematically in Fig. 3.2(c). We verify the model is still thermalising in the orthogonal subspace by computing the mean level spacing $\langle r\rangle = 0.5365$ at $N = 24$, consistent with level spacings obeying the

Wigner-Surmise distribution as expected of an ergodic subspace.

As a consequence of the exact su(2) embedding the $|\mathbb{Z}_4\rangle$ state revives perfectly, whereas generic initial states from the orthogonal sector still thermalise as expected from the ETH. Thus, local observables and local autocorrelation functions, which generically equilibrate, may exhibit long-lived non-stationary behaviour following a quench from $|\mathbb{Z}_4\rangle$, Fig. A.2.

A.1.3   PXP $\mathbb{Z}_4$ second order su(2) corrections

For completeness, here we provide the full list of the 36 second order corrections to the embedded su(2) representation responsible for $\mathbb{Z}_4$ revivals. These terms are identified by an iterative scheme summarised in Fig. 4.1. We do not consider every term which contributes an error to the broken Lie algebra but restrict to the subset of terms containing a single spin flip. Note, at second order only three perturbations to H^+ (Eq. A.19) dominate with coefficient $O(1)$ after optimising for $\mathbb{Z}_4$ revivals. These are found to be:

$$
\begin{align}
\delta_1^+ &= PPQP\sigma_{4n+3}^+P + P\sigma_{4n+1}^+PQPP, & \text{(A.29)} \\
\delta_2^+ &= PP\sigma_{4n+2}^+PP, & \text{(A.30)} \\
\delta_3^+ &= PP\sigma_{4n+2}^+P\sigma^zPP + PP\sigma^zP\sigma_{4n+1}PP. & \text{(A.31)}
\end{align}
$$

Optimising the coefficients of all 36 terms with respect to $\mathbb{Z}_4$ fidelity revivals at $N = 16$ we find the coefficients of the above three terms are $[1.5621, 1.9337, -1.4312]$. Before listing the full set of perturbations, we first introduce the following abbreviated notation:

$$
ABC..., \quad n, \quad m = \sum_i A_{ni+m}B_{ni+m+1}C_{ni+m+2}...,
$$

where n is understood as the periodicity of the repeating unit while m is the offset of the far left operator. Listing multiple terms for a given perturbation is to be understood as implicitly implying addition. The complete set of second order $\mathbb{Z}_4$

su(2) corrections to H^+ are as follows:

$$
\begin{aligned}
\delta^+_{(2),1} \;=\; & PP\sigma^+ P, \quad 4, \quad 3 \\
& P\sigma^+ PP, \quad 4, \quad 2 \\
& P\sigma^- PP, \quad 4, \quad 3 \\
& PP\sigma^- P, \quad 4, \quad 2 \quad\quad\quad\quad\quad (A.32)
\end{aligned}
$$

$$
\begin{aligned}
\delta^+_{(2),2} \;=\; & PP\sigma^+ PP, \quad 4, \quad 3 \\
& PP\sigma^+ PP, \quad 4, \quad 1 \quad\quad\quad\quad\quad (A.33)
\end{aligned}
$$

$$
\begin{aligned}
\delta^+_{(2),3} \;=\; & PPP\sigma^+ P, \quad 4, \quad 3 \\
& P\sigma^+ PPP, \quad 4, \quad 1 \quad\quad\quad\quad\quad (A.34)
\end{aligned}
$$

$$
\begin{aligned}
\delta^+_{(2),4} \;=\; & PPQP\sigma^+ P, \quad 4, \quad 3 \\
& P\sigma^+ PQPP, \quad 4, \quad 0 \quad\quad\quad\quad\quad (A.35)
\end{aligned}
$$

$$
\begin{aligned}
\delta^+_{(2),5} \;=\; & P\sigma^- PQP, \quad 4, \quad 3 \\
& PQP\sigma^- P, \quad 4, \quad 1 \quad\quad\quad\quad\quad (A.36)
\end{aligned}
$$

$$
\begin{aligned}
\delta^+_{(2),6} \;=\; & P - P\sigma^z P, \quad 4, \quad 3 \\
& P\sigma^z P\sigma^- P, \quad 4, \quad 1 \quad\quad\quad\quad\quad (A.37)
\end{aligned}
$$

$$
\begin{aligned}
\delta^+_{(2),7} \;=\; & P - P\sigma^z PP, \quad 4, \quad 3 \\
& PP\sigma^z P\sigma^- P, \quad 4, \quad 0 \quad\quad\quad\quad\quad (A.38)
\end{aligned}
$$

$$
\begin{aligned}
\delta^+_{(2),8} \;=\; & P\sigma^z P\sigma^+ P, \quad 4, \quad 3 \\
& P\sigma^+ P\sigma^z P, \quad 4, \quad 1 \quad\quad\quad\quad\quad (A.39)
\end{aligned}
$$

$$
\begin{aligned}
\delta^+_{(2),9} \;=\; & P\sigma^+ PPP, \quad 4, \quad 2 \\
& PPP\sigma^+ P, \quad 4, \quad 2 \quad\quad\quad\quad\quad (A.40)
\end{aligned}
$$

$$
\begin{aligned}
\delta^+_{(2),10} \;=\; & PP\sigma^+ PPP, \quad 4, \quad 1 \\
& PPP\sigma^+ PP, \quad 4, \quad 2 \quad\quad\quad\quad\quad (A.41)
\end{aligned}
$$

$$
\begin{aligned}
\delta^+_{(2),11} \;=\; & P\sigma^z P\sigma^+ PP, \quad 4, \quad 3 \\
& PP\sigma^+ P\sigma^z P, \quad 4, \quad 0 \quad\quad\quad\quad\quad (A.42)
\end{aligned}
$$

$$
\delta^+_{(2),12} \;=\; PP\sigma^- PP, \quad 4, \quad 2 \quad\quad\quad\quad\quad (A.43)
$$

$$
\begin{aligned}
\delta^+_{(2),13} &= PP\sigma^+P, \quad 4, \quad 0 \\
& P\sigma^+PP, \quad 4, \quad 0 \\
& PP\sigma^+P, \quad 4, \quad 1 \\
& P\sigma^+PP, \quad 4, \quad 1 \quad\quad\quad\quad\quad\quad (A.44)
\end{aligned}
$$

$$
\delta^+_{(2),14} = PP\sigma^+PP, \quad 4, \quad 0 \quad\quad\quad\quad\quad\quad (A.45)
$$

$$
\begin{aligned}
\delta^+_{(2),15} &= P\sigma^+PPP, \quad 4, \quad 0 \\
& PPP\sigma^+P, \quad 4, \quad 0 \quad\quad\quad\quad\quad (A.46)
\end{aligned}
$$

$$
\begin{aligned}
\delta^+_{(2),16} &= P\sigma^+PQP, \quad 4, \quad 0 \\
& PQP\sigma^+P, \quad 4, \quad 0 \quad\quad\quad\quad\quad (A.47)
\end{aligned}
$$

$$
\begin{aligned}
\delta^+_{(2),17} &= PPQP\sigma^-P, \quad 4, \quad 0 \\
& P\sigma^-PQPP, \quad 4, \quad 3 \quad\quad\quad\quad (A.48)
\end{aligned}
$$

$$
\begin{aligned}
\delta^+_{(2),18} &= PP\sigma^+PPP, \quad 4, \quad 0 \\
& PPP\sigma^+PP, \quad 4, \quad 3 \quad\quad\quad\quad (A.49)
\end{aligned}
$$

$$
\begin{aligned}
\delta^+_{(2),19} &= PQP\sigma^+P, \quad 4, \quad 3 \\
& P\sigma^+PQP, \quad 4, \quad 1 \quad\quad\quad\quad\quad (A.50)
\end{aligned}
$$

$$
\begin{aligned}
\delta^+_{(2),20} &= PP\sigma^zP\sigma^+P, \quad 4, \quad 2 \\
& P\sigma^+P\sigma^zPP, \quad 4, \quad 1 \quad\quad\quad\quad (A.51)
\end{aligned}
$$

$$
\begin{aligned}
\delta^+_{(2),21} &= P\sigma^-PPP, \quad 4, \quad 3 \\
& PPP\sigma^-P, \quad 4, \quad 1 \quad\quad\quad\quad\quad (A.52)
\end{aligned}
$$

$$
\begin{aligned}
\delta^+_{(2),22} &= P\sigma^zP+P, \quad 4, \quad 0 \\
& P\sigma^+P\sigma^zP, \quad 4, \quad 0 \quad\quad\quad\quad\quad (A.53)
\end{aligned}
$$

$$
\begin{aligned}
\delta^+_{(2),23} &= P\sigma^zP\sigma^+PP, \quad 4, \quad 0 \\
& PP\sigma^+P\sigma^zP, \quad 4, \quad 3 \quad\quad\quad\quad (A.54)
\end{aligned}
$$

$$
\begin{aligned}
\delta^+_{(2),24} &= PP\sigma^-PPP, \quad 4, \quad 2 \\
& PPP\sigma^-PP, \quad 4, \quad 1 \quad\quad\quad\quad (A.55)
\end{aligned}
$$

$$\begin{aligned}
\delta^+_{(2),25} &= P\sigma^+ P\sigma^z PP, & 4, & \quad 0 \\
& \quad PP\sigma^z P\sigma^+ P, & 4, & \quad 1 \\
& \quad PP\sigma^z P\sigma^+ P, & 4, & \quad 3 \\
& \quad P\sigma^+ P\sigma^z PP, & 4, & \quad 2 & (A.56)
\end{aligned}$$

$$\begin{aligned}
\delta^+_{(2),26} &= P\sigma^z P\sigma^+ P, & 4, & \quad 2 \\
& \quad P\sigma^+ P\sigma^z P, & 4, & \quad 2 & (A.57)
\end{aligned}$$

$$\begin{aligned}
\delta^+_{(2),27} &= PP\sigma^+ P\sigma^z P, & 4, & \quad 1 \\
& \quad P\sigma^z P\sigma^+ PP, & 4, & \quad 2 & (A.58)
\end{aligned}$$

$$\begin{aligned}
\delta^+_{(2),28} &= PPP\sigma^+ PP, & 4, & \quad 0 \\
& \quad PP\sigma^+ PPP, & 4, & \quad 3 & (A.59)
\end{aligned}$$

$$\begin{aligned}
\delta^+_{(2),29} &= PP\sigma^- P\sigma^z P, & 4, & \quad 2 \\
& \quad P\sigma^z P\sigma^- PP, & 4, & \quad 1 & (A.60)
\end{aligned}$$

$$\begin{aligned}
\delta^+_{(2),30} &= P\sigma^+ PPPP, & 4, & \quad 0 \\
& \quad PPPP\sigma^+ P, & 4, & \quad 3 & (A.61)
\end{aligned}$$

$$\begin{aligned}
\delta^+_{(2),31} &= PP\sigma^z P\sigma^- PP, & 4, & \quad 0 \\
& \quad PP\sigma^- P\sigma^z PP, & 4, & \quad 2 & (A.62)
\end{aligned}$$

$$\begin{aligned}
\delta^+_{(2),32} &= PP\sigma^z P\sigma^+ PP, & 4, & \quad 1 \\
& \quad PP\sigma^+ P\sigma^z PP, & 4, & \quad 1 & (A.63)
\end{aligned}$$

$$\begin{aligned}
\delta^+_{(2),33} &= P\sigma^+ PPPP, & 4, & \quad 2 \\
& \quad PPPP\sigma^+ P, & 4, & \quad 1 & (A.64)
\end{aligned}$$

$$\begin{aligned}
\delta^+_{(2),34} &= PP\sigma^z P\sigma^+ PP, & 4, & \quad 3 \\
& \quad PP\sigma^+ P\sigma^z PP, & 4, & \quad 3 & (A.65)
\end{aligned}$$

$$\begin{aligned}
\delta^+_{(2),35} &= P\sigma^+ PPPP, & 4, & \quad 1 \\
& \quad PPPP\sigma^+ P, & 4, & \quad 2 & (A.66)
\end{aligned}$$

$$\begin{aligned}
\delta^+_{(2),36} &= PP\sigma^+ P\sigma^z PP, & 4, & \quad 0 \\
& \quad PP\sigma^z P\sigma^+ PP, & 4, & \quad 2 & (A.67)
\end{aligned}$$

Perturbations to the PXP Hamiltonian (Eq. 2.41) follow from $V_{(2),m} = \delta^+_{(2),m} + (\delta^+_{(2),m})^\dagger$. Optimising coefficients of these terms at $N = 16$ with respect to the first maximum of $|\langle \mathbb{Z}_4 | e^{-iHt} | \mathbb{Z}_4 \rangle|^2$ at $N = 16$ we find:

$$
\begin{aligned}
\lambda_i^* = \ & [0.0888, 0.2559, 0.0796, 1.5621, \\
& 0.1776, -0.0028, -0.0325, 0.0099, \\
& 0.1333, 0.0321, -0.0148, 0.1490, \\
& 0.0728, 1.9337, 0.0001, 0.0587, \\
& 0.0902, 0.0001, 0.1109, 0.0104, \\
& 0.0468, 0.0277, -0.0023, 0.1046, \\
& 0.0667, 0.0299, 0.0437, 0, \\
& 0.0031, 0.0002, -0.0189, 0.0995, \\
& 0.1531, 0.0001, 0.0001, -1.4312].
\end{aligned}
\tag{A.68}
$$

A.2   Embedded hypercubes

A.2.1   Hypergrid subgraphs in the (2,3) model

The key difference between the PXP and (2,3) models can be traced to the underlying subgraph associated with the revivals from the Néel and $|11001100\ldots\rangle$ initial states. While in the PXP and other models studied up to this point the relevant subgraph was a union of hypercubes sharing a single vertex (Section 5.4), in the (2,3) model we find a different type of subgraph consisting of two *hypergrids* of dimension $N/2$. A hypergrid graph arises as the adjacency matrix of a spin-1 free paramagnet, in contrast to a hypercube which is the adjacency matrix of a spin-1/2 free paramagnet. In this section, we provide analytical and numerical evidence that the hypergrid subgraphs are indeed responsible for the atypical dynamics and many-body scarring in the (2,3) model.

Proof of the existence of two hypergrids in the (2,3) graph

A hypergrid graph G_m^d is defined as the Cartesian product

$$G_m^d = \underbrace{L_m \square L_m \square \ldots \square L_m}_{d}, \qquad (A.69)$$

where L_m stands for a linear graph of order m (with m vertices) and we are only interested in hypergrids with the same order in all dimensions. For example, the hypergrid G_2^d is simply the hypercube of dimension d. Similarly, the hypergrid graph G_{2S+1}^d, having $2S+1$ states in each dimension, is isomorphic to an unweighted graph of a free spin model with d spin-S degrees of freedom. This is because each vertex of G_m^d can be labelled by a string $\{1, 2, \ldots m\}^d$, and only vertices with a single site differing by 1 are connected by an edge. Note that for $S>1$ the matrix elements of the free spin-S model Hamiltonian are no longer equal, and the model can no longer be described solely by an unweighted graph. We will not consider such cases in this paper.

Next we show that there are two distinct hypergrids $G_3^{N/2}$ that can be identified as subgraphs of the (2,3) model. One of these hypergrids is sketched in Fig. A.3. The proof is based on grouping sites into pairs (70, 118). Let us first
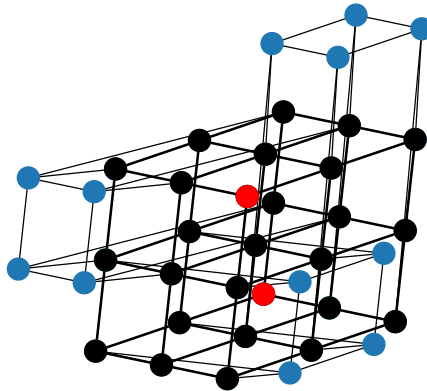
Figure A.3: Adjacency graph of the (2,3) model for system size $N=6$. The subgraph associated with many-body scarring is outlined in black, while the Néel states are shown in red. Blue vertices denote bridges connecting vertices in the subgraph. The subgraph is isomorphic to a hypergrid $G_3^{N/2}$. Note that there are two such hypergrids, but for clarity only one of them is highlighted here.

define the states $|o\rangle = |00\rangle$, $|L\rangle = |10\rangle$, $|R\rangle = |01\rangle$, $|2\rangle = |11\rangle$. In this formulation, the only forbidden configurations are $|2L\rangle$, $|R2\rangle$, and of course $|22\rangle$. The Hamiltonian acting on the $N/2$ pairs of sites can be written as

$$H_{(2,3)} = \sum_{b=1}^{N/2} h_{b-1,b,b+1}, \tag{A.70}$$

where the local Hamiltonian term is

$$
\begin{aligned}
h_{b-1,b,b+1} = {}& \mathbb{1} \otimes \big(|o\rangle \langle R| + |R\rangle \langle o| \big) \otimes \big(\mathbb{1} - |2\rangle \langle 2| \big) \\
& + \big(\mathbb{1} - |2\rangle \langle 2| \big) \otimes \big(|o\rangle \langle L| + |L\rangle \langle o| \big) \otimes \mathbb{1} \\
& + \big(|o\rangle \langle o| + |L\rangle \langle L| \big) \otimes \Big[|L\rangle \langle 2| + |2\rangle \langle L| \\
& + |R\rangle \langle 2| + |2\rangle \langle R| \Big] \otimes \big(|o\rangle \langle o| + |R\rangle \langle R| \big).
\end{aligned}
\tag{A.71}
$$

Let us take $N=8$ as an example. Start from the Néel state $|\mathbb{Z}_2\rangle = |10101010\rangle$ and group the cells into pairs $(1,2)$, $(3,4)$, $(5,6)$ and $(7,8)$. Then $|\mathbb{Z}_2\rangle = |LLLL\rangle$ and every pair of sites can be freely flipped $|L\rangle \rightleftarrows |o\rangle \rightleftarrows |R\rangle$, like a spin 1. This means that there is a hypergrid graph G_3^4 between the Néel state $|LLLL\rangle$ and the anti-Néel $|RRRR\rangle$. It is important to note that while in the $(2,3)$ model under some condition the flips $|L\rangle \rightleftarrows |2\rangle$ and $|R\rangle \rightleftarrows |2\rangle$ are possible, they correspond to bridging out of this hypergrid graph. Beyond the Néel states, we would expect to also see revivals from other corners of this hypergrid, i.e., from states in which all cells have an extremal value (either L or R). Indeed, this would mean that all cells would precess freely with the same frequency. However, the only other corners of this graph that have no edges going out of the hypergrid are $|LRLR\rangle = |10011001\rangle$ and $|RLRL\rangle = |01100110\rangle$. Indeed, from Eq. (A.71), one can see that any LLR or LRR configuration can be changed to an $L2R$ one which is not in the hypergrid.

Alternatively, the sites can be paired up as $(8,1)$, $(2,3)$, $(4,5)$ and $(6,7)$. In this case the Néel state is $|RRRR\rangle$ and the same spin-1 argument holds. However, this hypergrid graph G_3^4 is different from the last one, as can be seen by looking at the corners $|LRLR\rangle = |00110011\rangle$ and $|RLRL\rangle = |11001100\rangle$. In the first formulation these states would be $|o2o2\rangle$ resp. $|2o2o\rangle$, which are not in the corresponding hypergrid graph.

The two hypergrids identified above are not equivalent but share several vertices, and their union can be taken as a model on its own, which we refer to as '2HG' model. In fact all states with no neighbouring excitations belong to both hypergrids, so their intersection gives back the PXP graph. Because of this, the total number of states in the 2HG model is asymptotically given by $3^{N/2} - \phi^N$, where ϕ is the Golden Ratio.

A single hypergrid has perfect state transfer and revivals from any corner state. While the revivals in the 2HG graph are no longer perfect, they are still present with a similar frequency. The two Néel states are corners of both hypergrids and they are the best reviving basis states in the (2,3) model, while the states $|110011\dots1100\rangle$ are all corner of only one of the hypergrids and their revivals are found to be weaker, as expected from their position in the graph. All other basis states are either not corners of these hypergrids or they have additional edges extending out of the 2HG, and thus they are not expected to revive. Finally, if N is even but not a multiple of 4, the two Néel states are the only reviving ones, as all other corners of the hypergrid have edges going outside of it.

Numerical evidence for the relevance of hypergrids for many-body scarring

In Fig. A.4, we numerically test the relevance of the 2HG subgraph for many-body scarring in the (2,3) model. We compare the dynamics and eigenstate properties in the (2,3) model with their projection into the 2HG model. In both models, we observe revivals of the wave function, with similar frequencies, see Fig. A.4(a). However, the amplitude of revivals decays more rapidly in the 2HG model compared to the (2,3) model. This difference can be related to the eigenstate overlap with the Néel state shown in Fig. A.4(b). The overlap between the Néel state and the eigenstates of the (2,3) model shows clear tower structures with an energy spacing close to that in the 2HG model. However, in the 2HG model there is no top band of states that is well-separated from the bulk like in the (2,3) model or the PXP model in Fig. 5.8. Thus, the revivals decay faster as more states participate in the dynamics.

The hypergrids also seem to play an important role in stabilising the first step
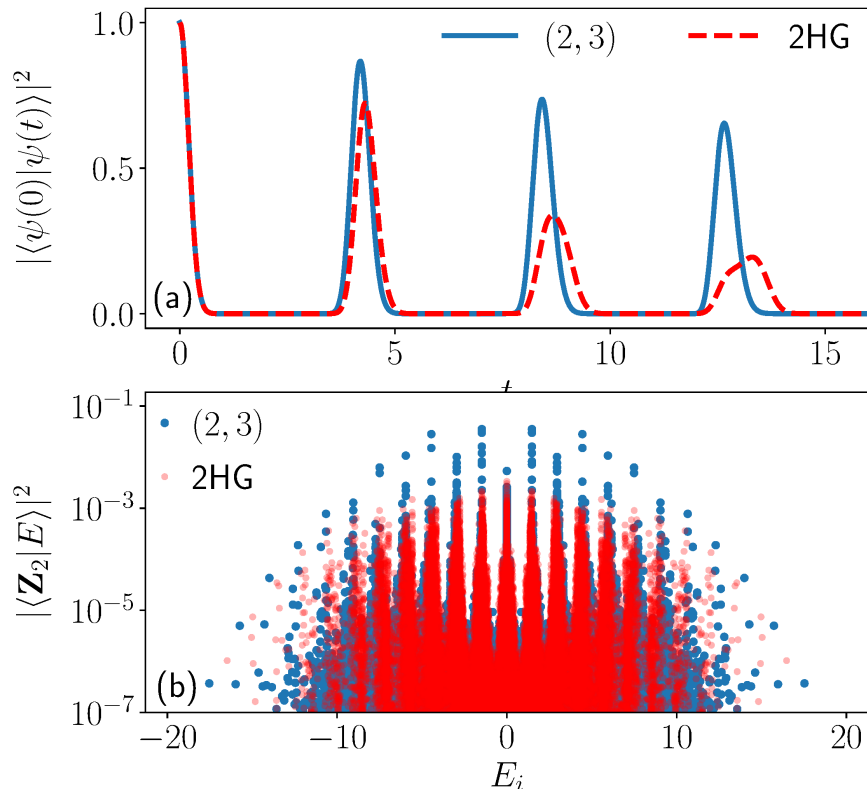
Figure A.4: Scarred dynamics and eigenstate properties in the (2,3) model and its 2HG subgraph. (a) The revivals from the Néel state have very close frequency in the two models, but their decay is more pronounced in 2HG model. This can be attributed to the absence of a well-separated band of scarred eigenstates for this model, as can be seen in (b). Data is for system size $N=24$.

of the FSA. Indeed, because of the constraint it is possible to add excitations to a state already in the second Hamming layer. This means that only the first step of the FSA is the same as in the two-hypercube model. Based on that we would expect to only have a single exact FSA step and thus poor revivals as in (3,4) and (4,5) models. However, in practice we observe that the first two FSA steps are exact, as is also the case in the 2HG model.

The bridges added on top of 2HG to form the (2,3) model seem to stabilise the revivals from the Néel state. The exact mechanism by which this happens is unclear to us, however we believe that the mechanism is non-generic as the addition of random bridges is found to consistently lead to poorer revivals. At the

same time, the revivals from most other states are destroyed by additional bridges. As we demonstrate in the next section, this mechanism of revival stabilisation due to a small density of bridges is also realised in the two-hypercube model describing the many-body scarring in the PXP model.

A.2.2 Random bridges on two connected hypercubes

In order to test how sensitive our conclusions in Chapter 5 are to the details of the graph structure, we devised a protocol for random sampling of models that interpolate between two joined hypercubes and the full hypercube. As two joined hypercubes of dimension $N/2$ are contained in a hypercube of dimension N, the protocol works by adding back states from the full hypercube to the two smaller hypercubes. In order to match the constraints in the considered models, at each step the Hamiltonian can be written as Eq. (2.27) with constraints only on *excitations* (meaning that it is always possible to remove excitations) and with translation symmetry conserved. The process also ensures that the graph remains unweighted, i.e., the matrix elements of the Hamiltonian are all equal.

To formalise the protocol, let us denote each basis state by a binary string $u \in B^N$, with $B = 0, 1$. Consider two states u and v; we say that $u \leq v$ if $u_i \leq v_i$ for $i = 1$ through N. This is strictly equivalent to saying that u can be obtained by only removing excitations from v. Then, in all these models, if $v \in G$ and $u \leq v$, then $u \in G$ as well. Because an excitation can always be removed, all these models are 'daisy cubes' (63):

Definition 1. *A daisy cube is defined by a N dimensional hypercube graph G_2^N and a set of states X, such that all elements of X are in G_2^N. Then the set of vertices in the corresponding daisy cube is defined as $V(G_2^N(X)) = \{v \in G_2^N | \exists x \in X \ s.t \ v \leq x\}$. The graph $G_2^N(X)$ is the subgraph of G_2^N induced by $V(G_2^N(X))$. Equivalently, there is an edge between two states in $G_2^N(X)$ if their strings differ by a single element.*

This formulation also implies that different sets X can correspond to the same graph. In particular, if $x, y \in X$ and $y \leq x$, then $G_2^N(X) = G_2^N(X \backslash \{y\})$. However it is clear that there exists a unique set $\hat{X}$ of maximal vertices such that it has

the minimum cardinality of all sets representing the same daisy cube. For the PXP model in Eq. (2.41) with $N=6$ for example, the maximal vertices set is

$$\hat{X}_{\text{PXP},N=6} = \{101010,\ 010101,\ 100100,\ 010010,\ 001001\}.$$

The graph which has H as its adjacency matrix is the daisy cube $G_2^6(\hat{X}_{\text{PXP},N=6})$.

We will use the binary string and daisy cubes notations to define the sampling algorithm. The translation operator T acts on the strings as $(Tu)_i=u_{i-1}$, with periodic boundary conditions such that $u_N=u_0$. Because of translation symmetry, the two stitched hypercubes correspond to the daisy cube $G_2^N(X)$, $X = \{\mathbb{Z}_2, T\mathbb{Z}_2\}$, where $\mathbb{Z}_2$ is the Néel state $1010\ldots10$. The hypercubes are added in increasing dimension from $k=2$ to $k=N$, and after each addition the revivals from the Néel state are computed. The interpolation parameter λ is also computed at each step, as defined in Eq. (5.27) in the Chapter 5. The exact algorithm is :

Algorithm 1 Random bridges on 2 hypercubes

    Set $X = \{\mathbf{Z}_2, T\mathbf{Z}_2\}$
    Set the graph as $G = G_2^N(X)$
    Set $k = 2$
    while $k \leq N$ **do**
        Pick $u \in G_2^N$ such that $\sum_{i=1}^N u_i=k$, $u \nleq \mathbf{Z}_2$ and $u \nleq T\mathbf{Z}_2$
        if $u \in G$ **then**
            $k = k + 1$
        else
            for $r = 0$ to $N - 1$ **do**
                $X = X \cup \{T^r u\}$
            end for
            Update the graph as $G = G_2^N(X)$
            Get the Hamiltonian as $H = \text{Adj}(G)$
            Compute $\lambda(G)$
            Compute the revivals from the Néel state
        end if
    end while

A.2.3 The effect of low-density bridges on the two connected hypercubes

In Chapter 5 we showed that adding bridges to the two-hypercube model at first leads to an increase of revival fidelity at small λ, before a decrease at larger λ values. In this section we examine in detail the former regime and show that it can be understood as a tuning of the symmetric and anti-symmetric sectors of the two-hypercube model.

We focus on the first steps of the algorithm described in Appendix A.2.2, when the number of excitations of the vertices added is equal to 2. We will refer to these as bridges of dimension 2. As all states with two excitations on the same sublattice are already in the two hypercubes, all vertices added will have one excitation on each sublattice. These states are all located on the Hamming layer $N+1$, the same Hamming layer as the shared vertex that contains no excitations. Intuitively, in the many-body picture one can think these new states as helping 'spread' the support of the wave function on several states instead of just 'funnelling' the wave function onto a single state, $|000\ldots000\rangle$. This means that even if the wave function still reflects from this vertex, the reflected part of the wave function will have smaller magnitude, as there is no longer a high concentration of the wave function on this vertex – see Fig. A.5(a). However, as more bridges of dimension two are added, the degree of the vertices in the Hamming layers N and $N+2$ increases, and this could lead to reflection in this layer. In order to completely get rid of reflection one would need a smooth coupling profile, which can be achieved by also adding vertices in other Hamming layers, like in the PXP model. This would help get rid of reflection but at the price of having an inexact FSA. This is in line with what we observe as random bridges are added: no reflection but a leakage outside the FSA subspace.

For two-dimensional bridges, enforcing translation symmetry has the effect of modifying the edges between the Hamming layers N, $N+1$ and $N+2$ in an isotropic fashion. As a consequence, the FSA remains exact but the middle couplings are changed. Normally, both of these couplings are equal to $\beta_{\mathrm{middle}}{=}\sqrt{N}$, however adding V vertices changes the coupling to $\beta_{\mathrm{middle}}{=}\sqrt{N+V/N}$. In order to simplify computations, let us assume that N is even. Then there are
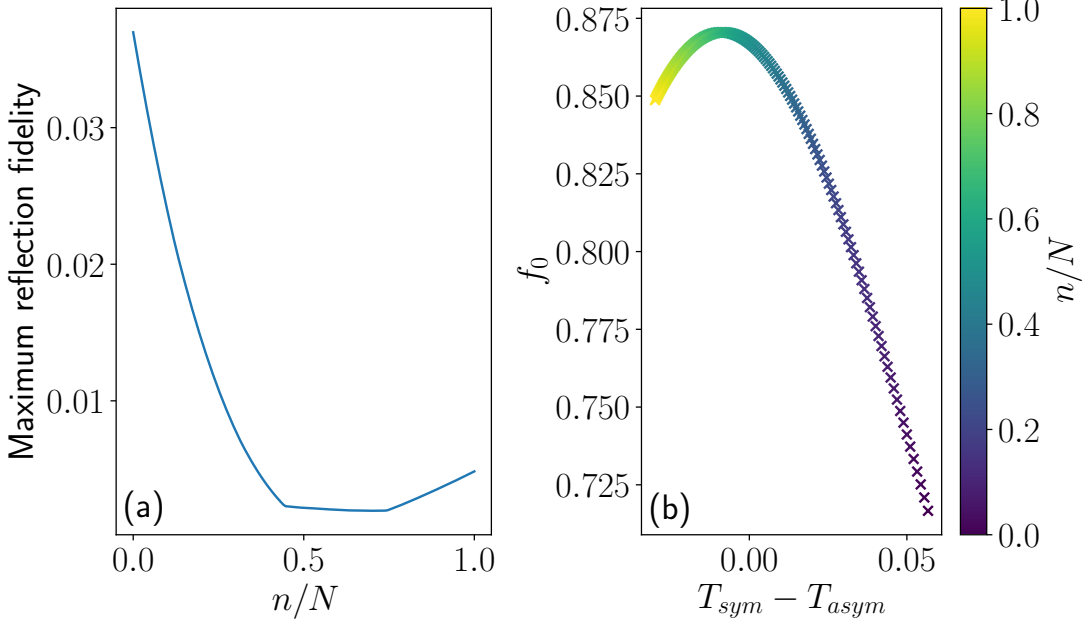
Figure A.5: Fidelity of revivals and reflection for two linked hypercubes of dimension $N=300$ as two-dimensional bridges are added. (a) Maximum fidelity of the reflection peak. (b) Fidelity of revivals with respect to the period difference between the symmetric and antisymmetric sectors.

$N/2$ bridges that can be added such that they are not equivalent under translation, and adding any of these implies adding $2N$ vertices. This means that the middle FSA couplings can take values $\beta_{\mathrm{middle}}=\sqrt{N+n}$, $n=0,2,4,\ldots,N$, hence $\sqrt{N}\leq\beta_{\mathrm{middle}}\leq\sqrt{2N}$. Furthermore, it means that details of the bridges do not matter, but only their number. So all random processes will be identical if only hypercubes of dimension 2 are added. The results of this process for two joined hypercubes of different sizes can be seen in Fig. A.5 (b), where the colour indicates the density of these bridges.

The results in Fig. A.5 can be understood in terms of the the two symmetry sectors mentioned in Section 5.4. Indeed, the bridges considered here only affect the symmetric sector, changing its coupling between the last two states from $\sqrt{2N}$ to $\sqrt{2(N+n)}$. This reduces the revival period of this sector, making it closer to the period of the anti-symmetric sector until it overshoots and makes them further apart. This can be seen in Fig. A.5, where the correlation between

the density of bridges n/N, the revival fidelity, and the period difference between the sectors is apparent. This also makes the reflection peak much smaller, as the two sectors almost exactly cancel out at $T \approx \pi$. The only thing preventing the reflection to be exactly 0 is the difference of revival amplitude between them.

A.3 Kinetically constrained scarred models: analytical derivation of $N_c = 4$ scarred regions

In Chapter 6, we presented a diagram, Fig. 6.8, showing regions of phase space of models of the form $H = \sum_n P_{n-1}^0 C_n P_{n+1}^0$ with local Hilbert space dimension $N_c = 4$ which host QMBS. We noted that optimal models in these diagrams could be roughly predicted by determining the values of parameters that yield a single-site Hamiltonian C_n with evenly spaced eigenvalues, such that the single-site dynamics is periodic. Further models with weaker revivals are obtained for C whose eigenvalue spacings differed by a ratio of 2. In the following we derive analytical expressions for the lines in Fig. 6.8 in Chapter 6.

Varying the matrix elements of C, we consider all Hermitian, purely imaginary, non-diagonal C, in analogy with the clock and spin Hamiltonians discussed in Chapter 6. We are free to rescale C such that one coupling has magnitude 1, so for $N_c = 4$, 5 couplings can be varied. We consider two slices of this 5 dimensional parameter space: (A) vary the next-nearest neighbour hoppings, $C_{02} = C_{13} = \alpha i$, while also varying $C_{03} = -\beta i$; (B) switch off next-nearest-neighbour hoppings while varying $C_{12} = -\alpha i$ and $C_{03} = -\beta i$. Explicitly:

$$
C_n^{(A)} = \begin{pmatrix} 0 & -i & \alpha i & -\beta i \\ i & 0 & -i & \alpha i \\ -\alpha i & i & 0 & -i \\ \beta i & -\alpha i & i & 0 \end{pmatrix},
\tag{A.72}
$$

$$
C_n^{(B)} = \begin{pmatrix} 0 & -i & 0 & -\beta i \\ i & 0 & -\alpha i & 0 \\ 0 & \alpha i & 0 & -i \\ \beta i & 0 & i & 0 \end{pmatrix}.
\tag{A.73}
$$
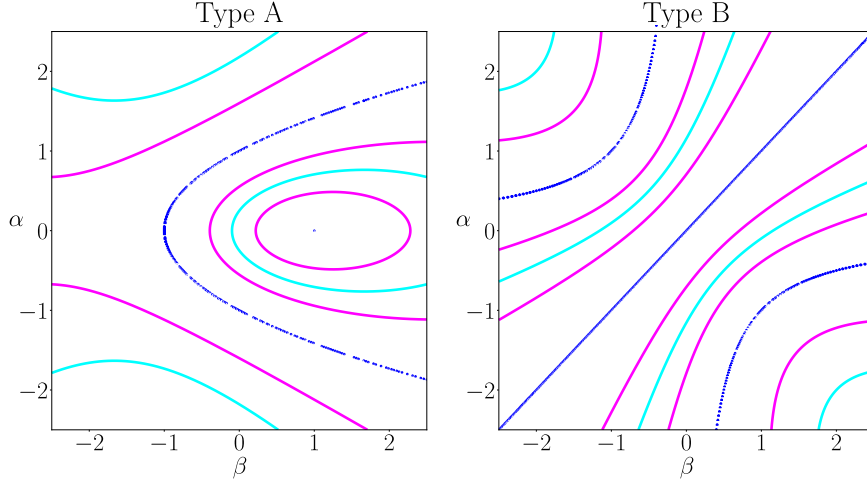
Figure A.6: Prediction of scarred models with strongest revivals based on the eigenvalue spacings of the single site operator C for $N_c = 4$. Left and right panels refer to two deformations of C in Eqs. (A.72), (A.73). Plotted here are: (a) equidistant eigenvalues, Eq. (A.79) (cyan), (b) eigenvalue spacings commensurate with ratio 2 (pink), Eq. (A.80),(A.81), (c) degenerate eigenvalues, Eq. (A.82), (A.83) (blue). These lines coincide with the regions of strong revivals in Fig. 6.8 in Chapter 6.

The characteristic eigenvalue equation for both these matrices reduces to the form

$$E^4 - aE^2 + b = 0, \tag{A.74}$$

with a and b being:

$$(A) \quad a = 3 + 2\alpha^2 + \beta, \tag{A.75}$$
$$b = 2\beta - 2\alpha^2 - 2\alpha^2\beta + \alpha^4 + \beta^2 + 1, \tag{A.76}$$
$$(B) \quad a = \alpha^2 + \beta^2 + 2, \tag{A.77}$$
$$b = 2\alpha\beta + \alpha^2\beta^2 + 1. \tag{A.78}$$

It follows that the eigenvalues E take the form

$$E_{1,\dots,4} = \mp \frac{1}{\sqrt{2}} \sqrt{a \pm \sqrt{a^2 - 4b}}.$$

These eigenvalues are symmetric about zero, such that the spacings $\Delta E_1 = \Delta E_3$, with $\Delta E_n = E_n - E_{n-1}$. The analytic prediction for robust scarred models, based on the single-site analysis, then reads:

- Equidistant eigenvalues:

$$9a^2 = 100b, \qquad \Delta E_2 = \Delta E_1, \tag{A.79}$$

- Commensurate eigenvalues with ratio 2:

$$4a^2 = 25b, \qquad \Delta E_2 = 2\Delta E_1, \tag{A.80}$$

$$25^2 = 676b, \qquad \Delta E_2 = \frac{1}{2}\Delta E_1, \tag{A.81}$$

- Degenerate eigenvalues:

$$a^2 = 4b, \qquad \Delta E_1 = \Delta E_3 = 0, \tag{A.82}$$

$$b = 0, \qquad \Delta E_2 = 0 \tag{A.83}$$

These equations are plotted in terms of parameters α, β in Fig A.6. These lines give the band of scarred models in our $N_c = 4$ scarred model diagram in Fig. 6.8 in Chapter 6.

A.4 PXP quantum hardware implementation: exponential scaling of ansatz bond dimension

In this appendix we will argue by induction that the L layer unitary circuit used to simulate the PXP model, Eq. (7.4), when expressed as a matrix product state

A. APPENDICES

(MPS), has a bond dimension which scales exponentially in the number of layers.

Recall in Section 7.2.2, we derived the form of the MPO which is equivalent to the unitary circuit ansatz with a single layer, that is, $L = 1$. This MPO is given in Eq. (7.7). To argue inductively that the bond dimension of the L layer MPS scales exponentially, we wish to express the $L = 2$ layer circuit ansatz $|\psi(\vec{\phi})\rangle = U(\vec{\phi})^2|000...\rangle$ as an MPS. For simplicity, consider the ansatz angles to be equivalent in the first and second layers. By repeated application of the unitary MPO $U(\vec{\phi})$ given in Eq. (7.7), we find this state can expressed as an MPS with bond dimension $D = 4$:

$$|\psi(\vec{\phi})\rangle = \sum_{\sigma,\theta} A^{\sigma_0}_{\theta_0} A^{\sigma_1}_{\theta_0\theta_1} A^{\sigma_2}_{\theta_1\theta_2}...A^{\sigma_{N-2}}_{\theta_{N-3}\theta_{N-2}} A^{\sigma_{N-1}}_{\theta_{N-2}}|\vec{\sigma}\rangle$$

$$A^{\sigma_0=0} = (\cos^2\phi_0, -\sin^2\phi_0, 0, 0)$$

$$A^{\sigma_0=1} = \left(0, 0, -\frac{i}{2}\sin 2\phi_0, -\frac{i}{2}\sin 2\phi_0\right)$$

$$A^{\sigma_n=0} = \begin{pmatrix} \cos^2\phi_n & -\sin^2\phi_n & 0 & 0 \\ \cos\phi_n & 0 & 0 & 0 \\ \cos\phi_n & 0 & 0 & 0 \\ 1 & 0 & 0 & 0 \end{pmatrix}$$

$$A^{\sigma_n=1} = \begin{pmatrix} 0 & 0 & -\frac{i}{2}\sin 2\phi_n & -\frac{i}{2}\sin 2\phi_n \\ 0 & 0 & -i\sin\phi_n & 0 \\ 0 & 0 & 0 & -i\sin\phi_n \\ 0 & 0 & 0 & 0 \end{pmatrix}$$

$$A^{\sigma_{N-1}=0} = (\cos 2\phi_{N-1}, \cos\phi_{N-1}, \cos\phi_{N-1}, 1)$$

$$A^{\sigma_{N-1}=1} = (-i\sin 2\phi_{N-1} - i\sin\phi_{N-1}, -i\sin\phi_{N-1}, 0)$$

To verify the dimension of the L layer MPS grows exponentially as 2^L, we must verify no svd compression is possible on the MPS states $|\psi(\vec{\phi})\rangle = U(\vec{\phi})^L|000...\rangle$. We check this explicitly for the $L = 2$ MPS.

Consider a tensor in the bulk:

$$A^{\sigma_n}_{\theta_n \theta_{n+1}} = A_{(\sigma_n \theta_n), \theta_{n+1}}$$
$$= U_{(\sigma_n \theta_n), \rho} S_{\rho, \rho} V^{\dagger}_{\rho, \theta_{n+1}}$$

Where $USV^{\dagger}$ is the singular value decomposition of the matrix $A_{(\sigma_n \theta_n), \theta_{n+1}}$. If any of the singular values in S are zero, we can carry out an exact truncation and the bond dimension D will not be maximal ($D < 4$). We compute the singular values as the eigenvalues of $AA^{\dagger}$ and verify that $D = 4$.

$$A_{(\sigma_n \theta_n), \theta_{n+1}} = \begin{pmatrix} \cos^2 \phi_n & -\sin^2 \phi_n & 0 & 0 \\ \cos \phi_n & 0 & 0 & 0 \\ \cos \phi_n & 0 & 0 & 0 \\ 1 & 0 & 0 & 0 \\ 0 & 0 & -\frac{i}{2} \sin 2\phi_n & -\frac{i}{2} \sin 2\phi_n \\ 0 & 0 & -i \sin \phi_n & 0 \\ 0 & 0 & 0 & -i \sin \phi_n \\ 0 & 0 & 0 & 0 \end{pmatrix}$$

$$AA^{\dagger} = \begin{pmatrix} \cos^4 \phi_n + \sin^4 \phi_n & \cos^3 \phi_n & \cos^3 \phi_n & \cos^2 \phi_n \\ \cos^3 \phi_n & \cos^2 \phi_n & \cos^2 \phi_n & \cos \phi_n \\ \cos^3 \phi_n & \cos^2 \phi_n & \cos^2 \phi_n & \cos \phi_n \\ \cos^2 \phi_n & \cos \phi_n & \cos \phi_n & 1 \end{pmatrix}$$
$$\bigoplus \begin{pmatrix} 2\cos^2 \phi_n \sin^2 \phi_n & \cos \phi_n \sin^2 \phi_n & \cos \phi_n \sin^2 \phi_n & 0 \\ \cos \phi_n \sin^2 \phi_n & \sin^2 \phi_n & 0 & 0 \\ \cos \phi_n \sin^2 \phi_n & 0 & \sin^2 \phi_n & 0 \\ 0 & 0 & 0 & 0 \end{pmatrix}$$

From the eigenvalues of $AA^{\dagger}$, we find the 4 singular values of $A_{(\sigma_n \theta_n), \theta_{n+1}}$ are:

$$\sigma^2 = \frac{1}{8} \Big(\pm 2\sqrt{2} \sqrt{\cos^4 \phi_n (-4\cos 2\phi_n + \cos 4\phi_n + 35)} + 4\cos 2\phi_n + \cos 4\phi_n + 11 \Big), \sin^2 \phi_n, \sin^2 \phi_n (\cos 2\phi_n + 2)$$

A. APPENDICES

For generic ϕ_n, we see no singular values are 0, thus we cannot truncate the tensor, such that the bond dimension is indeed $D = 4$. Given the $L = 2$ MPS state cannot be truncated, we conclude by induction that the scaling of the bond dimension of the MPS representation of the variational circuit ansatz scales exponentially as 2^L.

Bibliography

[1] Anderson, P. W. (1958). Absence of diffusion in certain random lattices. *Phys. Rev.*, 109:1492–1505. 1, 23

[2] Arute, F. et al. (2019). Quantum supremacy using a programmable super-conducting processor. *Nature*, 574(7779):505–510. 141, 157

[3] Babelon, O., Bernard, D., and Talon, M. (2003). *Introduction to Classical Integrable Systems*. Cambridge Monographs on Mathematical Physics. Cambridge University Press. 8

[4] Bai, Z., Demmel, J., Dongarra, J., Ruhe, A., and van der Vorst, H. (2000). *Templates for the Solution of Algebraic Eigenvalue Problems: A Practical Guide.* SIAM. 46, 48

[5] Basko, D., Aleiner, I., and Altshuler, B. (2006). Metal–insulator transition in a weakly interacting many-electron system with localized single-particle states. *Annals of Physics*, 321(5):1126 – 1205. 1

[6] Baxter, R. (1989). A simple solvable Z_N Hamiltonian. *Physics Letters A*, 140(4):155 – 157. 132

[7] Bernien, H., Schwartz, S., Keesling, A., Levine, H., Omran, A., Pichler, H., Choi, S., Zibrov, A. S., Endres, M., Greiner, M., Vuletic, V., and Lukin, M. D. (2017). Probing many-body dynamics on a 51-atom quantum simulator. *Nature*, 551:579. iv, xi, 2, 5, 24, 25, 26, 27, 31, 44, 120, 140, 159, 162

[8] Berry, M. V. and Tabor, M. (1977). Level clustering in the regular spectrum. *Proceedings of the Royal Society of London. A. Mathematical and Physical Sciences*, 356:375 – 394. 15

[9] Beugeling, W., Moessner, R., and Haque, M. (2014). Finite-size scaling of eigenstate thermalization. *Phys. Rev. E*, 89:042112. 18

[10] Beugeling, W., Moessner, R., and Haque, M. (2015). Off-diagonal matrix elements of local operators in many-body quantum systems. *Phys. Rev. E*, 91:012144. 18

[11] Bharti, K., Cervera-Lierta, A., Kyaw, T. H., Haug, T., Alperin-Lea, S., Anand, A., Degroote, M., Heimonen, H., Kottmann, J. S., Menke, T., Mok, W.-K., Sim, S., Kwek, L.-C., and Aspuru-Guzik, A. (2022). Noisy intermediate-scale quantum algorithms. *Rev. Mod. Phys.*, 94:015004. 141, 143

[12] Bohm, A., Ne'eman, Y., and Barut, A. O. (1988). *Dynamical Groups and Spectrum Generating Algebras: Vol. 1, 2.* World Scientific, Singapore, Singapore. 55

[13] Boixo, S., Isakov, S. V., Smelyanskiy, V. N., Babbush, R., Ding, N., Jiang, Z., Bremner, M. J., Martinis, J. M., and Neven, H. (2018). Characterizing quantum supremacy in near-term devices. *Nature Physics*, 14(6):595–600. 141

[14] Bravyi, S., DiVincenzo, D. P., and Loss, D. (2011). Schrieffer–wolff transformation for quantum many-body systems. *Annals of Physics*, 326(10):2793 – 2826. 28

[15] Buca, B., Tindall, J., and Jaksch, D. (2019). Non-stationary coherent quantum many-body dynamics through dissipation. *Nature Communications*, 10(1):1730. 1, 118

[16] Bull, K., Desaules, J.-Y., and Papić, Z. (2020). Quantum scars as embeddings of weakly broken Lie algebra representations. *Phys. Rev. B*, 101:165139. i, iv, 63, 120

[17] Bull, K., Martin, I., and Papić, Z. (2019). Systematic construction of scarred many-body dynamics in 1D lattice models. *Phys. Rev. Lett.*, 123:030601. ii, 112, 120

[18] Bunimovich, L. A. (1974). On ergodic properties of certain billiards. *Functional Analysis and Its Applications*, 8:254–255. 8, 10

[19] Bunimovich, L. A. (1979). On the ergodic properties of nowhere dispersing billiards. *Communications in Mathematical Physics*, 65:295–312. 8, 10

[20] Cerezo, M., Arrasmith, A., Babbush, R., Benjamin, S., Endo, S., Fujii, K., Mcclean, J., Mitarai, K., Yuan, X., Cincio, L., and Coles, P. (2021). Variational quantum algorithms. *Nature Reviews Physics*, 3:1–20. 142

[21] Chandran, A., Kim, I. H., Vidal, G., and Abanin, D. A. (2015). Constructing local integrals of motion in the many-body localized phase. *Phys. Rev. B*, 91:085425. 2, 23

[22] Chattopadhyay, S., Pichler, H., Lukin, M. D., and Ho, W. W. (2020). Quantum many-body scars from virtual entangled pairs. *Phys. Rev. B*, 101:174308. 54, 56

[23] Choi, S., Turner, C. J., Pichler, H., Ho, W. W., Michailidis, A. A., Papić, Z., Serbyn, M., Lukin, M. D., and Abanin, D. A. (2019). Emergent SU(2) dynamics and perfect quantum many-body scars. *Phys. Rev. Lett.*, 122:220603. i, 44, 51, 54, 75, 77, 108, 122, 160, 161

[24] Cirac, J. I., Pérez-García, D., Schuch, N., and Verstraete, F. (2021). Matrix product states and projected entangled pair states: Concepts, symmetries, theorems. *Rev. Mod. Phys.*, 93:045003. 142, 144

[25] D'Alessio, L., Kafri, Y., Polkovnikov, A., and Rigol, M. (2016). From quantum chaos and eigenstate thermalization to statistical mechanics and thermodynamics. *Adv. Phys.*, 65(3):239. 1, 5, 17

[26] Debnath, S., Linke, N., Figgatt, C., Landsman, K., Wright, K., and Monroe, C. (2016). Demonstration of a small programmable quantum computer with atomic qubits. *Nature*, 536:63–66. 142

[27] Desaules, J.-Y., Bull, K., Daniel, A., and Papić, Z. (2022). Hypergrid subgraphs and the origin of scarred quantum walks in many-body hilbert space. *Phys. Rev. B*, 105:245137. i, 85, 110, 120

[28] Desaules, J.-Y., Hudomal, A., Turner, C. J., and Papić, Z. (2021). Proposal for realizing quantum scars in the tilted 1D Fermi-Hubbard model. *Phys. Rev. Lett.*, 126:210601. 117

[29] Deutsch, J. M. (1991). Quantum statistical mechanics in a closed system. *Phys. Rev. A*, 43:2046. 1, 5, 16

[30] Deutsch, J. M. (2010). Thermodynamic entropy of a many-body energy eigenstate. *New Journal of Physics*, 12(7):075021. 19

[31] Deutsch, J. M. (2018). Eigenstate thermalization hypothesis. *IOPscience Reports on Progress in Physics*, 81(8):082001. 1, 5, 12, 17, 27, 167

[32] Deutsch, J. M., Li, H., and Sharma, A. (2013). Microscopic origin of thermodynamic entropy in isolated systems. *Phys. Rev. E*, 87:042135. 19

BIBLIOGRAPHY

[33] Falcioni, M., Marconi, U. M. B., and Vulpiani, A. (1991). Ergodic properties of high-dimensional symplectic maps. *Phys. Rev. A*, 44:2263–2270. 9

[34] Feder, D. L. (2006). Perfect quantum state transfer with spinor bosons on weighted graphs. *Phys. Rev. Lett.*, 97:180502. 120

[35] Fedorov, D., Peng, B., Govind, N., and Alexeev, Y. (2022). Vqe method: a short survey and recent developments. *Materials Theory*, 6. 142

[36] Fendley, P. (2014). Free parafermions. *Journal of Physics A: Mathematical and Theoretical*, 47(7):075001. 121, 122, 132, 135

[37] Figgatt, C., Maslov, D., Landsman, K., Linke, N., Debnath, S., and Monroe, C. (2017). Complete 3-qubit grover search on a programmable quantum computer. *Nature Communications*, 8:1918. 142

[38] Frey, P. and Rachel, S. (2022). Realization of a discrete time crystal on 57 qubits of a quantum computer. *Science Advances*, 8(9):eabm7652. 142

[39] García-Pérez, G., Rossi, M., and Maniscalco, S. (2020). Ibm q experience as a versatile experimental testbed for simulating open quantum systems. *npj Quantum Information*, 6:1. 142

[40] Gogolin, C. and Eisert, J. (2016). Equilibration, thermalisation, and the emergence of statistical mechanics in closed quantum systems. *Rep. Prog. Phys.*, 79(5):056001. 1, 5

[41] Golkar, S., Nguyen, D. X., and Son, D. T. (2016). Spectral sum rules and magneto-roton as emergent graviton in fractional quantum hall effect. *Journal of High Energy Physics*, 2016(1):21. 142

[42] Görg, F., Sandholzer, K., Minguzzi, J., Desbuquois, R., Messer, M., and Esslinger, T. (2019). Realisation of density-dependent peierls phases to couple dynamical gauge fields to matter. *Nat. Phys.* 140

[43] Haake, F. (2001). *Quantum Signatures of Chaos.* Physics and astronomy online library. Springer. 121

[44] Haldane, F. D. M. (2011). Geometrical description of the fractional quantum hall effect. *Phys. Rev. Lett.*, 107:116801. 142

[45] Hall, B. (2015). Lie groups, lie algebras, and representations. *Graduate Texts in Mathematics*, 222. 64

[46] Heller, E. J. (1984). Bound-state eigenfunctions of classically chaotic hamiltonian systems: Scars of periodic orbits. *Phys. Rev. Lett.*, 53:1515. 5, 23, 24, 38

[47] Ho, W. W., Choi, S., Pichler, H., and Lukin, M. D. (2019). Periodic orbits, entanglement, and quantum many-body scars in constrained models: Matrix product state approach. *Phys. Rev. Lett.*, 122:040603. 38, 121, 127

[48] Hudomal, A., Vasić, I., Regnault, N., and Papić, Z. (2020). Quantum scars of bosons with correlated hopping. *Communications Physics*, 3(1):99. 41, 117

[49] Huse, D. A., Nandkishore, R., and Oganesyan, V. (2014). Phenomenology of fully many-body-localized systems. *Phys. Rev. B*, 90:174202. 1, 5

[50] Iachello, F. (2006). *Spectrum Generating Algebras and Dynamic Symmetries*, pages 163–172. Springer Berlin Heidelberg, Berlin, Heidelberg. 55

[51] Iadecola, T. and Schecter, M. (2020). Quantum many-body scar states with emergent kinetic constraints and finite-entanglement revivals. *Phys. Rev. B*, 101:024306. 54, 56, 58, 59, 61, 160, 164

[52] IBM (2022a). Ibm quantum. `https://quantum-computing.ibm.com/`. 142

[53] IBM (2022b). Qiskit. `https://qiskit.org/`. 143

[54] IonQ (2022). Trapped ion quantum computing. `https://ionq.com/`. 142

[55] Jaksch, D., Cirac, J., Zoller, P., Rolston, S., Côté, R., and Lukin, M. (2000). Fast quantum gates for neutral atoms. *Physical Review Letters*, 85(10):2208. 24, 26

[56] Jordan, P. and Wigner, E. (1928). Über das paulische äquivalenzverbot. *Zeitschrift für Physik*, 47:631–651. 19

[57] Keesling, A., Omran, A., Levine, H., Bernien, H., Pichler, H., Choi, S., Samajdar, R., Schwartz, S., Silvi, P., Sachdev, S., Zoller, P., Endres, M., Greiner, M., Vuletic, V., and Lukin, M. D. (2019). Quantum Kibble-Zurek mechanism and critical dynamics on a programmable Rydberg simulator. *Nature*, 568(7751):207–211. 140

[58] Khatami, E., Pupillo, G., Srednicki, M., and Rigol, M. (2013). Fluctuation-dissipation theorem in an isolated system of quantum dipolar bosons after a quench. *Phys. Rev. Lett.*, 111:050403. 17, 18

BIBLIOGRAPHY

[59] Khemani, V., Hermele, M., and Nandkishore, R. M. (2020). Localization from hilbert space shattering: From theory to physical realizations. *Physical Review B*, 101:174204. 41

[60] Khemani, V., Laumann, C. R., and Chandran, A. (2019). Signatures of integrability in the dynamics of Rydberg-blockaded chains. *Phys. Rev. B*, 99:161101(R). 75, 112, 122

[61] Kim, I. H., Chandran, A., and Abanin, D. A. (2014). Local integrals of motion and the logarithmic lightcone in many-body localized systems. *arXiv preprint: 1412.3073*. 2

[62] Kirmani, A., Bull, K., Hou, C.-Y., Saravanan, V., Saeed, S. M., Papić, Z., Rahmani, A., and Ghaemi, P. (2022). Probing geometric excitations of fractional quantum hall states on quantum computers. *Phys. Rev. Lett.*, 129:056801. 142

[63] Klavžar, S. and Mollard, M. (2019). Daisy cubes and distance cube polynomial. *European Journal of Combinatorics*, 80:214–223. 181

[64] Kramer, P. and Saraceno, M., editors (1981). *Geometry of the TDVP*. Springer Berlin Heidelberg, Berlin, Heidelberg. 38

[65] Lanczos, C. (1950). An iteration method for the solution of the eigenvalue problem of linear differential and integral operators. *Journal of research of the National Bureau of Standards*, 45:255–282. 42

[66] Landau, L. D. and Lifshitz, E. M. (1976). *Mechanics, Third Edition: Volume 1 (Course of Theoretical Physics)*. Butterworth-Heinemann, 3 edition. 6

[67] Levkovich-Maslyuk, F. (2016). The bethe ansatz. *Journal of Physics A: Mathematical and Theoretical*, 49(32):323004. 13

[68] Li, H. and Haldane, F. D. M. (2008). Entanglement spectrum as a generalization of entanglement entropy: Identification of topological order in non-abelian fractional quantum Hall effect states. *Phys. Rev. Lett.*, 101:010504. 18

[69] Lieb, E., Schultz, T., and Mattis, D. (1961). Two soluble models of an antiferromagnetic chain. *Annals of Physics*, 16:407–466. 19

[70] Lin, C.-J. and Motrunich, O. I. (2019). Exact quantum many-body scar states in the Rydberg-blockaded atom chain. *Phys. Rev. Lett.*, 122:173401. 177

[71] Lin, S.-H., Dilip, R., Green, A. G., Smith, A., and Pollmann, F. (2021). Real- and imaginary-time evolution with compressed quantum circuits. *PRX Quantum*, 2:010342. 149

[72] Mark, D. K., Lin, C.-J., and Motrunich, O. I. (2020). Unified structure for exact towers of scar states in the Affleck-Kennedy-Lieb-Tasaki and other models. *Phys. Rev. B*, 101:195131. 118

[73] McDonald, S. W. and Kaufman, A. N. (1979). Spectrum and eigenfunctions for a hamiltonian with stochastic trajectories. *Phys. Rev. Lett.*, 42:1189–1191. 5

[74] Medenjak, M., Buča, B., and Jaksch, D. (2020). Isolated Heisenberg magnet as a quantum time crystal. *Phys. Rev. B*, 102:041117(R). 118

[75] Mehta, M. L. (2004). *Random matrices*, volume 142. Elsevier, 3rd edition. 12, 13, 110

[76] Michailidis, A. A., Turner, C. J., Papić, Z., Abanin, D. A., and Serbyn, M. (2020). Slow quantum thermalization and many-body revivals from mixed phase space. *Phys. Rev. X*, 10:011055. 38, 147, 149, 150, 151, 153

[77] Milek, B. and Seba, P. (1990). Singular continuous quasienergy spectrum in the kicked rotator with separable perturbation: Possibility of the onset of quantum chaos. *Physical Review A*, 42:3213–3220. 140

[78] Moudgalya, S., Bernevig, B. A., and Regnault, N. (2020a). Quantum many-body scars in a Landau level on a thin torus. *Phys. Rev. B*, 102:195150. 43

[79] Moudgalya, S., Bernevig, B. A., and Regnault, N. (2022). Quantum many-body scars and hilbert space fragmentation: a review of exact results. *Reports on Progress in Physics*, 85:086501. 2

[80] Moudgalya, S., Prem, A., Nandkishore, R. M., Regnault, N., and Bernevig, B. A. (2021). Thermalization and its absence within krylov subspaces of a constrained hamiltonian. *Memorial Volume for Shoucheng Zhang*, pages 147–209. 1, 3, 35, 39, 43, 45, 83, 160

[81] Moudgalya, S., Regnault, N., and Bernevig, B. A. (2018). Entanglement of exact excited states of Affleck-Kennedy-Lieb-Tasaki models: Exact results, many-body scars, and violation of the strong eigenstate thermalization hypothesis. *Phys. Rev. B*, 98:235156. 112, 118, 163

[82] Moudgalya, S., Regnault, N., and Bernevig, B. A. (2020b). η-pairing in hubbard models: From spectrum generating algebras to quantum many-body scars. *Phys. Rev. B*, 102:085140. 55, 56

[83] Nam, Y. S., Chen, J.-S., Pisenti, N. C., Wright, K., Delaney, C., Maslov, D. L., Brown, K. R., Allen, S., Amini, J. M., Apisdorf, J., Beck, K. M., Blinov, A., Chaplin, V., Chmielewski, M., Collins, C., Debnath, S., Ducore, A. M., Hudek, K. M., Keesan, M. J., Kreikemeier, S. M., Mizrahi, J., Solomon, P., Williams, M., Wong-Campos, J. D., Monroe, C. R., and Kim, J. (2020). Ground-state energy estimation of the water molecule on a trapped-ion quantum computer. *npj Quantum Information*, 6:1–6. 142

[84] Neill, C. et al. (2021). Accurately computing the electronic properties of a quantum ring. *Nature*, 594(7864):508–512. 141

[85] Nielsen, M. A. and Chuang, I. L. (2010). *Quantum Computation and Quantum Information: 10th Anniversary Edition*. Cambridge University Press. 18, 143

[86] Nándor, S. (2004). Proof of the ergodic hypothesis for typical hard ball systems. *Annales Henri Poincaré*, 5:203–233. 7

[87] O'Brien, T. E., Abanin, D. A., Vidal, G., and Papić, Z. (2016). Explicit construction of local conserved operators in disordered many-body systems. *Phys. Rev. B*, 94:144208. 2, 23

[88] O'Connor, P. W. and Heller, E. J. (1988). Quantum localization for a strongly classically chaotic system. *Phys. Rev. Lett.*, 61:2288–2291. 23

[89] O'Dea, N., Burnell, F., Chandran, A., and Khemani, V. (2020). From tunnels to towers: Quantum scars from Lie algebras and q-deformed Lie algebras. *Phys. Rev. Research*, 2:043305. 56, 118

[90] Oganesyan, V. and Huse, D. A. (2007). Localization of interacting fermions at high temperature. *Phys. Rev. B*, 75:155111. 16, 80, 110, 126

[91] Ok, S., Choo, K., Mudry, C., Castelnovo, C., Chamon, C., and Neupert, T. (2019). Topological many-body scar states in dimensions one, two, and three. *Phys. Rev. Research*, 1:033144. 40

[92] Paeckel, S., Köhler, T., Swoboda, A., Manmana, S., Schollwöck, U., and Hubig, C. (2019). Time-evolution methods for matrix-product states. *Annals of Physics*, 411:167998. 38, 149

[93] Pai, S. and Pretko, M. (2019). Dynamical scar states in driven fracton systems. *Phys. Rev. Lett.*, 123:136401. 41, 82

[94] Papic, Z. and Balram, A. C. (2022). Fractional quantum hall effect in semiconductor systems. *arXiv preprint: 2205.03421*. 142

[95] Pathria, R. K. and Beale, P. D. (2011). *Statistical Mechanics*. Academic Press, Boston, MA, third edition. 7, 18

[96] Patrick, K., Caudrelier, V., Papić, Z., and Pachos, J. K. (2019). Interaction distance in the extended xxz model. *Phys. Rev. B*, 100:235128. 18

[97] Poulin, D., Hastings, M., Wecker, D., Wiebe, N., Doherty, A., and Troyer, M. (2014). The trotter step size required for accurate quantum simulation of quantum chemistry. *Quantum Information and Computation*, 15. 149

[98] Quantinuum (2022). Pytket documentation. `https://cqcl.github.io/tket/pytket/api/index.html`. 143

[99] Rigol, M. (2009a). Breakdown of thermalization in finite one-dimensional systems. *Phys. Rev. Lett.*, 103:100403. 18

[100] Rigol, M. (2009b). Quantum quenches and thermalization in one-dimensional fermionic systems. *Phys. Rev. A*, 80:053607. 18

[101] Rigol, M., Dunjko, V., and Olshanii, M. (2008). Thermalization and its mechanism for generic isolated quantum systems. *Nature*, 452:854–858. 18

[102] Robinson, N. J., James, A. J. A., and Konik, R. M. (2019). Signatures of rare states and thermalization in a theory with confinement. *Phys. Rev. B*, 99:195108. 1

[103] Roffe, J. (2019). Quantum error correction: an introductory guide. *Contemporary Physics*, 60(3):226–245. 141

[104] Rokhsar, D. S. and Kivelson, S. A. (1988). Superconductivity and the quantum hard-core dimer gas. *Phys. Rev. Lett.*, 61:2376–2379. 60

[105] Ros, V., Müller, M., and Scardicchio, A. (2015). Integrals of motion in the many-body localized phase. *Nuclear Physics B*, 891(0):420 – 465. 2, 23

[106] Sachdev, S. (2011). *Quantum Phase Transitions*. Cambridge University Press, 2 edition. 19

[107] Sala, P., Rakovszky, T., Verresen, R., Knap, M., and Pollmann, F. (2020). Ergodicity breaking arising from hilbert space fragmentation in dipole-conserving hamiltonians. *Phys. Rev. X*, 10:011047. 41, 43

[108] Sandvik, A. (2011). Computational studies of quantum spin systems. *AIP Conference Proceedings*, 1297:135. 31

[109] Santos, L. F., Polkovnikov, A., and Rigol, M. (2011). Entropy of isolated quantum systems after a quench. *Phys. Rev. Lett.*, 107:040601. 19

[110] Santos, L. F. and Rigol, M. (2010). Onset of quantum chaos in one-dimensional bosonic and fermionic systems and its relation to thermalization. *Phys. Rev. E*, 81:036206. 18

[111] Saxena, N., Severini, S., and Shparlinski, I. (2007). Parameters of integral circulant graphs and periodic quantum dynamics. *International Journal of Quantum Information*, 5. 120

[112] Schecter, M. and Iadecola, T. (2019). Weak ergodicity breaking and quantum many-body scars in spin-1 XY magnets. *Phys. Rev. Lett.*, 123:147201. 54, 56, 118, 160

[113] Schollwöck, U. (2011). The density-matrix renormalization group in the age of matrix product states. *Annals of Physics*, 326(1):96 – 192. 142, 144, 151

[114] Schrieffer, J. R. and Wolff, P. A. (1966). Relation between the Anderson and Kondo Hamiltonians. *Phys. Rev.*, 149:491–492. 28

[115] Schweizer, C., Grusdt, F., Berngruber, M., Barbiero, L., Demler, E., Goldman, N., Bloch, I., and Aidelsburger, M. (2019). Floquet approach to $\mathbb{Z}_2$ lattice gauge theories with ultracold atoms in optical lattices. *Nature Physics*, 15:1168–1173. 140

[116] Serbyn, M., Abanin, D. A., and Papić, Z. (2021). Quantum many-body scars and weak breaking of ergodicity. *Nature Physics*, 17(6):675–685. iv, 2, 39, 43

[117] Serbyn, M., Papić, Z., and Abanin, D. A. (2013). Local conservation laws and the structure of the many-body localized states. *Phys. Rev. Lett.*, 111:127201. 1

[118] Shiraishi, N. (2019). Connection between quantum-many-body scars and the Affleck–Kennedy–Lieb–Tasaki model from the viewpoint of embedded Hamiltonians. *Journal of Statistical Mechanics: Theory and Experiment*, 2019(8):083103. 41, 177

[119] Shiraishi, N. and Mori, T. (2017). Systematic construction of counterexamples to the eigenstate thermalization hypothesis. *Phys. Rev. Lett.*, 119:030601. 1, 3, 35, 39, 41, 45, 83, 160

[120] Shriner, J. F., Mitchell, G. E., and von Egidy, T. (1991). Fluctuation properties of spacings of low-lying nuclear levels. *Zeitschrift für Physik A Hadrons and Nuclei*, 338:309–318. 13

[121] Sinai, Y. G. (1970). Dynamical systems with elastic reflections. ergodic properties of dispersing billiards. *Russian Mathematical Surveys*, 25:137–189. 7

[122] Sopena, A., Gordon, M. H., Sierra, G., and López, E. (2021). Simulating quench dynamics on a digital quantum computer with data-driven error mitigation. *Quantum Science and Technology*, 6(4):045003. 142

[123] Srednicki, M. (1994). Chaos and quantum thermalization. *Phys. Rev. E*, 50:888. 1, 5, 12, 16, 17

[124] Srednicki, M. (1996). Thermal fluctuations in quantized chaotic systems. *Journal of Physics A: Mathematical and General*, 29(4):L75. 12, 17

[125] Srednicki, M. (1999). The approach to thermal equilibrium in quantized chaotic systems. *Journal of Physics A: Mathematical and General*, 32(7):1163. 12, 17

[126] Surace, F. M., Dalmonte, M., and Silva, A. (2021). Quantum local random networks and the statistical robustness of quantum scars. *arXiv preprint: 2107.00884*. 117

[127] Surace, F. M., Mazza, P. P., Giudici, G., Lerose, A., Gambassi, A., and Dalmonte, M. (2020). Lattice gauge theories and string dynamics in rydberg atom quantum simulators. *Phys. Rev. X*, 10:021041. 140

[128] Sutherland, B. (2004). *Beautiful Models: 70 Years of Exactly Solved Quantum Many-body Problems*. World Scientific. 1, 5

[129] Turner, C. J., Desaules, J.-Y., Bull, K., and Papić, Z. (2021). Correspondence principle for many-body scars in ultracold rydberg atoms. *Phys. Rev. X*, 11:021021. 39

[130] Turner, C. J., Michailidis, A. A., Abanin, D. A., Serbyn, M., and Papic, Z. (2018a). Weak ergodicity breaking from quantum many-body scars. *Nat. Phys.*, 14:745. iv, 2, 5, 24, 30, 35, 37, 61, 73, 78

[131] Turner, C. J., Michailidis, A. A., Abanin, D. A., Serbyn, M., and Papić, Z. (2018b). Quantum scarred eigenstates in a Rydberg atom chain: Entanglement, breakdown of thermalization, and stability to perturbations. *Phys. Rev. B*, 98:155134. 3, 27, 30, 44, 51, 53, 54, 77, 78, 112, 133, 160, 167

[132] van Voorden, B., Marcuzzi, M., Schoutens, K., and Minář, J. v. (2021). Disorder enhanced quantum many-body scars in Hilbert hypercubes. *Phys. Rev. B*, 103:L220301. 117

[133] Verhulst, F. (1990). *Nonlinear Differential Equations and Dynamic Systems*. Springer Berlin, Heidelberg. 10

[134] Vernier, E., O'Brien, E., and Fendley, P. (2019). Onsager symmetries in -invariant clock models. *Journal of Statistical Mechanics: Theory and Experiment*, 2019(4):043107. 122

[135] von Neumann, J. (1929). Beweis des ergodensatzes und des h-theorems in der neuen mechanik. *Zeitschrift für Physik*, 57:30–70. 12

[136] Wang, Y., Li, Y., Yin, Z.-q., and Zeng, B. (2018). 16-qubit ibm universal quantum computer can be fully entangled. *npj Quantum Information*, 4. 142

[137] Weimer, H., Müller, M., Lesanovsky, I., Zoller, P., and Büchler, H. P. (2010). A Rydberg quantum simulator. *Nature Physics*, 6:382 EP –. Article. 24

[138] Whitsitt, S., Samajdar, R., and Sachdev, S. (2018). Quantum field theory for the chiral clock transition in one spatial dimension. *Phys. Rev. B*, 98:205118. 122, 123

[139] Wigner, E. P. (1955). Characteristic vectors of bordered matrices with infinite dimensions i. *Annals of Mathematics*, 62:541–545. 13, 14

[140] Wigner, E. P. (1958). On the distribution of the roots of certain symmetric matrices. *Annals of Mathematics*, 67:325. 15

[141] Wootton, J. R. (2020). Benchmarking near-term devices with quantum error correction. *Quantum Science and Technology*, 5(4):044004. 141

[142] Yang, B., Hu, Z.-X., Papić, Z., and Haldane, F. D. M. (2012). Model wave functions for the collective modes and the magnetoroton theory of the fractional quantum hall effect. *Phys. Rev. Lett.*, 108:256807. 142

[143] Yang, C. N. (1989). η pairing and off-diagonal long-range order in a hubbard model. *Phys. Rev. Lett.*, 63:2144–2147. 55

[144] Yilmaz, Y. and Bogomolny, E. (2015). Quantum ising model in transverse and longitudinal fields: Chaotic wave functions. *Journal of Physics A: Mathematical and Theoretical*, 50. 19

[145] Yoshinaga, A., Hakoshima, H., Imoto, T., Matsuzaki, Y., and Hamazaki, R. (2022). Emergence of hilbert space fragmentation in ising models with a weak transverse field. *Phys. Rev. Lett.*, 129:090602. 117

[146] Zee, A. (2016). *Group Theory in a Nutshell for Physicists*. In a Nutshell. Princeton University Press. 64

[147] Zhao, H., Vovrosh, J., Mintert, F., and Knolle, J. (2020). Quantum many-body scars in optical lattices. *Physical review letters*, 124 16:160604. 41